Dissertation zur Erlangung des Doktorgrades
der Fakultät Chemie und Pharmazie
der Ludwig-Maximilians-Universität München

Moisture Stability of Hybrid Perovskite Solar Cells

Yinghong Hu

aus

Hefei, China

2018

Erklärung

Diese Dissertation wurde im Sinne von § 7 der Promotionsordnung vom 28. November 2011 von Herrn Dr. Pablo Docampo betreut und von Herrn Prof. Dr. Thomas Bein von der Fakultät für Chemie und Pharmazie vertreten.

Eidesstattliche Versicherung

Diese Dissertation wurde eigenständig und ohne unerlaubte Hilfe bearbeitet.

München, den 25.05.2018 .....

Yinghong Hu

Dissertation eingereicht am:	25.05.2018
Erstgutachter:	Prof. Dr. Thomas Bein
Zweitgutachter:	Senior Lecturer Dr. Pablo Docampo
Tag der mündlichen Prüfung:	03.07.2018

Acknowledgement

First and foremost, I would like to express my deepest gratitude to my supervisors, Dr. Pablo Docampo and Prof. Dr. Thomas Bein. Your guidance and support during the past four years during my Master and PhD studies were invaluable for me to accomplish my goals and to evolve into an independent, truly passionate scientist. Thank you for your contributions to all our publications and for reviewing this thesis.

Pablo, I can't thank you enough for putting so much effort in teaching me everything about perovskite photovoltaics starting from the beginning of my Master's thesis and for always taking your time for discussions. Your drive and enthusiasm ("This is f***ing awesome!") motivated me to strive for more, even if I did not always see the significance of my work at the first glance. You taught me the importance of keeping good collaborations running, which were often decisive for the success of my projects. Thank you for being my mentor and a good friend, it was a pleasure to work and enjoy some good laughs with you in the lab! I finally learned that it is not that hard to use a razorblade for the sample preparation.

Thomas, I am very grateful to be part of your research group. Thank you for giving me the freedom and the means to pursue my scientific interests and for your valuable advices during our numerous subgroup meetings. Under your guidance, I learned the importance of being excited about my research without neglecting a critical evaluation of the results. Besides, your endless support in terms of applications for awards and conference participations allowed me to gain more self-confidence and to expand my scientific network at various international conference meetings.

Of course, my PhD thesis would not have been possible without the contributions of my numerous collaboration partners, within and outside the LMU.

Many thanks go to my in-house collaborators Prof. Dr. Achim Hartschuh from the LMU for funding my work via the BMBF project CISOVKSIT, as well as Dr. Matthias Handloser and Irene Grill for ToF measurements. Working with AK Hartschuh helped me to get a better understanding of charge transport in solar cells. I would also like to thank my CISOVSKIT collaborators from the ZSW in Stuttgart, Dr. Erik Ahlswede, Moritz Schultes and especially Dr. Jonas Hanisch for ToF-SIMS measurements. I really appreciate your efforts and reliability.

My special thanks go to Piers Barnes, Aurélien Leguy, Davide Moia, Philip Calado, Diego Alonso-Alvarez, Andrew Telford and Xiaoe Li from Imperial College London. We had so many fruitful collaboration projects due to your incredible knowledge in the photophysics of solar cells

and I am grateful for the opportunity to work with you. Thank you for hosting me during my three-week visit at ICL. It was a fantastic time at the physics department and I learned a lot about TPV, TrotTr, and PL measurements.

Aurel, if you ask me, you deserve the Oscar for the most efficient collaborator more than I do. Sharing the nice hydration paper with you still feels like a great honor to me and who would have thought that it would become the foundation for my thesis! Thanks as well for inviting me to the awesome skiing trip in Les Gets with Piers, Sian, Davide, James and Flo aka Kommander Bimberle with the sneaky eyes. I will never forget how much fun we had together, especially when we played sausage-themed *Balderdash* and when I tricked you in *Avalon*.

Davide, you have been a great collaboration partner as well. You were always helpful whenever I visited ICL, thank you so much for your time and efforts! I hope that the electroabsorption results of the numerous devices I have sent will soon start to answer some really interesting questions (instead of creating more of them) about perovskite solar cells. Maaaa!

I would like to thank my collaborators Prof. Dr. Peter Müller-Buschbaum and Johannes Schlipf from TU Munich for GIWAXS measurements. Johannes, thank you for your patience and the long discussions through which I learned a lot about GIWAXS. It was not only a pleasure for me to work with you on scientific projects, but also to have you as a member of the NIM student board. Singing *Purple Rain* with you during the NIM-GP summer retreat at Schloss Hirschberg remains a truly memorable moment for me.

Furthermore, I would like to thank Dr. Tom Savenije and Eline Hutter from TU Delft for our great collaboration using their expertise in TRMC measurements, which allowed me to learn a lot about charge recombination and transport. Eline, it was an incredible experience for me to have you as a collaboration partner. Since I admired how efficiently you always work, I was trying my best to speed up my correspondence, my lab work and the data analysis (without forgetting to eat and sleep). But keeping up with you is… really hard, if not impossible. Tom and Eline, the paper machine! :)

My gratitude also goes to Prof. Dr. Vladimir Dyakonov, Dr. Andreas Baumann, Dr. Kristofer Tvingstedt and Philipp Rieder from the Julius-Maximilians-Universität Würzburg. Our collaboration based on your expertise in TSC experiments helped me to broaden my horizon regarding the characterization of trap states in solar cells. Besides, it was always fun to meet you at conferences and to have a good time together!

Moreover, I would like to thank Prof. Dr. Wolfram Jaegermann and Michael Wussler from TU Darmstadt for XPS measurements.

Many thanks also go to Dr. Steffen Schmidt from the LMU for the vast amount of SEM images and insightful discussions about EDX analysis.

Furthermore, I would like to thank many people who made my stay as a visiting student at CSIRO in Clayton, Australia an unforgettable, incredibly life-enhancing episode of my PhD, especially Dr. Anthony Chesman and Dr. Askhat Jumabekov. Anthony, thank you so much for your assistance to enable my visit and for making me feel welcome in your group from the very start. I appreciated your scientific inputs as well as your open and friendly way of communicating, which helped me to reflect a lot on good leadership qualities. Ash, I would not have been able to have this great experience of working at CSIRO without your support. I am extremely thankful for everything you have done for me, from helping me to initiate our collaboration, to teaching me the art of fabricating back-contact perovskite solar cells, to introducing me to so many great people in Australia. I would like to thank my CSIRO co-workers, especially Dechan, Doojin, Mei, Regine, Aron, Mark, Giovanni, Jack, Daniel, Jay, Yeonsu, Emma and Kevin. In addition, my gratitude goes to the groups of my collaboration partners at Monash University, Prof. Dr. Udo Bach and Prof. Dr. Christopher McNeill.

In this context, I would like to thank NIM for supporting and sponsoring my visit at CSIRO. Special thanks go to Dr. Peter Sonntag and Silke Mayerl-Kink, who were always willing to assist me with NIM-related organisational issues. Criss, thanks a lot for the beautiful cover image you designed for me! I would also like to acknowledge CeNS for the travel award which allowed me to attend the PSCO conference 2017 in Oxford.

In terms of administrative issues, I am thankful that I could always rely on the assistance of our secretary Regina, followed by Corinna. My thanks also go to our technical assistant Tina, who ensures that our everyday work in the lab is going smoothly. Furthermore, I would like to thank Ralf Hiermaier, Tomas Gisičius and Fabian Kreuzer from the fine mechanics workshop, who were always extremely helpful to me.

I feel lucky to get the opportunity to supervise four talented students during my PhD: Harry Rodriguez, Verena Langowski, Laura Spies and Harry Jones. Thank you all for your passion, dedication and happiness you brought into the lab. Some of my projects would not have been realized without your hard work. Each one of you had a different personality and individual strengths, which allowed me to learn about different facets of leading and mentoring. It was always a pleasure to work and laugh with you.

One of the reasons why I really enjoyed going to the lab in the last four years was certainly the nice working atmosphere in our research group. Whenever I faced a problem, I could count on a

helping hand within the group. AK Bein group events such as BBQs, Wiesn visits or skiing/hiking days made me feel blessed to be part of a big family. My special thanks go to the perovskite subgroup: Meltem Aygüler, Nadja Giesbrecht, Michiel Petrus, Andreas Binek, Fabian Hanusch, Enrico Greul, Maximilian (Ed) Sirtl, Philipp Angloher and Chia-Hong (Charles) Chung. I cherish you guys not only as colleagues but also as my friends. I highly appreciate that our relationship was always built on trust, open-mindedness and respect for each other. Scientific and non-scientific discussions during the lunch breaks were often enlightening, sometimes silly, but always entertaining. Thank you for making my PhD enjoyable every day!

Andi, thank you so much for making our lab the most organized and clean lab I know. I agree with you, going on conferences with you and Michiel was simply legendary, I will miss that a lot.

Of course, my two perovschica office mates who accompanied my journey as a PhD student from the very start deserve my special thanks: Nadja, thank you for feeding us with delicious cupcakes, for your accurate weather forecasts, and for not breaking anything that was vital for my PhD. :) Meltem, thank you for being my “twin sister”, for all the unforgettable conference/holiday trips, and for laughing with me so loudly that our office neighbors started to complain. Aşkım!

I would also like to thank my dear friends, Alex, Steffi, Franzi, Roland and Kim for always being there for me. My deepest gratitude goes to my family, especially to my parents and my sister Amy for their unconditional love and endless support.

亲爱的爸爸，我在此也想非常感谢你。如果没有你不断的支持与无尽的父爱，也就不会有我今天这篇博士论文。谢谢你的指导！

Finally, I want to thank a very special person. Michiel, you are the best colleague, friend and partner I could wish for. I am incredibly lucky that our ways were meant to cross and that we share the memories of three awesome years at the LMU. Thank you for your support, advice, humor, creativity (What would my thesis be without our hydration bag?) and the sausage/Kungfu Panda lab coat, which was the perfect revenge for the fairy/fries lab coat (credits to Pablo as well). I am deeply grateful for having you in my life.

Table of contents

List of abbreviations

0D	Zero-dimensional
1D	One-dimensional
2D	Two-dimensional
3D	Three-dimensional
AFM	Atomic force microscopy
ALD	Atomic layer deposition
AM 1.5G	Air mass 1.5 global
a-Si	Amorphous silicon
at%	Atomic percentage
BA	*n*-Butylammonium
BAI	*n*-Butylammonium iodide
BAMAPI	*n*-Butylammonium methylammonium lead iodide
CB	Conduction band
CIGS	Copper indium gallium diselenide
CP	Critical point
c-Si	Crystalline silicon
DC	Direct current
deg	Degree(s)
DMF	*N*,*N*-Dimethylformamide
DMSO	Dimethyl sulfoxide
DSSC	Dye-sensitized solar cell
EDX	Energy dispersive X-ray
EMA	Effective medium
EQE	External quantum efficiency
ETL	Electron transport layer
ETM	Electron transporting material
FA	Formamidinium

FAI	Formamidinium iodide
FF	Fill factor
FTO	Fluorine-doped tin oxide
FWHM	Full width half maximum
GIWAXS	Grazing-incidence wide-angle X-ray scattering
HOMO	Highest occupied molecular orbital
HTL	Hole transport layer
HTM	Hole transporting material
IPA	Isopropyl alcohol
ITO	Indium tin oxide
J-V	Current-voltage
kWh	Kilowatt hour(s)
LED	Light-emitting diode
Li-TFSI	Lithium bistrifluoromethanesulfonimidate
LOC	Long-chained organic cation
LPK	Layered perovskite
MA	Methylammonium
MABr	Methylammonium bromide
MAI	Methylammonium iodide
$MAPbI_3$	Methylammonium lead iodide
MAPI	Methylammonium lead iodide
MPP	Maximum power point
MSE	Mean squared error
NREL	National Renewable Energy Laboratory
OPO	Optical parametric oscillator
OPV	Organic photovoltaics
PCBM	[6,6]-Phenyl-C_{61}-butyric acid methyl ester
PCE	Power conversion efficiency
PEA	Phenylethylammonium
PEAI	Phenylethylammonium iodide

PEAMAPI	Phenylethylammonium methylammonium lead iodide
PEDOT:PSS	Poly(3,4-ethylenedioxythiophene)-poly(styrenesulfonate)
PentA	Pentylammonium
PentAI	Pentylammonium iodide
PentAMAPI	Pentylammonium methylammonium lead iodide
PL	Photoluminescence
PMMA	Poly(methyl methacrylate)
PSC	Perovskite solar cell
PTAA	Poly(triarylamine)
PV	Photovoltaic(s)
QDSC	Quantum dot solar cell
RH	Relative humidity
rms	Root mean square
rpm	Revolutions per minute
SEM	Scanning electron microscopy
spiro-OMeTAD	2,2',7,7'-*tetrakis*-(*N*,*N*-di-*p*-methoxyphenylamine)-9,9'-spirobifluorene
tBP	4-*tert*-Butylpyridine
TCO	Transparent conductive oxide
TCSPC	Time-correlated single photon counting
THTO	Tetrahydrothiophene-1-oxide
ToF	Time-of-flight
ToF-SIMS	Time-of-flight secondary ion mass spectrometry
TRMC	Time-resolved microwave conductivity
TSC	Thermally stimulated current
TWy	Terawatt year(s)
UV	Ultraviolet
UV-Vis	Ultraviolet-visible
VB	Valence band
VBM	Valence band maximum

wt%	Weight percentage
XPS	X-ray photoelectron spectroscopy
XRD	X-ray diffraction

Abstract

Thin film photovoltaics based on organic-inorganic hybrid perovskites has advanced as one of the most promising solar cell technologies within the last decade. Record device efficiencies exceeding 22% have been recently achieved, making perovskite solar cells (PSCs) a serious contender for established silicon-based and other thin film photovoltaic technologies. Long-term device stability is crucial for the commercial realization of this emerging solar cell technology. Identifying the factors which affect the stability of PSCs and understanding the degradation mechanisms in hybrid perovskites are key aspects that need to be addressed for the development of environmentally stable solar cells. In particular, elucidating and improving the moisture stability of PSCs remains one of the major challenges.

In this thesis, we first investigate the moisture-induced degradation in the archetypal hybrid perovskite: methylammonium lead iodide $CH_3NH_3PbI_3$. Using *in situ* X-ray diffraction (XRD) techniques, we identify the initial degradation products upon exposure to humid air. We examine the reversibility of the hydration reaction in the perovskite material and its implication for solar cell performance. Furthermore, we reveal that the precursor stoichiometry strongly affects the device efficiency and the moisture stability of the resulting PSCs.

In addition, state-of-the-art perovskites comprising Cs and Rb cation additives are subjected to our investigations. Since these multiple-cation mixed-halide perovskites show better device performance and higher moisture stability than $CH_3NH_3PbI_3$, understanding the role of the different cations promise to unlock further improvements regarding efficiency and stability. We unravel the effect of Cs and Rb additives on the trap landscape, the recombination kinetics and the charge carrier mobility in the resulting PSCs by combining three different characterization techniques: time-of-flight (ToF), time-resolved microwave conductivity (TRMC) and thermally stimulated current (TSC) measurements. Besides, we study the impact of these inorganic cation additives on the moisture stability of multiple-cation mixed-halide perovskite thin films. Our results indicate that particularly Rb ions can lead to rapid phase segregation upon exposure to a high level of humidity, which is detrimental to device performance.

Furthermore, we present the concept of dimensionality engineering as an approach to improve the moisture stability of hybrid perovskites. The introduction of long-chained, hydrophobic organic cations leads to the formation of 2D perovskites, which show increased resilience against exposure to humidity compared to classical 3D hybrid perovskite materials such as $CH_3NH_3PbI_3$.

By optimizing the deposition protocols regarding solvent additives and the annealing process, we show that the phase purity and crystal orientation in 2D perovskite thin films can be carefully controlled. This is important to tune the optoelectronic properties of the 2D perovskite and the desired charge transport direction according to the application field.

Finally, we demonstrate a novel 2D/3D perovskite bilayer architecture in order to increase the moisture stability of PSCs without compromising device efficiency. We show that a thin layer of 2D perovskite can be created on top of a 3D perovskite film via a facile solution-based process. The 2D perovskite layer not only acts as a moisture barrier but additionally improves the interface between the perovskite and the hole transporting material, which increases the open-circuit voltage of the resulting PSC. We believe that the combined dimensionality and interfacial engineering can become a universal approach to achieve high-efficiency PSCs with long-term stability.

1 Introduction

1.1 Photovoltaics

1.1.1 The need for photovoltaics

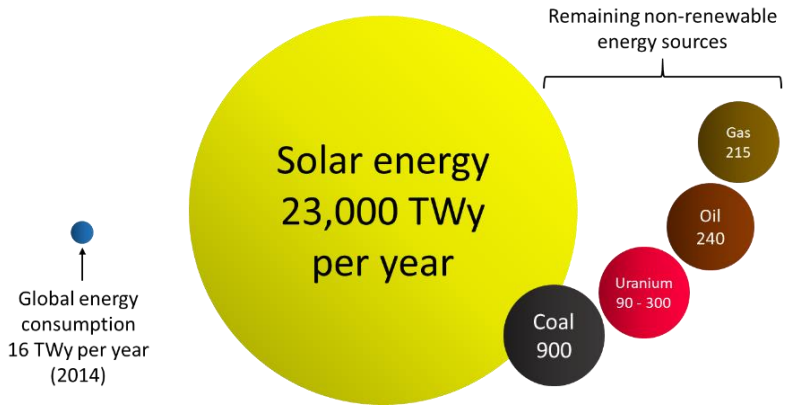

Figure 1.1 Schematic illustration of the abundance of solar energy compared to non-renewable energy sources and the annual global energy consumption in 2014.[1] The size of the spheres corresponds to the approximate amount of energy provided by the respective source.

The exit from nuclear and fossil-fuel energy is unavoidable, and the reasons are manifold. First, the global population and therewith the demand for energy is rapidly growing, while non-renewable energy sources, such as uranium, coal, fossil oil and gas are steadily dwindling. Second, the combustion of fossil fuels and the associated amount of CO_2 emission contribute to global climate change, which will have dramatic economic and political and social impacts. In order to counteract these scenarios, it is imperative to increase the contribution of renewable energy sources (such as wind, water and sun) to the generation of power.

The energy of the sun can play a key role in this endeavour thanks to its great abundance. Every year, the solar energy reaching the surface of the earth is about 23,000 terawatt years (TWy), while the global energy consumption is 16 TWy in 2014 (Figure 1.1).[1] In other words, the solar power that reaches our globe in six hours would be sufficient to cover the world energy consumption for a full year, if we can harvest the energy of the sunlight in an efficient way.

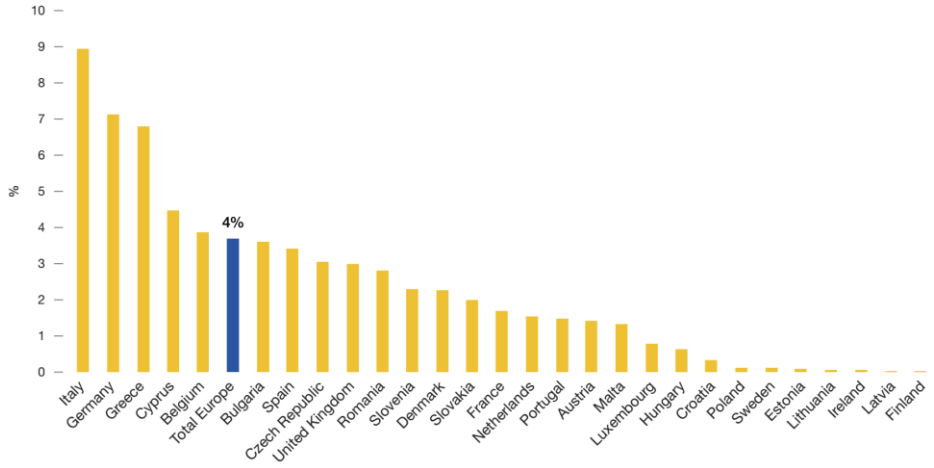

Figure 1.2 Share of electricity demand covered by solar power in 28 European countries (EU-28) in 2016.[2]

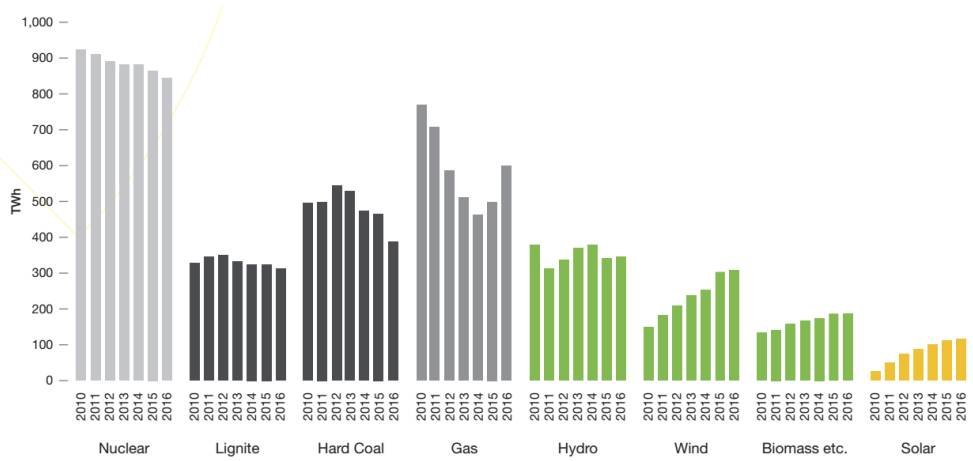

Figure 1.3 Development of power output by different technologies from 2010 to 2016 in the EU-28 countries.[2]

Photovoltaics (PV) is the technology that directly converts solar energy in the form of light into electricity. In PV industry, cost per Watt is the evaluation parameter for the profitability of PV technologies and it depends on several factors, e.g. installation costs, module efficiency and solar cell lifetime. Although the price for PV systems has been declining by around 75% in less than 10 years, reaching 2.4 US cents per kilowatt hour (kWh) in 2016, the share of electricity demand covered by solar energies reaches only 4% in Europe (Figure 1.2). Currently, the total power generation in Europe is still dominated by non-renewable energy sources such as hard coal, lignite and nuclear resources (Figure 1.3).[2] The development of more efficient and low-cost PV

innovations is necessary to further accelerate the growth of the global solar power capacity, targeting the 900 GW mark in the year 2021 (Figure 1.4).

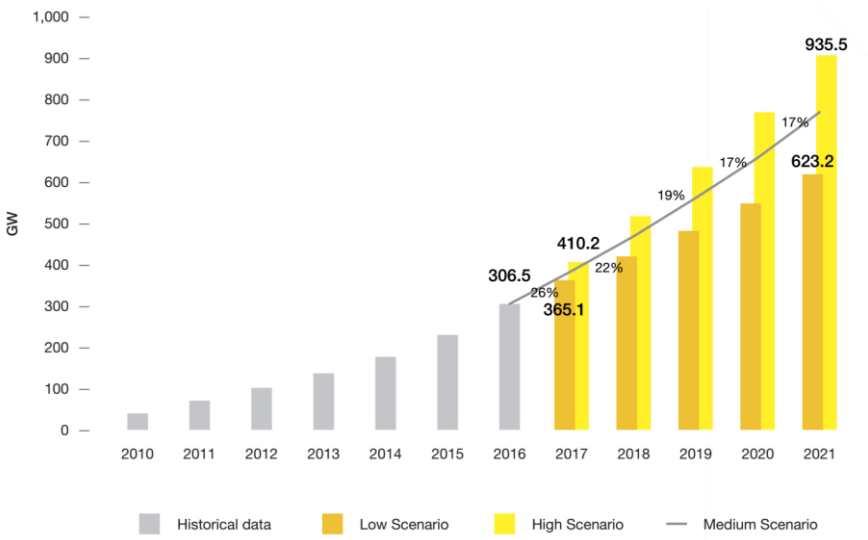

Figure 1.4 Development of world total solar PV market scenarios 2017–2021. The grey columns represent historical values for the total global installed PV capacity. The yellow columns, the grey solid line and the orange columns are anticipated growth of the PV market according to low, medium and high scenarios, respectively.[2]

1.1.2 Development of solar cells

The photovoltaic effect was first discovered by the French physicist Edmond Becquerel in 1839,[3] while the first working solar cell based on selenium was invented by Charles Fritts more than 40 years later, in 1883.[4] However, the rise of coal-fired electric power plants established by Thomas Edison in the 1880's slowed down the development of alternative energy sources, among others, also photovoltaic devices. It was not until 1941 when Russell Ohl, an engineer who worked at the Bell Laboratories, patented the first silicon p-n junction solar cell that PV started its advancement to a realistic contender for large-scale power generation.[5, 6]

Currently, the photovoltaic market is dominated by silicon-based solar cells. The first-generation PV technologies employ crystalline silicon (c-Si) as photoabsorber, not only showing respectable device performances with lab record efficiencies around 25% but also longevity. With an average degradation rate of 0.5% per year, c-Si solar cells can guarantee functionality for 25 years under

working conditions.[7] However, c-Si is a semiconductor with an indirect band gap, meaning that a thick c-Si layer of several hundred microns is required to absorb the major part of the incident sunlight.[8] The large film thickness does not only mean higher material costs but also limits c-Si solar modules to rigid glass substrates, which results in fragility towards mechanical forces. Besides, very high purity and low defect concentrations within the photoabsorber are necessary for Si-wafer-based solar cells to perform optimally. This leads to time- and energy-intensive manufacturing processes, relatively high production costs and a slow return on investment.

Second-generation PV technologies use thin films of cadmium telluride (CdTe) or copper indium gallium diselenide (CIGS) as the light-absorbing layer.[9-11] These inorganic semiconductors have a direct band gap and high absorption coefficients. This, in turn, reduces the required film thickness of the photoactive material to only a few µm in order to absorb sufficient sunlight (Figure 1.5) and to reach efficiencies close to c-Si devices (up to 22.6% for CIGS solar cells).[12] Using less raw material for the absorption layer promises to decrease the production costs of thin film PV compared to c-Si-based PV.

However, the disadvantages are the need for rare (Te) or toxic (Cd) metal precursors and their production processes under high-vacuum and/or high-temperature conditions. The latter leads to high energy costs for the device fabrication as well as a restricted choice of substrates. These drawbacks are overcome by another thin film PV technology based on amorphous silicon (a-Si), which can be vacuum-processed at low temperatures. Nevertheless, a-Si solar cells tend to yield comparably poor efficiencies of about 10% because of high defect concentrations in the silicon layer associated with the lack of crystallinity.[13]

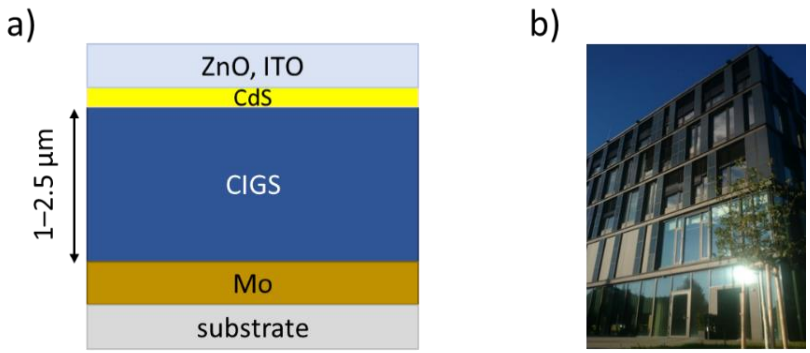

Figure 1.5 (a) Schematic cross-section of a CIGS thin film solar cell. (b) CIGS solar panel installed on the facade of the Center for Solar Energy and Hydrogen Research Baden-Württemberg (Zentrum für Sonnenenergie- und Wasserstoffforschung, ZSW) in Stuttgart, Germany.

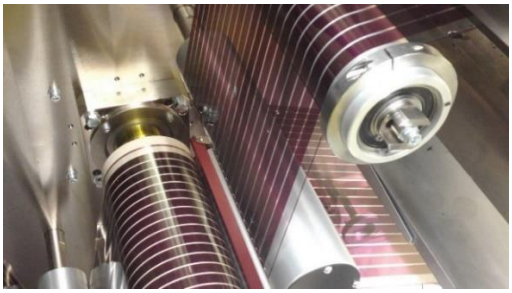

Figure 1.6 Fabrication of flexible organic photovoltaic (OPV) devices using roll-to-roll printing techniques.

More recently, several alternatives such as dye-sensitized solar cells (DSSCs), organic photovoltaics (OPV) and quantum dot solar cells (QDSCs) have been developed to meet the demand for low-cost solar cells.[14-19] These emerging PV technologies rely on solution-based, low-temperature device fabrication and therefore offer compatibility with flexible substrates and the potential for large-scale roll-to-roll processing (Figure 1.6). The feasibility of light-weight solar installations paired with the enormous variability of the device color and design pattern makes architectural integration of these PV technologies attractive for windows and facades (Figure 1.7). In terms of device performance, however, DSSCs (11.9% record efficiency), OPV (11.5%) and QDSCs (13.4%) still lag far behind conventional c-Si solar cells.[20] Additionally, these types of solar cells suffer from rapid degradation and the insufficient device stability diminishes their market potential.

Figure 1.7 The SwissTech Convention Center at the École Polytechnique Fédérale de Lausanne (EPFL) in Switzerland, equipped with a glass facade composed of colorful dye-sensitized solar cells (DSSCs).

In the past few years, a new class of thin film PV termed perovskite solar cells (PSCs) have been evolving at an unprecedented pace into one of the most promising PV technologies (Figure 1.8). PSCs have attracted a large degree of attention in the scientific community because they show the unique combination of outstanding performance and facile solution processability. Holding the promise for low-cost, light-weight and high-efficiency solar cells, PSCs have the potential to revolutionize the PV market.

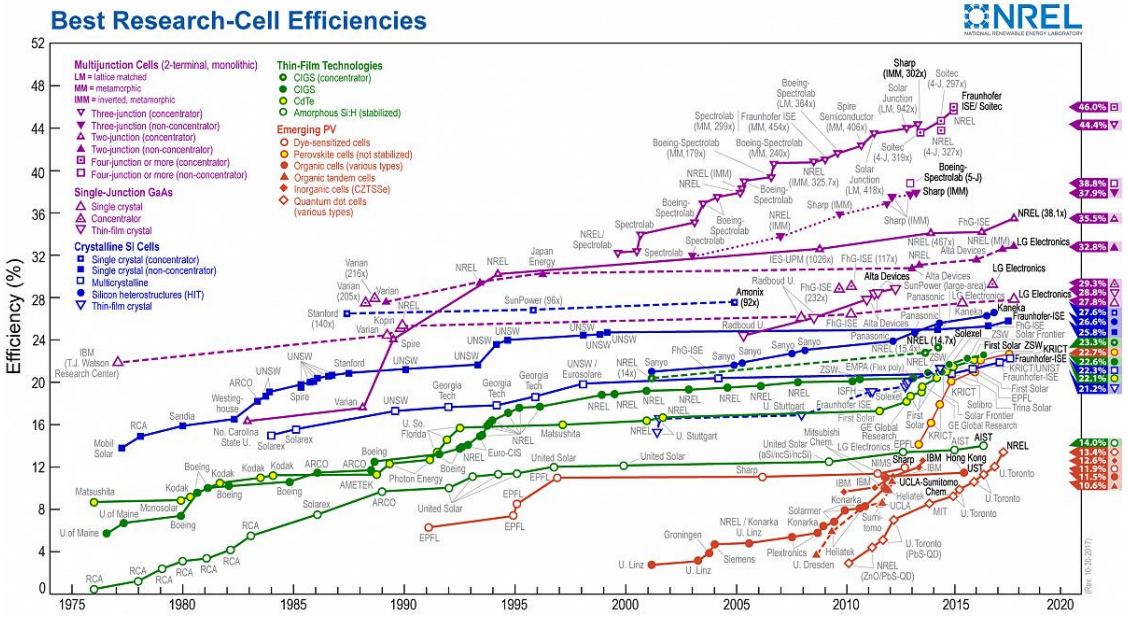

Figure 1.8 Record efficiencies of different photovoltaic technologies published by the National Renewable Energy Laboratory (NREL).[20]

1.2 Emergence of perovskite solar cells

1.2.1 Crystal structure of organic-inorganic hybrid perovskites

The heart of a PSC is its light-absorbing layer, comprising an intriguing semiconducting material termed “hybrid perovskite”. In general, perovskites are compounds that crystallize in the same crystal structure as calcium titanate $CaTiO_3$, a mineral named after the Russian mineralogist Lev Aleksevich Perovski.[21] Figure 1.9 illustrates the typical perovskite crystal structure with the composition ABX_3, where A represents a cation, B is usually a metal cation and X represents the

anions. From a crystallographic point of view, if we look at an ideal cubic perovskite crystal structure, the smaller B cation is located at the corners of a cubic unit cell, octahedrally coordinated by 6 X anions, thus forming a three-dimensional network of corner-sharing BX_6 octahedra. The larger A cation resides in the void created by eight octahedra, therefore cuboctahedrally coordinated by 12 X anions.

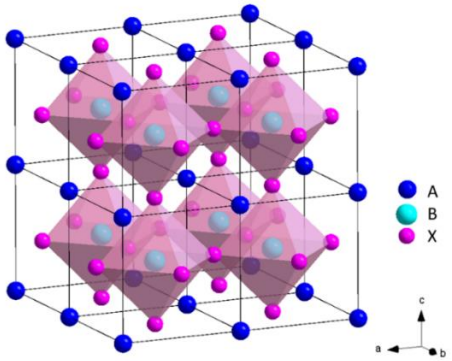

Figure 1.9 Schematic representation of the cubic ABX_3 perovskite crystal structure.

For photovoltaic applications, the currently most interesting perovskite materials are organic-inorganic hybrid compounds incorporating small organic A cations such as methylammonium (MA) $CH_3NH_3^+$, Pb^{2+} ions as B cations, and halide ions (I^-, Br^- or Cl^-) as X. Methylammonium lead iodide, first described by Weber in 1978, can be seen as the archetype of hybrid perovskite compounds for photovoltaics.[22] Moreover, mixtures of different ion species occupying the A, B or X site are also possible, depending on the ionic radii of the components.

In order to predict the intrinsic stability of ABX_3 perovskite structures, an empirical evaluation parameter referred to as the tolerance factor *t* was introduced by Goldschmidt:[23]

$$t = \frac{R_A + R_B}{\sqrt{2}(R_B + R_X)} \tag{1.1}$$

where R_A, R_B and R_X are the ionic radii for the corresponding ions (A, B and X), respectively. Based on an idealized solid-sphere model, the tolerance factor equals 1 for the ideal cubic perovskite crystal structure. Most of the stable hybrid lead halide perovskites exhibit a tolerance factor of $0.81 < t < 1.11$,[24] leading to deviations from the cubic structure at room temperature. However, phase transitions from less symmetric to higher symmetric structures are common for hybrid perovskites at elevated temperatures. This is in agreement with the fact that

methylammonium lead iodide ($MAPbI_3$) with t = 0.83 forms a stable tetragonal structure at room temperature, while its cubic phase is stabilized upon heating above 327 K.[24, 25]

1.2.2 Properties of hybrid perovskites

The immense interest in methylammonium lead iodide perovskite has been triggered by its exciting optoelectronic properties which have been under extensive investigations during the last decade. This classical hybrid perovskite exhibits various outstanding features, such as high absorption coefficient,[26] narrow direct band gap,[27] extraordinarily long charge diffusion length[28] and high photoluminescence quantum efficiency.[29] These intriguing properties make this class of semiconductors highly promising candidates for photovoltaic applications.

Figure 1.10 Photograph of cesium lead halide perovskite nanocrystal dispersions with varying halide compositions, yielding a broad range of fluorescence colors under UV-light illumination.

Furthermore, the optoelectronic properties of the perovskite material (e.g. the band gap and therewith the fluorescence wavelength) can be easily fine-tuned by tailoring their chemical composition (Figure 1.10). In addition to the archetypal $MAPbI_3$ perovskite compound, a broad variety of related hybrid perovskite materials has been explored by introducing different inorganic or organic ions into the crystal structure, such as formamidinium (FA, $CH(NH_2)_2^+$), guanidinium ($C(NH_2)_3^+$), Cs^+, Sn^{2+}, Br^- or Cl^-.[30-37] The great structural and optical variety of hybrid perovskites makes this family of semiconductors attractive for applications beyond PV, for example in light-emitting diodes (LEDs),[38, 39] lasers,[29, 40] or field effect transistors.[41, 42]

In the PV research community, impressive achievements regarding PSCs device efficiency within an astonishingly short developmental period have been fueling the excitement about hybrid perovskites. In particular, the efficiency of PSCs rapidly advanced through the introduction of the solid-state hole transporter spiro-OMeTAD which was simultaneously reported by Lee *et al.* and

Kim *et al.* in 2012.[43, 44] Subsequent research activities have been focused on the improvement of the perovskite deposition technique, compositional engineering of the perovskite material and optimization of contact layers. Within only eight years, PSC efficiency has soared from 3.81% reported by Miyasaka and co-workers,[45] to 22.1% (highest reported certified PCE, 2017),[46] leapfrogging other competing PV technologies such as OPV or DSSCs.

In addition, unlike other high-performance PV materials which require expensive vacuum-deposition techniques or high processing temperatures, hybrid perovskite thin films can be synthesized using solution-based fabrication methods. The mild deposition conditions allow the usage of polymer-based substrates with low melting points for PSCs, which makes flexible and light-weight PV modules feasible.[47, 48] Simple deposition methods combined with the abundance of precursor materials and high device efficiency propel the rise of PSCs as a potential low-cost alternative to established PV technologies.

1.2.3 Working principle of perovskite solar cells

A typical PSC comprises a multi-layer device architecture, where the individual functional layers have a thickness of only 10–600 nm. Therefore, PSCs are classified as thin film PV technology. Commonly, a transparent substrate such as glass or polymer foil is covered with a patterned transparent conductive oxide (TCO) electrode layer. Indium tin oxide (ITO) and fluorine-doped tin oxide (FTO) are the most regularly used TCOs as front contacts. Subsequently, a charge selective layer with high transmittance is deposited, followed by the hybrid perovskite as the light-absorbing layer and another charge selective extraction layer. After deposition of the rear contact, mostly through evaporation of a metal electrode (e.g. Au, Ag), the solar cell is completed.

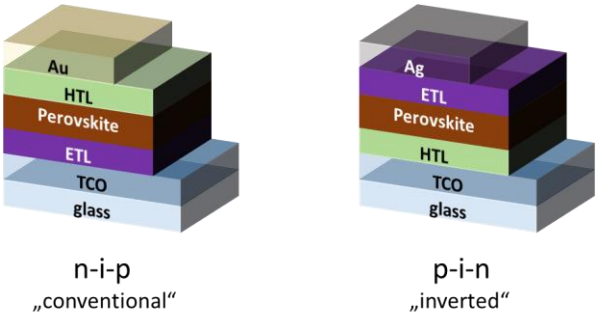

Figure 1.11 Different device configurations of planar heterojunction perovskite solar cells.

Charge selective layers can be either n-type (electron transport layer, ETL) or p-type (hole transport layer, HTL) between which the perovskite photoabsorber is sandwiched. Depending on the order of the charge selective layers, two different device configurations for PSCs can be distinguished (see Figure 1.11). The "conventional" n-i-p architecture is derived from dye-sensitized solar cells, in which the perovskite was first employed as a photoactive dye in a mesoporous TiO_2 scaffold.[45] Later, the thickness of the mesoporous TiO_2 layer for electron extraction was gradually reduced until only a thin compact TiO_2 layer served as a transparent ETL, followed by the perovskite and HTL (e.g. spiro-OMeTAD) deposition. Consequently, the resulting device had a planar n-i-p heterojunction configuration. By comparison, in the "inverted" p-i-n architecture, the TCO is covered first with an HTL (e.g. poly(3,4-ethylenedioxythiophene)-poly(styrenesulfonate), PEDOT:PSS), completed by the perovskite layer and the ETL (e.g. [6,6]-phenyl-C_{61}-butyric acid methyl ester, PCBM).[49] To optimize device performance and stability through variation of the interfaces between perovskite and charge-selective layers, a large variety of materials has been explored for ETL and HTL.[50-53]

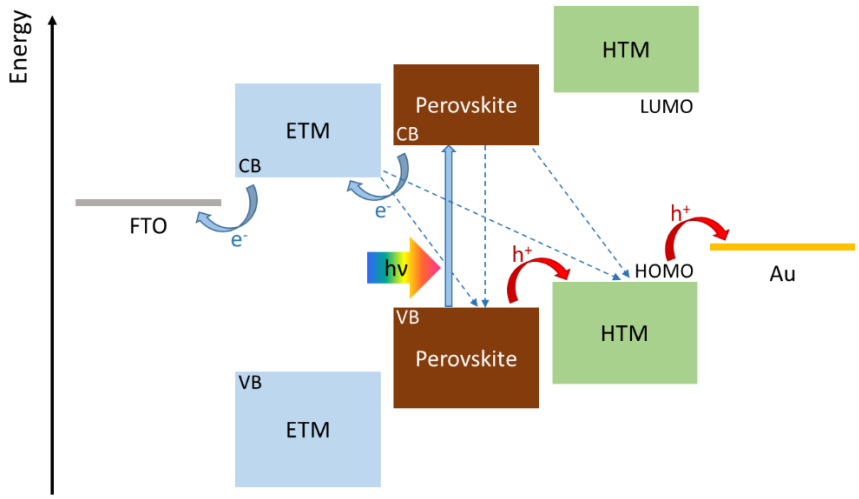

Figure 1.12 Schematic illustration of charge transfer and recombination processes in a perovskite solar cell. The thick blue and red arrows indicate the desirable transfer processes for electrons from the perovskite to the electron transporting material (ETM) and holes from the perovskite to the hole transporting material (HTM), respectively. The dashed arrows indicate undesirable losses associated with recombination processes.

A simplified scheme of the working principle of a planar heterojunction perovskite solar cell is depicted in Figure 1.12. Sunlight passes through the transparent FTO-glass substrate and electron

transport material, before getting absorbed by the thin perovskite layer. Absorbed photons with energies larger than the band gap of the perovskite semiconductor are able to excite electrons from the valence band (VB) to the conduction band (CB) of the material, leaving a "hole" behind in the VB, which can be treated as a positively charged quasi-particle. The created electron-hole pair (also referred to as an exciton) dissociates into free charge carriers within picoseconds. Given the fact that the exciton binding energy in methylammonium lead iodide is considered to be lower than kT (~25 meV), rapid exciton dissociation already at room temperature is likely.

Owing to the long diffusion length (>1 µm) which is usually larger than the perovskite film thickness, photo-generated charge carriers live long enough to travel to the respective interface between perovskite and the electron transporting material (ETM) or hole transporting material (HTM). The electrons are selectively transported through the ETM, while the holes are blocked at this interface. By contrast, only holes are allowed to pass the hole extraction layer. After overcoming the selective charge extraction barriers, the carriers are then transported to the respective electrodes (e.g. FTO as cathode and Au as the anode), which are connected via an electric circuit and a current flow is generated.

In reality, not 100% of the incident photons are converted into electrons and contribute to the power output of a solar cell. An important figure of merit is the charge carrier lifetime, defined as the time frame in which free electrons and holes can exist before recombination occurs. During the charge transport process, recombination events (indicated by dashed arrows in Figure 1.12) lead to decreased carrier density and thus, losses in the photovoltaic device performance. The different recombination mechanisms contributing to the decay in charge carrier density $n(t)$ over time can be expressed through the following rate equation:[54]

$$\frac{dn}{dt} = -k_1 n - k_2 n^2 - k_3 n^3 \qquad (1.2)$$

Here, k_1 is the rate constant for trap-assisted (monomolecular) recombination, k_2 is associated with band-to-band (bimolecular) recombination and k_3 is the rate constant related to a many-body Auger recombination process. Reducing the number of recombination pathways both within the bulk materials as well as at the individual interfaces is of vital importance for the maximization of solar cell performance.

For efficient charge extraction at the selective contacts, a good energy level alignment between ETM or HTM and the perovskite layer is necessary. Importantly, the conduction bands (CBs) of ETM and perovskite need to match to enable "downhill" electron transfer as shown in Figure 1.12. By contrast, the valence band (VB) of the perovskite needs to be placed above the highest occupied molecular orbital (HOMO) level of the HTM to enable "uphill" hole transfer. Balanced

charge extraction avoids the accumulation of a charged species at one interface and can have a strong influence on solar cell efficiency.[55] Overcoming losses via recombination processes by meticulous interfacial engineering is currently dominating the research activities in the field of PSCs.[56-61]

1.3 Stability of perovskite solar cells

Despite the potential for high-efficiency, low-cost photovoltaics that hybrid perovskite materials hold, we still face several challenges that impede the commercialization of PSCs. One of the main obstacles that PSCs must overcome is their poor environmental stability upon exposure to heat, UV-light, oxygen or humidity. Besides PCE, the main factor that determines the cost per kWh is the lifetime of PV devices. Market-dominating crystalline silicon solar cells set a high standard for long-term stability with an average degradation rate of 0.5% losses per year.[7] This guarantees a module lifetime around 25 years under operational conditions. PSCs must target comparable levels of stability to become economically feasible and to compete with established technologies on the PV market.

While the pursuit of high device efficiencies has dominated at the initial stage of PSC research, the focus of recent research activities has been slowly shifting towards stability-related limitations. In the pasts few years, various extrinsic and intrinsic degradation factors that are detrimental to device lifetime have been identified.[7] Extrinsic degradation factors arise from the multi-layered device architecture, where changes within the charge extraction layers under working conditions affect the device efficiency. For instance, crystallization of the hole transporter spiro-OMeTAD under thermal stress, as well as migration of dopant salts within the HTM or gold atoms from the electrode have been related to an irreversible decrease in solar cell performance.[62-64] Besides, it has been reported that mesoporous TiO_2 as ETL absorbs UV-light which triggers degradation reactions within the PSC.[65] Degradation related to extrinsic factors can be addressed by replacing the contact materials and the introduction of appropriate buffer layers.[53]

By contrast, intrinsic degradation factors arise from the nature of the perovskite material and are therefore less straightforward to resolve. Understanding the origin of the intrinsic instability of hybrid perovskites provides valuable guidance for tailoring the perovskite materials accordingly in order to improve their environmental stability. For example, lead halide perovskites show ion migration under bias and illumination, which can result in anomalous hysteresis in current-voltage

scans.[66-69] Additionally, the light-induced migration of halide ions in mixed-halide perovskites can affect device performance due to phase segregation into iodide- and bromide-rich regions.[70-73]

In addition to ionic movements in hybrid perovskites that usually lead to reversible losses in PCE, the rapid, irreversible decomposition of the photoabsorber remains a major challenge in the field of PSCs. In particular, organic-inorganic hybrid perovskites are notorious for their susceptibility to moisture, which overshadows the exciting PSC results achieved in laboratories under exclusion of humidity.

The correlation between perovskite degradation and moisture is a highly complex issue and has caused some debate in the scientific community. The interaction between hybrid perovskite and water molecules depends on several factors, such as perovskite composition, level of humidity and time of exposure. While low humidity conditions have been reported to be beneficial for perovskite film formation, high humidity levels generally result in degradation of unencapsulated devices (Figure 1.13).

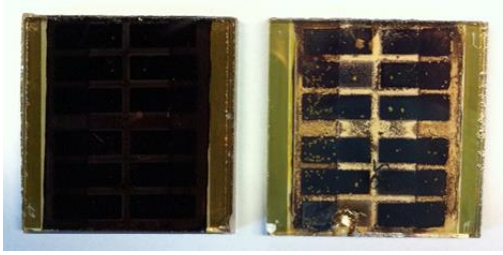

Figure 1.13 Photograph of an intact PSC (left) and a degraded device after exposure to moisture (right).

The presence of a low degree of humidity (around 30% relative humidity in air) during film processing has been shown to improve perovskite crystal morphology and to enhance PSC performance.[74-76] The state-of-the-art PSCs are fabricated in a dry box under controlled air humidity below 1%. It has been suggested that moisture-assisted perovskite film growth benefits from the adsorption of water molecules at grain boundaries, which induces the merging of perovskite crystals, thus increasing grain size and reducing the number of pinholes. On the other hand, it has been demonstrated that exposure of PSCs to relative humidity levels higher than 50% generally leads to degradation of the photoactive layer which has detrimental consequences for device performance. A systematic, comprehensive study of the moisture-induced degradation mechanisms in PSCs is necessary to counteract these reaction pathways and to prolong device

lifetime. Different experimental and theoretical approaches have been developed to rationalize the degradation processes occurring in hybrid perovskites.

Niu *et al.* proposed the following reaction equations for the irreversible decomposition of $CH_3NH_3PbI_3$ into PbI_2, HI and CH_3NH_2 in the presence of water.[77] According to the authors, the hygroscopic nature of MAI allows it to be easily leached out from the perovskite structure by water. MAI further decomposes into the volatile components methylamine, CH_3NH_2 and hydroiodic acid, HI which can evaporate from the sample. Furthermore, HI can also be oxidized by oxygen in air to form elemental iodine and water. The authors suggested that the driving force for this reaction is the shift of the reaction equilibrium to the degradation side by irreversible removal of volatile degradation products according to Le Châtelier's principle. Similarly, Frost *et al.* proposed an acid-base reaction between the $CH_3NH_3^+$ cation and H_2O as the first degradation step, where the deprotonation of MA results in the phase change of both HI and methylamine, ultimately leaving behind PbI_2 as the only byproduct.[78]

In contrast, other authors reported that water can also induce the crystallization of hydrate phases in hybrid perovskites. The formation of a hydrate structure of $CH_3NH_3PbI_3$ was first suggested by Weber.[22] Later, Vincent *et al.* investigated the properties of $(CH_3NH_3)_4PbI_6 \cdot 2\ H_2O$, a crystal phase which forms by the addition of aqueous $Pb(NO_3)_2$ to an aqueous solution of CH_3NH_3I.[79] The pale yellow dihydrate phase spontaneously transforms into the black $CH_3NH_3PbI_3$ perovskite phase under low humidity conditions, which hints towards the reversibility of this hydration reaction. More recently, Christians *et al.* and Yang *et al.* reported the formation of an intermediate degradation product which is similar but not identical to the previously reported dihydrate $(CH_3NH_3)_4PbI_6 \cdot 2\ H_2O$ upon exposure to highly humid air, before decomposition to PbI_2 occurs.[80, 81] This indicates that the initial step for moisture-induced degradation at very high humidity levels might be the uptake of water molecules into the perovskite crystal structure under the formation of hydrated phases, rather than an acid-base reaction. Furthermore, it was found that slow degradation occurs in ambient humidity levels (~50% RH at 20 °C) over the course of tens of days, whereas exposure to 80% RH or even higher humidity levels leads to significantly more rapid degradation within less than three days. Therefore, we need to take into consideration that different decomposition routes are possible depending on the humidity level.

Understanding the degradation mechanisms upon moisture exposure facilitates the development of strategies to increase the moisture resilience of hybrid perovskites. Since the moisture sensitivity of $CH_3NH_3PbI_3$ is closely related to the hydrophilicity of the organic methylammonium cation, the replacement of MA with more hydrophobic organic cations is one possible approach. The introduction of bulky organic cations incorporating a long alkyl chain

and/or an aryl group instead of a short methyl group has been found to result in the formation of so-called 2D perovskites, which show remarkable resilience to humid environments. Here, extended sheets of the long-chained organic cations separate a defined number of lead halide octahedra interlayers (Figure 1.14). Smith *et al.* reported a layered perovskite with significantly enhanced moisture stability by incorporating hydrophobic phenylethylammonium cations into the perovskite structure.[82] However, the photovoltaic performance of 2D perovskite solar cells is rather low (<5% in steady-state efficiency measurements) compared to conventional devices based on $CH_3NH_3PbI_3$ as photoabsorber.

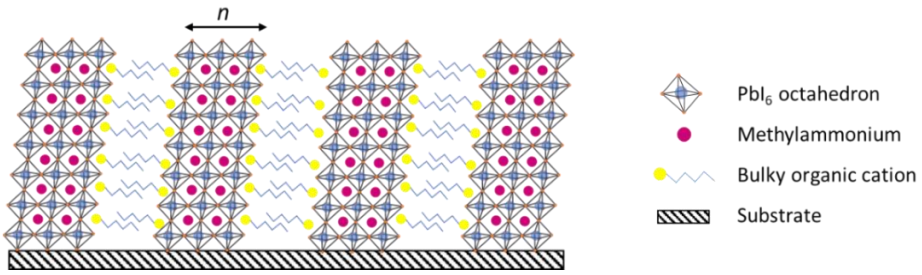

Figure 1.14 Schematic representation of a layered 2D perovskite structure comprising alternating layers of PbI_6 octahedra interlayers accommodating small methylammonium cations and extended sheets of bulky organic cations. In this scheme, the number of corner-sharing lead halide octahedra layers is $n = 3$.

At the current stage, existing studies reveal interesting facets of the chemical stability and propose possible degradation pathways of hybrid perovskites upon exposure to moisture. First approaches to increase the hydrophobicity of the perovskite layer have been developed to tackle the moisture sensitivity of PSCs. However, in-depth studies employing *in situ* characterization techniques under controlled environmental conditions are lacking. Monitoring the evolution of various perovskite materials in real-time upon exposure to humidity promises to shed light on their detailed degradation mechanism, which is of paramount importance to design PSCs with high efficiency and long-term stability.

1.4 Outline of the thesis

The work presented here is dedicated to the understanding of moisture-induced degradation processes occurring in organic-inorganic hybrid perovskites, the implication of these processes

for solar cell performance, and the development of new perovskite structures to overcome the present moisture instabilities.

First, chapter 3 describes our work on identifying and characterizing the fundamental degradation pathways in the archetypal hybrid perovskite compound – methylammonium lead iodide – upon exposure to an elevated level of humidity. We reveal the (partial) reversibility of the two sequential hydration steps producing two different hydrate species in single crystals, thin films and solar cells.

In chapter 4, we study methylammonium lead iodide perovskite films made from precursor solutions with a slight PbI_2 excess, stoichiometric mixtures or an MAI excess. We investigate how the precursor stoichiometry in the perovskite solution influences the initial device performance and identify the different humidity-induced degradation pathways via *in situ* X-ray diffraction measurements.

In chapter 5, we focus on state-of-the-art multiple-cation mixed-halide hybrid perovskites and elucidate the role of commonly used cesium and rubidium additives in the enhancement of solar cell efficiency. By combining three complementary probing techniques, we confirm the different effects of cesium and rubidium cations on the structural and electronic properties of the perovskite material, which we correlate to the observed device characteristics.

Following our work on multiple-cation mixed-halide perovskites, we discuss the impact of cesium and rubidium cation additives on the moisture stability of the resulting films and devices in chapter 6. By analyzing the chemical composition of different phase segregation products which form during film crystallization or upon exposure to humidity, we disclose the instability of rubidium-containing perovskites.

Chapter 7 introduces the concept of 2D perovskites, which represent an attractive class of semiconductors not only due to their structural and optoelectronic tunability but also because of their robustness against moisture exposure. We elaborate on the identification and control of phase purity in oriented 2D perovskite thin films.

Finally, in chapter 8, we present a novel 2D/3D hybrid perovskite bilayer architecture to ensure high device efficiency, while simultaneously improving the moisture stability of perovskite solar cells. We establish a facile solution-based method for the dimensionality engineering process and characterize the resulting changes in the perovskite crystal structure. Furthermore, we demonstrate an increase in photovoltaic performance in the form of enhanced open-circuit voltage and enhanced moisture tolerance for the 2D/3D perovskite devices.

1.5 References

[1] http://energieinitiative.org/prognosen-und-trends-der-solarenergie/ (accessed: 21-04-2018)

[2] M. Schmela, *Global Market Outlook For Solar Power 2017 - 2021*, SolarPower Europe, 2017.

[3] A. E. Becquerel, *Comptes Rendus de l' Academie des Sciences* **1839**, *9*, 145.

[4] C. E. Fritts, *Am. J. Sci.* **1883**, *26*, 465.

[5] M. Riordan, L. Hoddeson, *IEEE Spectrum* **1997**, *34*, 46.

[6] R. S. Ohl, *U.S. Patent US2402662A*, 1941.

[7] J.-P. Correa-Baena, M. Saliba, T. Buonassisi, M. Grätzel, A. Abate, W. Tress, A. Hagfeldt, *Science* **2017**, *358*, 739.

[8] K. Rajkanan, R. Singh, J. Shewchun, *Solid-State Electronics* **1979**, *22*, 793.

[9] M. Powalla, S. Paetel, D. Hariskos, R. Wuerz, F. Kessler, P. Lechner, W. Wischmann, T. M. Friedlmeier, *Engineering* **2017**, *3*, 445.

[10] C. S. Ferekides, U. Balasubramanian, R. Mamazza, V. Viswanathan, H. Zhao, D. L. Morel, *Solar Energy* **2004**, *77*, 823.

[11] J. M. Burst, J. N. Duenow, D. S. Albin, E. Colegrove, M. O. Reese, J. A. Aguiar, C. S. Jiang, M. K. Patel, M. M. Al-Jassim, D. Kuciauskas, S. Swain, T. Ablekim, K. G. Lynn, W. K. Metzger, *Nat. Energy* **2016**, *1*, 16015.

[12] P. Jackson, R. Wuerz, D. Hariskos, E. Lotter, W. Witte, M. Powalla, *physica status solidi (RRL) – Rapid Research Letters* **2016**, *10*, 583.

[13] J. Y. Huang, C. Y. Lin, C.-H. Shen, J.-M. Shieh, B.-T. Dai, *Sol. Energy Mater. Sol. Cells* **2012**, *98*, 277.

[14] M. Grätzel, *J. Photochem. Photobiol., C* **2003**, *4*, 145.

[15] S. Ito, S. M. Zakeeruddin, R. Humphry-Baker, P. Liska, R. Charvet, P. Comte, M. K. Nazeeruddin, P. Péchy, M. Takata, H. Miura, S. Uchida, M. Grätzel, *Adv. Mater.* **2006**, *18*, 1202.

[16] J. Xue, S. Uchida, B. P. Rand, S. R. Forrest, *Appl. Phys. Lett.* **2004**, *84*, 3013.

[17] B. Kippelen, J.-L. Bredas, *Energy. Environ. Sci.* **2009**, *2*, 251.

[18] A. J. Nozik, *Physica E: Low-dimensional Systems and Nanostructures* **2002**, *14*, 115.

[19] P. V. Kamat, *J. Phys. Chem. C* **2008**, *112*, 18737.

[20] National Renewable Energy Laboratory (NREL), *NREL Best Research-Cell Photovoltaic Efficiency Chart*, https://www.nrel.gov/pv/assets/images/efficiency-chart.png (accessed: 20-04-2018)

[21] M. De Graef, M. E. McHenry, *Structure of Materials: An Introduction to Crystallography, Diffraction and Symmetry*, Cambridge University Press, New York 2007.

[22] D. Weber, *Z. Naturforsch., B: Chem. Sci.* **1978**, *33*, 1443.

[23] V. M. Goldschmidt, *Naturwissenschaften* **1926**, *14*, 477.

[24] M. A. Green, A. Ho-Baillie, H. J. Snaith, *Nat. Photon.* **2014**, *8*, 506.

[25] C. Quarti, E. Mosconi, J. M. Ball, V. D'Innocenzo, C. Tao, S. Pathak, H. J. Snaith, A. Petrozza, F. De Angelis, *Energy. Environ. Sci.* **2016**, *9*, 155.

[26] S. De Wolf, J. Holovsky, S.-J. Moon, P. Löper, B. Niesen, M. Ledinsky, F.-J. Haug, J.-H. Yum, C. Ballif, *J. Phys. Chem. Lett.* **2014**, *5*, 1035.

[27] S. Sun, T. Salim, N. Mathews, M. Duchamp, C. Boothroyd, G. Xing, T. C. Sum, Y. M. Lam, *Energy. Environ. Sci.* **2014**, *7*, 399.

[28] S. D. Stranks, G. E. Eperon, G. Grancini, C. Menelaou, M. J. P. Alcocer, T. Leijtens, L. M. Herz, A. Petrozza, H. J. Snaith, *Science* **2013**, *342*, 341.

[29] F. Deschler, M. Price, S. Pathak, L. E. Klintberg, D.-D. Jarausch, R. Higler, S. Hüttner, T. Leijtens, S. D. Stranks, H. J. Snaith, M. Atatüre, R. T. Phillips, R. H. Friend, *J. Phys. Chem. Lett.* **2014**, *5*, 1421.

[30] A. Binek, F. C. Hanusch, P. Docampo, T. Bein, *J. Phys. Chem. Lett.* **2015**, *6*, 1249.

[31] T. Liu, Y. Zong, Y. Zhou, M. Yang, Z. Li, O. S. Game, K. Zhu, R. Zhu, Q. Gong, N. P. Padture, *Chem. Mater.* **2017**.

[32] M. Saliba, T. Matsui, J.-Y. Seo, K. Domanski, J.-P. Correa-Baena, M. K. Nazeeruddin, S. M. Zakeeruddin, W. Tress, A. Abate, A. Hagfeldt, M. Gratzel, *Energy. Environ. Sci.* **2016**, *9*, 1989.

[33] D. P. McMeekin, G. Sadoughi, W. Rehman, G. E. Eperon, M. Saliba, M. T. Hörantner, A. Haghighirad, N. Sakai, L. Korte, B. Rech, M. B. Johnston, L. M. Herz, H. J. Snaith, *Science* **2016**, *351*, 151.

[34] H. Choi, J. Jeong, H.-B. Kim, S. Kim, B. Walker, G.-H. Kim, J. Y. Kim, *Nano Energy* **2014**, *7*, 80.

[35] S. Colella, E. Mosconi, P. Fedeli, A. Listorti, F. Gazza, F. Orlandi, P. Ferro, T. Besagni, A. Rizzo, G. Calestani, G. Gigli, F. De Angelis, R. Mosca, *Chem. Mater.* **2013**, *25*, 4613.

[36] Z. Zhao, F. Gu, Y. Li, W. Sun, S. Ye, H. Rao, Z. Liu, Z. Bian, C. Huang, *Advanced Science* **2017**, *4*, 1700204.

[37] N. De Marco, H. Zhou, Q. Chen, P. Sun, Z. Liu, L. Meng, E.-P. Yao, Y. Liu, A. Schiffer, Y. Yang, *Nano Lett.* **2016**, *16*, 1009.

[38] Z.-K. Tan, R. S. Moghaddam, M. L. Lai, P. Docampo, R. Higler, F. Deschler, M. Price, A. Sadhanala, L. M. Pazos, D. Credgington, F. Hanusch, T. Bein, H. J. Snaith, R. H. Friend, *Nat. Nanotech.* **2014**, *9*, 687.

[39] S. Kumar, J. Jagielski, N. Kallikounis, Y. H. Kim, C. Wolf, F. Jenny, T. Tian, C. Hofer, Y.-C. Chiu, W. J. Stark, T.-W. Lee, C.-J. Shih, *Nano Lett.* **2017**.

[40] S. A. Veldhuis, P. P. Boix, N. Yantara, M. Li, T. C. Sum, N. Mathews, S. G. Mhaisalkar, *Adv. Mater.* **2016**, *28*, 6804.

[41] S. P. Senanayak, B. Yang, T. H. Thomas, N. Giesbrecht, W. Huang, E. Gann, B. Nair, K. Goedel, S. Guha, X. Moya, C. R. McNeill, P. Docampo, A. Sadhanala, R. H. Friend, H. Sirringhaus, *Sci. Adv.* **2017**, *3*, e1601935.

[42] C. R. Kagan, D. B. Mitzi, C. D. Dimitrakopoulos, *Science* **1999**, *286*, 945.

[43] M. M. Lee, J. Teuscher, T. Miyasaka, T. N. Murakami, H. J. Snaith, *Science* **2012**, *338*, 643.

[44] H.-S. Kim, C.-R. Lee, J.-H. Im, K.-B. Lee, T. Moehl, A. Marchioro, S.-J. Moon, R. Humphry-Baker, J.-H. Yum, J. E. Moser, M. Grätzel, N.-G. Park, *Sci. Rep.* **2012**, *2*, 591.

[45] A. Kojima, K. Teshima, Y. Shirai, T. Miyasaka, *J. Am. Chem. Soc.* **2009**, *131*, 6050.

[46] W. S. Yang, B.-W. Park, E. H. Jung, N. J. Jeon, Y. C. Kim, D. U. Lee, S. S. Shin, J. Seo, E. K. Kim, J. H. Noh, S. I. Seok, *Science* **2017**, *356*, 1376.

[47] P. Docampo, J. M. Ball, M. Darwich, G. E. Eperon, H. J. Snaith, *Nat. Commun.* **2013**, *4*.

[48] K. K. Sears, M. Fievez, M. Gao, H. C. Weerasinghe, C. D. Easton, D. Vak, *Solar RRL* **2017**, *1*, 1700059.

[49] C. Momblona, L. Gil-Escrig, E. Bandiello, E. M. Hutter, M. Sessolo, K. Lederer, J. Blochwitz-Nimoth, H. J. Bolink, *Energy. Environ. Sci.* **2016**, *9*, 3456.

[50] K. Mahmood, S. Sarwar, M. T. Mehran, *RSC Advances* **2017**, *7*, 17044.

[51] J. You, L. Meng, T.-B. Song, T.-F. Guo, Y. Yang, W.-H. Chang, Z. Hong, H. Chen, H. Zhou, Q. Chen, Y. Liu, N. De Marco, Y. Yang, *Nat. Nanotech.* **2015**, *11*, 75.

[52] S. N. Habisreutinger, T. Leijtens, G. E. Eperon, S. D. Stranks, R. J. Nicholas, H. J. Snaith, *Nano Lett.* **2014**, *14*, 5561.

[53] N. Arora, M. I. Dar, A. Hinderhofer, N. Pellet, F. Schreiber, S. M. Zakeeruddin, M. Grätzel, *Science* **2017**.

[54] L. M. Herz, *Annu. Rev. Phys. Chem.* **2016**, *67*, 65.

[55] R. Ihly, A.-M. Dowgiallo, M. Yang, P. Schulz, N. J. Stanton, O. G. Reid, A. J. Ferguson, K. Zhu, J. J. Berry, J. L. Blackburn, *Energy. Environ. Sci.* **2016**, *9*, 1439.

[56] G. Grancini, C. Roldan-Carmona, I. Zimmermann, E. Mosconi, X. Lee, D. Martineau, S. Narbey, F. Oswald, F. De Angelis, M. Graetzel, M. K. Nazeeruddin, *Nat. Commun.* **2017**, *8*, 15684.

[57] Y. Li, Y. Zhao, Q. Chen, Y. Yang, Y. Liu, Z. Hong, Z. Liu, Y.-T. Hsieh, L. Meng, Y. Li, Y. Yang, *J. Am. Chem. Soc.* **2015**, *137*, 15540.

[58] N. Li, Z. L. Zhu, Q. S. Dong, J. W. Li, Z. L. Yang, C. C. Chueh, A. K. Y. Jen, L. D. Wang, *Adv. Mater. Interfaces* **2017**, *4*, 1700598.

[59] F. Yang, H. E. Lim, F. Wang, M. Ozaki, A. Shimazaki, J. Liu, N. B. Mohamed, K. Shinokita, Y. Miyauchi, A. Wakamiya, Y. Murata, K. Matsuda, *Adv. Mater. Interfaces* **2018**, *5*, 1701256.

[60] W. Nie, H. Tsai, J. C. Blancon, F. Liu, C. C. Stoumpos, B. Traore, M. Kepenekian, O. Durand, C. Katan, S. Tretiak, J. Crochet, P. M. Ajayan, M. Kanatzidis, J. Even, A. D. Mohite, *Adv. Mater.* **2018**, *30*, 1703879.

[61] Y. Hou, X. Du, S. Scheiner, D. P. McMeekin, Z. Wang, N. Li, M. S. Killian, H. Chen, M. Richter, I. Levchuk, N. Schrenker, E. Spiecker, T. Stubhan, N. A. Luechinger, A. Hirsch, P. Schmuki, H.-P. Steinrück, R. H. Fink, M. Halik, H. J. Snaith, C. J. Brabec, *Science* **2017**.

[62] A. Abate, S. Paek, F. Giordano, J.-P. Correa-Baena, M. Saliba, P. Gao, T. Matsui, J. Ko, S. M. Zakeeruddin, K. H. Dahmen, A. Hagfeldt, M. Gratzel, M. K. Nazeeruddin, *Energy. Environ. Sci.* **2015**, *8*, 2946.

[63] K. Domanski, J.-P. Correa-Baena, N. Mine, M. K. Nazeeruddin, A. Abate, M. Saliba, W. Tress, A. Hagfeldt, M. Grätzel, *ACS Nano* **2016**, *10*, 6306.

[64] Z. Li, C. Xiao, Y. Yang, S. P. Harvey, D. H. Kim, J. A. Christians, M. Yang, P. Schulz, S. U. Nanayakkara, C.-S. Jiang, J. M. Luther, J. J. Berry, M. C. Beard, M. M. Al-Jassim, K. Zhu, *Energy. Environ. Sci.* **2017**, *10*, 1234.

[65] T. Leijtens, G. E. Eperon, S. Pathak, A. Abate, M. M. Lee, H. J. Snaith, *Nat. Commun.* **2013**, *4*, 2885.

[66] P. Calado, A. M. Telford, D. Bryant, X. Li, J. Nelson, B. C. O'Regan, P. R. F. Barnes, *Nat. Commun.* **2016**, *7*, 13831.

[67] H. J. Snaith, A. Abate, J. M. Ball, G. E. Eperon, T. Leijtens, N. K. Noel, S. D. Stranks, J. T.-W. Wang, K. Wojciechowski, W. Zhang, *J. Phys. Chem. Lett.* **2014**, *5*, 1511.

[68] Y. Zhao, W. Zhou, W. Ma, S. Meng, H. Li, J. Wei, R. Fu, K. Liu, D. Yu, Q. Zhao, *ACS Energy Lett.* **2016**, *1*, 266.

[69] W. Tress, N. Marinova, T. Moehl, S. M. Zakeeruddin, M. K. Nazeeruddin, M. Gratzel, *Energy. Environ. Sci.* **2015**, *8*, 995.

[70] G. F. Samu, C. Janáky, P. V. Kamat, *ACS Energy Lett.* **2017**, *2*, 1860.

[71] A. J. Barker, A. Sadhanala, F. Deschler, M. Gandini, S. P. Senanayak, P. M. Pearce, E. Mosconi, A. J. Pearson, Y. Wu, A. R. Srimath Kandada, T. Leijtens, F. De Angelis, S. E. Dutton, A. Petrozza, R. H. Friend, *ACS Energy Lett.* **2017**, *2*, 1416.

[72] S. J. Yoon, M. Kuno, P. V. Kamat, *ACS Energy Lett.* **2017**, *2*, 1507.

[73] S. Draguta, O. Sharia, S. J. Yoon, M. C. Brennan, Y. V. Morozov, J. S. Manser, P. V. Kamat, W. F. Schneider, M. Kuno, *Nat. Commun.* **2017**, *8*, 200.

[74] G. E. Eperon, S. N. Habisreutinger, T. Leijtens, B. J. Bruijnaers, J. J. van Franeker, D. W. deQuilettes, S. Pathak, R. J. Sutton, G. Grancini, D. S. Ginger, R. A. J. Janssen, A. Petrozza, H. J. Snaith, *ACS Nano* **2015**.

[75] J. You, Y. Yang, Z. Hong, T.-B. Song, L. Meng, Y. Liu, C. Jiang, H. Zhou, W.-H. Chang, G. Li, Y. Yang, *Appl. Phys. Lett.* **2014**, *105*, 183902.

[76] G. E. Eperon, V. M. Burlakov, P. Docampo, A. Goriely, H. J. Snaith, *Adv. Funct. Mater.* **2014**, *24*, 151.

[77] G. D. Niu, W. Z. Li, F. Q. Meng, L. D. Wang, H. P. Dong, Y. Qiu, *J. Mater. Chem. A* **2014**, *2*, 705.

[78] J. M. Frost, K. T. Butler, F. Brivio, C. H. Hendon, M. van Schilfgaarde, A. Walsh, *Nano Lett.* **2014**, *14*, 2584.

[79] B. R. Vincent, K. N. Robertson, T. S. Cameron, O. Knop, *Can. J. Chem.* **1987**, *65*, 1042.

[80] J. A. Christians, P. A. Miranda Herrera, P. V. Kamat, *J. Am. Chem. Soc.* **2015**.

[81] J. Yang, B. D. Siempelkamp, D. Liu, T. L. Kelly, *ACS Nano* **2015**, *9*, 1955.

[82] I. C. Smith, E. T. Hoke, D. Solis-Ibarra, M. D. McGehee, H. I. Karunadasa, *Angew. Chem. Int. Ed.* **2014**, *53*, 11232.

2 Characterization techniques

2.1 X-ray diffraction (XRD)

X-ray diffraction (XRD) is the most common technique to study the atomic structure of crystalline materials. The wavelength of X-ray radiation is in the range of only a few Angstroms (10^{-10} m) and it is therefore in the same range as the interatomic distances occurring in a crystal lattice. This allows us to obtain valuable information about the examined sample, such as composition, crystallinity, size of crystal domains or crystal orientation.

In a conventional XRD setup, X-rays are generated in a high vacuum tube where electrons are extracted from an incandescent filament (cathode) and accelerated towards the positively charged metal anode by applying a high voltage, typically around 50 kV. These high energetic electrons collide with the anode material (e.g. Cu, Mo or Cr) and if an electron is deviated by the electromagnetic interaction with the nucleus of a metal atom, it loses a part of its energy and an X-ray photon is emitted. The energy of the emitted photon can take any value up to a maximum corresponding to the acceleration voltage between cathode and anode, creating a continuous spectrum ("Bremsstrahlung").

The accelerated electron can also remove an inner shell electron of a metal atom and if the vacancy is filled by an electron from an outer shell, an X-ray photon is emitted by this relaxation process. The energy of the photon corresponds to the well-defined difference in binding energy between the two shells and is characteristic of the anode material. By using a monochromator, these characteristic X-rays with a single wavelength (e.g. Cu K_α line) can be filtered out from the polychromatic radiation and utilized for XRD measurements.

Among the richness of possible interactions of electromagnetic waves with matter, XRD is based on the so-called scattering process. When incident X-ray waves are elastically scattered by the electron clouds of periodically arranged atoms in a crystalline sample, constructive or destructive interference can occur, depending on the path difference between the two scattered waves. Figure 2.1 shows a schematic illustration of the optical paths of incident X-ray waves 1 and 2 by the atoms A and B in a crystal lattice, respectively.

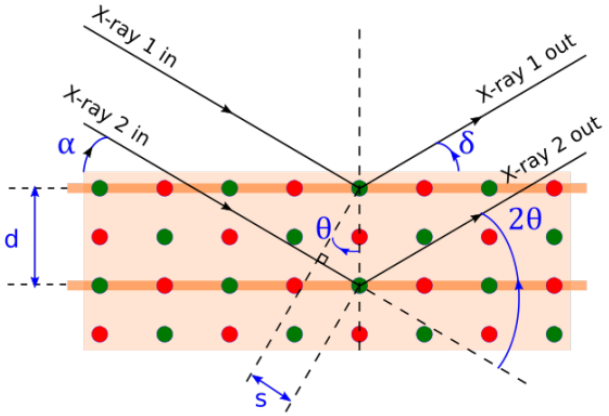

Figure 2.1 Schematic illustration of X-ray diffraction in a crystal lattice. The red and green circles represent diffraction centers (atoms), α is the incidence angle, δ is the exit angle, θ is the Bragg angle, d is the distance between reflecting crystal planes and s is the half distance of the path difference between X-ray 1 and 2.[1]

Constructive interference occurs if two scattered X-ray beams are in phase, which means that their path difference is an integer multiple of the X-ray wavelength, as given by Bragg's law of diffraction:

$$n\lambda = 2d\ sin\theta \tag{2.1}$$

where n is diffraction order, λ is the X-ray wavelength, d is the distance between the two reciprocal lattice planes and θ is the Bragg angle.

If the Bragg condition is fulfilled, atoms located on the sequence of crystal planes parallel to each other with the interplanar spacing d will diffract in phase and a diffraction peak occurs in the corresponding XRD pattern. The position and the relative intensities of diffraction peaks correspond to the crystal structure and the involved types of atoms, thus revealing the composition of the sample. In the most common XRD scanning mode (the so-called Bragg-Brentano or locked couple geometry), the incident angle and the detection angle are scanned simultaneously. Thus, only Bragg planes which are parallel to the substrate produce diffraction peaks, giving a hint on the crystallite orientation within thin film samples (Figure 2.2).

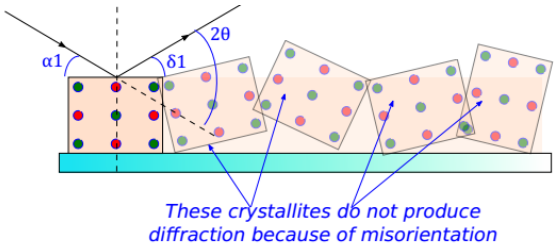

Figure 2.2 Schematic illustration of XRD measurements operated in the Bragg-Brentano scanning geometry. Only crystallites with Bragg planes oriented parallel to the substrate (where the plane normal is perpendicular to the substrate) produce diffraction peaks.[1]

In addition, the broadening of peaks in a diffraction pattern correlates with the average size of the crystallites in a powder sample which can be estimated by using the Scherrer equation:[2]

$$D = \frac{K\lambda}{\beta cos\theta} \tag{2.2}$$

where D is the mean diameter of the crystalline domain, K is a dimensionless shape factor whose value is close to unity, λ is the X-ray wavelength, β is the line broadening at half the maximum intensity in radians and θ is the Bragg angle.

2.2 2D grazing-incidence wide-angle X-ray scattering (GIWAXS)

Grazing-incidence wide-angle X-ray scattering (GIWAXS) is a widely-used XRD technique for thin film characterization. The fixed, low incidence angle with usually $\alpha < 1°$ can lead to an increased signal yield compared to a conventional locked-couple scan, since more X-rays are absorbed by the sample rather than the substrate (Figure 2.3), therefore reducing measurement time. Another benefit over the Bragg-Brentano geometry lies in the possibility to obtain depth profiles of the examined film.[1, 3] By carefully varying the incidence angle around the so-called critical angle for total X-ray external reflection, the penetration depth of the incident beams can be adjusted, which allows the investigation of either the film's surface or its bulk properties.

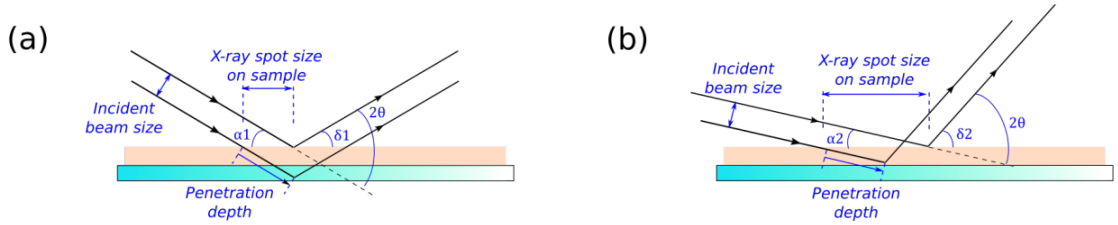

Figure 2.3 (a) XRD at high incident angle with small spot size and large penetration depth. (b) Using a small, grazing-incidence angle, the spot size is larger and the penetration depth is reduced.[1]

Combining GIWAXS with a 2D detector offers the possibility to obtain diffraction patterns which contain much more information than one-dimensional detectors, for instance in order to analyze crystallite orientation within thin film samples. Perfectly polycrystalline samples with low textures produce Debye diffraction rings, whereas highly textured samples with preferential crystallite orientations typically show partial rings or dots (Figure 2.4). An integration of a particular diffraction ring (i.e. fixed q) results in a pole figure, where the azimuthal angle χ indicates the orientation of certain crystal planes with respect to the substrate. This makes it possible to compare the degree of texture or crystal disorder between two samples. A radial cut along $\chi = 0°$ corresponds to a 1D XRD pattern recorded in the Bragg-Brentano geometry, where q is directly related to 2θ, revealing the out-of-plane features of the thin film. In contrast, a radial cut along $\chi = 90°$ provides in-plane information about the sample. The area under the 1D diffraction curves can be evaluated for comparing the relative degree of crystallinity among different samples.

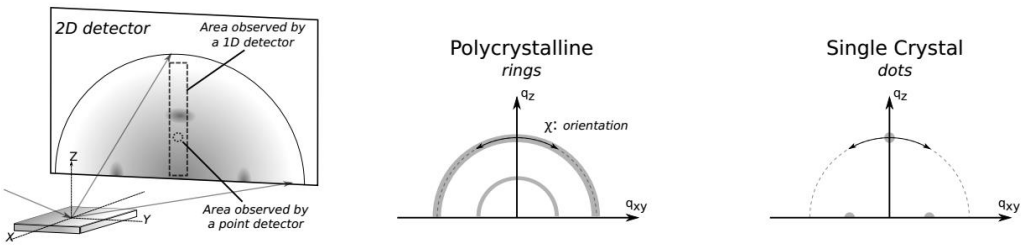

Figure 2.4 Schematic illustration of the measurement geometry of XRD with a 2D detector, and illustration of image data from samples with different textures. Polycrystalline films produce diffraction rings where the azimuthal angle χ indicates the crystal orientation with respect to the substrate, while single crystals produce dots.[1]

2.3 Scanning electron microscopy (SEM)

Scanning Electron Microscopy (SEM) is a routinely used imaging technique to study the micro- and nanostructured morphology of materials. In electron microscopy, the imaging process is based on interactions of the incoming electron beam with the sample atoms. Compared to optical microscopes, a high resolution in the range of only a few nanometers can be achieved in SEM due to the much smaller de Broglie wavelength of electrons than photons in the visible range.

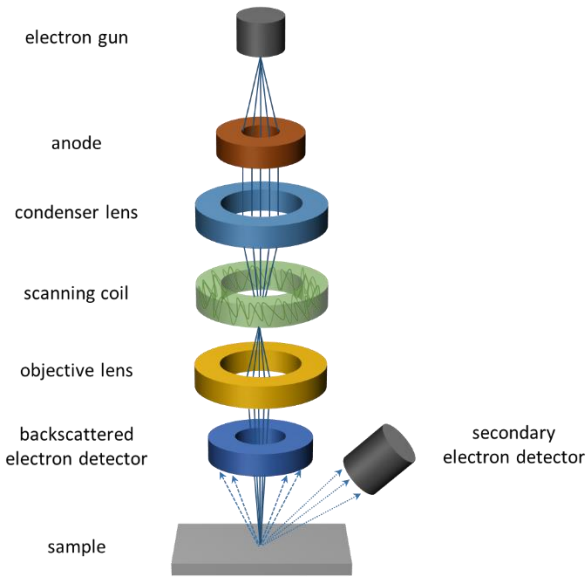

Figure 2.5 Schematic representation of a Scanning Electron Microscope.

In a typical SEM setup (Figure 2.5) an electron beam is emitted from an electron gun in high vacuum, either thermionically by a tungsten filament cathode or by using a field emission gun. The energy of the electron beam is proportional to the applied acceleration voltage between the cathode and an anode, which is usually 1–40 kV. The electron beam is then focused with the aid of condenser lenses and an objective lens to obtain a small beam diameter of a few nanometers. After passing through an aperture, the primary beam strikes the surface region of the sample material which results in a multitude of different interactions.[4]

An Everhart-Thornley photomultiplier detector records the low-energetic secondary electrons (10–50 eV) which are emitted by atoms excited by the primary electron beam in an inelastic scattering process. Secondary electrons are those signals which are responsible for the topological contrast in common SEM. In contrast, backscattered electrons can reveal the sample's chemical composition

because the detected intensity depends on the atomic number of the sample atoms. High-energetic backscattered primary electrons result from elastic scattering at the atom cores and can be detected by a semiconductor device. By scanning the surface area in a raster pattern with the help of scanning coils, an SEM image can be visualized.

2.4 Energy dispersive X-ray spectroscopy (EDX)

Energy dispersive X-ray spectroscopy (EDX) in combination with SEM is widely employed for elemental mapping within a micron- or nano-sized area.[5] To spatially resolve the elemental composition in an SEM micrograph, a focused beam of high-energy electrons is scanned over the specimen and interacts with the atoms of the sample surface. This interaction can lead to the excitation and ejection of an electron from the inner shell of a certain atom, creating a hole which can be filled by an electron from an outer shell at a higher energy level (Figure 2.6).

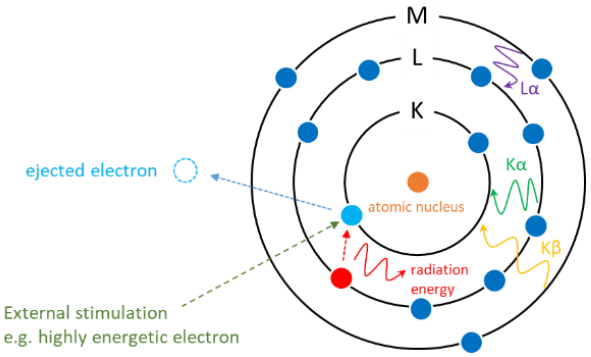

Figure 2.6 Schematic illustration of the X-ray emission process in an atom upon external stimulation.

If the energy difference between the inner and the outer shell is released in the form of an X-ray, its energy is characteristic for each type of atom and can be detected by an energy-dispersive spectrometer. Si(Li) detectors cooled with liquid nitrogen or silicon drift detectors equipped with Peltier cooling systems are most commonly used to convert the X-ray energy into voltage signals. The resulting EDX profile indicates the number and energy of the emitted X-rays, which in turn reveal the chemical composition of the sample surface.

2.5 Atomic force microscopy (AFM)

Atomic force microscopy (AFM) is a widely used technique to characterize the surface topography of solid samples, which can be used to calculate surface properties such as roughness parameters.

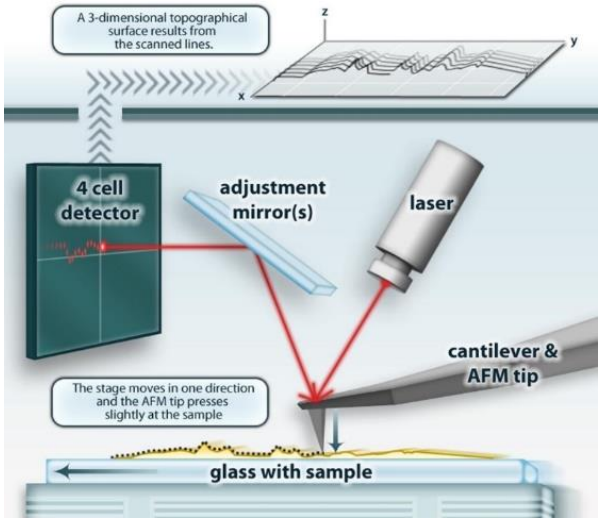

Figure 2.7 Schematic representation of the operational principle of an atomic force microscope.[6]

In a standard AFM setup, the specimen surface is moved underneath a sharp probe tip at the end of a cantilever by a piezoelectric scanner (Figure 2.7). Attractive or repulsive forces between the tip and the sample lead to a deflection of the cantilever which acts as a spring. This displacement is detected by a laser beam which is reflected on the top surface of the cantilever and a shift in the reflected beam is measured with an array of photodiodes. A topographic image of the sample surface can be constructed by combining the information about the position of the tip with respect to the specimen and the recorded force.

One of the most common operational modes in AFM is called “tapping mode”,[7] which means that the cantilever is driven to oscillate near its resonance frequency with an amplitude around 100–200 nm. When the tip comes closer to the surface by attractive interaction forces, the oscillation amplitude would decrease. In order to maintain a defined oscillation amplitude, a piezoelectric actuator adjusts the height of the cantilever above the sample. Thus, the tapping mode is a frequently used contact-less method to avoid damage to the specimen and the AFM tip.

2.6 Time-of-flight secondary ion mass spectrometry (ToF-SIMS)

Time-of-flight secondary ion mass spectrometry (ToF-SIMS) is a powerful, surface-sensitive technique to obtain detailed information about the elemental and molecular composition of solids. It does not only offer surface analysis, but also depth profiling, essentially enabling a full 3D elemental analysis of thin layers.[8]

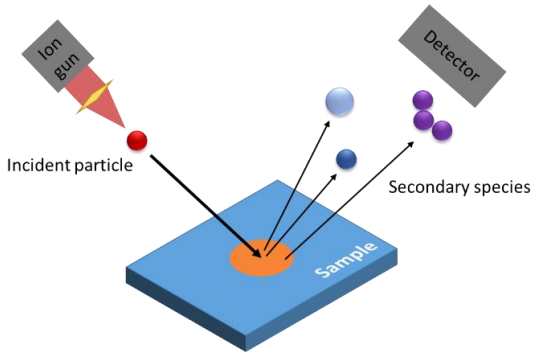

Figure 2.8 Schematic illustration of the operational principle of time-of-flight secondary ion mass spectrometry.

ToF-SIMS relies on the combination of two analytical methods: secondary ion mass spectrometry (SIMS) and time-of-flight mass analysis (ToF). First, a pulsed particle gun operated at a few keV bombards the solid sample with primary ions (typically Cs, Ga or Bi) to remove atoms and molecules from the uppermost one or two monolayers of the sample. The liberated fragment species ("secondary ions") are subsequently accelerated into a circular or linear flight-tube towards a detector (Figure 2.8). Since heavier particles require a longer "time-of-flight" along their drift path than lighter particles before they reach the detector, which can be measured on the nanosecond scale. Consequently, the mass of secondary ion fragments can be determined with extremely high precision.

Raster scanning the specimen surface with a focused primary ion beam produces a map for different elements and molecules with a good lateral resolution (<60 nm). For local depth profiling, the ToF-SIMS setup is usually operated in a dual beam mode.[9] A low energy ion gun (e.g., producing oxygen ion clusters) is continuously forming a sputter crater over a larger area, while the bottom of the crater is progressively analyzed with a pulsed primary ion beam from a liquid metal ion source. The sputter time then correlates with the sampling depth.

2.7 Ultraviolet-visible (UV-Vis) absorption spectroscopy

Ultraviolet-visible (UV-Vis) absorption spectroscopy is a technique to characterize the light absorption properties of liquid or solid samples. The photon energy which is needed for the excitation of an electron from its electronic ground state to an excited state corresponds to the energy difference between the two states. Therefore, qualitative and quantitative information about the photoinduced transitions can be gained according to the characteristic absorption spectrum of a material. The absorbance A of a material at a certain wavelength λ depends on the concentration of the absorbing species and the sample thickness. This relation is given by the Lambert-Beer law:

$$A = -log\left(\frac{I}{I_0}\right) = \varepsilon c d \qquad (2.3)$$

where I is the measured intensity of transmitted light, I_0 is the intensity of incident light, ε is the extinction coefficient of the sample, c is the concentration of the absorbing species and d is the path length of light travelling through the sample.

However, the Lambert-Beer law is not unrestrictedly valid for the characterization of samples consisting of several different layers. Each interface between two media reflects a certain fraction of the incident light and must be taken into account. Measurements with an integrating sphere and a suitable reference substrate are necessary to obtain reliable values for the absorbance of the photoactive layer. The reference should have the same architecture as the sample substrate, except for the active layer. Figure 2.9 shows the typical setup of a UV-Vis spectrophotometer equipped with an integrating sphere.

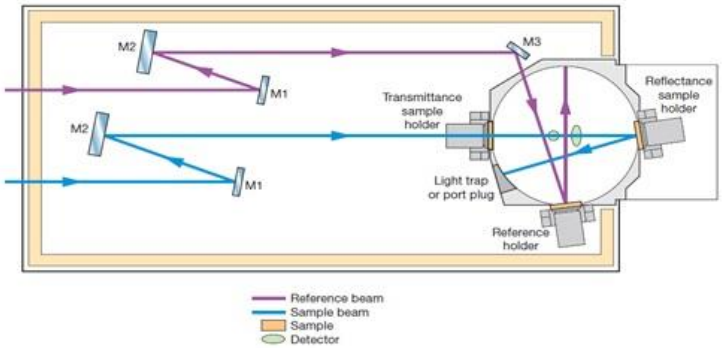

Figure 2.9 Schematic setup of a UV-Vis spectrophotometer equipped with an integrating sphere.[10]

A standard UV-Vis spectrometer combines a xenon lamp to produce light in the visible wavelength region and a deuterium lamp for the ultraviolet region in order to generate a continuous spectrum. A monochromator can select a certain wavelength and by scanning over the whole spectral range, an analytical spectrum can be obtained.

First, the instrument baseline needs to be measured without any samples in the transmission port (100%T) and a Spectralon white standard in the reflectance port (100%R). Then, the transmittance (%T) of both the sample and the reference at the transmission port is measured, followed by reflectance (%R) measurements where the specimen is positioned outside the integrating sphere.

Assuming that all incident light is either transmitted, reflected or absorbed, the percentage of absorbed light %A (absorptance) can be calculated as:

$$\%A = 1 - \%T - \%R \tag{2.4}$$

The absorbance is then given by:

$$A = -log(1 - \%A) \tag{2.5}$$

Finally, the actual absorbance of a film is:

$$A_{film} = A_{sample} - A_{reference} \tag{2.6}$$

2.8 Photoluminescence spectroscopy (PL)

Photoluminescence (PL) spectroscopy is a common technique for the characterization of electronic states in molecules or semiconductors. PL measurements are based on fluorescence which is generally defined as the property of a material to emit light with a particular wavelength upon the transition from an excited electronic state to the electronic ground state after light absorption.

In the case of semiconductors, if light with sufficient energy is absorbed, an electron can be excited from the valence band to the conduction band, accompanied by the generation of a hole in the valence band. The excited electron can quickly relax to a state corresponding to the conduction band minimum (e.g. via vibrational relaxation). If radiative charge recombination takes place, the photoexcited electron falls back into its electronic ground state and recombines with a hole under the emission of a photon (Figure 2.10). The wavelength of the fluorescence photon detected in a PL experiment is related to the band gap of the material, which is the difference between the energy levels of the valence and the conduction band. The steady-state PL spectrum provides information

about the wavelength and the amount of the emitted photons, thus giving insight into the electronic landscape of semiconductors, but also the effectiveness of charge transfer processes.

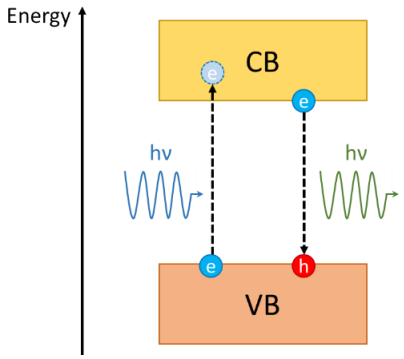

Figure 2.10 Schematic energy level diagram illustrating the photo-excitation and radiative relaxation pathway of an electron as the foundation for PL measurements.

Besides steady-state PL measurements, time-resolved PL techniques such as time-correlated single photon counting (TCSPC) are frequently used to investigate the recombination kinetics of photo-excited charge carriers. The fluorescence lifetime determines how long a photo-excited species remains in the excited state before returning to its ground state via emission of a fluorescence photon. In a typical TCSPC experiment, the specimen is exposed to a pulsed laser beam and the time between a laser pulse and the detection of a fluorescence photon is recorded with a very high temporal resolution on the picosecond timescale. By pulsing the laser with a repetition rate of 100 kHz – 50 MHz, a multitude of excitation-recombination events can be generated and the results can be depicted in a histogram where the single photon counts are plotted against the detection time (Figure 2.11).[11] The plot usually follows an exponential decay and by fitting the decay curve from the TCSPC method with an appropriate function, fluorescence lifetimes can be calculated.

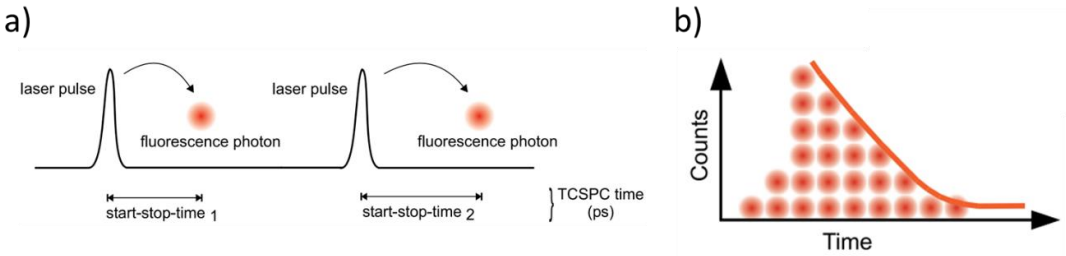

Figure 2.11 Working principle of TCSPC. (a) Measurement of start-stop-times between pulsed laser excitation and photon detection. (b) Histogram of binned start-stop-times.[11]

2.9 Ellipsometry

Ellipsometry is a contact-less, very sensitive technique for thin film characterization that allows the determination of film thickness, roughness, composition and crystallinity by measuring the dielectric properties of the sample. The principle of ellipsometry is based on the change in the polarisation state of an incident light beam after being reflected by the sample due to light-matter interactions depending on the optical constants (index of refraction and absorption coefficient) of the sample material.[12]

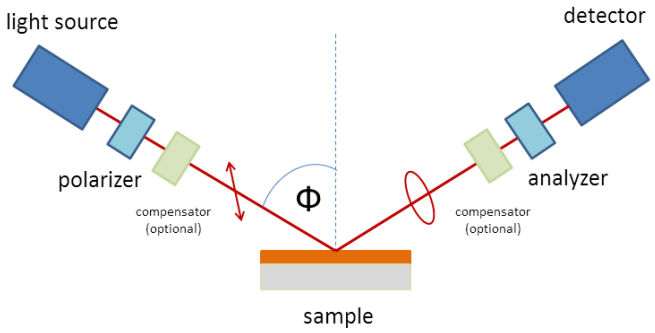

Figure 2.12 Schematic illustration of an ellipsometry setup, where Φ is the specular incident angle of the light beam.

As a probe beam, light is linearly polarized by a polarizer and reaches the sample under a fixed incident angle Φ. After specular reflection at the sample surface, the reflected beam is generally elliptically polarized. The elliptical polarization state can be determined by rotating a second polarizer (analyzer) between the reflected beam and the detector and measuring the complex reflectance ratio (Figure 2.12). The latter can be parametrized by the phase difference Δ and the amplitude value Ψ, which give insights into the dielectric function of the sample material. Since the direct translation of Ψ and Δ to the optical constants is only possible for homogeneous bulk materials with perfectly flat interfaces, the data analysis generally requires fitting of the experimental ellipsometry data to a model of the dielectric function. For each component in the sample, an initial model of the optical transitions is designed from which the dielectric function is calculated and the values of Ψ and Δ simulated. A regression algorithm finally fits the simulated graph to the experimental curve by varying the free parameters, such as the film thickness.[13]

2.10 Time-resolved microwave conductivity (TRMC)

Time-resolved microwave conductivity (TRMC) is a versatile, contact-less technique to study the light-induced generation of charge carriers and their recombination dynamics in both bulk materials and at interfaces. This method measures the perturbation of the initial microwave absorbance of the sample upon the generation and decay of free charge carriers after pulsed laser excitation at a certain wavelength.[14, 15] The obtained TRMC traces reflect an impressive set of properties, such as charge carrier lifetimes, mobilities, trap densities and interfacial charge transfer rates, which can be determined by fitting the decay curves according to an appropriate kinetic model (Figure 2.13).[16]

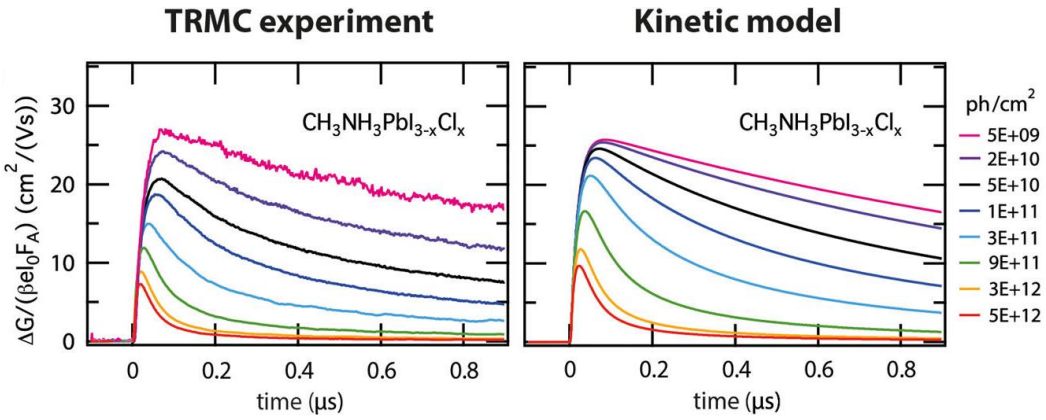

Figure 2.13 Experimental TRMC traces of a perovskite film (left) and fitted TRMC curves according to a kinetic model (right) for various intensities of the incident light pulse.[16]

In a typical TRMC experiment, thin solid films on quartz substrates are placed in a microwave cell. A slow repetition rate of the excitation laser (~10 Hz) ensures full relaxation of all photo-induced charges to the ground state before the next laser pulse hits the sample. Neutral density filters are used to vary the intensity of the incident light, typically ranging over several orders of magnitude, from 10^9 to 10^{13} photons/cm^2 (10^{-4} to 1 µJ/cm^2 per pulse). The time-resolved change in conductance $\Delta G(t)$ can be obtained from the photo-excitation-induced change in microwave power ΔP(t), which are related by a sensitivity factor K:

$$\frac{\Delta P(t)}{P} = -K\Delta G(t) \qquad (2.7)$$

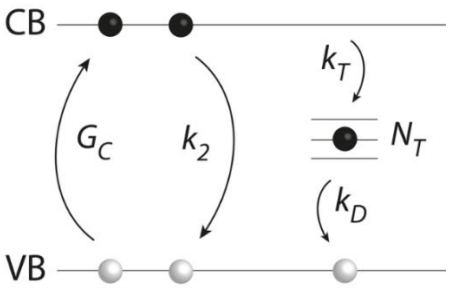

Figure 2.14 Kinetic model of processes occurring on photo-excitation of perovskite films. Here, G_C represents the time-dependent photo-excitation of electrons from the valence band (VB) to the conduction band (CB), k_2 the rate constant for second order recombination, k_T the rate constant for electron trapping and k_D the rate constant for recombination between a trapped electron and a free hole. The trap density is given by N_T.

A kinetic model is used to obtain quantitative information from the intensity-dependent TRMC traces (Figure 2.14). This model is based on a homogeneous generation of charges, which can be experimentally realized by using an excitation wavelength close to the absorption onset. The initial number of photo-excitations n depends on the light intensity of the laser I_0 (number of photons/cm^2) and the optical absorption at the excitation wavelength (F_A):

$$n = \frac{I_0 \times F_A}{L} \tag{2.8}$$

where L is the film thickness. Upon absorption of light, electrons (n_e) are excited to the conduction band (CB), leaving holes (n_h) in the valence band (VB). The laser pulse (G_C) initially generates equal concentrations of excess electrons ($\Delta n_{CB} = \Delta n_e$) and holes ($-\Delta n_{VB} = \Delta n_h$). Assuming that every absorbed photon yields a single free electron and hole, then the electrons can recombine with holes via second order recombination (k_2) or traps (k_T and k_D). The time-dependent change in the electron concentrations in the CB, VB and trap states (N_T) are described by the coupled differential Equations 2.9 to 2.11, respectively.

$$\frac{dn_{CB}}{dt} = \frac{dn_e}{dt} = G_c - k_2 n_e n_h - k_T n_e (N_T - n_T) \tag{2.9}$$

$$\frac{dn_{VB}}{dt} = -\frac{dn_h}{dt} = -G_c + k_2 n_e n_h + k_D n_t n_h \tag{2.10}$$

$$\frac{dn_t}{dt} = k_T n_e (N_T - n_T) - k_D n_t n_h \tag{2.11}$$

The charge generation in the G_C is determined by the temporal profile and the intensity of the laser pulse in combination with the optical absorption of the sample at the wavelength used. Solving the equations using numerical methods yields the time-dependent concentrations of n_e, n_h, and n_t. The

change in photoconductance as a function of time is calculated from the product of charge carrier concentrations and mobilities according to:

$$\Delta G(t) = e(n_e(t)\mu_e + n_h(t)\mu_h)\beta L \qquad (2.12)$$

In which L is the film thickness, μ_e and μ_h are the electron and hole mobilities, respectively, and β is the ratio of the inner dimensions of the microwave cell. The trapped charge carriers, n_t are assumed to be immobile and do not contribute to ΔG.

2.11 Current-voltage (*J*-*V*) measurements

The performance of solar cells is generally rated by their power conversion efficiency (PCE) under standardized conditions. The PCE of a photovoltaic device can be characterized by measuring its current-voltage (*J*-*V*) properties with a solar simulator under illumination using the standard air-mass 1.5 global (AM 1.5G) spectrum at a total irradiance of 100 mW cm^{-2}.[17] By scanning the applied external voltage in a certain range and recording the corresponding current density of the photovoltaic device, a *J*-*V* curve (Figure 2.15) is obtained. Several characteristic photovoltaic parameters can be extracted from the *J*-*V* curve as figures of merit to evaluate the quality of solar cells.

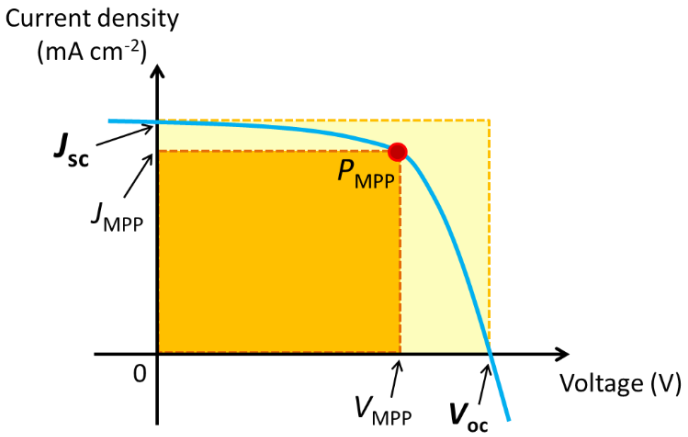

Figure 2.15 Typical *J*-*V* curve (blue) of a solar cell and its characteristic photovoltaic parameters.

The open-circuit voltage V_{oc} is defined as the voltage at which the net current flow through the solar cell is zero. In general, V_{oc} increases with increasing band gap of the material, but it also depends on the recombination processes, and therefore on the charge carrier lifetime. The short-circuit current

density J_{sc} is the maximum current that crosses the solar cell per active area unit at zero external bias. J_{sc} depends on the charge generation rate (which is mainly connected to the light intensity, the absorption/reflection properties and the band gap of the material), as well as the charge collection efficiency. The maximum power point (MPP) on the *J-V* curve defines the maximum power P_{MPP} that a solar cell generates, which is given by the product between V_{MPP} and J_{MPP}, forming the largest rectangular area between the *J-V* curve and the coordinate axes. The fill factor (FF) is defined as the ratio between the obtained maximum power of the solar cell (represented by the orange area in Figure 2.15) and the product of J_{sc} and V_{oc} (yellow square). This relation is reflected in the equation:

$$\mathrm{FF} = \frac{P_{MPP}}{V_{oc}J_{sc}} = \frac{V_{MPP}J_{MPP}}{V_{oc}J_{sc}} \tag{2.13}$$

The fill factor is also a key parameter to evaluate the device performance and it is strongly affected by internal losses such as series resistance and shunt resistance within the solar cell.

Finally, the PCE which describes how efficiently the power of incident light (P_{in}) can be converted into electric power is given by the relation:

$$\mathrm{PCE} = \frac{P_{MPP}}{P_{in}} = \frac{J_{sc}V_{oc}\mathrm{FF}}{P_{in}} \tag{2.14}$$

It is important to note that PSCs often show anomalous *J-V* hysteresis, meaning that different *J-V* curves are obtained from the same device, depending on the direction of the voltage scan (Figure 2.16). Due to the inconsistency between forward and reverse scans of *J-V* curves for hysteretic solar cells, monitoring the evolution of the maximum power point under operational conditions has been considered a more reliable assessment of device efficiency. To determine the stabilized power output, a constant voltage V_{MPP} is applied and the resulting J_{MPP} is tracked over time under illumination.

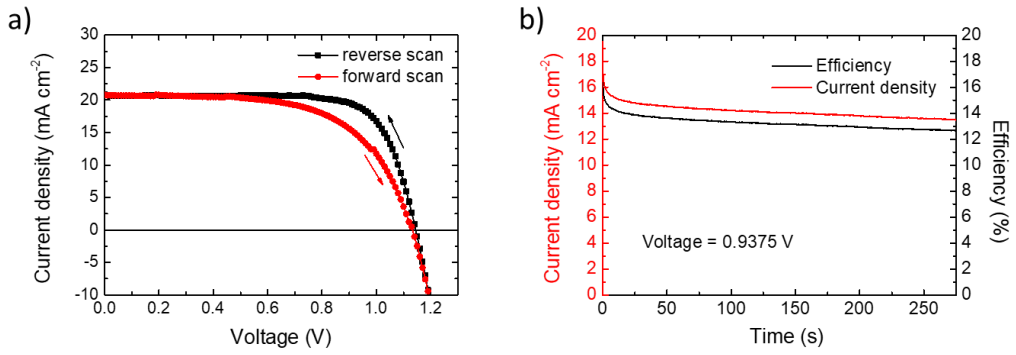

Figure 2.16 (a) Typical *J-V* hysteresis in a perovskite solar cell showing different curves for forward and reverse voltage scans. (b) Maximum power point tracking to determine the steady-state power output of the solar cell.

2.12 Time-of-flight (ToF) measurements

Time-of-flight (ToF) is a useful method to probe the charge transport properties within semiconductor thin films. For a typical ToF experiment, laterally contacted thin film samples with inter-electrode distances ideally in the range of a few microns (depending on the diffusion length of the sample material) are fabricated. Charge carriers in the specimen layer are generated by illumination using pulsed laser excitation close to one of the gold electrodes. By simultaneously applying a constant external electric field, the photo-generated charge carriers move across the film within the gap towards the opposite Au electrode. Depending on the polarity of the applied electric field, either holes or electrons can be probed as the mobile species since charges are locally generated near one electrode. The transit time t_{tr} that is required for charge carriers to travel laterally from the excitation spot to the opposite Au contact increases with increasing electrode distances. To extract t_{tr} from the measured photocurrent transient, linear fit functions were employed to fit the initial plateau and the decay of the curve. The transit time is then determined by the intersection of the two linear fits.[18] The average charge carrier mobility μ in the thin film sample can be approximated by the equation:

$$\mu = \frac{d}{E \cdot t_{tr}} \tag{2.15}$$

where d is the inter-electrode distance, E is the applied electric field and t_{tr} the ToF transit time. By plotting t_{tr} against d, the slope of the linear regression is a direct measure for the mobility.

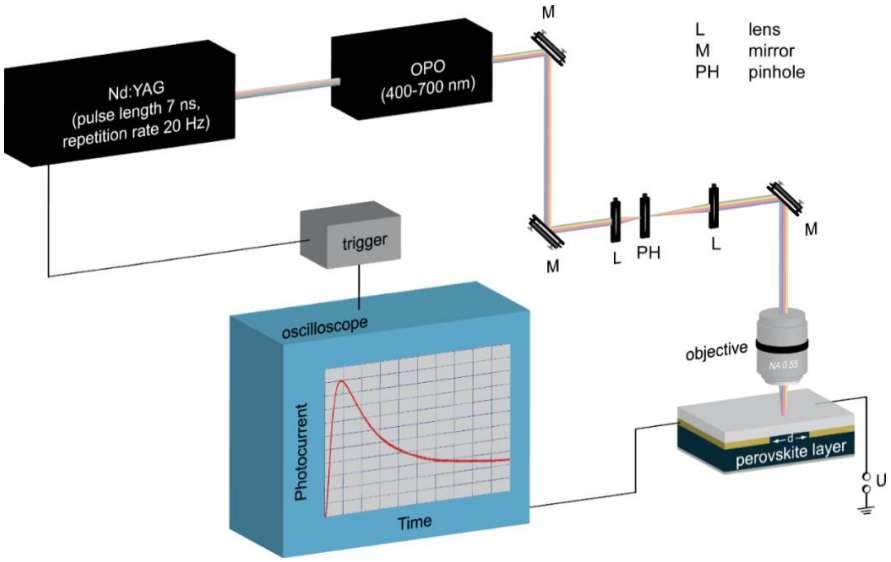

Figure 2.17 Schematic illustration of a time-of-flight experimental setup.[19]

2.13 Thermally stimulated current (TSC) measurements

Thermally stimulated current (TSC) measurements are used to investigate electronic trap states in semiconducting materials or complete photovoltaic devices. Typically, the contacted thin film or device is first cooled to a very low temperature (~30 K) well below the activation energy of the investigated trap states, while being kept in the dark. Subsequently, charge carriers are generated by illumination with a cold LED array and the sample is held at a constant (low) temperature to allow the charge carriers to relax inside of the density of states and occupy possible trap states. Afterwards, the sample is slowly heated up at a constant rate, and the charge carriers are gradually released from their trap levels, which induces a current flow in the device sample (Figure 2.18).[20]

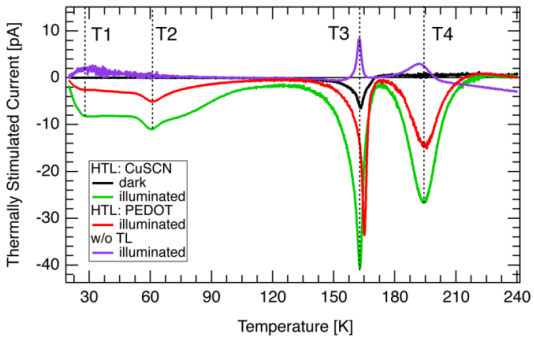

Figure 2.18 Thermally stimulated current (TSC) signals for different PSCs.[20]

The TSC signal in relation to the temperature offers insights into the depth, the density and the activation energy of the trap states. Shallow traps are released already at low temperatures, whereas charge carriers in deep states require higher thermal energy for release. Assuming that the initial rise of the TSC peak corresponds to the start of trap release due to thermal activation following an Arrhenius process, fitting the initial rise of the TSC peak can be used to estimate the activation energy of the trap states according to the following equation:

$$I_{TSC} \propto exp\left(-\frac{E_A}{k_B T}\right) \tag{2.16}$$

where E_A is the activation energy, k_B is the Boltzmann constant and T the temperature, at which the TSC signal I_{TSC} starts to rise.

2.14 References

[1] N. Widjonarko, *Coatings* **2016**, *6*, 54.

[2] J. I. Langford, A. J. C. Wilson, *J. Appl. Crystallogr.* **1978**, *11*, 102.

[3] H. Dosch, B. W. Batterman, D. C. Wack, *Phys. Rev. Lett.* **1986**, *56*, 1144.

[4] D. C. Joy, in *Mater. Sci. Technol.*, Wiley-VCH GmbH, 2006, 223.

[5] A. J. D'Alfonso, B. Freitag, D. Klenov, L. J. Allen, *Phys. Rev. B* **2010**, *81*, 100101.

[6] P. Schön, *Methods* **2016**, *103*, 25.

[7] B. Rogers, L. Manning, T. Sulchek, J. D. Adams, *Ultramicroscopy* **2004**, *100*, 267.

[8] A. Benninghoven, *Angew. Chem. Int. Ed.* **1994**, *33*, 1023.

[9] *Technical Note on TOF. SIMS 5*, IONTOF GmbH, München 2017.

[10] *Application Note on Transmission Measurements Using Integrating Spheres*, PerkinElmer, Inc., 2004.

[11] M. Wahl, S. Orthaus-Müller, *Technical Note on Time Tagged Time-Resolved Fluorescence Data Collection in Life Sciences*, PicoQuant GmbH, Berlin 2014.

[12] H. Fujiwara, *Spectroscopic Ellipsometry*, Wiley, 2007.

[13] A. M. A. Leguy, Y. Hu, M. Campoy-Quiles, M. I. Alonso, O. J. Weber, P. Azarhoosh, M. van Schilfgaarde, M. T. Weller, T. Bein, J. Nelson, P. Docampo, P. R. F. Barnes, *Chem. Mater.* **2015**, *27*, 3397.

[14] S. T. Martin, H. Herrmann, W. Choi, M. R. Hoffmann, *J. Chem. Soc., Faraday Trans.* **1994**, *90*, 3315.

[15] R. Brenot, R. Vanderhaghen, B. Drevillon, I. French, P. Roca i Cabarrocas, *Thin Solid Films* **1997**, *296*, 94.

[16] E. M. Hutter, G. E. Eperon, S. D. Stranks, T. J. Savenije, *J. Phys. Chem. Lett.* **2015**, *6*, 3082.

[17] *Standard Tables for Reference Solar Spectral Irradiances, Standard G173-03e*, The American Society for Testing and Materials, 2006.

[18] I. Grill, K. Handloser, F. C. Hanusch, N. Giesbrecht, T. Bein, P. Docampo, M. Handloser, A. Hartschuh, *Sol. Energy Mater. Sol. Cells* **2017**, *166*, 269.

[19] Y. Hu, E. M. Hutter, P. Rieder, I. Grill, J. Hanisch, M. F. Aygüler, A. G. Hufnagel, M. Handloser, T. Bein, A. Hartschuh, K. Tvingstedt, V. Dyakonov, A. Baumann, T. J. Savenije, M. L. Petrus, P. Docampo, *Adv. Energy Mater.* **2018**, *8*, 1703057.

[20] A. Baumann, S. Väth, P. Rieder, M. C. Heiber, K. Tvingstedt, V. Dyakonov, *J. Phys. Chem. Lett.* **2015**, *6*, 2350.

3 Humidity-induced degradation of $CH_3NH_3PbI_3$

This chapter is based on the following publication:

A. M. A. Leguy,† **Y. Hu**,† M. Campoy-Quiles, M. I. Alonso, O. J. Weber, P. Azarhoosh, M. van Schilfgaarde, M. T. Weller, T. Bein, J. Nelson, P. Docampo and P. R. F. Barnes, Reversible Hydration of $CH_3NH_3PbI_3$ in Films, Single Crystals, and Solar Cells. *Chem. Mater.* **2015**, *27* (9), 3397–3407. (DOI: 10.1021/acs.chemmater.5b00660)

† These authors contributed equally to this work.

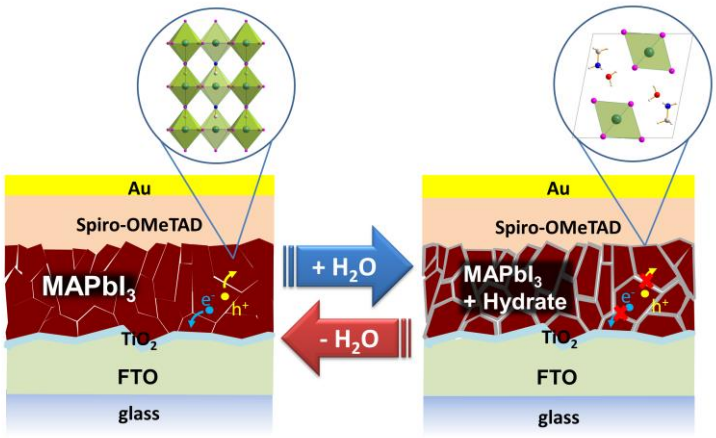

Adapted with permission.[1] Copyright 2015, American Chemical Society.

3.1 Abstract

Solar cells comprising methylammonium lead iodide perovskite (MAPI) are notorious for their sensitivity to moisture. We show that hydrated crystal phases are formed when MAPI is exposed to water vapor at room temperature and that these phase changes are fully reversed when the material is subsequently dried. The reversible formation of $CH_3NH_3PbI_3 \cdot H_2O$ followed by $(CH_3NH_3)_4PbI_6 \cdot 2\ H_2O$ (upon long exposure times) was observed using time-resolved XRD and ellipsometry of thin films prepared using 'solvent engineering', single crystals, and state-of-the-art solar cells. In contrast to water vapor, the presence of liquid water results in the irreversible decomposition of MAPI to form PbI_2. MAPI changes from dark brown to transparent on hydration; the precise optical constants of $CH_3NH_3PbI_3 \cdot H_2O$ formed on single crystals were determined, with a band gap at 3.1 eV. Using the single crystal optical constants and thin film ellipsometry measurements, the time dependent changes to MAPI films exposed to moisture were modelled. The results suggest that the monohydrate phase forms independently of the depth in the film suggesting rapid transport of water molecules along grain boundaries. Vapor phase hydration of an unencapsulated perovskite solar cell (initially $J_{sc} \approx 19$ mA cm^{-2} and $V_{oc} \approx 1.05$ V at 1 sun) resulted in more than a 90% drop in short circuit photocurrent and around 200 mV loss in open circuit potential, but these losses were fully reversed after the device was exposed to dry nitrogen for 6 h. Hysteresis in the current-voltage characteristics was significantly increased after this dehydration, which may be related to changes in the defect density and morphology of MAPI following recrystallization from the hydrate. Based on our observations we suggest that irreversible decomposition of MAPI in the presence of water vapor only occurs significantly once a grain has been fully converted to the monohydrate phase.

3.2 Introduction

Methylammonium lead iodide (which for simplicity we will refer to as MAPI) perovskite is generating frenzied interest in the field of alternative photovoltaics as a promising material for achieving the optimum paradigm of the technology: simplicity of processing combined with outstanding optoelectronic properties. The rapid progression of the claimed power conversion efficiencies of MAPI devices – exceeding 20%[2] within five years of the first publication[3] – raises the hope that the technology will lead to the manufacture of highly efficient photovoltaic modules with a short energy payback time relative to established technologies.[4]

Ensuring the stability of MAPI photovoltaics under operational conditions is one of the biggest barriers to commercializing the technology. At present, little is understood about the failure mechanisms of devices. To develop effective strategies to improve stability and achieve market standards, the degradation pathways under different environmental conditions must be elucidated.

Unmistakably, MAPI is sensitive to moisture, which may have both detrimental and beneficial effects depending on the context. The presence of humidity during film processing has been shown to significantly influence thin film morphology[5] and was claimed to lead to an improvement of the performance of solar cells.[6, 7] But the presence of water has also been suggested, e.g. by Frost *et al.*, to catalyze the irreversible decomposition of MAPI into aqueous HI, solid PbI_2 and CH_3NH_2 either released as gas or dissolved in water.[8] Experimental evidence has been published to confirm degradation of MAPI into PbI_2 [9] while, in parallel, water was suggested to provoke the crystallization of a perovskite species incorporating isolated $[PbI_6]^{4-}$ octahedra.[10] It has been shown that the exposure of MAPI solar cells to relative humidity greater than around 50% has rapid detrimental consequences on device performance.[11] Thus efforts to prevent moisture ingress[12] or careful device encapsulation are required to achieve significant stability under operation.[13]

This paper concerns the interaction of MAPI with water. The formation of colorless mono-hydrated methyl ammonium lead iodide ($CH_3NH_3PbI_3 \cdot H_2O$) from MAPI crystals in aqueous solution at temperatures below 40 °C was described in 1987 by Poglitsch and Weber.[14] The structure of this monohydrate was later determined by Hao *et al.*[15] The compound $(CH_3NH_3)_4PbI_6 \cdot 2\ H_2O$, which we will occasionally refer to as di-hydrated methylammonium lead iodide can also be formed by a similar method, as described by Vincent *et al.*[16] Pale yellow dihydrate crystals result when MAPI is cooled to below 40 °C in a mother liquor of aqueous $Pb(NO_3)_2$ and methylammonium iodide solution. Christians and co-workers recently investigated the interaction of MAPI and water vapor by exposing both MAPI films cast on mesoporous Al_2O_3 and full solar cells to controlled humidity,[17] while, concurrently, Yang *et al.* have investigated the influence of different hole transport materials on devices exposed to moisture.[18] Both identified the degradation product as $(CH_3NH_3)_4PbI_6 \cdot 2\ H_2O$; we note here that their diffraction patterns suggest a significant contribution from the monohydrate species. Additionally, Christians *et al.* observed a decrease in performance of solar cells that were stored in moist air depending on the level of humidity. Zhao *et al.*[19] reported instant optical bleaching of MAPI thin films upon exposure to ammonia vapor that was fully reversible. Their observation was characterized by the appearance of a new Bragg (Cu-K_α) reflection around 2θ = 11.6° in the XRD pattern of the bleached MAPI species. Although not yet widely appreciated, MAPI clearly shows a propensity to form new solvated crystal structures at room temperature by incorporating small polar molecules. The full reversibility of the stepwise hydration of MAPI has – to the best of our knowledge – not yet been demonstrated.

Here, we combine time-resolved ellipsometry with X-ray diffraction measurements to identify the degradation products and monitor the dynamics of the decomposition reactions on thin films, single crystals and full devices in the presence of moisture. Beside the precise derivation of the optical constants of both MAPI single crystals and the hydrate species, our results elucidate the hydration mechanisms and differentiate between reversible hydration and the irreversible formation of lead iodide, thus constituting a crucial step towards engineering long-term stability in perovskite solar cells. Finally, we show that devices that have been exposed to moisture exhibit a dramatic loss of performance which may be recovered by a simple drying step at room temperature so long as water condensation on the perovskite surface did not occur.

3.3 Results and discussion

3.3.1 Single crystals

The hydration mechanism was first investigated optically by varying angle spectroscopic ellipsometry on single crystals of MAPI. The single crystals were prepared via the method of Poglitsch and Weber[14] recapitulated in the Methods section. Figure 3.1 shows the optical characterization and reversibility upon hydration of what was initially a single crystal of MAPI. When exposed to 70% relative humidity (RH) at room temperature, the band gap of the crystal underwent a change from about 1.6 to 3.1 eV in ca. 60 h. The final product is a hydrate constituting a new phase which does not show any of the features of the pristine material. It will be shown below that this hydrate, observed to form at the early stages of the hydration of MAPI crystal is the monohydrate phase. When subsequently exposed to dry atmosphere, the hydrate instantly starts to convert back to the initial MAPI perovskite structure, the process ending in the full recovery of the material (see Figure 3.2a) in about 4 h. The layer thickness probed by ellipsometry can be estimated crudely from the optical penetration depth δ_P (where $\delta_P = \lambda_0/4\pi\kappa$ with λ_0 the incident wavelength and κ the extinction coefficient). The probed depth thus varies between approximately 300 nm for 1.6 eV photons to only about 30 nm at 3.1 eV. Since the hydrate spectrum presents no feature around 1.6 eV, we conclude that full conversion from MAPI to the hydrate occurred to at least the penetration depth within the crystal such that only one species was being examined in each measurement.

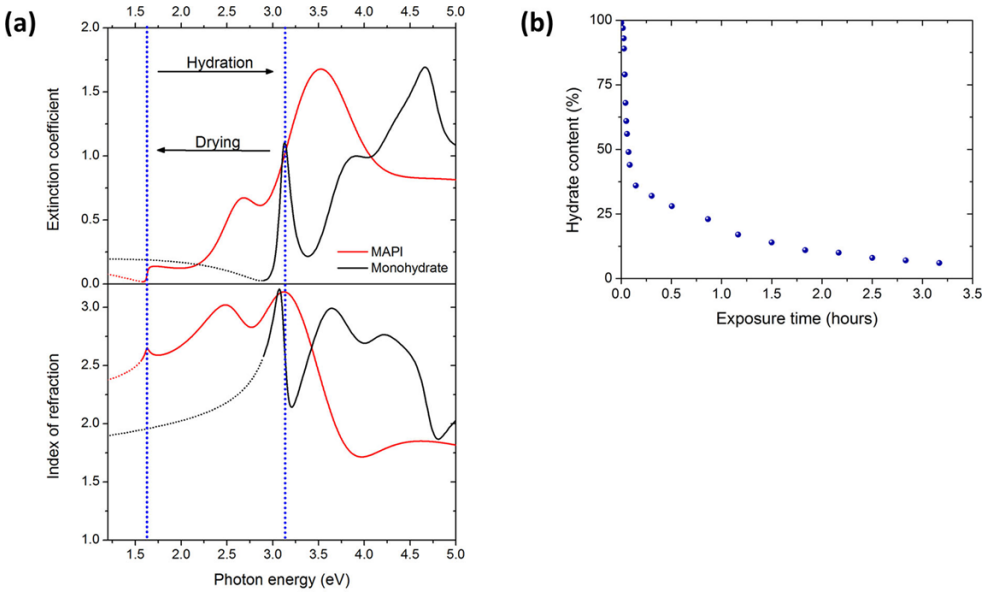

Figure 3.1 (a) Optical constants of MAPI (solid red line) and the hydration product (solid black line) modelled from single crystal ellipsometry. The dotted part of the spectra corresponds to the sub-band gap region. The vertical dotted blue lines help to visualize the shift of the band gap energy upon hydration and drying. (b) Fraction of $CH_3NH_3PbI_3 \cdot H_2O$ that has not been converted back to MAPI as a function of drying time. The measurement was performed on a single crystal of MAPI that had previously been hydrated by exposure to moisture (70% RH, room temperature) for 60 h until no MAPI was detectable by ellipsometry.

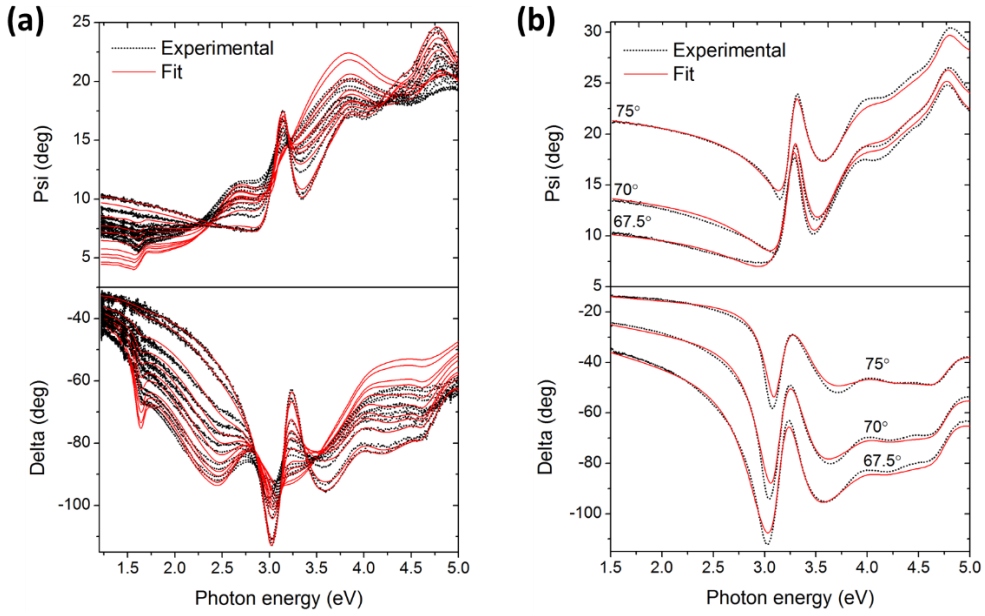

Figure 3.2 (a) Fit of the ellipsometry spectra for the back-conversion from hydrate to MAPI. The spectra were acquired at fixed angle of incidence of 67.5° every 5 s during the first 10 min and at 2 min intervals after that. The spectra were modelled by a Bruggeman approximation using an effective medium (EMA) consisting of

the two compounds shown in Figure 3.1, and voids (accounting for morphological changes due to re-crystallization). The fit parameters were the thickness of the roughness layer on top of the EMA bulk crystal and the relative ratio of MAPI and its hydrate in the mixture, determined in a similar way as for the films. (b) Fit of the ellipsometry parameters for a hydrated MAPI single crystal. The experimental spectra (dotted black lines) were acquired at three different angles of incidence 67.5°, 70° and 75° (the range of measurable angles is limited by the shape of the slits of the hydration chamber). The fitted critical point model (solid red lines) was obtained with the critical point model presented in Table 3.1.

The dielectric functions of both MAPI and the monohydrate phase were modelled by fitting an ensemble of critical points (CPs) of the joint density of states to the measured ellipsometry parameters according to the approach described in the Methods section. The fits of the ellipsometry parameters of the hydrate are given in Figure 3.2b; we believe this is the first optical characterization of this material. The precise derivation of the optical properties of MAPI single crystals will be published separately and are consistent with the recent optical characterization of MAPI thin films in literature.[20-22] We note that literature values of the MAPI band gap range from 1.5 to 1.6 eV. The spread in this quantity appear to be due to differences in the measurement techniques and definition of the band gap[20-24] and recent observations suggests aging effects may also increase the band gap.[25] For the purposes of this study we will use the energy of the first critical point required to fit the ellipsometry data which is also consistent with the energy of the photoluminescence peak. We note that this quantity is not identical to the band gap determined from a Tauc plot of powder reflectance which requires a more accurate determination of the absorption tail, a feature that is not well characterized by ellipsometry. Excitonic critical points (0D, $n = -1$ in Equation 3.1) were suitable for describing the optical transitions. In particular, the band gap transition was found to be strongly excitonic (see Figure 3.3 and Table 3.1) of symmetric Lorentzian line shape due to a high degree of localization of the exciton on the octahedra, as explained below.

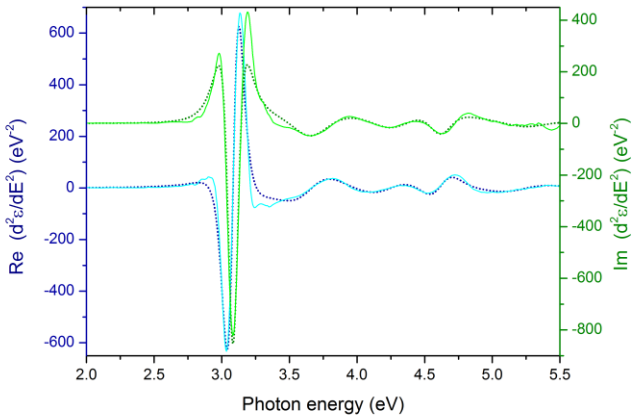

Figure 3.3 Fit of the second derivative of the dielectric constant of hydrated MAPI obtained by spectroscopic ellipsometry. On the axis label, 'Re' and 'Im' stand for real part and imaginary part, respectively. The experimental derivatives were numerically built using 5th grade smoothing polynomials with appropriate numbers of correlated points to obtain the best smoothing without inducing too much distortion to the experimental line shape.[26] The critical point model obtained for the best fits is given in Table 3.2. It shows that the hydrate can be described by 0D critical points with phase parameters close to 0, which indicates the localized excitonic nature of these transitions.

Table 3.1 Critical point model of hydrated MAPI obtained when fitting the second derivative of the dielectric constant. The CP *i* is described by the amplitude A_i, energy Ec_i, linewidth Γ_i, and the exciton phase angle Φ_i was set to 0. The numbers given in parenthesis give the errors in the last significant digits of the fitted values.

CP	*A*	E_{ci} (eV)	Γ	Φ (deg)	*n*
1	0.51(3)	3.083(2)	0.106(2)	0	-1
2	1.27(2)	3.655(1)	0.356(10)	0	-1
3	0.96(7)	4.250(23)	0.393(30)	0	-1
4	0.27(9)	4.618(23)	0.217(30)	0	-1
5	0.5(1)	5.24(26)	0.40(5)	0	-1

Table 3.2 Critical point model of hydrated MAPI. The CP *i* is described by the amplitude A_i, energy Ec_i, linewidth Γ_i, and an exciton phase angle Φ_i. UV_{term} = -2.1693 in this model.

CP	*A*	E_{ci} (eV)	Γ	Φ (deg)	*n*
1	0.3980	3.1045	0.06380	-22.70	-1
2	1.7226	3.6298	0.3136	-77.23	-1
3	0.5949	4.1516	0.2679	-114.91	-1
4	0.5101	4.7024	0.1584	65.38	-1
5	69.35	10.8992	7.9632	-23.30	-1

Surface roughness was modelled by an effective medium approximation layer, as explained in the Methods section. The best fits gave values of the surface irregularity around 20 nm for MAPI single crystals and 15 nm in its hydrated form (note that these values should be considered as fitting parameters accounting for the imperfection of the crystal surface rather than representing the absolute rms roughness). Some uncertainty remains regarding the optical constants in the sub-band gap region (red and black dotted lines in Figure 3.1a), as the calculated values can be influenced by the tail of the critical points.

A comparison between the position of the CPs of MAPI and its hydrated counterpart is given in Table 3.3. The position of the fifth CP of the hydrate is ambiguous as it is located outside the probed spectral region. It accounts for transitions occurring at higher energies which could not be accurately characterized with the apparatus employed in this study.

Table 3.3 Critical point energies obtained for the best fit of MAPI and its hydrate.

CP	CP position in MAPI (eV)	CP position in the hydrate (eV)
1	1.6	3.1
2	2.6	3.6
3	3.1	4.2
4	3.6	4.7
5	4.8	10.9

We now analyze the structure of hydrated MAPI. X-ray diffraction (XRD) patterns were collected from MAPI single crystals that were exposed to water vapor (80% RH during 60 h). The XRD pattern in Figure 3.5a indicates that the MAPI single crystal has converted to a monohydrate, $CH_3NH_3PbI_3 \cdot H_2O$. The simulated XRD patterns for each phase[16, 27] (also shown in Figure 3.5a) enable clear identification of the strong reflections at $2\theta = 8.47°$ and $2\theta = 10.54°$ as MAPI monohydrate.

The monohydrate, $CH_3NH_3PbI_3 \cdot H_2O$, was reported to form metastable, thin, pale yellow needles (see Figure 3.4) which dehydrate spontaneously in air, forming polycrystalline MAPI.[27] Figure 3.5c shows the refined crystal structure of this intercalation compound.[27] It incorporates one-dimensional (1D), isolated $[PbI_3]^-$ double-chains, in which each $[PbI_6]^{4-}$ octahedron is connected to two neighboring octahedra by a common corner forming a two-octahedra wide 'ribbon' (extending out of the page, along the b-axis in Figure 3.5c. These negatively charged $[PbI_3]^-$ chains are charge balanced by the intercalated $CH_3NH_3^+$ cations. Additionally, the H_2O molecules which are inserted between the $[PbI_3]^-$ chains provide further stability to the structure via symmetrically bifurcated

hydrogen bonds between the H-atoms of the water molecules and the N-atom of methylammonium cations ($d_{(O\text{-}N)}$ = 2.829 Å).[27] The calculated XRD pattern of $CH_3NH_3PbI_3 \cdot H_2O$ exhibits intense Bragg peaks at the 2θ positions 8.10°, 8.66° and 10.66°, corresponding to the (001), (100) and ($\bar{1}$01) reflections of a monoclinic P 2_1/m crystal structure. In the XRD pattern of the MAPI film exposed to moisture in Figure 3.5a, the presence of monohydrate can be recognized by reflections around 8.6° and 10.5°.

Figure 3.4 Photograph of synthesized crystals of $(CH_3NH_3)_4PbI_6 \cdot 2\ H_2O$ in the mother liquor.

The monohydrate, $CH_3NH_3PbI_3 \cdot H_2O$, should not be confused with the related dihydrate crystal structure, $(CH_3NH_3)_4PbI_6 \cdot 2\ H_2O$. Dihydrate crystals are obtained –together with the monohydrate species– in directly synthesized hydrated MAPI needle shaped crystals prepared from solution (Methods section, photographs in Figure 3.4, characteristic reflection at 2θ = 11.39° in the XRD pattern in Figure 3.5a). The dihydrate, $(CH_3NH_3)_4PbI_6 \cdot 2\ H_2O$, can be considered as a zero-dimensional network of isolated $[PbI_6]^{4-}$ octahedra, neutralized by surrounding $CH_3NH_3^+$ cations. The crystal structure can be related to a distorted NaCl-type lattice consisting of $[PbI_6]^{4-}$ octahedra and $(CH_3NH_3\cdots H_2O\cdots CH_3NH_3)_2^{4+}$ dimers (see Figure 3.5d).[16] The simulated XRD pattern in Figure 3.5a shows that this compound has a diffraction peak around 11.4°. Papavassiliou *et al.* reported the value of 3.87 eV for the position of the band gap of $(CH_3NH_3)_4PbI_6 \cdot 2\ H_2O$ by optical absorption spectroscopy.[28] The absence of any feature in the absorption spectrum obtained from the ellipsometry results in Figure 3.1 combined with the clear assignment of the XRD peaks to $CH_3NH_3PbI_3 \cdot H_2O$ in Figure 3.5a rules out the presence of any significant amount of dihydrate in the hydrated MAPI single crystals.

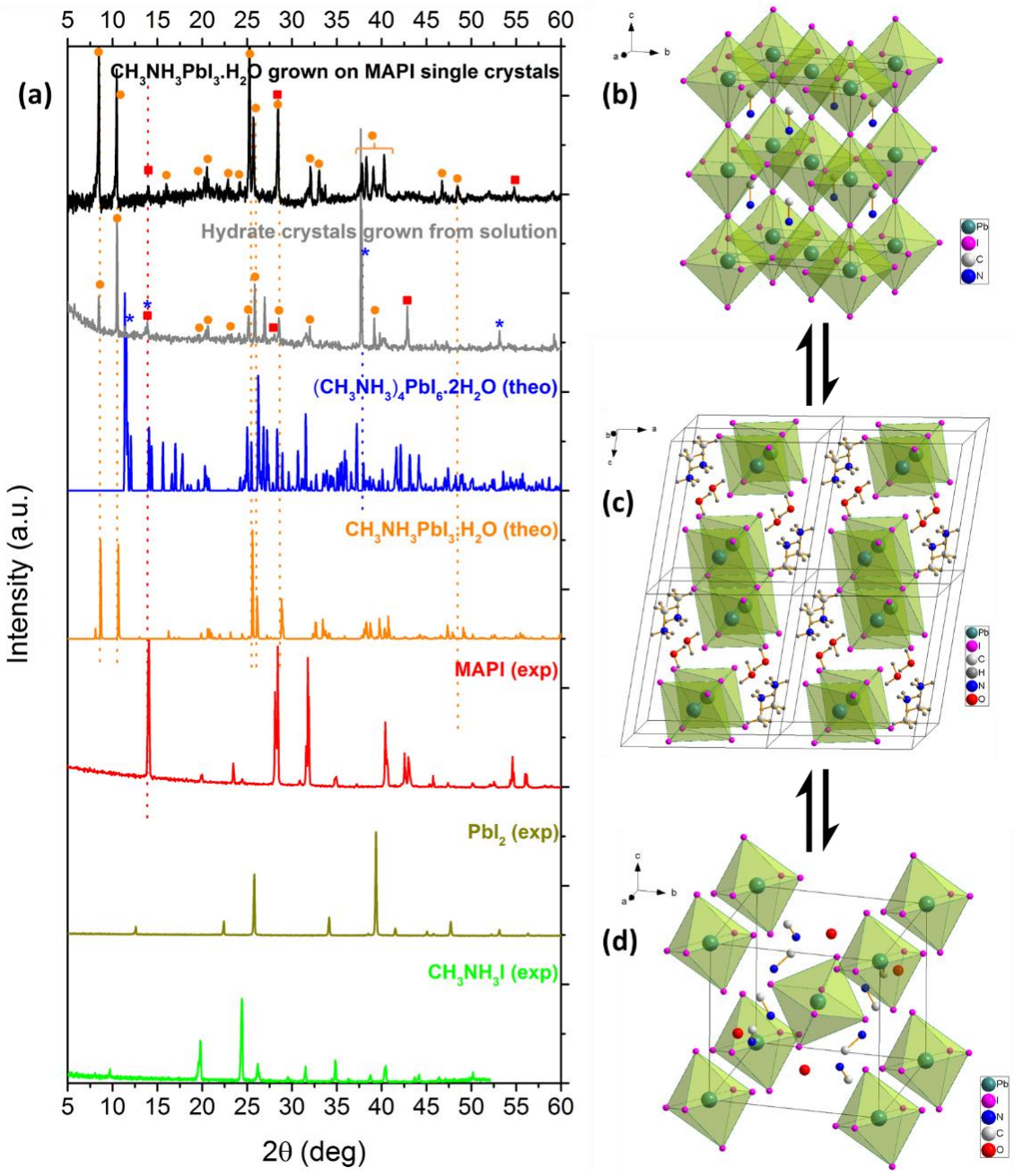

Figure 3.5 (a) Identification of the composition of the hydrate species grown on MAPI single crystals (at long exposure to water vapors) and of MAPI hydrate crystals (polycrystalline, obtained from solution) by X-ray diffraction (patterns in black and grey). The five patterns below these show species the hydrate is likely to contain. Symbols are used to tag the main features according to the color of their respective spectra. (b) Shows the structure of MAPI in its cubic phase, while (c) shows the structure of the monohydrate phase, $CH_3NH_3PbI_3 \cdot H_2O$ and (d) displays the structure of the dihydrate, $(CH_3NH_3)_4PbI_6 \cdot 2\ H_2O$. The position of the hydrogens on the $CH_3NH_3^+$ ions and the water is not assigned in (b) and (d).

3.3.2 Thin films and polycrystals

The study was next extended to thin films. MAPI films were prepared on glass using the 'solvent engineering' approach and then exposed to air with a relative humidity of ~80% for 2 h. The XRD patterns displayed in Figure 3.6a show that the exposure to moist air resulted in the conversion of MAPI to both the mono- and dihydrate species.

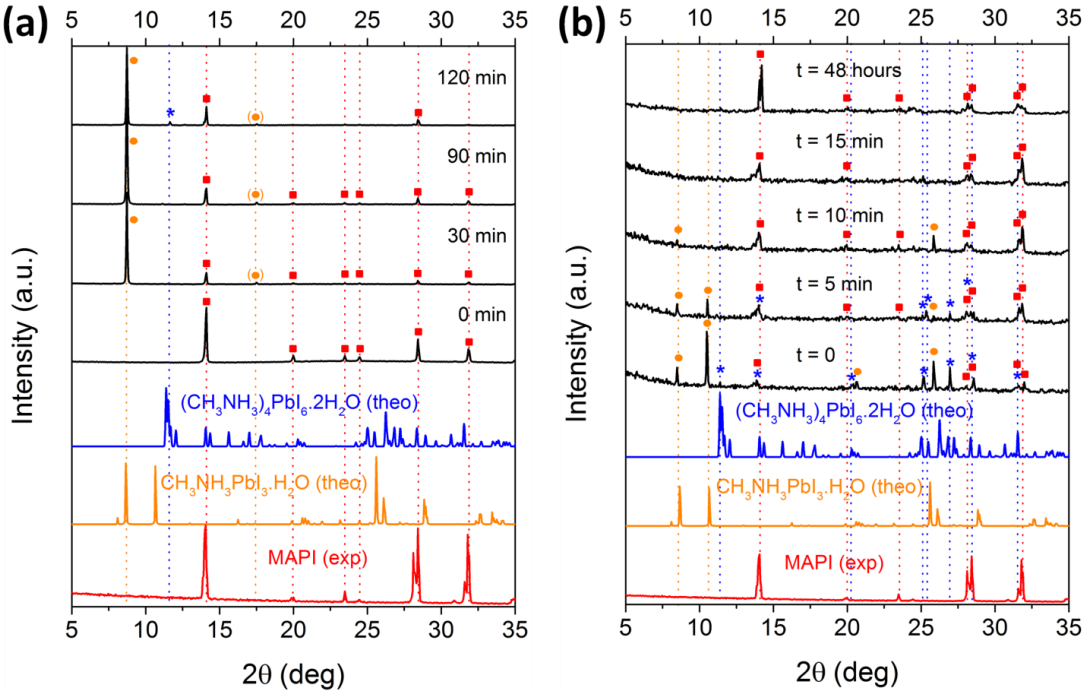

Figure 3.6 Time-resolved XRD patterns of polycrystalline MAPI: (a) hydration of a MAPI thin film and (b) dehydration of directly synthesized hydrate needle-like crystals.

Although both hydrate species coexist in the MAPI film after prolonged exposure to moisture, their formation is not simultaneous. Time-resolved XRD experiments were performed to monitor the dynamics of the hydration and dehydration processes in MAPI and to identify the composition of the samples at different transformation stages. The MAPI films were exposed to an airflow containing (80 ± 5)% RH. For exposure times of 30 min and 60 min, the XRD patterns exhibit a very strong diffraction peak at 8.72° in addition to the characteristic reflections of pristine MAPI, indicating the formation of $CH_3NH_3PbI_3 \cdot H_2O$ (see Figure 3.6a). After 120 min, an additional reflection at 11.64° was detected, indicating the formation of crystalline $(CH_3NH_3)_4PbI_6 \cdot 2\ H_2O$ in the perovskite film. We conclude that the hydration reaction of MAPI is a two-step process, in which the crystal structure

of MAPI is first progressively saturated with one water molecule per formula unit, followed by the formation of a new structure with two water molecules per formula unit upon longer exposure to humidity. The intercalation of water molecules into the crystal structure of MAPI induces a rearrangement resulting in the separation of the $[PbI_6]^{4-}$ octahedra, corresponding to the transition from a 3D network of octahedra in pristine MAPI, to 1D double-chains in the monohydrated MAPI species, and finally resulting in a 0D framework of isolated octahedra in the MAPI dihydrate. This crystallographic observation substantiates the idea of a high degree of localization of the exciton in the MAPI hydrate which is suggested by our ellipsometry measurements.[29]

The composition of the hydrate species and their sequential formation suggests the following stoichiometric equation:

$$4\ (CH_3NH_3)PbI_3 + 4\ H_2O \rightleftharpoons 4\ [CH_3NH_3PbI_3 \cdot H_2O] \rightleftharpoons (CH_3NH_3)_4PbI_6 \cdot 2\ H_2O + 3\ PbI_2 + 2\ H_2O$$

The monohydrate is an intermediate product that can be easily converted back to MAPI.[27] When the reaction is driven further to the right by prolonged exposure to water vapor, the formation of the dihydrate is initiated, accompanied by the formation of lead iodide and the release of two water molecules. Only traces of PbI_2 were detected in the XRD patterns. The reason may be that the PbI_2 formed is initially in an amorphous or nanocrystalline phase, presumably pushed out of the hydrate crystals to grain boundaries. The release of water as the reaction goes from the monohydrate to the dihydrate suggests partial self-sustainability of the conversion process as the water molecules released can be reused to convert remaining MAPI into the monohydrate. It seems likely that the reversibility of mono- to dihydrate conversion may be limited by phase separation of the reaction products. Eventually, when the whole film is converted, an excess of water may result in the dissolution of $CH_3NH_3^+$, irreversibly degrading the structure:

$$(CH_3NH_3)_4PbI_6 \cdot 2\ H_2O\ (s) \xrightarrow{H_2O(l)} 4\ CH_3NH_3I\ (aq) + PbI_2\ (s) + 2\ H_2O\ (l)$$

The exposure of $(CH_3NH_3)_4PbI_6 \cdot 2\ H_2O$ to light may also result in its irreversible decomposition without the requirement for excess water.[12, 30]

The reverse dehydration reactions were observed to spontaneously occur when hydrated MAPI crystals were exposed to air with low humidity (35% RH at 21°C). In order to track the dehydration reactions, XRD patterns were recorded in 5 minute intervals, shown in Figure 3.6b. During the exposure to ‘dry’ air the crystals changed color from yellow to dark grey, indicating the formation of polycrystalline MAPI as water molecules were lost.

Figure 3.6b shows that after only a few minutes of drying, characteristic XRD reflections of pristine MAPI appeared in the diffraction patterns. Longer drying led to the disappearance of the reflection

at 11.39° corresponding to complete transformation of crystalline MAPI dihydrate to other phases. The reduction of this reflection intensity is accompanied by a decrease of the reflection intensities associated with MAPI monohydrates and a concomitant increase in the intensity of the crystalline MAPI reflections. This gradual transformation of hydrated MAPI into MAPI perovskite crystals ends in the formation of MAPI within ca. 15 min, as demonstrated by the XRD patterns showing only the reflections of tetragonal MAPI. We observed that for crystallites of similar sizes, dehydration appears to be a faster process that hydration at room temperature.

Although crystallites of hydrated MAPI were previously reported to have a pale yellow color,[16, 27] our optical characterization, which we assign to the monohydrate phase, indicated that the material is almost colorless. This observation is corroborated by reflectometry measurements performed by Hirasawa *et al.* in the 1990's.[31] The pale yellow color of macroscopic MAPI hydrate needles reported previously may originate from defects, disorder or impurities, for example traces of elemental iodine which can evolve in the mother liquor from oxidation of concentrated HI solutions, or from the formation of lead iodide when $CH_3NH_3PbI_3 \cdot H_2O$ converts to $(CH_3NH_3)_4PbI_6 \cdot 2\ H_2O$.

We reiterate that the MAPI film hydration process did not initially lead to the formation of a substantial amount of crystalline lead iodide. We speculate that the mechanism of irreversible decomposition of MAPI into HI, PbI_2 and CH_3NH_2 can only happen in the presence of excess or liquid water which can dissolve the methylammonium ions. We substantiated this hypothesis by exposing a thin film of MAPI to warm water vapors (see Figure 3.7). Water condensation resulted due to the temperature difference between sample and humid air. Lead iodide was formed with no detectable trace of the hydrate crystals. This reaction was not reversible.

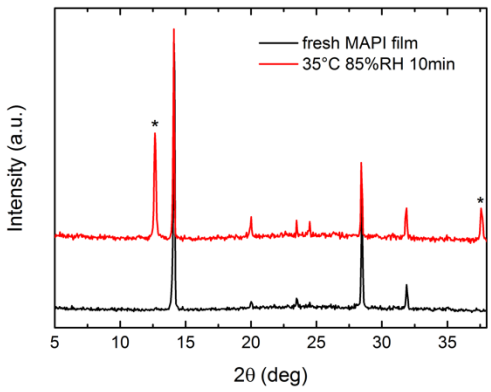

Figure 3.7 XRD patterns of a MAPI thin film before (black line) and after 10 min exposure to humid air (85% RH) upon slight heating at 35 °C (red line) showing irreversible degradation. Formation of PbI_2 (*) can be observed.

We now propose a mechanism to describe how hydration occurs in thin films based on the interpretation of the ellipsometry observations. Ellipsometry spectra were recorded every 10 or 20 min during the conversion of a crystalline MAPI film to $CH_3NH_3PbI_3 \cdot H_2O$ by exposure to air with RH 80% over a period of 100 min.

Figure 3.8a shows a diagram of the conversion model that yielded the most accurate description of the transient ellipsometry data. It describes the hydration process as isotropic and homogenous, which corresponds mathematically to a Bruggeman-type mixture of both pristine MAPI and its hydrated counterparts (see the Methods section for details on the Bruggeman approximation). The optical constants of both MAPI and the hydrate phase were determined from a MAPI single crystal and a MAPI single crystal hydrated by exposure to a moist airflow (80% RH) for 60 h (see Figure 3.1). The three fit parameters in this model are: the thickness of the solid thin film, the thickness of the roughness layer on top of the film, and the relative ratio of MAPI and its hydrate in the mixture forming the film and roughness layer. The thickness of the roughness layer was a free parameter during the whole fitting procedure. The thickness of the film and the ratio of its constituents were iteratively defined as fit parameters to avoid the issues arising from the high correlation between these two variables.

Figure 3.8b shows representative fits to the measured elliposmetry parameters using the isotropic Bruggeman hydration model described in the previous paragraph. In addition to the qualitative agreement, the model is confirmed by a figure of merit, the mean squared error calculated for the simultaneous fit of the 9 curves (MSE = 5.9) indicating a close match between modelled and experimental data. An alternative model was also tested which describes the anisotropic formation of the hydrate as a layer on top of a MAPI film, with progressive conversion of MAPI to hydrate from top to bottom. However, this model could not account for the collected ellipsometry data. Other more sophisticated models such as graded compositions did not improve significantly the fits either. Thus we conclude the conversion is isotropic on macroscopic scales (i.e. the average film composition is independent of depth), although the phases are likely to separate on a microscopic scale. This suggests a high degree of penetration of water molecules into MAPI thin films that might arise from diffusion of water molecules along grain boundaries.

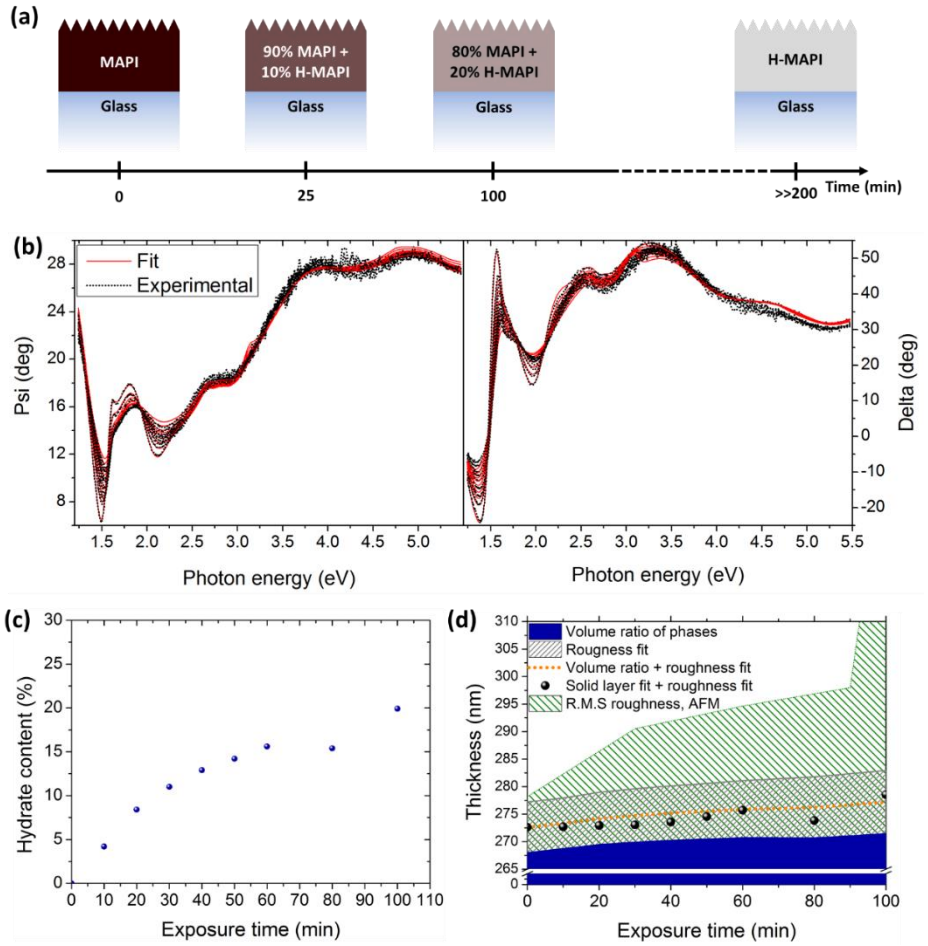

Figure 3.8 (a) The Bruggeman-type degradation mechanism used to model the ellipsometry parameters. (b) Representative fits of the ellipsometry parameters obtained using the Bruggeman model at different exposure times. (c) Hydrate proportion in the thin film as a function of exposure time to humid air (80% RH). (d) Cumulative plot of the thickness increase due to conversion from MAPI to hydrate species. The blue area shows the solid layer thickness inferred from the relative ratio of phases determined from fit of ellipsometry models. The hatched grey area is the surface roughness inferred from the fit of the ellipsometry model assuming 50% of voids and 50% of solid layer (blue) in the rough region. The orange dotted line gives the total equivalent layer thickness defined by the blue area plus half of the grey. It can be compared with the black dots showing the total equivalent layer thickness obtained from the fit of the ellipsometry model assuming solid layer (blue) and half of grey. The hatched green area gives the root mean square roughness R_{rms} measured by AFM.

Our isotropic model cannot describe the complete degradation process of thin films at exposure times longer than 100 min for two reasons. Firstly because the optical constants obtained in the single crystal study are those of the monohydrate. The formation of the dihydrate at longer exposure times modifies the optical constants of the compound, which would require a different, three component Bruggeman model. Secondly, a significant increase of the top layer roughness is observed at long

exposure times, which causes a dramatic increase of the proportion of scattered light (atomic force micrographs of the film surface for different moisture exposure times are shown in Figure 3.9, and the change in surface roughness with time is given in Table 3.4). Significant roughness (above a value of ~λ/10, λ wavelength of the probe beam) has to be analyzed with models that are more complex than a single EMA layer with voids. We note that the probe spot of the ellipsometer (~1 mm) has a large diameter compared to the characteristic grain size (~50 to 400 nm), which reconciles our homogenous and isotropic macroscopic conversion model with the microscopic model.

Table 3.4 Measured root mean square roughness of MAPI films exposed to moisture.

Exposure time, *t* [min]	0	30	60	90	120
Roughness, R_{rms} [nm]	10.2	21.8	25.2	28.1	165.1

Figure 3.8c shows the evolution of the modelled hydrate content against moist air exposure time obtained from the ellipsometry fit. It can be correlated with the results from time-resolved X-ray diffraction presented in Figure 3.6a. Conversely, Figure 3.8b shows the disappearance of $CH_3NH_3PbI_3 \cdot H_2O$ upon drying of a hydrated single crystal of MAPI. Conversion of MAPI perovskite to $CH_3NH_3PbI_3 \cdot H_2O$ causes a lattice expansion of 6%, based on the relative lattice parameters of the two phases (247 $Å^3$ per formula unit for MAPI, and 263 $Å^3$ for $CH_3NH_3PbI_3 \cdot H_2O$).[16, 27] Using the fitted hydrate content as a function of exposure time (Figure 3.6), values of the increase of the solid layer thickness due to its expansion on partial hydration can be estimated. Since the roughness of the top layer is also increased by exposure to moisture, the expansion of the total equivalent thickness is obtained by adding the increase of the measured top layer roughness to the dilatation of the lattice inferred from the relative ratio of phases. Figure 3.8d shows that the thickness predicted from the volume fraction and values directly inferred from the ellipsometry fit follow a very similar trend, as would be expected if our model is internally self-consistent. At early exposure times (<60 min), however, the measured total thickness is increasing slowly compared with the amount of hydrate present in the film. This could indicate that the hydrate is filling voids within the granular films.

The increase of roughness appearing together with the discoloration of MAPI thin films due to hydration is shown in Figure 3.9 as a function of exposure time. A dramatic increase in roughness is observed at exposure times longer than 90 min, caused by the crystallization of needle shaped structures on the surface of the films. This corresponds to the appearance of dihydrate XRD

reflections in Figure 3.6a. It is therefore likely that these new structures are dihydrate crystals (cf. photograph of directly synthesized needle like hydrate crystals in Figure 3.4). Note that volume of the dihydrate phase and PbI_2 released on conversion from $CH_3NH_3PbI_3 \cdot H_2O$ is 28% greater than the original volume of MAPI.

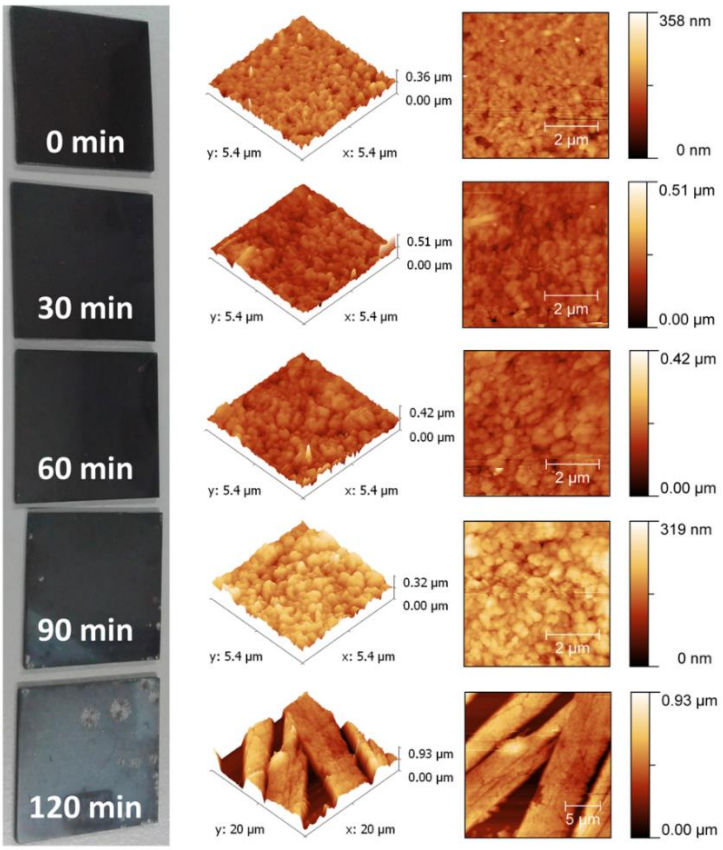

Figure 3.9 Photographs of thin films of MAPI deposited on glass at different hydration times (left) showing discoloration and AFM measurements in 3D (middle) and 2D representations (right).

3.3.3 State-of-the-art solar cells

Finally, we now extend our investigations to state-of-the-art solar cells to demonstrate the reversibility of the hydration process in functional devices. The solar cells were fabricated according to the protocol detailed in the Methods section. Figure 3.10a shows the forward to reverse bias photocurrent-voltage scans measured at different times during exposure of the device to moist air (77% RH) for 3 h followed by exposure to a dry nitrogen stream for approximately 5 h. Figure 3.10b

shows the corresponding photocurrent-voltage (*J-V*) curves measured with reverse to forward bias scans. It is apparent for both scan directions that there is almost an order of magnitude drop in the photocurrent and around a 200 mV loss in photovoltage after the device was exposed to moisture for 3 h. Strikingly, following exposure of the device to dry nitrogen for 5 h the *J-V* curve recovered to very close to its original state in the case of the forward to reverse bias scan. For the reverse to forward bias scan this recovery was much less complete and we see that the magnitude of the hysteresis[32] in the device's *J-V* curves has increased following the hydration-dehydration cycle.

Figure 3.10c demonstrates the concomitant appearance of the characteristic XRD peaks of the monohydrate with the loss in photovoltaic performance seen in Figure 3.10a–b. The XRD measurement was performed on the complete solar cell exposed to moisture and demonstrates the formation of MAPI monohydrate in devices.

The combination of time-resolved XRD and *J-V* measurements suggests that partial hydration is already sufficient to cause a dramatic drop in PCE. Our ellipsometry modelling implied that the hydration process was isotropic on a macroscopic scale. This observation, combined with the granular nature of the thin film (see Figure 3.10c) suggests efficient penetration of moisture within the MAPI film along grain boundaries or micro-/mesopores. These arguments lead us to propose the microscopic degradation mechanism displayed in Figure 3.10e. Here, the significant loss of PCE after partial conversion to MAPI hydrate may be due to the isolation of the grains from each other which would rapidly impede charge carrier transport resulting in increased recombination at grain interfaces.

It is interesting that the exposure of devices comprising MAPI to moist air at 77% RH and 21 °C did not lead to the irreversible decomposition of MAPI into lead iodide and HI, as would be the case in the presence of liquid water. In fact, the effect of moisture exposure could be reversed by exposure to a dry gas flow for several hours. However, it is likely that the underlying film underwent micro-structural reorganization during this process, which may account for the significantly increased hysteresis observed following the hydration-dehydration cycle.[33]

This same process can however be beneficial during film processing. Since the presence of water vapor appears to catalyse dynamic recrystallization within the film between the hydrated and pure crystalline phases, this may lead to higher quality films under the optimized processing conditions as long as water is subsequently completely removed by thermal annealing. We note that the humidity in these studies[6, 7] is lower than ~50%. 60% appears to be a threshold where films are no longer good quality.

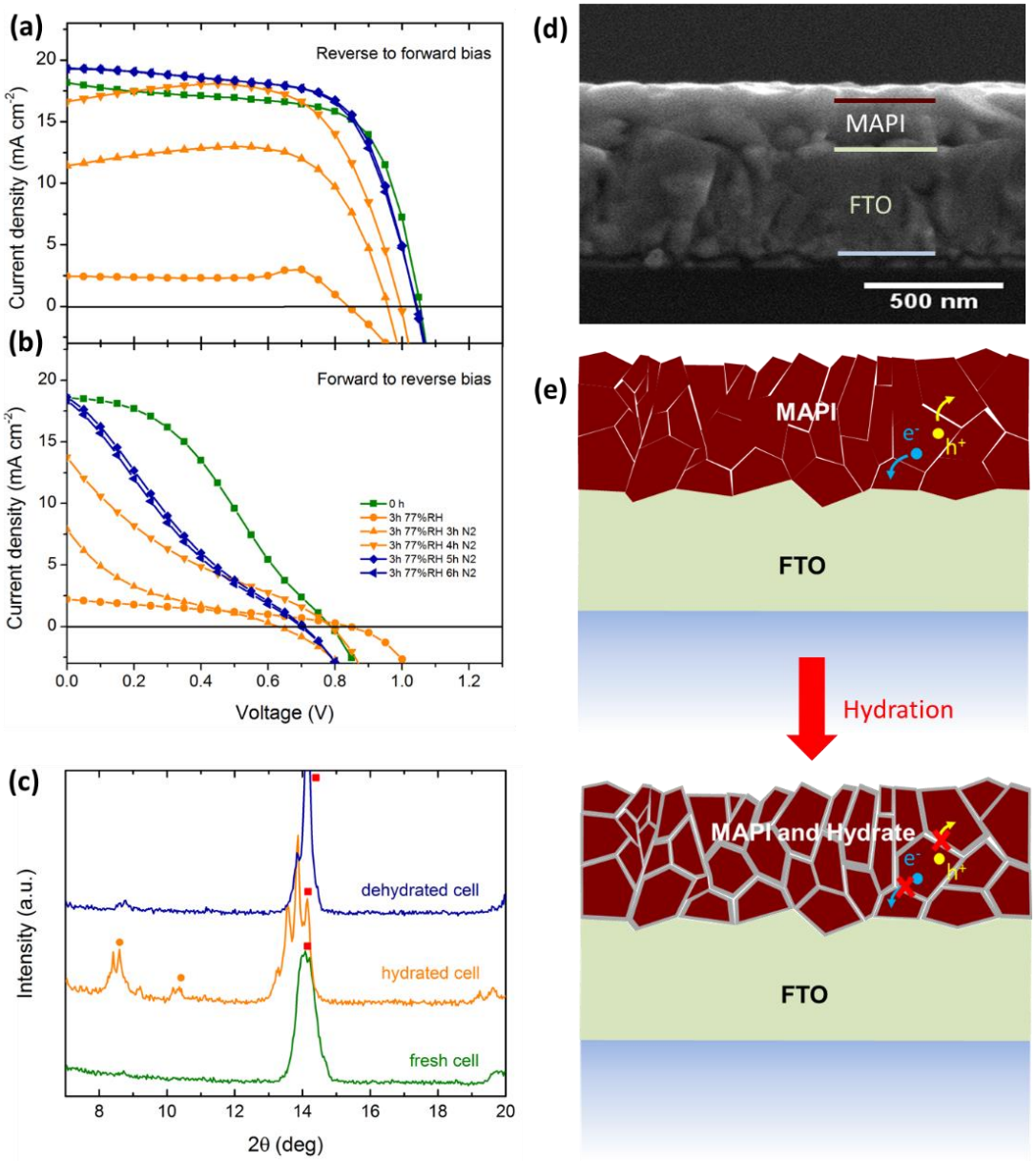

Figure 3.10 (a) and (b) Current-voltage characteristics showing full recovery of a planar heterojunction MAPI solar cell upon exposure to moisture; scanned from reverse to forward bias and from forward to reverse, respectively. The corresponding performances of the devices are given in Table 3.5. Note that the steady state performance of cells prepared in a similar way indicated lower steady state photocurrents at the maximum power point (see Figure 3.11). (c) XRD patterns of a device before and after hydration showing the emergence of the hydrate species. Dots are used to tag the main features according to the color of their respective spectra. (d) Cross-sectional SEM image of MAPI deposited on a FTO-coated glass slide. (e) Presumed microscopic degradation model of MAPI thin films under partial hydration.

Table 3.5 Current-voltage characteristics of a typical perovskite solar cell undergoing a hydration/ dehydration cycle. The values are for the reverse scans. PCE refers to the nominal efficiency that would be inferred from the reverse *J*-*V* scan.

Sample	J_{sc} (mA cm^{-2})	V_{oc} (V)	FF	PCE (%)
MAPI 0h 77% RH	18.16	1.05	0.68	12.90
MAPI 3h 77% RH	2.46	0.85	1.01	2.10
MAPI 3h 77% RH 3h N_2	11.42	0.95	0.77	8.39
MAPI 3h 77% RH 4h N_2	16.63	1.00	0.70	11.70
MAPI 3h 77% RH 5h N_2	19.34	1.05	0.66	13.41
MAPI 3h 77% RH 6h N_2	19.30	1.05	0.66	13.28

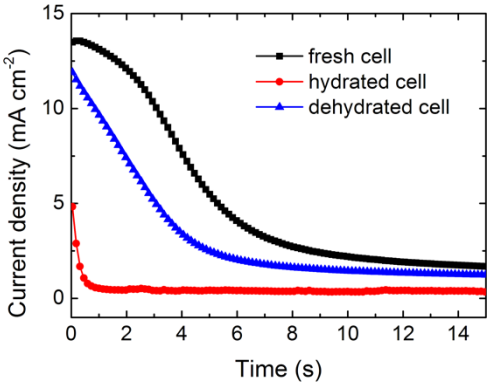

Figure 3.11 Example of photocurrent at maximum power point (MPP) against time, for a fresh, hydrated and dehydrated cell. The devices were held in light at forward bias (2.5 V) before switching to the MPP voltage.

3.4 Conclusions

In conclusion, in addition to the precise optical characterization of MAPI and $CH_3NH_3PbI_3 \cdot H_2O$, we have shown that the moisture in air induces a reversible hydration process of methylammonium lead iodide perovskite (MAPI). The key difference separating reversible and irreversible degradation seems to be the presence of condensed water. In its absence, no crystalline lead iodide was produced and the reaction can be reversed by blowing dry air over the samples. We demonstrated that the conversion happens isotropically within the granular thin films. The rapid drop of PCE of the devices

upon partial hydration led us to propose that the formation of a hydrated layer on the grains has an insulating effect resulting in recombination of photo-generated charge carriers prior to collection.

3.5 Methods

Sample preparation

MAPI single crystals: Methylammonium lead iodide single crystals were grown according to the method of Poglitsch and Weber.[14] 2.5 g of lead acetate trihydrate ($Pb(CH_3CO_2)_2 \cdot 3\ H_2O$, Sigma) was dissolved in 10 mL hydroiodic acid (HI_{aq}, 57 wt%, Sigma) in a 50 mL round bottom flask and heated to 100 °C in an oil bath. Separately, 0.597 g of CH_3NH_2 (aq, 40%, Sigma) was added dropwise to a further 2 mL of HI_{aq} kept at 0 °C in an ice bath under stirring. The methylammonium iodide solution was then added to the lead acetate solution and the mixture was cooled over five days to a temperature of 46 °C, resulting in the formation of black crystals with largest face length around 8 nm. The content of the flasks was subsequently filtered and dried for 12 h at 100 °C.

MAPI hydrate single crystals: The formation of a hydrated form of MAPI perovskite single crystals below 40 °C was first mentioned by Weber.[34] In a 250 mL round-bottom flask, 12 mL CH_3NH_2 (40 wt% in H_2O, Sigma) was neutralized by an aqueous solution of concentrated HI solution (57 wt% in H_2O) until the indicator paper showed pH = 7, and the mixture was heated up to 100 °C. Subsequently, 3.86 g of $Pb(NO_3)_2$ dissolved in 18 mL H_2O was added dropwise to the hot MAI solution under vigorous stirring and black MAPI crystallites started to precipitate. Cooling the solution slowly down to room temperature (over 4 h) led to the transformation of the black crystallites into thin, pale yellow needles. After exposing the crystals to the mother liquor overnight in a refrigerator, the pale yellow needles were filtrated, washed with 50 mL dichloromethane and dried under vacuum (50 mbar) for 1 h. The product obtained was metastable and turned into greyish polycrystalline MAPI by spontaneous loss of its crystalline water under ambient conditions. The sample was stored in a jar at 77% RH in order to prevent dehydration in air (~35% RH).

MAI crystals: CH_3NH_3I (MAI) single crystals were synthesized by reacting 24 mL CH_3NH_2 (33 wt% in absolute ethanol, Sigma) diluted in 100 mL absolute ethanol and 10 mL HI (57 wt% in H_2O, Sigma) at 0 °C in a 250 mL round-bottom flask for 2 h under stirring at room temperature, respectively. After removal of the solvent with a rotary evaporator at 50 °C the white precipitate was recrystallized from absolute ethanol, washed with diethyl ether and dried in vacuum for 12 h.

Thin film preparation: Perovskite thin film preparation was conducted in a glove box under dry nitrogen atmosphere. Thin films of MAPI were fabricated following a 'solvent engineering' procedure reported by Xiao *et al.*.[35] First, glass substrates with dimensions 2.5 × 2.5 cm were cleaned with deionized water, absolute ethanol, dried under air flow and then treated in a plasma-cleaner with oxygen plasma for 5 min. For an equimolar 1.25 M MAPI perovskite precursor solution, 0.4 g MAI and 1.156 g PbI_2 (99%, Aldrich) were dissolved in 2 mL DMF (anhydrous, 99.8%, Aldrich) under stirring at 100 °C. Subsequently, 50 µL of the solution was dynamically spin-coated on a clean glass substrate at 6000 rpm. After a delay of 4 s, 150 µL chlorobenzene (anhydrous, 99.8%, Aldrich) was quickly added to the spinning substrate. After 30 s total spinning time, the substrate was immediately annealed at 100 °C for 10 min to evaporate residual solvents and to further promote crystallization. Dark brown, lustrous films of MAPI were obtained with a thickness of approximately 270 nm, as determined with a Veeco Dektak profilometer.

Solar cell fabrication: FTO-coated glass substrates (Pilkington, 7 Ω/sq) were cut into pieces of 3 × 3 cm and patterned by etching with Zn metal powder and 3 M HCl diluted in deionized water. The substrates were then cleaned with an aqueous 2% Hellmanex detergent solution, rinsed with deionized water, acetone and ethanol, and finally dried under air flow. The patterned substrates were cleaned with oxygen plasma for 5 min. A TiO_2 compact layer was deposited on top of the substrates by a sol-gel process. For this purpose, a solution containing 35 µL of 2 M HCl and 2.5 mL dry 2-propanol (IPA) was added dropwise to a solution of 369 µL titanium isopropoxide (≥97%, Sigma) in 2.5 mL dry IPA under strong stirring. The substrates were coated with the TiO_x sol-gel solution by spin-coating dynamically at 2000 rpm for 45 s and then quickly placed on a hotplate at 150 °C for 10 min. To complete the transformation of TiO_x into the anatase phase, the coated substrates were gradually heated to 500 °C (ramp 8 °C/min) and sintered for 45 min in air. A 280 nm MAPI perovskite thin film was deposited on top of the TiO_2 compact layer by following the same 'solvent engineering' process as employed for thin films, but with a slightly slower spinning rate during spin-coating (5000 rpm).

In order to add the hole transporter to the devices, a solution of 2,2',7,7'-*tetrakis*-(*N*,*N*-di-*p*-methoxyphenylamine)-9,9'-spirobifluorene (spiro-OMeTAD, 99.56%, Borun Chemicals) in anhydrous chlorobenzene (100 mg/mL) was filtered with a 0.45 µm syringe filter and mixed with 10 µL of 4-*tert*-butylpyridine (tBP, Aldrich, 96%) and 30 µL of a 170 mg/mL solution of lithium bistrifluoromethanesulfonimidate (Li-TFSI, 99.95%, Aldrich) in acetonitrile (anhydrous, 99.8%, Aldrich) per 1 mL spiro-OMeTAD solution. The hole transporter solution was coated onto the device substrate by a consecutive two-step spin-coating process at 1500 rpm and 2000 rpm for 40 s and 5 s, respectively. Afterwards, the substrates were removed from the glove box and stored overnight in a desiccator at ~35% RH. Finally, a 40 nm thick gold layer was deposited by thermal evaporation

through a patterned shadow mask under high vacuum conditions (4×10^{-6} mbar) to form the counter electrode. The active area under the mask was 0.083 cm^2.

Ellipsometry measurement

Spectrometric ellipsometry data on thin films were gathered using an ellipsometer ESM-300 from J. A. Woollam Co., Inc. Measurements on single crystals were performed with a SOPRALAB GES5E rotating polarizer ellipsometer mounted in a vertical configuration which is better suited for single crystals. Optical spectra on single crystals were recorded from ca. 1.2 eV to 5.5 eV, at three incidence angles for each sample (67.5°, 70° and 75°). *In situ* measurements during hydration and dehydration were performed at fixed incidence (67.5° for single crystals and 75° for thin films). For the single crystal measurements, the ellipsometer was equipped with a chamber fitted with two small slits to offer the possibility to measure the samples at different angles of incidence. In the case of thin films, the measurement was taken through quartz windows, the gas flow being introduced through a side opening. The acquisition time of a spectrum was sufficiently short (5 s) compared to the timescale of the measurement to be considered as instantaneous in the analysis.

Hydration setup for ellipsometry measurements: For single crystal ellipsometry, the relative humidity was fixed at (70 ± 5)% by controlling the ratio of a mixture of dry nitrogen to humid nitrogen that travelled through a bubbler at room temperature (21 °C). The gas mixture was used to fill the measurement chamber, which had a positive pressure difference relative to the lab atmosphere. A similar setup was employed for the analysis of *in situ* hydration of thin films and full solar cell devices, but compressed filtered air as carrier gas with relative humidity of (80 ± 5) % was used in place of nitrogen. The relative humidity was controlled with a calibrated hygrometer.

Ellipsometry fitting

Spectrometric data acquired by means of varying angle spectroscopic ellipsometry was analyzed using the WVASE 32 software from J. A. Woollam Co., Inc. for thin films and Winelli2 from SOPRALAB for single crystals. To fit the experimental data, an initial model of the optical transitions was built for each layer constituting the sample. The dielectric constant was described as sum critical points (CPs) of the joint density of states:

$$\varepsilon(E) = UV_{\text{term}} - \sum_{i=1}^{N}\left[A_i e^{j\phi_i}(E - E_{ci} + j\Gamma_i)^n\right] \quad (3.1)$$

where N is the number of CPs in the model, E is the incident photon energy, j is the imaginary unit and UV_{term} is a constant accounting for high energy transitions. The i^{th} CP is described by the amplitude A_i, energy Ec_i, linewidth Γ_i, exciton phase angle Φ_i and dimensionality n_i.[36] The dielectric function is then calculated from the model, which enables the software to simulate spectrometric values of the ellipsometry parameters, ψ and Δ, at the angles of incidence used for the acquisition via transfer matrix calculations. The ellipsometry parameters relate to the Fresnel coefficients R_p and R_s for p- and s- polarized light:

$$\frac{R_p}{R_s} = \tan(\psi)\, e^{i\Delta} \tag{3.2}$$

Finally, a regression algorithm was used to fit the modelled curve to the experimental ψ and Δ data by varying the free parameters (for example: the layer thickness and the amplitude or energy center of an oscillator). The figure of merit describing quantitatively the quality of the fits is the mean square error (MSE), given by:

$$MSE = \sqrt{\frac{1}{2N'-M}\sum_{i=1}^{N'}\left[\left(\frac{\psi_i^{\mathrm{mod}}-\psi_i^{\mathrm{exp}}}{\sigma_{\psi,i}^{\mathrm{exp}}}\right)^2+\left(\frac{\Delta_i^{\mathrm{mod}}-\Delta_i^{\mathrm{exp}}}{\sigma_{\Delta,i}^{\mathrm{exp}}}\right)^2\right]} \tag{3.3}$$

where N' is the number of (ψ, Δ) pairs, M the number of variable parameters in the model ('mod') and σ describes the standard deviations on the experimental ('exp') data points.

The Bruggeman approximation: The Bruggeman approximation is an analytical averaging method commonly used to study the macroscopic properties of composite materials. In the case of ellipsometry modelling, the approximation is used to estimate the optical constants of two (or more) intimately mixed phases. It assumes a homogenous dispersion of one phase into another resulting into an effective medium (EMA). The effective dielectric function $\tilde{\varepsilon}$ of a material composed of two constituents A and B (with respective volume fractions f_A and f_B) can thus be written:

$$f_A \frac{\tilde{\varepsilon}_A-\tilde{\varepsilon}}{\tilde{\varepsilon}_A-2\tilde{\varepsilon}} = -f_B \frac{\tilde{\varepsilon}_B-\tilde{\varepsilon}}{\tilde{\varepsilon}_B-2\tilde{\varepsilon}} \tag{3.4}$$

This complex equation, also referred to as coherent potential approximation, is solved numerically for $\tilde{\varepsilon}$. Surface roughness between two layers is also commonly described by an EMA layer consisting of a composite of top and bottom material in equal proportion. In the particular case of top layer roughness, an EMA is used with identical volume proportion of both the top layer and voids.[37]

X-ray diffraction measurements

XRD measurements on both thin films and powder samples were carried out with a Bruker D8 Discover X-ray diffractometer operating at 40 kV and 30 mA, employing Ni-filtered Cu-K_α-radiation (λ = 1.5406 Å) and a position-sensitive detector (LynxEye). During the XRD measurements, the samples were exposed to ambient conditions (21 °C, 35–40% RH). In order to minimize the influence of the environmental factors on the samples during the measurements, the XRD patterns were acquired by recording at a standard 2θ step size of 0.05 deg and a scan speed of 0.1 s per step.

Measurements on solar cells

The *J-V* characteristics of planar perovskite solar cell devices were measured using a Newport OrielSol 2A solar simulator with a Keithley 2401 source meter. The devices were illuminated through a shadow mask, yielding an active area of 0.083 cm^2. The *J-V* curves were recorded under standard AM 1.5G illumination, calibrated to a light intensity of 100 mW cm^{-2} with a silicon cell (Fraunhofer ISE certified). The input bias voltage was scanned from reverse (-2 V) to forward (0 V) (referred to as backward scan) in 0.05 V steps with a rate of 0.5 V s^{-1} and then from forward to reverse bias (0 to -2 V, forward scan) at the same rate.

3.6 References

[1] A. M. A. Leguy, Y. Hu, M. Campoy-Quiles, M. I. Alonso, O. J. Weber, P. Azarhoosh, M. van Schilfgaarde, M. T. Weller, T. Bein, J. Nelson, P. Docampo, P. R. F. Barnes, *Chem. Mater.* **2015**, *27*, 3397.

[2] M. A. Green, K. Emery, Y. Hishikawa, W. Warta, E. D. Dunlop, *Prog. Photovolt. Res. Appl.* **2015**, *23*, 1.

[3] A. Kojima, K. Teshima, Y. Shirai, T. Miyasaka, *J. Am. Chem. Soc.* **2009**, *131*, 6050.

[4] H. J. Snaith, *J. Phys. Chem. Lett.* **2013**, *4*, 3623.

[5] G. E. Eperon, V. M. Burlakov, P. Docampo, A. Goriely, H. J. Snaith, *Adv. Funct. Mater.* **2014**, *24*, 151.

[6] K. K. Bass, R. E. McAnally, S. Zhou, P. I. Djurovich, M. E. Thompson, B. C. Melot, *Chem. Commun.* **2014**, *50*, 15819.

[7] H. Zhou, Q. Chen, G. Li, S. Luo, T.-B. Song, H.-S. Duan, Z. Hong, J. You, Y. Liu, Y. Yang, *Science* **2014**, *345*, 542.

[8] J. M. Frost, K. T. Butler, F. Brivio, C. H. Hendon, M. van Schilfgaarde, A. Walsh, *Nano Lett.* **2014**, *14*, 2584.

[9] G. Niu, X. Guo, L. Wang, *J. Mater. Chem. A* **2015**.

[10] A. Wakamiya, M. Endo, T. Sasamori, N. Tokitoh, Y. Ogomi, S. Hayase, Y. Murata, *Chem. Lett.* **2014**, *43*, 711.

[11] J. H. Noh, S. H. Im, J. H. Heo, T. N. Mandal, S. I. Seok, *Nano Lett.* **2013**, *13*, 1764.

[12] S. N. Habisreutinger, T. Leijtens, G. E. Eperon, S. D. Stranks, R. J. Nicholas, H. J. Snaith, *Nano Lett.* **2014**, *14*, 5561.

[13] C. Law, L. Miseikis, S. Dimitrov, P. Shakya-Tuladhar, X. Li, P. R. F. Barnes, J. Durrant, B. C. O'Regan, *Adv. Mater.* **2014**, *26*, 6268.

[14] A. Poglitsch, D. Weber, *The Journal of Chemical Physics* **1987**, *87*, 6373.

[15] F. Hao, C. C. Stoumpos, D. H. Cao, R. P. H. Chang, M. G. Kanatzidis, *Nat. Photon.* **2014**, *8*, 489.

[16] B. R. Vincent, K. N. Robertson, T. S. Cameron, O. Knop, *Can. J. Chem.* **1986**, *65*, 1042.

[17] J. A. Christians, P. A. Miranda Herrera, P. V. Kamat, *J. Am. Chem. Soc.* **2015**.

[18] J. Yang, B. D. Siempelkamp, D. Liu, T. L. Kelly, *ACS Nano* **2015**, *9*, 1955.

[19] Y. Zhao, A. M. Nardes, K. Zhu, *J. Phys. Chem. Lett.* **2014**, *5*, 490.

[20] J. M. Ball, S. D. Stranks, M. T. Horantner, S. Huttner, W. Zhang, E. J. W. Crossland, I. Ramirez, M. Riede, M. B. Johnston, R. H. Friend, H. J. Snaith, *Energy Environ. Sci.* **2015**, *8*, 602.

[21] Q. Lin, A. Armin, R. C. R. Nagiri, P. Burn, P. Meredith, *Nat. Photon.* **2015**, *9*, 106

[22] P. Loper, M. Stuckelberger, B. Niesen, J. Werner, M. Filipic, S.-J. Moon, J.-H. Yum, M. Topic, S. De Wolf, C. Ballif, *J. Phys. Chem. Lett.* **2015**, *6*, 66.

[23] T. Baikie, Y. Fang, J. M. Kadro, M. Schreyer, F. Wei, S. G. Mhaisalkar, M. Graetzel, T. J. White, *J. Mater. Chem. A* **2013**, *1*, 5628.

[24] D. Shi, V. Adinolfi, R. Comin, M. Yuan, E. Alarousu, A. Buin, Y. Chen, S. Hoogland, A. Rothenberger, K. Katsiev, Y. Losovyj, X. Zhang, P. A. Dowben, O. F. Mohammed, E. H. Sargent, O. M. Bakr, *Science* **2015**, *347*, 519.

[25] J. Xie, Y. Liu, J. Liu, L. Lei, Q. Gao, J. Li, S. Yang, *J. Power Sources* **2015**, *285*, 349

[26] P. Lautenschlager, M. Garriga, S. Logothetidis, M. Cardona, *Phys. Rev. B* **1987**, *35*, 9174.

[27] F. Hao, C. C. Stoumpos, Z. Liu, R. P. H. Chang, M. G. Kanatzidis, *J. Am. Chem. Soc.* **2014**, *136*, 16411.

[28] I. B. Koustelas, L. Ducasse, G. C. Papavassiliou, *J. Phys.: Condens. Matter* **1996**, *8*, 1217.

[29] M. Campoy-Quiles, J. Nelson, D. D. C. Bradley, P. G. Etchegoin, *Phys. Rev. B* **2007**, *76*, 235206.

[30] J. A. Christians, P. A. M. Herrera, P. V. Kamat, *J. Am. Chem. Soc.* **2015**, *137*, 1530.

[31] M. Hirasawa, T. Ishihara, T. Goto, *J. Phys. Soc. Jpn.* **1994**, *63*, 3870.

[32] H. J. Snaith, H. Abad, J. M. Ball, G. E. Eperon, T. Leijtens, N. K. Noel, S. D. Stranks, J. T.-W. Wang, K. Wojciechowski, W. Zhang, *J. Phys. Chem. Lett.* **2014**, *5*, 1511.

[33] H.-S. Kim, N. G. Park, *J. Phys. Chem. Lett.* **2014**, *5*, 2927.

[34] D. Weber, *Z. Naturforsch., B: Chem. Sci.* **1978**, *33*, 1443.

[35] Z. Xiao, Q. Dong, C. Bi, Y. Shao, Y. Yuan, J. Huang, *Adv. Mater.* **2014**, *26*, 6503.

[36] P. Y. Yu, M. Cardona, *Fundamentals of Semiconductors*, Springer-Verlag, 2001.

[37] H. Fujiwara, J. Koh, P. I. Rovira, R. W. Collins, *Phys. Rev. B* **2000**, *61*, 10832.

4 Influence of precursor stoichiometry on the moisture stability of $CH_3NH_3PbI_3$

This chapter is based on the following publication:

M. L. Petrus,[†] **Y. Hu**,[†] D. Moia, P. Calado, A. M. A. Leguy, P. R. F. Barnes, P. Docampo, The Influence of Water Vapor on the Stability and Processing of Hybrid Perovskite Solar Cells Made from Non-Stoichiometric Precursor Mixtures. *ChemSusChem* **2016**, *9* (18), 2699-2707. (DOI: 10.1002/cssc.201600999)

[†] These authors contributed equally to this work.

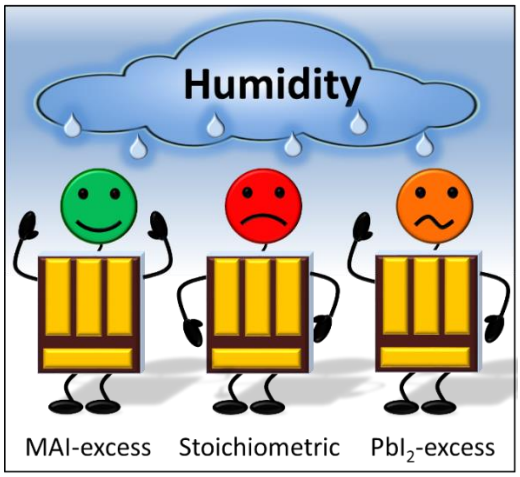

Adapted with permission.[1] Copyright 2016, John Wiley and Sons, Ltd.

4.1 Abstract

We investigated the influence of moisture on $CH_3NH_3PbI_3$ perovskite films and solar cells derived from non-stoichiometric precursor mixtures. We followed both the structural changes under controlled air humidity via *in situ* X-ray diffraction, and the electronic behavior of devices prepared from these films. A small PbI_2 excess in the films improved the stability of the perovskite compared to stoichiometric samples. We assign this to excess PbI_2 layers at the perovskite grain boundaries or to the termination of the perovskite crystals with lead and iodine. In contrast, the MAI-excess films composed of smaller perovskite crystals showed increased electronic disorder and reduced device performance due to poor charge collection. Upon exposure to moisture followed by dehydration ("solvent annealing"), these films recrystallized to form larger, highly oriented crystals with fewer electronic defects and a remarkable improvement in photocurrent and photovoltaic efficiency.

4.2 Introduction

In the past few years hybrid lead halide perovskites have emerged as a promising material for photovoltaic applications due to their outstanding optoelectronic properties.[2-4] The abundance of the precursor materials and the possibility of solution processing raises the hope of low-cost, highly efficient solar cells with a short energy payback time compared to currently established technologies.[5-9]

The Achilles heel of hybrid perovskite photovoltaic devices is their poor stability, especially under operating conditions, creating a considerable barrier to commercialization of the technology.[10] Beside environmental factors such as thermal stress and UV-light irradiation in air,[10-12] humidity-induced changes to the perovskite structure have been identified as one of the major degradation pathways which strongly affects device lifetime.[13, 14] Degradation upon exposure to moisture has so far only been suppressed by physical encapsulation or through the introduction of organic or inorganic passivation layers[15-17] which may place constraints on device performance. Fully understanding the effect of water on perovskite processing and degradation is thus important to formulate new solutions to this challenge.

The influence of humid air on hybrid perovskite films has been investigated by several groups. We have recently reported the formation of intermediate hydrate crystals as first degradation products of the perovskite, followed by their irreversible decomposition into PbI_2.[18] In general, the hygroscopic and volatile nature of the organic compound, methylammonium iodide (MAI), is understood as the

weak spot of the perovskite crystal, leading to water ingress and film degradation.[19-21] To date, most of the stability studies have been performed on perovskite films fabricated from stoichiometric precursor solutions (PbI_2:MAI in 1:1 molar ratio) or with an excess of MAI.[18, 22-24] However, recently reported champion perovskite solar cells showing power conversion efficiencies (PCE) exceeding 20% contain a 5–10% molar excess of PbI_2.[25-29] The remnant PbI_2 excess within the final absorber layer is believed to improve perovskite crystallization and to reduce non-radiative recombination rates by passivation of crystal grain boundaries, which could explain the additional boost in PCE.[25, 30-33]

While the community agrees on the beneficial effect of a small PbI_2 excess in the perovskite layer on device performance, little is known about the moisture-stability of these non-stoichiometric perovskite films. Previously, Liu *et al.*[32] and Zhang *et al.*[34] prepared methylammonium lead iodide films via a two-step sequential deposition method to study the stability of these samples. In both cases, the incomplete conversion of PbI_2 into the perovskite phase leads to a residual PbI_2 interlayer between TiO_2 and perovskite, which is reported to accelerate the film degradation upon exposure to humidity. However, state-of-the-art devices are mostly derived from a one-step deposition method, where the perovskite precursor mixture is spin-coated on the substrate, followed by an "anti-solvent dripping" step to initialize crystal nucleation. Clearly, different fabrication protocols may result in different locations and morphologies of the PbI_2 excess within the device. This is likely to have a substantial effect on the degradation kinetics occurring within the perovskite film. Therefore, elucidating the link between PbI_2 passivation, moisture-induced processing and degradation effects is important to maximize both device efficiency and stability.

In this work, we studied the effect of moisture on methylammonium lead iodide ($MAPbI_3$) films derived from non-stoichiometric perovskite precursor mixtures, i.e. perovskite films containing a small excess of PbI_2 or MAI. We inferred the location of the initial PbI_2 excess within the perovskite film through X-ray diffraction (XRD) experiments. In order to improve the understanding of the degradation mechanism, we performed *in situ* XRD measurements under controlled humidity levels in air (see Figure 4.17). In contrast to previous reports, our results indicate that a small PbI_2 excess decelerates the decomposition of the perovskite film upon exposure to moisture compared to a stoichiometric perovskite film. Additionally, we found that devices containing an MAI excess first show very low PCEs due to small perovskite crystals sizes. These are likely to be surrounded by MAI-rich regions with a high concentration of electronic defects which impede charge collection. However, the performance of devices made from MAI-excess solutions is significantly improved after a short exposure of the films to humidity at room temperature. This results in recrystallization, grain reorientation and the removal of electronic disorder from the perovskite layer – a process which we can regard as a form solvent annealing with water vapor. Our findings are, in principle, also

applicable to mixed cation/halide systems as these films are also deposited from non-stoichiometric mixtures.[35] In this case we expect a similar effect upon exposure to moisture as the typical cations used, formamidinium and cesium, are also hygroscopic and will likely undergo a similar enhanced mobility in the presence of water.

4.3 Results and discussion

4.3.1 Effect of the hydration on the perovskite structure

In order to study the effect of the precursor stoichiometry on the stability of the perovskite structure, we prepared perovskite thin films which incorporated a 5% molar excess of MAI in the precursor solution, a stoichiometric mixture, and one incorporating a 5% molar excess of PbI_2; these samples are termed "MAI-excess", "stoichiometric" and "PbI_2-excess" in the following. The 1.25 M stoichiometric precursor solution was obtained by dissolving PbI_2 and MAI in a 1:1 molar ratio in a solvent mixture of *N*,*N*-dimethylformamide (DMF) and dimethyl sulfoxide (DMSO). The corresponding amount of solid MAI or PbI_2 was then added to the stoichiometric perovskite solution to yield the MAI-excess and PbI_2-excess solutions, respectively. By employing an anti-solvent assisted one-step deposition method similar to the previously reported protocol for state-of-the-art devices,[25, 27, 36] a comparable distribution of the precursor excess within the perovskite layer can be expected. In short, the perovskite solution is spin-coated onto a substrate, followed by chlorobenzene dripping to induce crystal nucleation. After annealing on a hotplate, the crystallization is complete and uniform, shiny perovskite films were obtained.

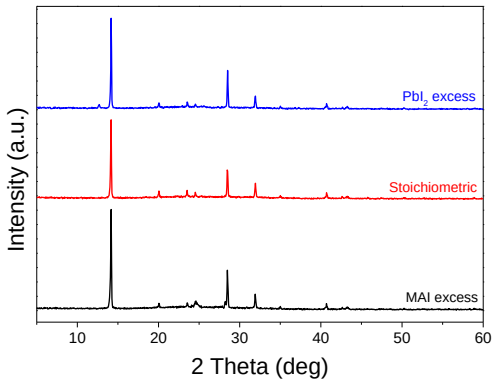

Figure 4.1 XRD patterns of the fresh perovskite films with different precursor ratios on glass. No significant difference in intensity of the perovskite reflections is observed.

Figure 4.1 shows the XRD patterns of the three different freshly prepared perovskite films. No significant differences in the intensity of the typical diffraction peaks originating from the tetragonal $MAPbI_3$ phase were observed. The expected (001) PbI_2 reflection at the 2θ value of 12.6° is obvious for the PbI_2-excess film, whereas it is not present in the other two samples. Previous studies report that the excess PbI_2 is located near the substrate,[31] however, its distribution strongly depends on the fabrication route. To infer the location of the PbI_2 excess within our absorber layer, we performed grazing-incidence XRD measurements at different incidence angles in the range of 0.3°–2.5°, as presented in Figure 4.2. At incidence angles of 0.6° and lower, the X-ray scattering depth is smaller than the total film thickness of 320 nm, thereby providing information about the distribution of the PbI_2 excess within the perovskite layer.[37] Our results show that at an incidence angle of 0.3°, the (001) peak of PbI_2 is still present in the diffractogram, indicating that the excess PbI_2 is not solely accumulated at the perovskite/TiO_2 interface but distributed throughout the entire perovskite film.

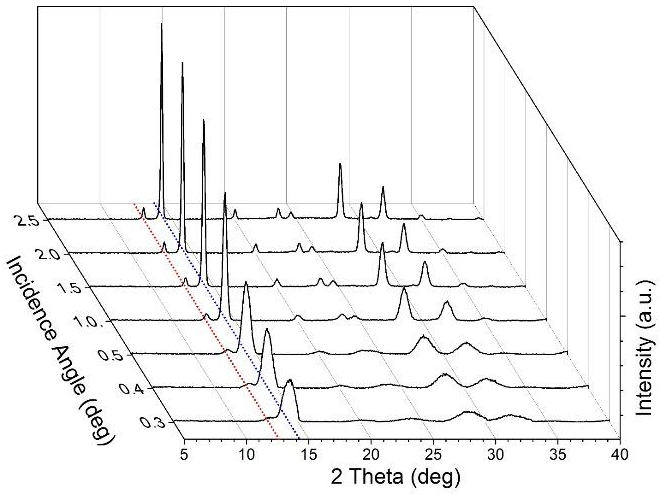

Figure 4.2 Grazing-incident XRD measurements on a PbI_2-excess $MAPbI_3$ sample. The (110) perovskite reflection is indicated with the blue dotted line. The PbI_2 peak (indicated with the red dotted line) is present for all incidence angles. For incidence angles of 0.5° and lower, the penetration depth is smaller than the film thickness indicating that the PbI_2 excess is distributed throughout the entire perovskite film.

Furthermore, monitoring the crystallization process of the non-stoichiometric perovskite layer can provide an insight into the formation and distribution of the excess PbI_2.[38] We performed *in situ* XRD measurements during the annealing process of a freshly deposited perovskite film prepared from a PbI_2-excess solution (Figure 4.3). Initially, we only observe the diffraction peaks assigned to the previously reported intermediate MAI-PbI_2-DMSO complex.[39, 40] During the first annealing step

at 40 °C the reflections of this MAI-PbI_2-DMSO complex become more narrow, indicating the growth of the intermediate phase crystals. At the same time, characteristic reflections of the $MAPbI_3$ phase (e.g. at $2\theta = 14.1°$ and 28.3°) appear. Upon further annealing, the perovskite peaks increase in intensity while the intensity of the MAI-PbI_2-DMSO reflections simultaneously decrease, suggesting the formation of $MAPbI_3$ crystals from the intermediate phase as DMSO is released. During the second annealing step at 100 °C, the last remaining solvent was removed from the film, after which the excess PbI_2 crystallized. Since the small amount of excess PbI_2 crystallizes only at the very end of the annealing procedure, we propose that PbI_2 is present at the grain surface of the previously formed perovskite crystals. This finding is in agreement with the incidence angle-dependent XRD measurements in Figure 4.2. Additionally, since the PbI_2 excess stays solvated until the final stage of the crystallization process, it is likely that this has an influence on the $MAPbI_3$ crystal termination.

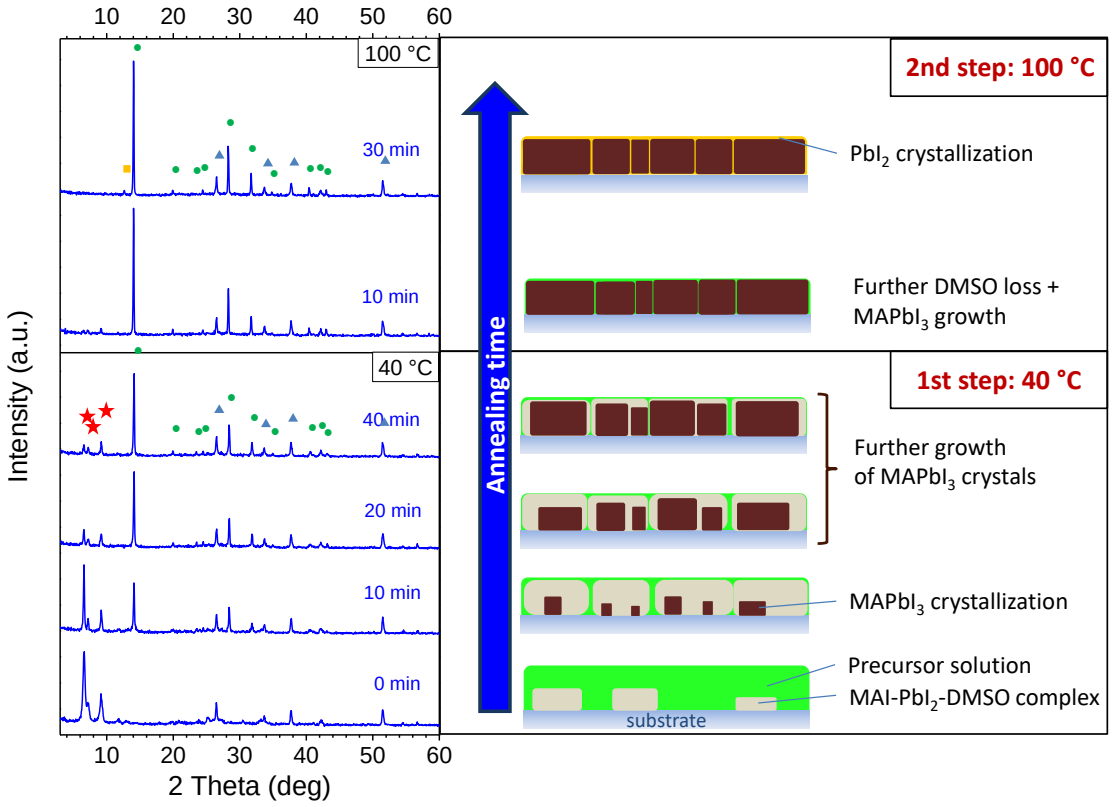

Figure 4.3 *In situ* XRD measurement during the annealing of a freshly spin-coated $MAPbI_3$ film prepared from a perovskite solution with 5 mol% PbI_2 excess. In the first step, the film was annealed for 40 min at 40 °C followed by a second step at 100 °C. The right panel shows a schematic representation of the crystal formation inferred from the XRD measurements. Initially, the MAI-PbI_2-DMSO complex (red stars in the XRD pattern) is formed, followed by the $MAPbI_3$ crystals (green dots) and at the end, after complete removal of the solvents, crystalline PbI_2 can be observed (yellow square). Reflections assigned to the FTO-glass substrate are marked with blue triangles.

Using XRD techniques to determine the location of a small MAI excess within the corresponding perovskite films is difficult as the diffraction intensity for MAI is relatively low. Since the same fabrication method is used for all samples, we expect the excess MAI to be also distributed homogeneously between the preformed $MAPbI_3$ crystals, presumably at the grain boundaries as reported by Son *et al.* [36]

Previous studies report the detrimental effect of residual PbI_2 material at the perovskite/TiO_2 interface on the film stability towards humidity.[32] Here, we investigate the influence of moisture on perovskite films with a more homogeneous distribution of the precursor material excess which is more comparable to the absorber layers used in state-of-the-art devices showing high efficiencies. In order to compare the moisture stability of the three $MAPbI_3$ films with different precursor stoichiometry, we exposed the samples to air with a constant relative humidity (RH) of 90% in a closed chamber at room temperature. We followed the changes in the composition of the films with *in situ* XRD measurements at regular intervals, as presented in Figure 4.4. Our results show that the stoichiometry of the precursor mixture critically affects the timescale of structural changes as well as the nature of the degradation products.

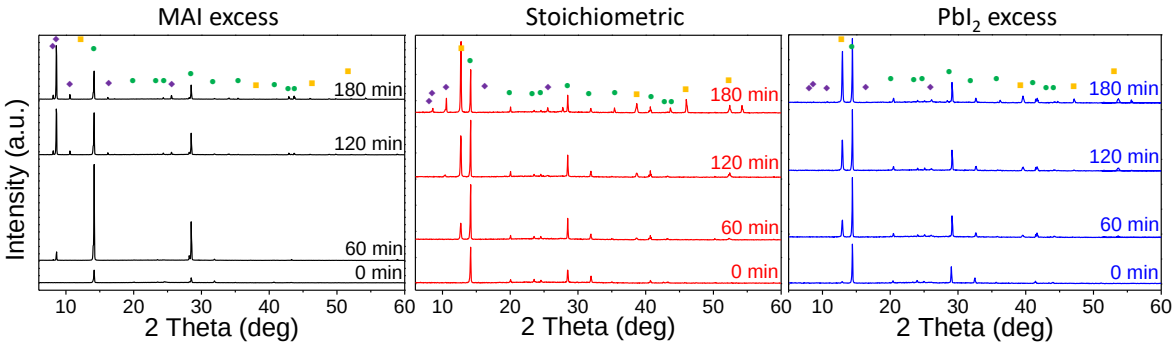

Figure 4.4 *In situ* XRD measurements of the hydration of perovskite films prepared from solutions with different precursor ratios. The films were exposed to 90% RH in air for 0–180 min. The positions of the XRD peak for $MAPbI_3$ (green circles), PbI_2 (yellow squares) and $CH_3NH_3PbI_3 \cdot H_2O$ (purple diamonds) are marked in the graphs.

For the perovskite films with a stoichiometric ratio of precursors we found that PbI_2 is initially formed as a degradation product (Figure 4.4). With prolonged exposure to humidity, the characteristic reflections of the monohydrated $MAPbI_3$ ($CH_3NH_3PbI_3 \cdot H_2O$) at the 2θ values 8.6° and 10.5° appear. Interestingly, the formation of additional PbI_2 as a result of degradation in the PbI_2-excess sample is significantly slower in comparison to the stoichiometric perovskite film. Similarly,

we observed the crystalline monohydrate phase after 90 min in the stoichiometric samples, while for the PbI_2-excess sample, the characteristic reflections of the monohydrate only appeared after 180 min. We compared the difference in the degradation rate between the stoichiometric and the PbI_2-excess samples by plotting the ratio between the (001) peak of PbI_2 at $2\theta = 12.6°$ and the (110) peak of the perovskite at $2\theta = 14.1°$ (Figure 4.5). Since we observe that perovskite crystal reorientation is similar and relatively minor for both samples, the graph indicates that the formation of PbI_2 in the stoichiometric sample is significantly faster than in the PbI_2-excess sample. We found that for both films, the monohydrate forms at a PbI_2:$MAPbI_3$ peak intensity ratio of around 3:4.

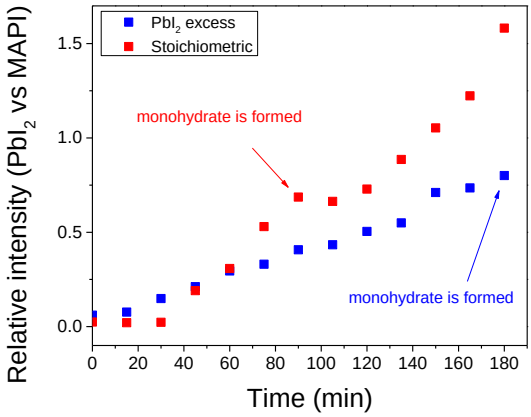

Figure 4.5 Relative XRD peak intensity of the (001) PbI_2 at $2\theta = 12.6°$ over the (110) peak of $MAPbI_3$ at $2\theta = 14.1°$ showing the difference in degradation speed.

In contrast, the MAI-excess sample does not show the formation of PbI_2 within the timescales studied. Surprisingly, during the first 60 min of exposure time, the XRD pattern does not exhibit any degradation products at all. Instead, the remarkable increase in the (110) and (220) reflections of $MAPbI_3$ indicate an improvement in crystallinity for the perovskite phase. After more than 60 min, the reflections of the monohydrate $CH_3NH_3PbI_3 \cdot H_2O$ appear in the diffraction pattern, which is in accordance with previously reported results by Leguy *et al.* where a 0.4% MAI molar excess was used to form the $MAPbI_3$ film.[18] Recent calculations suggest that the monohydrate phase should thermodynamically be stable at high relative humidities at room temperature.[21] These calculations also show that a dihydrate structure of the perovskite, $(CH_3NH_3)_4PbI_6 \cdot 2H_2O$, can form at lower relative humidities. However, this phase appears to be thermodynamically unstable relative to PbI_2 and MAI which may explain why it did not appear in the present study, since it is likely that it will only be observed under kinetically favorable conditions.

Scanning electron microscopy (SEM) cross-section images of the different perovskite films reveal the effect of hydration on the crystal morphology (Figure 4.6). For both stoichiometric and PbI_2-excess samples, we observe small protrusions over the crystals after exposure to humidity, which might originate from partial degradation of the perovskite crystals. In the case of MAI-excess we find no such protrusions, indicating a different process during the exposure to humidity. Initially, the film is composed of relatively small and irregularly shaped crystals. However, after a short hydration process at 90% RH, the previously small crystallites have since recrystallized to form large crystals. This observation is consistent with the increased intensities of the (110) and (220) perovskite diffraction peaks (Figure 4.4), suggesting higher crystallinity and a more preferential crystal orientation.

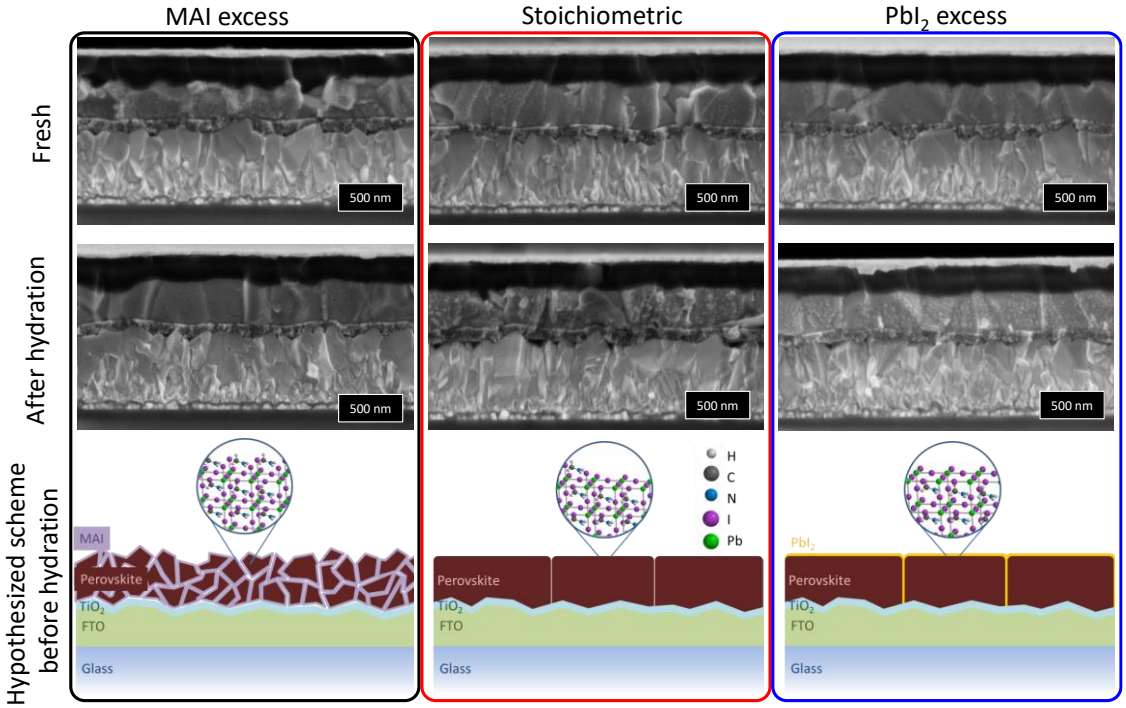

Figure 4.6 SEM cross-section of photovoltaic devices with a $MAPbI_3$ perovskite layer prepared with different precursor ratios. Top figures show SEM cross-sections of freshly prepared devices and figures below show the samples after exposure to 90% RH for 45 min before applying spiro-OMeTAD. The bottom images depict a schematic representation of the morphology of the perovskite film before hydration with an inset showing the hypothesized crystal surface termination for the perovskite grains at an atomic level. We note that water will be removed from these films by the SEM evacuation process.

These results strongly indicate that the precursor ratio during the perovskite film formation affects how water penetrates the perovskite crystals/films. We will discuss each case separately:

First, $MAPbI_3$ films fabricated with a PbI_2 excess exhibit markedly slower degradation dynamics and no immediate formation of hydrated perovskite species. We consider two possible mechanisms by which the initial excess of PbI_2 protects the perovskite against moisture: (I) a PbI_2 layer at the grain boundaries functions as a barrier against water infiltration, and/or (II) the excess of PbI_2 facilitates the termination of the perovskite crystals with lead and iodine atoms, preventing water ingress into the crystals. The first argument considers that, unlike MA^+ ions in $MAPbI_3$,[20] PbI_2 lacks strong hydrogen-bonding interactions with water molecules and therefore can be considered as a passivation layer. The second option is in agreement with computational studies performed by Mosconi *et al.*,[41] where the authors predict that PbI_2-terminated perovskite crystals are more robust against moisture-induced degradation than MAI-terminated surfaces. They also show that defects in the PbI_2-terminated slab are the initiation point for degradation of the perovskite, from which cavities can grow by gradual ingress of water molecules, allowing further decomposition of the perovskite. For clarification we illustrated these hypotheses schematically in Figure 4.6.

Second, stoichiometric $MAPbI_3$ films show relatively fast formation of PbI_2 and $CH_3NH_3PbI_3 \cdot H_2O$ upon exposure to a high level of humidity. SEM cross-section images (Figure 4.6) do not display any significant difference in crystal size between the stoichiometric and PbI_2-excess films, which is in agreement with literature.[26] This indicates that the faster degradation of the stoichiometric films is not merely the result of an increase in total grain surface which is exposed to humidity. It is noteworthy that the PbI_2 obtained as a result of degradation does not seem to protect the perovskite against humidity-induced degradation in the same way as the PbI_2 excess which was added to the precursor solution.

Third, the XRD patterns of the MAI-excess films exhibit a remarkable increase in the (110) and (220) reflections of the perovskite phase without any signs of degradation during the first 60 min (Figure 4.7a). Yang *et al*.[24] report the same increase in the respective XRD signals by annealing an MAI-excess $MAPbI_3$ film in air under ambient conditions. The authors assign the reformation of the $MAPbI_3$ crystals to the diffusion of MA^+ and I^- from MAI reservoirs into the thermally created vacancies. The dynamic perovskite-formation process allows the growth of large grains with high crystallinity and strong orientation along the (110) direction. We expect a comparable self-healing process to occur in our films during exposure to humid air. The infiltrated water degrades the perovskite under the evolution of methylamine and HI which are volatile and can escape the film. The MA^+ and I^- vacancies which are created as a result of the hydration can be refilled by the excess MAI. According to computational studies by Tong *et al.* and Mosconi *et al.*, MAI-terminated

perovskite surfaces are prone to the infiltration of water molecules which can strongly affect the perovskite structure.[41, 42] With this in mind, we suggest that water molecules penetrating the perovskite structure could increase the precursor mobility and allow the perovskite to recrystallize and reorient during the first 60 min (Figure 4.7c). This is supported by the SEM images, verifying the significant change in crystal morphology.

Figure 4.7b depicts the evolution of the (110) peak intensity relative to the (121) or (022) reflections with increasing hydration time. The highest relative intensity for the (110) diffraction peak can be found after 50 min, followed by a steady decrease upon longer exposure times. The employed fabrication route of the perovskite films already leads to a preferential orientation along the (110) planes. During the moisture-assisted recrystallization, this dominating orientation seems to dictate the direction in which the large crystals will emerge. Our observations indicate that, once the reservoir of excess MAI has been consumed, no further reorganization of the perovskite film due to the self-healing process takes place and degradation is initialized by the formation of the hydrated perovskite species.

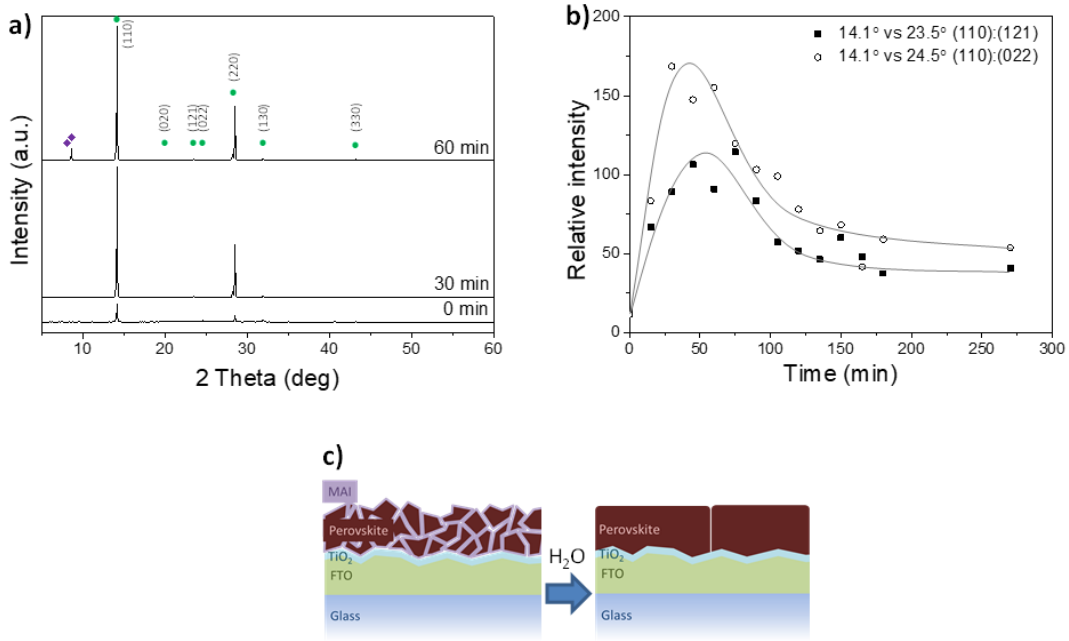

Figure 4.7 *In situ* XRD measurements monitoring the hydration of a perovskite film prepared with a 5 mol% excess of MAI. (a) XRD patterns of the perovskite film during the first hour of exposure to 90% RH. The $MAPbI_3$ peaks are labelled with green circles and the monohydrate peaks with purple diamonds. (b) Relative intensities of the (110) perovskite peak ($2\theta = 14.1°$) over the (121) and (022) orientations ($2\theta = 23.5$ and $24.5°$) as a function of time showing that the perovskite crystals become more oriented in the first hour of exposure to 90% RH. The grey lines are drawn as a guide to the eye. (c) Schematic representation of the change in morphology of the $MAPbI_3$ crystals after the hydration/dehydration treatment.

4.3.2 Effect of hydration on perovskite solar cells

In order to investigate the effect of precursor stoichiometry on the photovoltaic performance before and after exposure of the $MAPbI_3$ perovskite layer to moisture, we fabricated perovskite solar cells with the following planar device architecture: fluorine-doped tin oxide (FTO)/compact TiO_2/$MAPbI_3$/spiro-OMeTAD/Au. We prepared different perovskite layers employing non-stoichiometric mixtures and the same method as for the thin films. Consistent with reports by several other groups,[25, 26] we found that a small excess of PbI_2 (2–10 mol%) in the perovskite precursor solution increases the photovoltaic performance of the as-prepared devices (Figure 4.8).

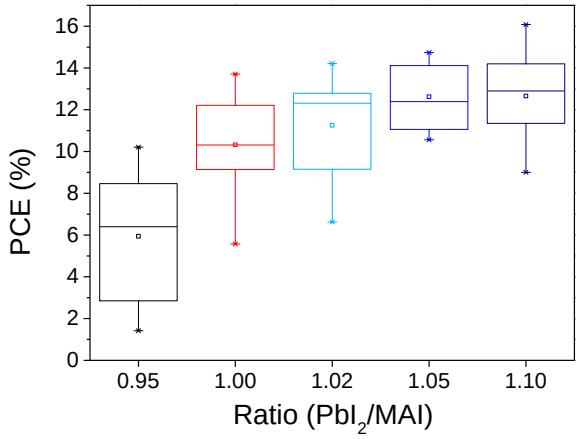

Figure 4.8 Photovoltaic performance of perovskite solar cells related to the precursor ratio.

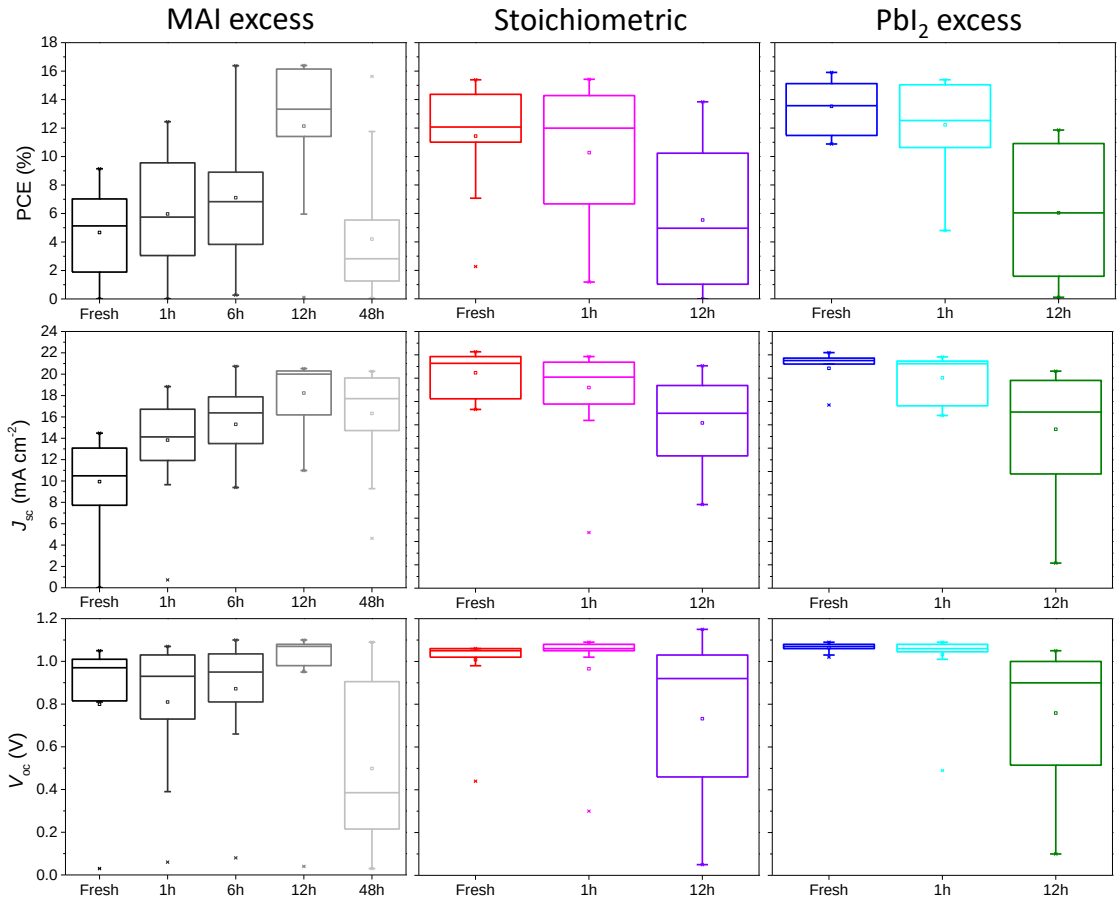

Figure 4.9 Photovoltaic performance of devices with different precursor ratios before and after hydration at 75% RH for different exposure times. The evaluation is based on the reverse *J-V* scans for a total of at least 18 individual devices for each type of perovskite film.

An optimized recipe using 5 mol% PbI_2 excess results in devices with an average PCE = 13.5% (Figure 4.9) compared to stoichiometric $MAPbI_3$ samples (average PCE = 11.4%). In contrast, we found that an excess of MAI is detrimental for the device performance, resulting in power conversion efficiencies of only 4.7% on average, mainly due to a loss in short-circuit current density (J_{sc}). UV-Vis absorption and spectroscopic ellipsometry measurements show that the lower J_{sc} does not originate from a reduced absorption of the film, which was found to be comparable for the different samples (Figure 4.10). We estimated the reported device characteristics from the measured *J-V* curves obtained from the reverse scan (from V_{oc} to J_{sc}). All as-prepared devices exhibit a comparable degree of hysteresis between the forward and reverse scans (Figure 4.11).

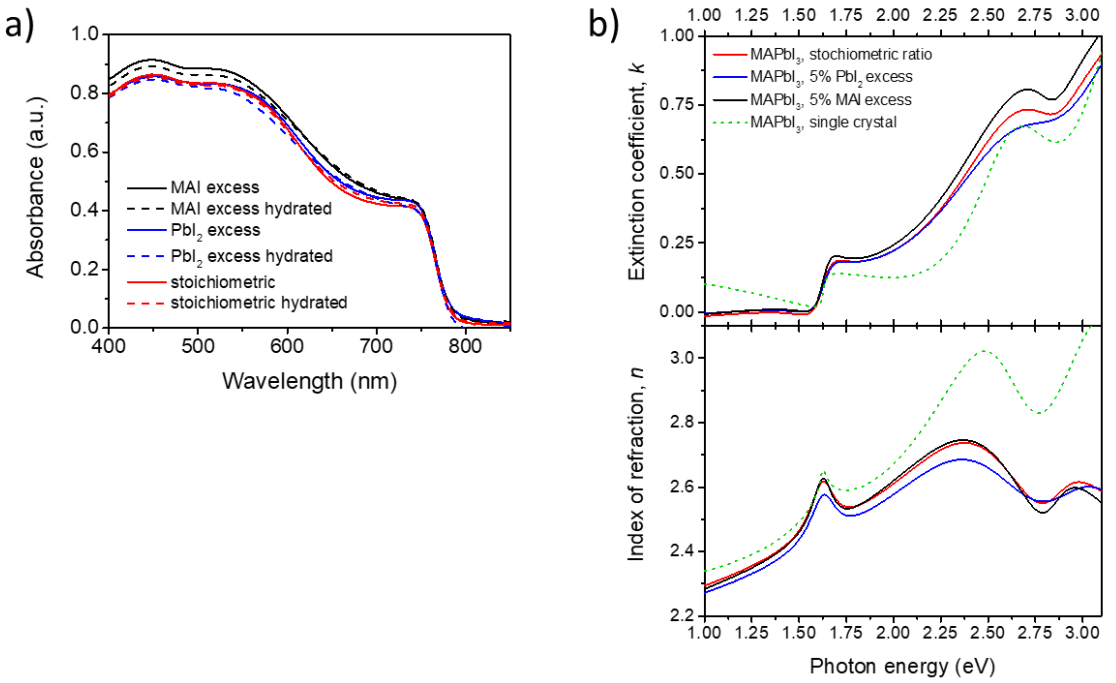

Figure 4.10 (a) UV-Vis absorption spectra of $MAPbI_3$ films prepared with different precursor solutions on glass. The absorption profiles were obtained before and after storing the films at 75% RH for 1 h. (b) Optical constants (extinction coefficient, top; index of refraction, bottom) modelled from spectroscopic ellipsometry data collected on thin films of $MAPbI_3$ deposited on glass with different precursor ratios. The data collected on a single crystal of $MAPbI_3$ is given for comparison (dashed green line).[43] The difference in absolute value between thin films and single crystal is attributed to the differences in surface roughness, microscopic structure and orientation, and possible differences in the material's density. There may also be differences in scattering induced depolarization which cannot be analyzed with our setup as we are not measuring the full Mueller Matrix. The reduced sharpness of the optical features in $MAPbI_3$ thin films prepared with 5% excess MAI is in agreement with the observation of smaller crystallites and rougher film surface. We note a slightly excitonic nature of the band gap in the 5% PbI_2-excess samples which might indicate large grains in the film.

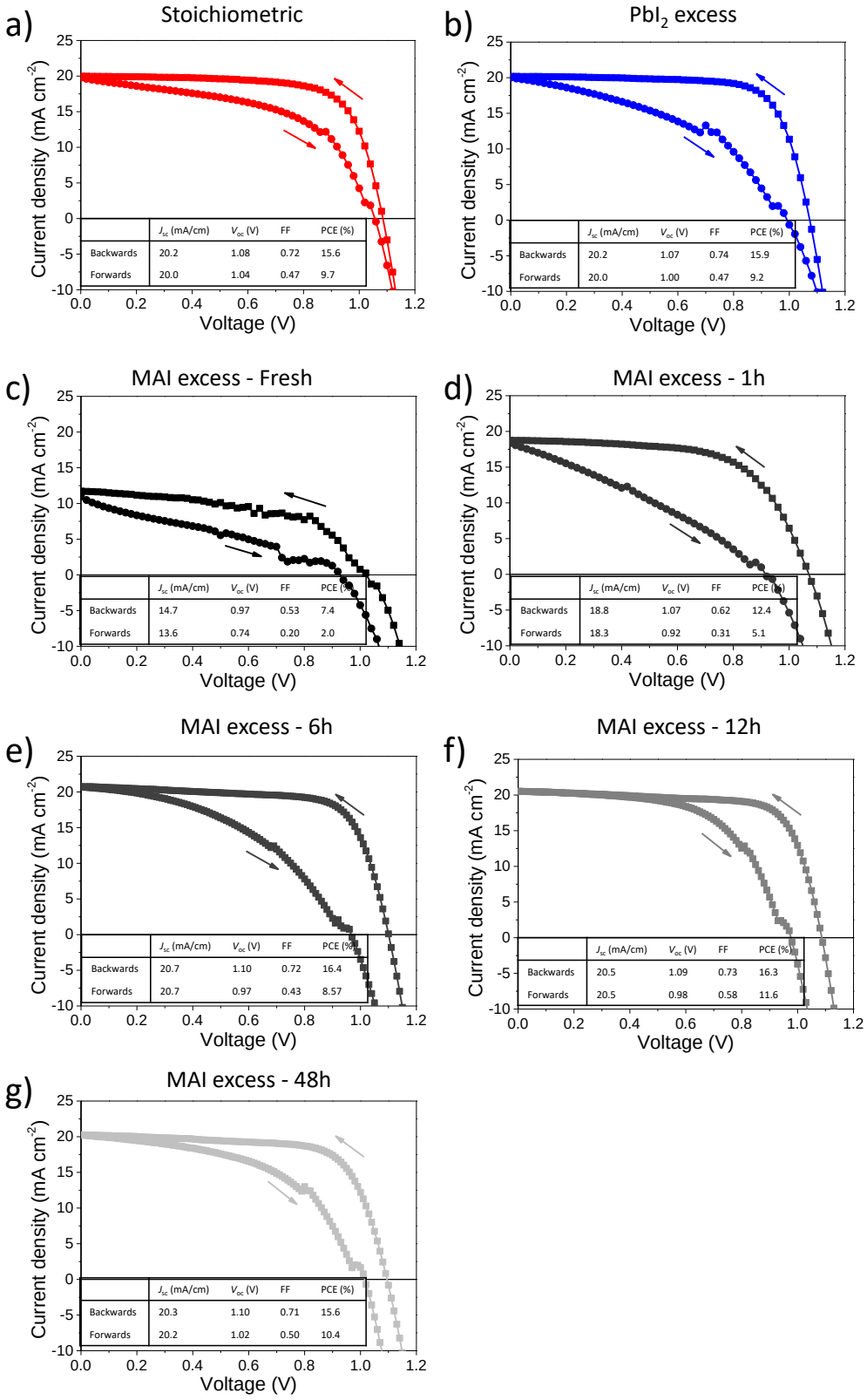

Figure 4.11 (a–c) *J-V* curves of photovoltaic devices before hydration exhibiting hysteresis. (d–g) *J-V* curves showing the hysteresis of photovoltaic devices with an MAI excess after different hydration times. Recorded under simulated AM 1.5G illumination, reverse and forward bias measured at a scan rate of 0.2 V s^{-1}.

To examine the effects of moisture on the films before they were fabricated into solar cells the perovskite films were stored in air with a controlled humidity of 75% RH in a closed chamber at room temperature. We note that the substrate underneath the perovskite film can influence the time-scale of hydration effects.[32, 44, 45] For this reason, the time-scale of degradation in perovskite films prepared on glass/FTO/TiO_2 substrates is not directly comparable to samples on glass substrates. After the hydration procedure, we transferred the samples to a nitrogen-filled glovebox and deposited spiro-OMeTAD as hole transporting layer, followed by thermally evaporating 40 nm thick gold electrodes under high vacuum. Our previous studies suggest that any monohydrate crystals which may have formed are likely to undergo dehydration and reconvert into the perovskite phase during these low humidity processing steps (note that this dehydration process will also have occurred for the films examined in the SEM in Figure 4.6).[18]

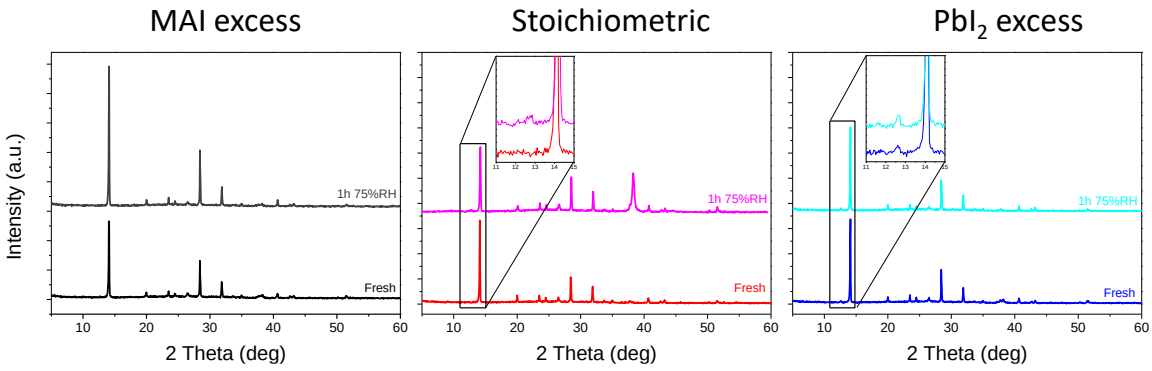

Figure 4.12 XRD patterns of perovskite solar cells prepared without hydration and after 1 h hydration at 75% RH. The XRD patterns show that the exposure to moisture results in an additional ~5 mol% PbI_2 in the film for the stoichiometric and PbI_2-excess film, while the (110) and (220) peak intensity of the MAI-excess sample increases by a factor of two. The PbI_2 formed as a degradation product does not improve the device performance as was observed by adding 5 mol% PbI_2 in the precursor solution, while the recrystallization and orientation in the MAI-excess film results in an improvement of device performance.

The photovoltaic performance of devices comprising stoichiometric and PbI_2-excess films is slightly lower after exposure at 75% RH for 1 h (Figure 4.9) relative to devices made from films that have not been exposed to moisture. During this relatively short exposure, an additional ~5 mol% PbI_2 was built up in the films as a degradation product (Figure 4.12). We consider this to be the reason for the loss in performance. Curiously, the PbI_2 which originates from degradation does not seem to improve the photovoltaic performance as we observed for the devices made by using a PbI_2 excess in the film preparation. This suggests that the PbI_2 formed upon hydration has a different (and detrimental)

spatial distribution or orientation relative to the PbI_2 excess which is added during the film preparation. It is known that PbI_2 exhibits an anisotropic electrical conductivity, which could function as a barrier for charge carriers, depending on the crystal orientation.[46, 47] Upon longer exposure of the films to humidity (12 h), a further decrease in the performance of the resulting devices for both types of samples indicates further degradation. Despite the slower decomposition of the PbI_2-excess sample in the *in situ* XRD measurements, we do not observe a large difference in the loss in performance between the stoichiometric and the PbI_2-excess devices.

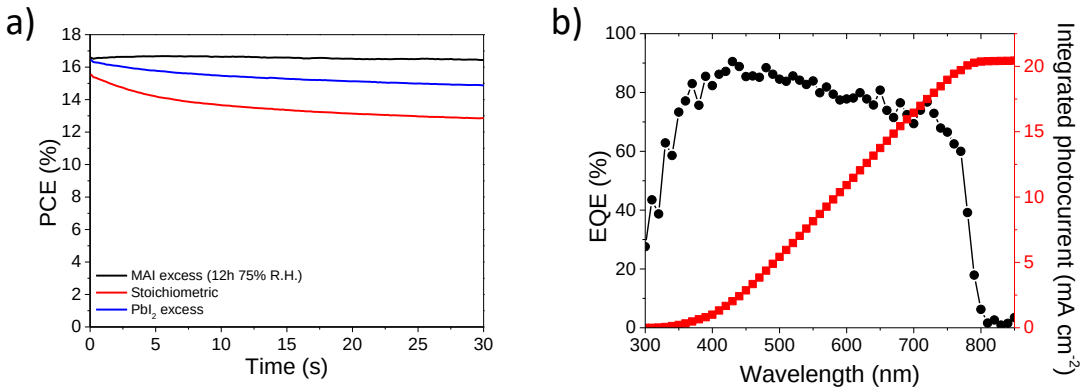

Figure 4.13 (a) PCE and photocurrent over time for fresh stoichiometric and PbI_2-excess devices and for the hydrated MAI-excess (12 h at 75% RH) devices. Especially the MAI-excess devices shows a very stable power output at the maximum power point. (b) External quantum efficiency (EQE; black circles) of a representative MAI-excess device after hydration. The integrated photocurrent density (red squares) of 20.4 mA cm^{-2} is in good agreement with the J_{sc} value obtained from the *J-V* curves.

Remarkably, many of the devices comprising a perovskite layer prepared with an MAI excess exhibit increased PCE values after hydration followed by dehydration. After only 1 h exposure to 75% RH, we found a clear improvement of PCEs (Figure 4.9). This positive trend holds for even longer exposure times up to 12 h, eventually resulting in hero(ine) cell efficiencies comparable to the best performing devices derived from fresh stoichiometric or PbI_2-excess perovskite films, with an excellent stabilized power output (Figure 4.13). The increased performance mainly originates from an improvement in J_{sc}. Our XRD and SEM results provide evidence that this improvement in device performance can be correlated to the increase in crystallinity and reorientation of the perovskite crystals upon humidity exposure (Figure 4.14).[48] Yang *et al.* also report high efficiency devices with excess MAI in the perovskite layer after an air-annealing step to induce grain-coarsening and formation of large crystals.[24] Since the annealing step was performed under exposure to air, it is

possible that this reported process is also moisture-assisted, which might be initiated already at room temperature. When the MAI-excess films are exposed for longer times and/or at higher levels of humidity (e.g. 48 h at 75% RH), the monohydrated species of $MAPbI_3$ is formed, which appears as transparent flower-like crystals on the film. The drastic change in crystal morphology and structure is expected to result in pinholes and thus shunts, as well as in a loss in optical absorption and conductivity in the monohydrate regions.[21] This could explain the decrease in V_{oc} and in the overall photovoltaic performance of the degraded MAI-excess devices prepared in this study.

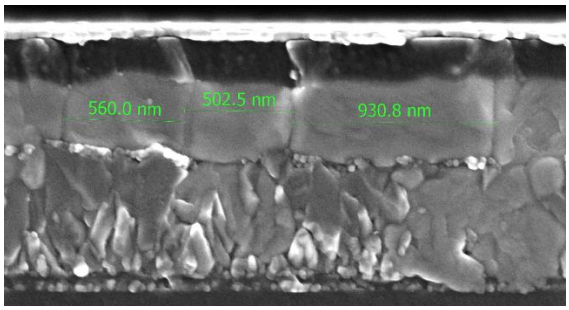

Figure 4.14 SEM cross-section of a photovoltaic device with an MAI excess after hydration for 12 h at 75% RH. The perovskite crystals have a size between 500–1000 nm after "solvent-annealing" in humid air.

Despite the high PCEs that can be obtained by exposing MAI-excess films to humidified air, we note that these solar cells suffer from a significantly broader distribution in PCE compared to the PbI_2-excess devices. Further optimization of the moisture-induced recrystallization ("solvent annealing") process may allow higher reproducibility and device efficiencies.

To further investigate the causes of the observed differences in solar cell performance for the different precursor formulations, we analyzed the charge carrier lifetime and differential capacitance of the devices. For the PbI_2-excess and MAI-excess cases we also explored the influence of the hydration step. The experimental protocol for these measurements is reported by O'Regan *et al*. and is also presented in the Methods section for completeness.[49] In our analysis, the differential capacitance (dQ/dV_{oc} where Q is charge generated per unit area) is calculated from the solar cells' electrical response upon pulsed LED illumination. It is determined from the ratio between the J_{sc} during the pulse, dQ/dt (without background light bias), and the initial positive slope of the open-circuit photovoltage transient, dV_{oc}/dt, at each background light intensity measured after stabilization (Figure 4.15). This approach yields capacitance values which account only for the movement of electronic charge, but we expect the quasi steady-state distribution of ionic charge in the device to be different for each background light intensity. For solar cells where the charge collection efficiency

is less than 100%, this approach is prone to errors since the photocurrent during a pulse will not represent the full charge generation rate. We present the details of this limitation in the Methods section, where we also show that the conclusions drawn from the comparison of different devices in the following paragraphs is still representative and meaningful.

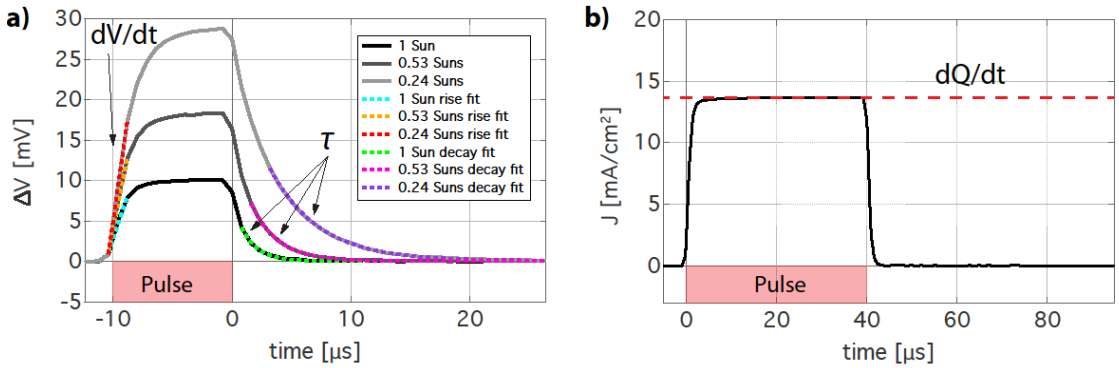

Figure 4.15 Optoelectronic transient measurements at different light intensities for a stoichiometric solar cell. (a) Photovoltage transient (after baseline subtraction) at different background light intensities. (b) Photocurrent measurement upon 40 µs red LED pulse.

Figure 4.16a shows the differential capacitance versus V_{oc} for all devices. In Figure 4.16b and Figure 4.16c we present the effect of hydration on carrier lifetime for MAI-excess and PbI_2-excess samples respectively (data points for the stoichiometric devices are also included). The key observation from Figure 4.16a is that the MAI-excess devices show a significantly higher differential capacitance as a function of V_{oc} relative to the stoichiometric and the PbI_2-excess devices. This difference can be interpreted as a variation in the density of electronic states (chemical capacitance) of cells prepared from different precursor solutions as a function of the Fermi level splitting in the device. The results can be interpreted in two possible ways: (1) the active layers fabricated with an MAI excess result in films with a higher density of traps states for a given V_{oc} or (2) the shift in the capacitance versus V_{oc} is related to a change in the interfacial energetics. In case 2, a variation in the active layer composition could give rise to dipole formation at the perovskite/TiO_2 and perovskite/spiro-OMeTAD interfaces, resulting in a lower effective built-in potential (V_{bi}) and reduced V_{oc} for a given light intensity. While a horizontal shift to lower V_{oc} values would be expected in this case, a reduced V_{bi} cannot account for the difference in slope of capacitance versus V_{oc} for the MAI-excess devices. Therefore, explanation 2 is unlikely to be dominant. A higher density of trap states corresponding to explanation 1 is consistent with the smaller crystal sizes observed in these films.

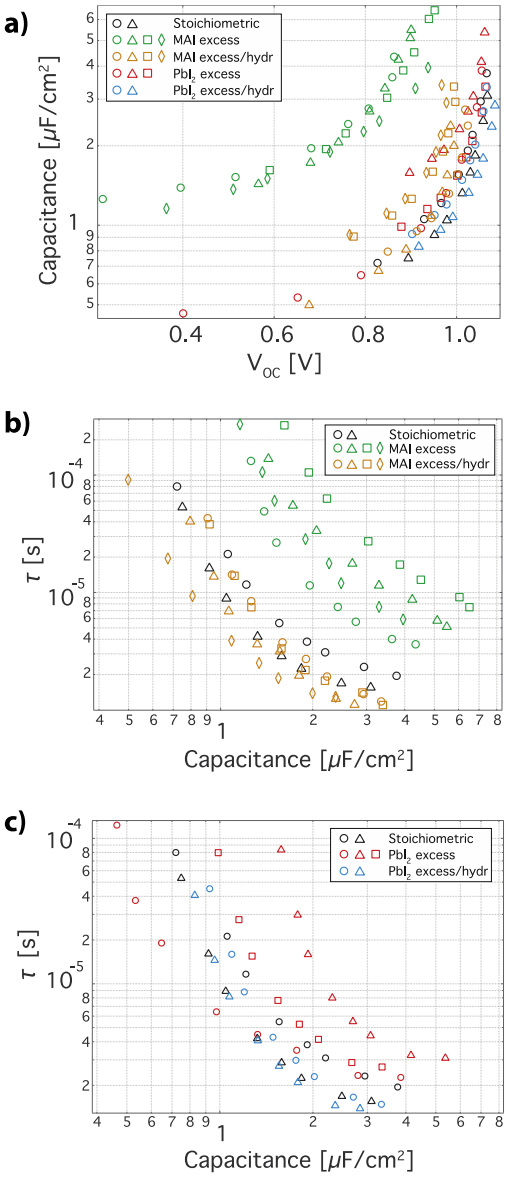

Figure 4.16 Optoelectronic transient measurements at different light intensities for stoichiometric, PbI_2-excess, MAI-excess, hydrated PbI_2-excess and hydrated MAI-excess devices. (a) Differential capacitance versus V_{oc}. (b–c) Lifetime extracted from photovoltage transients at open-circuit versus differential capacitance for (b) MAI-excess and (c) PbI_2-excess solar cells. Different symbols with the same color correspond to devices prepared with the same precursor ratio.

Strikingly, hydrating (or moisture annealing) the MAI-excess films before completing the devices resulted in capacitance versus V_{oc} relations that closely match the stoichiometric and PbI_2-excess cases. This reduction in capacitance is consistent with the structural analysis and device performance trend described in the previous sections. Figure 4.16a also shows that hydration of the PbI_2-excess

perovskite films does not lead to a significant change in capacitance versus V_{oc} and that both these devices approximately resemble the behavior observed for the stoichiometric case.

Figure 4.16b displays transient photovoltage lifetimes as a function of differential capacitance for the MAI-excess devices with or without the hydration step. Photovoltage lifetimes are often used to assess the relative recombination rate constants in devices,[50] however care must be taken interpreting the values if the energetic distribution of electronic states varies between devices,[21] as is the case here. Once again, the MAI-excess devices exhibit distinctly different behavior from the stoichiometric control. Analogous to the data displayed in Figure 6a, the hydration step results in solar cells with remarkably similar photovoltage decay times as a function of capacitance to the stoichiometric case. We note that changes in interfacial energetics at the electrodes' interface and V_{bi} between solar cells fabricated with different precursor ratios would not significantly affect the lifetime versus capacitance characteristics, further evidence that explanation 2 is unlikely. On the other hand, a difference in the degree of energetic disorder within the film (explanation 1) could explain this observation. A higher density of trap states and associated chemical capacitance could increase the observed photovoltage relaxation time constant without significantly accelerating the charge recombination processes. This picture involves trap states which do not act as fast recombination centers (similar to dye-sensitized solar cells).[51] We hypothesize that these traps may be present in MAI-rich regions surrounding the perovskite grains. These would inhibit electronic charge transport in MAI-excess devices, resulting in decreased collection efficiency and explaining the lower J_{sc} measured for these devices.

Finally, Figure 4.16c displays the trend of lifetimes observed for PbI_2-excess samples. These devices show longer lifetimes compared to the stoichiometric solar cells, consistent with the fractionally higher V_{oc} values. However, this difference is within statistical uncertainty. In a similar way to the hydrated MAI-excess samples, hydration of PbI_2-excess devices yields a trend in lifetime versus differential capacitance that closely matches the stoichiometric control.

4.4 Conclusion

In conclusion, we performed both *in situ* XRD and optoelectronic measurements to reveal the effects of moisture on $MAPbI_3$ perovskite films and solar cells derived from non-stoichiometric precursor solutions. Our findings indicate that the moisture stability of the perovskite film can be slightly improved by adding an excess of PbI_2 to the precursor solution. We assign the decelerated degradation process either to a PbI_2 layer formed at the grain boundaries during film crystallization

or to the termination of the perovskite crystal with lead and iodine atoms, both of which would function as a barrier towards moisture ingress. In contrast, perovskite films containing an initial MAI excess first recrystallize upon exposure to humidified air at room temperature, resulting in large crystals with a preferential (110) orientation, before degradation occurs. Solar cells comprising an MAI-excess film initially show poor photovoltaic performance which we attribute to a high density of trapping states and energetic disorder in MAI-rich regions at perovskite grain boundaries, inferred from differential capacitance measurements. These states are likely to impede charge collection, explaining the lower J_{sc} in the fresh MAI-excess devices as well as longer photovoltage decay times than the other devices. However, when these films are exposed to moisture prior to applying the top electrodes, we observe an impressive improvement in PCE. We attribute this to the recrystallization of the perovskite and a concomitant reduction in electronic disorder to the level observed in the stoichiometric or PbI_2-excess devices. Our results shed light on the role of moisture in the processing and degradation of non-stoichiometric perovskite films, and indicate a procedure in which water vapor can be used to improve the device performance by solvent annealing.

4.5 Methods

Film preparation for hydration studies

Glass substrates were subsequently cleaned with a 2% Hellmanex solution and rinsed with de-ionized water, ethanol and acetone. Directly before spin-coating the perovskite film, the substrates were plasma cleaned for 5 min. A 1.25 M precursor solution containing stoichiometric amounts of PbI_2 (TCI, >98%) and methylammonium iodide (Dyesol) in a 4:1 (v/v) mixture of *N*,*N*-dimethylformaid (DMF) and dimethyl sulfoxide (DMSO) was prepared. To obtain the solutions with a defined precursor excess, the required amount of MAI or PbI_2 was added to the stoichiometric solution, respectively. The solutions were spin-coated dynamically (first at 1000 rpm for 10 s, followed by a second step at 5000 rpm for 30 s) onto the substrate. After 25 s, chlorobenzene was added on top of the spinning substrate and afterwards the substrate was annealed on a hotplate (first at 40 °C for 40 min, followed by a second step at 100 °C for 10 min).

Solar cell preparation

Fluorine-doped tin oxide (FTO) coated glass sheets (7 Ω/sq, Pilkington, USA) were patterned by etching with zinc powder and 3 M HCl. The substrates were subsequently cleaned with a 2%

Hellmanex solution and rinsed successively with de-ionized water, ethanol and acetone. Directly before applying the hole blocking layer, last organic residues were removed by an oxygen plasma treatment for 5 min. A compact TiO_2 layer was prepared from a sol-gel precursor solution by spin-coating onto the substrates and calcination at 500 °C for 30 min in air. For the sol-gel solution a 27.2 mM solution of HCl in IPA was added dropwise to a vigorously stirred 0.43 mM solution of titanium isopropoxide (99.999%, Sigma-Aldrich) in dry IPA. After cooling down, the substrate was transferred to a nitrogen-filled glovebox. The perovskite films were prepared as described above and hydrated as mentioned in the text. The hole transporting material spiro-OMeTAD (Borun Chemicals, 99.5% purity) was applied on the perovskite film in a glovebox using a 75 mg/mL solution in chlorobenzene to which 10 µL tBP and 30 µL of a 170 mg/mL Li-TFSI solution in acetonitrile were added. This solution was spin-coated dynamically at 1500 rpm for 45 s. The devices were stored overnight under air at room temperature and <30% RH to allow the spiro-OMeTAD to oxidize. The top electrode with a thickness of 40 nm was deposited by thermal evaporation of gold under vacuum (at ~10^{-6} mbar).

Characterization

X-ray diffraction (XRD) analysis of perovskite films were carried out in reflection mode using a Bruker D8 Discover diffractometer with Ni-filtered Cu $K_{\alpha 1}$ radiation (λ = 1.5406 Å) and a position-sensitive semiconductor detector (LynxEye). For the *in situ* XRD measurements during the hydration process, a custom-made hydration chamber made of X-ray transparent polymers with a total volume around 250 mL was utilized. The air humidity within the hydration chamber was measured using a hygrometer and was held constant around 90% RH or 75% RH by employing vials filled with pure water or saturated sodium chloride solutions. All experiments were performed at room temperature (22 ± 1 °C) without illumination.

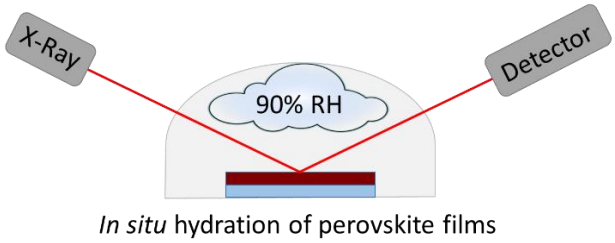

Figure 4.17 Schematic representation of the hydration chamber for *in situ* XRD measurements.

In situ XRD experiments during thermal annealing of the perovskite film were performed using a hot stage controlled by the diffractometer under ambient conditions. We note that the result might differ from experiments that are performed in the glovebox.

Extreme high resolution (XHR) SEM images were obtained using a FEI Helios Nanolab G3 UC DualBeam Scanning Electron Microscope. The cross-section samples were freshly cut shortly before the measurements to avoid film degradation after sample preparation.

Ultraviolet-visible (UV-Vis) absorption spectra were recorded using a Perkin Elmer Lambda 1050 spectrophotometer equipped with a 150 mm integrating sphere.

Spectrometric ellipsometry measurements were performed using a VASE-ellipsometer from J. A. Woollam Co., Inc. equipped with AutoretarderTM. Optical spectra on thin films were recorded from ca. 0.9 eV to 3.1 eV, at five incidence angles for each sample (55°, 60°, 65°, 70°, 75°). The collected spectra were analyzed using the WVASE 32 software from J. A. Woollam Co., Inc. A model of four critical points of the joint density of states was introduced following the modelling and fitting methodology as previously published.[1] The spectrometric ellipsometry measurement were performed at room temperature and low humidity (<30% RH).

J-V curves were recorded under ambient conditions with a Keithley 2400 source meter under simulated AM 1.5G sunlight, with an incident power of approximately 100 mW cm^{-2}, which was corrected for the exact light intensity using a Fraunhofer ISE certified silicon cell. The active area of the solar cells was defined with a square metal aperture mask of 0.0831 cm^2. The reported device characteristics were estimated from the measured *J-V* curves obtained from the reverse scan (from V_{oc} to J_{sc}) which was recorded at a scan rate of 0.2 V s^{-1} after pre-biasing at 1.5 V for 5 s under illumination. All as-prepared devices show a comparable degree of hysteresis between the forward and reverse scan. The stabilized power output was measured by tracking the current at the maximum power point. The devices were not pre-biased for this measurement.

External quantum efficiency measurements were performed at short-circuit and referenced to a Si photodiode (Hamamatsu). The device was illuminated using a white bias light (Solar light Co. Inc. Model S16, 150W xenon lamp ~100 W m^{-2}) and light from a 150 W Xe short arc lamp (LOT Oriel) was used as probe light and modulated with a mechanical chopper (12 Hz) and passed through a monochromator (Horiba MicroHR) to select the wavelength. The response was recorded using a lock-in amplifier (Ametek Signal Recovery SR 7230 DSP) with a low-noise pre-amplifier (Femto DLPCA-200).

Optoelectronic transient measurements

Optoelectronic transients were performed on perovskite solar cell devices using the TRACER system described in previous reports.[51]

Charge carrier lifetime measurements: transient photovoltage measurements were conducted by applying a 10 μs red LED pulse on top of a background white LED bias light set to different intensities. A monoexponential function was fitted to the tail of the voltage decay upon voltage baseline subtraction to extract the charge lifetimes, τ (see Figure 4.15). All photovoltage decays were performed after leaving the solar cell under the set light conditions for 100 s to allow stabilization of the V_{oc} and slow moving/ionic charge to reach a quasi-equilibrium distribution.

Determination of differential capacitance: the differential capacitance at different bias light intensities was calculated by considering the ratio between dQ/dt and dV/dt related to a red LED light pulse. dV/dt was evaluated at the different light intensities by fitting a straight line to the initial rise of the photovoltage transient. dQ/dt was evaluated by measuring the photocurrent resulting from illuminating the cell with the red LED (driven under the same condition as the transient photovoltage) for 40 μs. The average value of J_{sc} between 20 μs and 35 μs after switching on the LED was taken for this estimate (see Figure 4.15b). In order to maximize the collection efficiency of the devices, this measurement was performed after pre-biasing the device at 1 V for 100 s.

Error associated to differential capacitance determination: as discussed in the Results and discussion section, the analysis of the differential capacitance described above results in accurate estimates of the differential capacitance only under specific circumstances. In the case that all charges generated by the LED pulse contribute to the change in V_{oc} during the photovoltage transient measurements and can be extracted when performing a transient photocurrent measurement in the dark, then the method adopted in the analysis displayed in Figure 4.16 would yield reliable estimates. Given that collection efficiency in these devices is expected to be less than 100%, especially for the MAI-excess samples, we proceed to discuss the validity of this method. An alternative approach to the analysis of these data is presented in Figure 4.18. The figure is an analogous of Figure 4.16 in the Results and discussion section. However, here the value of dQ/dt used to calculate the differential capacitance has been set to be constant and equal to the maximum photocurrent resulting from red LED illumination measured *among all devices* considered in our studies. Assuming now that this were the value of charge excited in each of the device upon red light illumination contributing to the observed transient photovoltage dynamics, the data points presented in Figure 4.18 would be a closer estimate of the differential capacitance of the devices. It is clear from Figure 4.18 that the trends discussed in the Results and discussion section regarding Figure 4.16 are still valid in this case. We note that if the different values of photocurrent measured for different devices upon red LED illumination were

due to a difference in charge generation (due for example to differences in absorption) or to recombination processes which prevent the photo-generated charges from contributing to measurable changes in V_{oc} during transient photovoltage measurements, then the analysis presented in the Results and discussion section would be a more accurate description of the differential capacitance during photovoltaic operation.

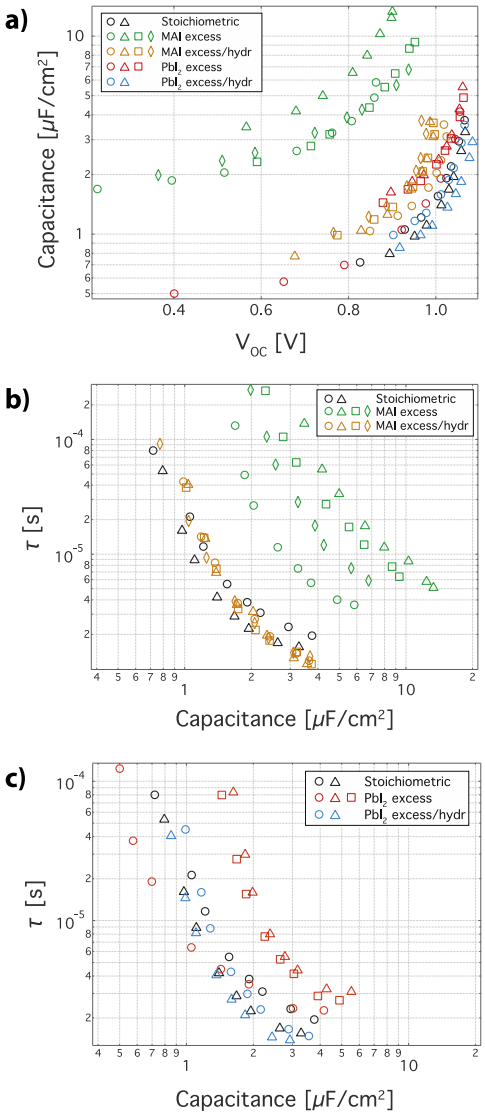

Figure 4.18 Optoelectronic transient measurements at different light intensities for stoichiometric, PbI_2-excess, MAI-excess, PbI_2-excess after hydration step and MAI-excess after hydration step devices. The maximum transient photocurrent among all devices was used to measure dQ/dt and hence calculate the differential capacitance (a) Differential capacitance versus open-circuit voltage; (b-c) Lifetime extracted from photovoltage transients at open-circuit versus differential capacitance for (b) MAI-excess and (c) PbI_2-excess solar cells.

4.6 References

[1] M. L. Petrus, Y. Hu, D. Moia, P. Calado, A. M. A. Leguy, P. R. F. Barnes, P. Docampo, *ChemSusChem* **2016**, *9*, 2699.

[2] National Renewable Energy Laboratory (NREL), *NREL Best Research-Cell Photovoltaic Efficiency Chart*, https://www.nrel.gov/pv/assets/images/efficiency-chart.png (accessed: 20-04-2018)

[3] M. A. Green, K. Emery, Y. Hishikawa, W. Warta, E. D. Dunlop, *Prog. Photovolt. Res. Appl.* **2016**, *24*, 905.

[4] A. Kojima, K. Teshima, Y. Shirai, T. Miyasaka, *J. Am. Chem. Soc.* **2009**, *131*, 6050.

[5] G. Hodes, *Science* **2013**, *342*, 317.

[6] M. Liu, M. B. Johnston, H. J. Snaith, *Nature* **2013**, *501*, 395.

[7] A. Binek, M. L. Petrus, N. Huber, H. Bristow, Y. Hu, T. Bein, P. Docampo, *ACS Appl. Mater. Interfaces* **2016**, *8*, 12881.

[8] M. L. Petrus, T. Bein, T. J. Dingemans, P. Docampo, *J. Mater. Chem. A* **2015**, *3*, 12159.

[9] T. M. Schmidt, T. T. Larsen‐Olsen, J. E. Carlé, D. Angmo, F. C. Krebs, *Adv. Energy Mater.* **2015**, *5*, 1500569.

[10] G. Niu, X. Guo, L. Wang, *J. Mater. Chem. A* **2015**.

[11] Y. Han, S. Meyer, Y. Dkhissi, K. Weber, J. M. Pringle, U. Bach, L. Spiccia, Y.-B. Cheng, *J. Mater. Chem. A* **2015**, *3*, 8139.

[12] S. N. Habisreutinger, T. Leijtens, G. E. Eperon, S. D. Stranks, R. J. Nicholas, H. J. Snaith, *Nano Lett.* **2014**, *14*, 5561.

[13] Z. Song, A. Abate, S. C. Watthage, G. K. Liyanage, A. B. Phillips, U. Steiner, M. Graetzel, M. J. Heben, *Adv. Energy Mater.* **2016**, 1600846.

[14] T. A. Berhe, W.-n. Su, C.-H. Chen, C.-J. Pan, J. Cheng, H.-M. Chen, M.-c. Tsai, L.-Y. Chen, A. A. Dubale, B. J. Hwang, *Energy. Environ. Sci.* **2015**.

[15] Y. Hu, J. Schlipf, M. Wussler, M. L. Petrus, W. Jaegermann, T. Bein, P. Muller-Buschbaum, P. Docampo, *ACS Nano* **2016**, *10*, 5999.

[16] J. Yang, B. D. Siempelkamp, D. Liu, T. L. Kelly, *ACS Nano* **2015**, *9*, 1955.

[17] X. Dong, X. Fang, M. Lv, b. lin, S. Zhang, J. N. Ding, N. Yuan, *J. Mater. Chem. A* **2015**.

[18] A. M. A. Leguy, Y. Hu, M. Campoy-Quiles, M. I. Alonso, O. J. Weber, P. Azarhoosh, M. van Schilfgaarde, M. T. Weller, T. Bein, J. Nelson, P. Docampo, P. R. F. Barnes, *Chem. Mater.* **2015**, *27*, 3397.

[19] L. Hu, G. Shao, T. Jiang, D. Li, X. Lv, H. Wang, X. Liu, H. Song, J. Tang, H. Liu, *ACS Appl. Mater. Interfaces* **2015**, *7*, 25113.

[20] J. M. Frost, K. T. Butler, F. Brivio, C. H. Hendon, M. van Schilfgaarde, A. Walsh, *Nano Lett.* **2014**, *14*, 2584.

[21] A. P. McMahon, N. P. Gallop, M. Acharya, M. Naderi, D. Williams, X. Li, N. M. Harrison, P. R. F. Barnes, *(under review)* **2016**.

[22] J. A. Christians, P. A. Miranda Herrera, P. V. Kamat, *J. Am. Chem. Soc.* **2015**.

[23] D. Li, S. A. Bretschneider, V. W. Bergmann, I. M. Hermes, J. Mars, A. Klasen, H. Lu, W. Tremel, M. Mezger, H.-J. Butt, S. A. L. Weber, R. Berger, *J. Phys. Chem. C* **2016**, *120*, 6363.

[24] M. Yang, Y. Zhou, Y. Zeng, C.-S. Jiang, N. P. Padture, K. Zhu, *Adv. Mater.* **2015**, n/a.

[25] C. Roldan-Carmona, P. Gratia, I. Zimmermann, G. Grancini, P. Gao, M. Graetzel, M. K. Nazeeruddin, *Energy. Environ. Sci.* **2015**, *8*, 3550.

[26] D. Bi, W. Tress, M. I. Dar, P. Gao, J. Luo, C. Renevier, K. Schenk, A. Abate, F. Giordano, J.-P. Correa Baena, J.-D. Decoppet, S. M. Zakeeruddin, M. K. Nazeeruddin, M. Grätzel, A. Hagfeldt, *Sci. Adv.* **2016**, *2*.

[27] M. Saliba, T. Matsui, J.-Y. Seo, K. Domanski, J.-P. Correa-Baena, M. K. Nazeeruddin, S. M. Zakeeruddin, W. Tress, A. Abate, A. Hagfeldt, M. Gratzel, *Energy. Environ. Sci.* **2016**, *9*, 1989.

[28] M. Saliba, S. Orlandi, T. Matsui, S. Aghazada, M. Cavazzini, J.-P. Correa-Baena, P. Gao, R. Scopelliti, E. Mosconi, K.-H. Dahmen, F. De Angelis, A. Abate, A. Hagfeldt, G. Pozzi, M. Graetzel, M. K. Nazeeruddin, *Nat. Energy* **2016**, *1*, 15017.

[29] T. Malinauskas, M. Saliba, T. Matsui, M. Daskeviciene, S. Urnikaite, P. Gratia, R. Send, H. Wonneberger, I. Bruder, M. Graetzel, V. Getautis, M. K. Nazeeruddin, *Energy. Environ. Sci.* **2016**, *9*, 1681.

[30] Q. Chen, H. Zhou, T.-B. Song, S. Luo, Z. Hong, H.-S. Duan, L. Dou, Y. Liu, Y. Yang, *Nano Lett.* **2014**, *14*, 4158.

[31] L. Wang, C. McCleese, A. Kovalsky, Y. Zhao, C. Burda, *J. Am. Chem. Soc.* **2014**, *136*, 12205.

[32] F. Liu, Q. Dong, M. K. Wong, A. B. Djurišić, A. Ng, Z. Ren, Q. Shen, C. Surya, W. K. Chan, J. Wang, A. M. C. Ng, C. Liao, H. Li, K. Shih, C. Wei, H. Su, J. Dai, *Adv. Energy Mater.* **2016**, *6*, 1502206.

[33] D. H. Cao, C. C. Stoumpos, C. D. Malliakas, M. J. Katz, O. K. Farha, J. T. Hupp, M. G. Kanatzidis, *APL Mater.* **2014**, *2*, 091101.

[34] H. Zhang, J. Mao, H. X. He, D. Zhang, H. L. Zhu, F. X. Xie, K. S. Wong, M. Gratzel, W. C. H. Choy, *Adv. Energy Mater.* **2015**, *5*, 1501354.

[35] T. J. Jacobsson, J.-P. Correa-Baena, E. Halvani Anaraki, B. Philippe, S. D. Stranks, M. E. F. Bouduban, W. Tress, K. Schenk, J. Teuscher, J.-E. Moser, H. Rensmo, A. Hagfeldt, *J. Am. Chem. Soc.* **2016**, *138*, 10331.

[36] D.-Y. Son, J.-W. Lee, Y. J. Choi, I.-H. Jang, S. Lee, P. J. Yoo, H. Shin, N. Ahn, M. Choi, D. Kim, N.-G. Park, *Nat. Energy* **2016**, *1*, 16081.

[37] H. Dosch, B. W. Batterman, D. C. Wack, *Phys. Rev. Lett.* **1986**, *56*, 1144.

[38] W. Zhang, M. Saliba, D. T. Moore, S. K. Pathak, M. T. Hörantner, T. Stergiopoulos, S. D. Stranks, G. E. Eperon, J. A. Alexander-Webber, A. Abate, A. Sadhanala, S. Yao, Y. Chen, R. H. Friend, L. A. Estroff, U. Wiesner, H. J. Snaith, *Nat. Commun.* **2015**, *6*.

[39] N. J. Jeon, J. H. Noh, Y. C. Kim, W. S. Yang, S. Ryu, S. I. Seok, *Nat. Mater.* **2014**, *13*, 897.

[40] N. Ahn, D.-Y. Son, I.-H. Jang, S. M. Kang, M. Choi, N.-G. Park, *J. Am. Chem. Soc.* **2015**, *137*, 8696.

[41] E. Mosconi, J. M. Azpiroz, F. De Angelis, *Chem. Mater.* **2015**, *27*, 4885.

[42] C.-J. Tong, W. Geng, Z.-K. Tang, C.-Y. Yam, X.-L. Fan, J. Liu, W.-M. Lau, L.-M. Liu, *J. Phys. Chem. Lett.* **2015**, *6*, 3289.

[43] A. M. A. Leguy, P. Azarhoosh, M. I. Alonso, M. Campoy-Quiles, O. J. Weber, J. Yao, D. Bryant, M. T. Weller, J. Nelson, A. Walsh, M. van Schilfgaarde, P. R. F. Barnes, *Nanoscale* **2016**, *8*, 6317.

[44] T. Leijtens, G. E. Eperon, S. Pathak, A. Abate, M. M. Lee, H. J. Snaith, *Nat. Commun.* **2013**, *4*.

[45] G. D. Niu, W. Z. Li, F. Q. Meng, L. D. Wang, H. P. Dong, Y. Qiu, *J. Mater. Chem. A* **2014**, *2*, 705.

[46] X. Zhu, H. Sun, D. Yang, P. Wangyang, X. Gao, *Journal of Materials Science: Materials in Electronics* **2016**, *27*, 11798.

[47] H. Sun, X. Zhu, D. Yang, Z. He, S. Zhu, B. Zhao, *Journal of Semiconductors* **2012**, *33*, 053002.

[48] F. Hanusch, M. Petrus, P. Docampo, in *Unconventional Thin Film Photovoltaics*, The Royal Society of Chemistry, 2016, 32.

[49] B. C. O'Regan, P. R. F. Barnes, X. Li, C. Law, E. Palomares, J. M. Marin-Beloqui, *J. Am. Chem. Soc.* **2015**, *137*, 5087.

[50] V. Roiati, S. Colella, G. Lerario, L. De Marco, A. Rizzo, A. Listorti, G. Gigli, *Energy. Environ. Sci.* **2014**, *7*, 1889.

[51] P. R. F. Barnes, K. Miettunen, X. Li, A. Y. Anderson, T. Bessho, M. Gratzel, B. C. O'Regan, *Adv. Mater.* **2013**, *25*, 1881.

5 High-efficiency multiple-cation mixed-halide perovskite solar cells

This chapter is based on the following publication:

Y. Hu,† E. M. Hutter,† P. Rieder,† I. Grill, J. Hanisch, M. F. Aygüler, A. G. Hufnagel, M. Handloser, T. Bein, A. Hartschuh, K. Tvingstedt, V. Dyakonov, A. Baumann, T. J. Savenije, M. L. Petrus, P. Docampo, Understanding the Role of Cesium and Rubidium Additives in Perovskite Solar Cells: Trap States, Charge Transport, and Recombination**.** *Adv. Energy Mater.* **2018**, 1703057. (DOI: 10.1002/aenm.201703057)

† These authors contributed equally to this work.

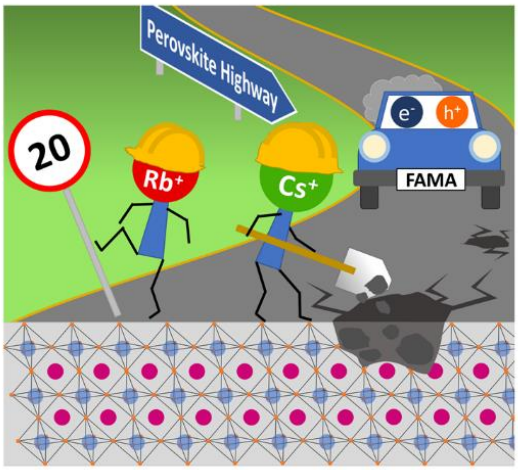

Adapted with permission.[1] Copyright 2018, John Wiley and Sons, Ltd.

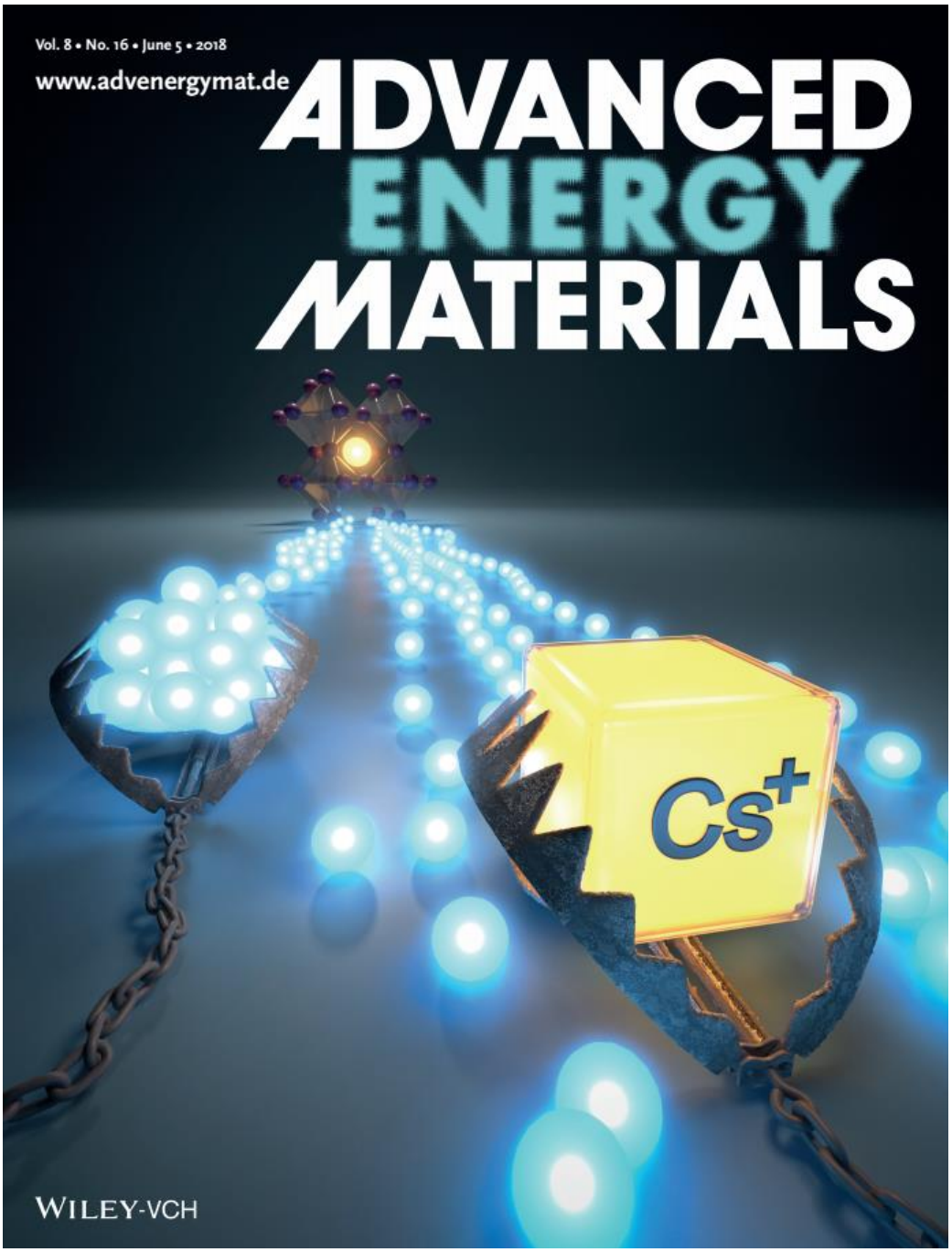

Front cover image in *Advanced Energy Materials* designed by Christoph Hohmann, Nanosystems Initiative Munich (NIM).

5.1 Abstract

Adding cesium (Cs) and rubidium (Rb) cations to $FA_{0.83}MA_{0.17}Pb(I_{0.83}Br_{0.17})_3$ hybrid lead halide perovskites results in a remarkable improvement in solar cell performance, but the origin of the enhancement has not been fully understood yet. In this work, time-of-flight (ToF), time-resolved microwave conductivity (TRMC), and thermally stimulated current (TSC) measurements were performed to elucidate the impact of the inorganic cation additives on the trap landscape and charge transport properties within perovskite solar cells. These complementary techniques allow for the assessment of both local features within the perovskite crystals and macroscopic properties of films and full devices. Strikingly, Cs-incorporation was shown to reduce the trap density and charge recombination rates in the perovskite layer. This is consistent with the significant improvements in the open-circuit voltage and fill factor of Cs-containing devices. By comparison, Rb-addition results in an increased charge carrier mobility, which is accompanied by a minor increase in device efficiency and reduced current-voltage hysteresis. By mixing Cs and Rb in quadruple cation (Cs–Rb–FA–MA) perovskites, the advantages of both inorganic cations can be combined. Our study provides valuable insights into the role of these additives in multiple-cation perovskite solar cells, which are essential for the design of high-performance devices.

5.2 Introduction

In the past few years, hybrid lead halide perovskites established themselves as outstanding materials for photovoltaic (PV) applications. Recently, inorganic cations such as rubidium (Rb) and cesium (Cs) have been added to the perovskite, resulting in a boost in the power conversion efficiency (PCE) up to 21.6%.[2] The state-of-the-art perovskite solar cells comprise a multi-cation mixed-halide hybrid perovskite and show impressive stabilized power output under working conditions.[2, 3] The inorganic cation additives have been shown to improve the phase stability of the photoactive formamidinium lead iodide ($FAPbI_3$) perovskite layer by suppressing the phase transition into the yellow non-perovskite structure at room temperature.[4-8] However, the stabilization of the black perovskite phase is based on fine-tuning the Goldschmidt tolerance factor, which can also be achieved by incorporation of smaller methylammonium (MA) cations into the formamidinium (FA)-dominated perovskite structure, without the need for the even smaller Cs or Rb cations.[9, 10] It is likely that the inorganic cation additives do not only stabilize the crystal structure, but also have a strong impact on the optoelectronic properties of the perovskite, leading to the observed enhancement in solar cell performance.

In order to reach record efficiencies and high stability, extensive device optimization work with a strong focus on the processing of the perovskite layer has been performed. Various combinations and ratios between the monovalent cations (FA, MA, Cs and Rb) and the halides (I and Br) have been explored and optimized along with different perovskite fabrication processes.[4-7, 10-16] However, the origin of the increased device performance that has been demonstrated for Rb- and Cs-containing perovskite solar cells remains rather unclear. In order to engineer perovskite solar cells with the highest possible device performance and stability, it is essential to understand the impact of the inorganic cation additives on the perovskite's optoelectronic properties.

In this work, we investigate the effect of Cs- and Rb-addition on the electronic landscape and the charge transport properties of the multiple-cation mixed-halide hybrid perovskite $FA_{0.83}MA_{0.17}Pb(I_{0.83}Br_{0.17})_3$ in state-of-the-art perovskite solar cells. We combine three complementary probing techniques: time-of-flight (ToF), time-resolved microwave conductivity (TRMC), and thermally stimulated current (TSC) measurements. Our results indicate that Cs markedly reduces the trap density, as well as the second order recombination rate of free mobile charges in the perovskite bulk material. Furthermore, the trap states in Cs-containing perovskites appear to be shallower than in non-modified perovskite devices. These improvements are in good agreement with a notable enhancement of device performance employing Cs-containing perovskites. By comparison, our results show that Rb-addition increases the charge carrier mobility, but that it has only a minor impact on the trap landscape within the perovskite solar cell and results in marginal improvements in device performance. Nevertheless, Rb reduces current–voltage hysteresis and leads to a more stabilized power output. After clarifying the individual role of each inorganic cation additive, the benefits of both Cs and Rb-addition can be found in quadruple cation (Cs–Rb–FA–MA) perovskites.

5.3 Results

5.3.1 Solar cell performance

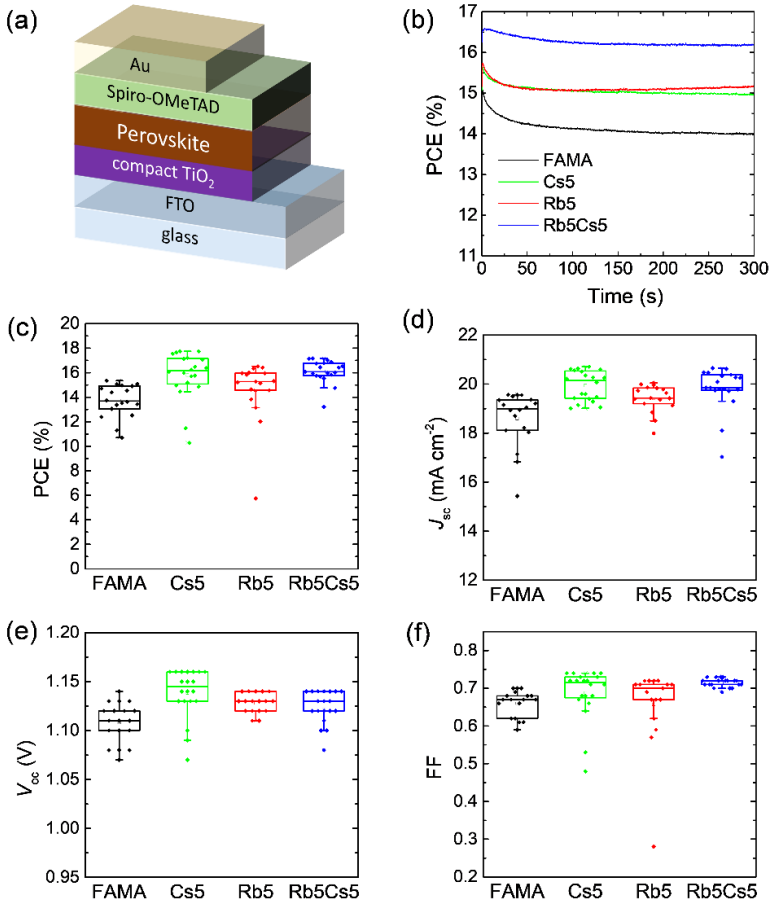

Figure 5.1 (a) Schematic representation of the device architecture of the perovskite solar cells. (b) Maximum power point tracking for encapsulated perovskite solar cells under constant AM 1.5G illumination measured in air. (c–f) Box chart representation of photovoltaic parameters of perovskite solar cells under simulated AM 1.5G sunlight. The current-voltage (*J*–*V*) curve of at least 17 cells for each type of perovskite layer were recorded at a scan rate of 0.1 V s^{-1}.

We investigated the influence of Rb and Cs cations as additives on the PV performance of planar perovskite solar cells with the following device architecture: glass/FTO/compact TiO_2/perovskite/spiro-OMeTAD/Au. According to a protocol reported by Saliba *et al.*[2], we synthesized the multi-cation mixed-halide perovskite $(FA_{0.83}MA_{0.17})Pb(I_{0.83}Br_{0.17})_3$ (FAMA), and added approximately 5 mol% of RbI, CsI or a combination of both to the FAMA precursor solution. The resulting samples are denoted in the following as Rb5, Cs5 and Rb5Cs5, i.e. Rb5 means that

5 mol% of Rb cations were added. Our previous XRD results show that the Cs is fully incorporated into the perovskite lattice, while the same amount of Rb preferentially forms a $RbPb(I_{1-x}Br_x)_3$ side phase.[17] The current–voltage (*J–V*) characteristics of at least 17 cells were evaluated for each type of perovskite layer under one sun illumination according to air mass 1.5 global (AM 1.5G) radiation. Figure 5.1 shows the schematic representation of the layered device architecture, the stabilized output under maximum power conditions at AM 1.5G sun illumination, as well as the distribution of the PV device parameters for FAMA, Rb5, Cs5 and Rb5Cs5 solar cells. Representative *J–V* curves of champion cells are shown in Figure 5.2. Scanning Electron Microscopy (SEM) cross-section images of the full devices are depicted in Figure 5.3.

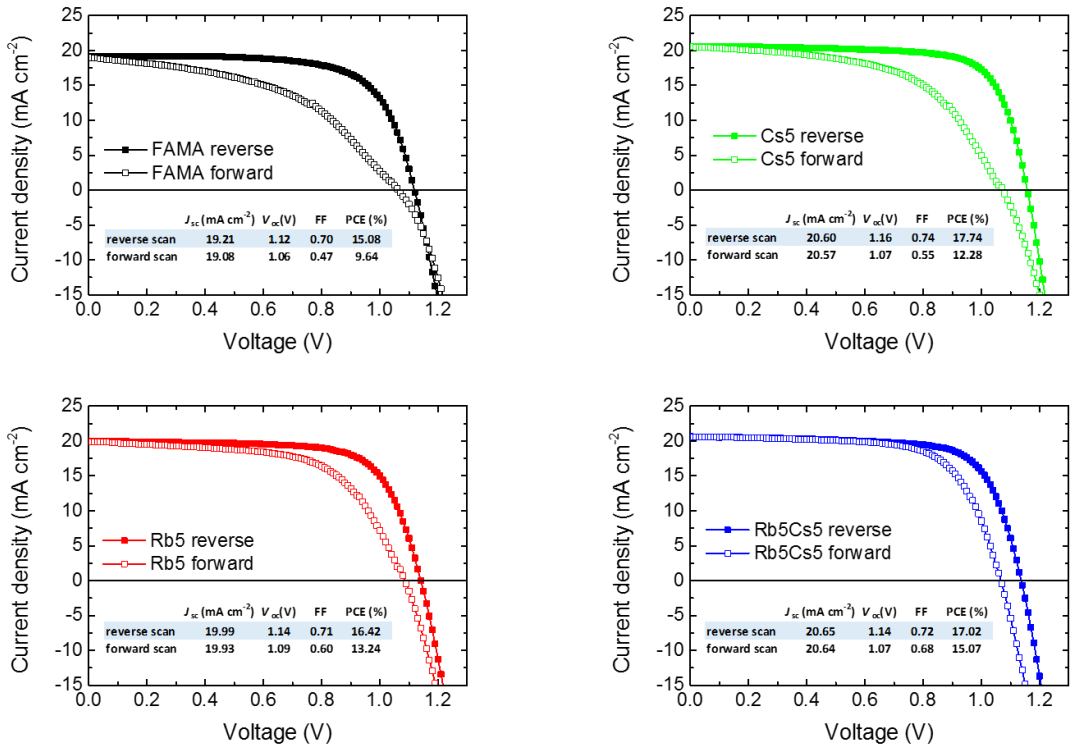

Figure 5.2 *J–V* curves of perovskite solar cells on compact TiO_2 as electron transport layer. Recorded under AM 1.5G illumination and with a scan rate of 0.1 V s^{-1}.

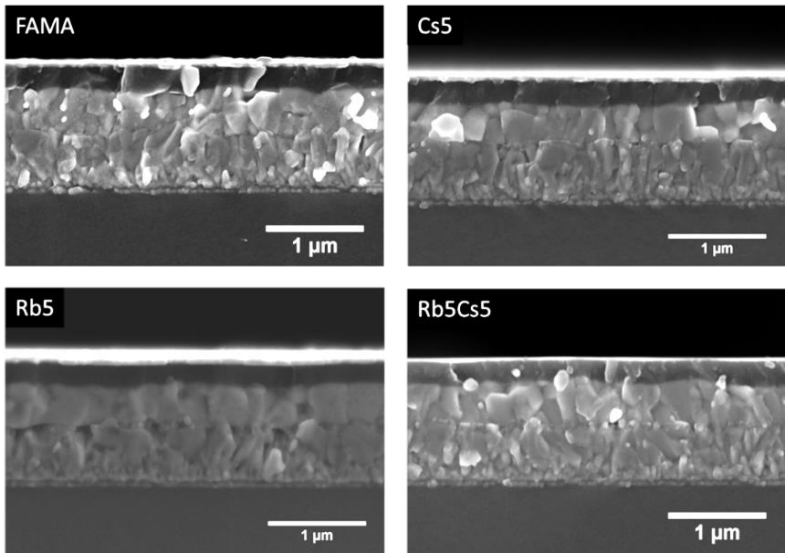

Figure 5.3 SEM cross-section images of the different perovskite solar cells with the device architecture glass/FTO/TiO_2/perovskite/spiro-OMeTAD/Au.

In accordance with previous reports, we find that the PV performance is substantially enhanced for Cs5 devices compared to plain FAMA-based devices.[3] The enhancement in power conversion efficiency upon CsI addition can be ascribed to a significant improvement in all solar cell parameters (Figure 5.1c–f), i.e. short-circuit current (J_{sc}), open-circuit voltage (V_{oc}) and fill factor (FF). The addition of RbI only leads to minor improvements in J_{sc}, V_{oc} and FF in the corresponding Rb5 device. When both Rb and Cs cations were used as additives, the resulting Rb5Cs5 devices show a comparable PV performance to that of the Cs5 devices. However, the presence of Rb results in a more narrow distribution of the Rb5Cs5 device performance parameters, indicating higher reproducibility. Moreover, the presence of Rb in the Rb5Cs5 perovskite film leads to the highest stabilized power output under constant illumination over 300 s (Figure 5.1b) which is superior to that of Cs5 and is in agreement with literature reports.[2, 3] Similar trends regarding J_{sc}, V_{oc} and stabilized power output were also observed for devices prepared on compact SnO_x films instead of TiO_2 serving as electron transport layers (Figure 5.4).

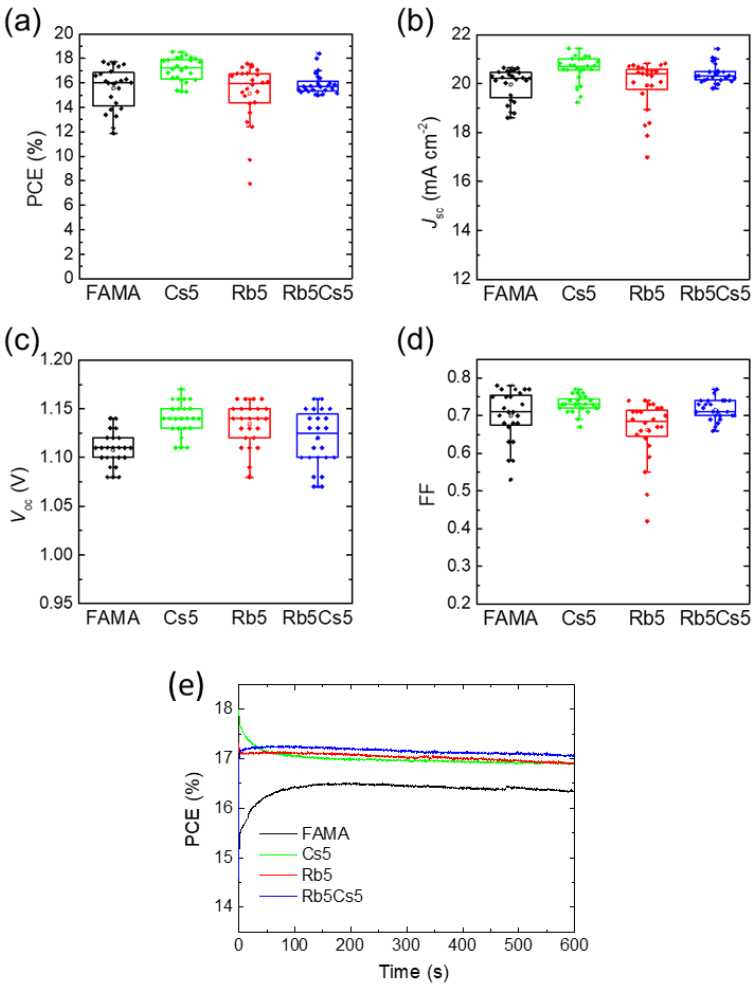

Figure 5.4 (a–d) Photovoltaic parameters of perovskite solar cells with the following device architecture: glass/FTO/SnO_x/perovskite/Spiro-OMeTAD/Au. 24 cells were measured for each type of perovskite layer and the *J*–*V* curve showing the higher PCE value was evaluated (scan speed: 0.2 V s^{-1}). (e) Maximum power point tracking for perovskite solar cells with SnO_x electron transport layer under constant AM 1.5G illumination. The encapsulated devices were measured in air under ~50% relative humidity.

The increase in J_{sc} upon addition of the inorganic cations is most likely related to the formation of a larger volume percentage of photoactive material through the reaction between the CsI or RbI additive and the excess of PbI_2 which is present in the non-stoichiometric FAMA solution. The excess PbI_2 was intentionally added to the perovskite precursor solution due to its potential passivation effect in perovskite solar cells, which is a standard procedure for the highest performing solar cells described in the literature.[2, 3, 18-20] By reacting the PbI_2 excess with the CsI or RbI additive, the absorptance of the resulting perovskite film increases (Figure 5.5a). Furthermore, external quantum efficiency (EQE) measurements were conducted and the measured integrated current densities are in close agreement with the J_{sc} values obtained from the *J*–*V* curves (Figure 5.5b). The EQE data

demonstrate an increase of ~4% in current density when 5% of Rb or Cs are added and overall, Rb5Cs5 leads to the highest current densities.

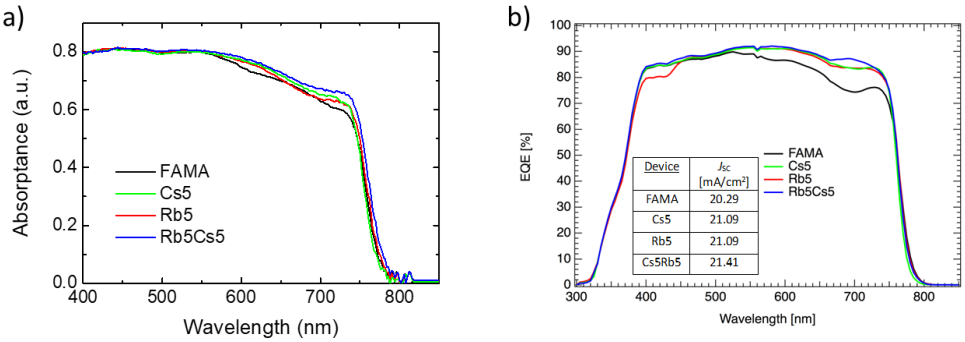

Figure 5.5 (a) UV-VIS absorption spectra of the different perovskite films measured with a spectrophotometer equipped with an integrating sphere. (b) Representative EQE spectra for FAMA, Cs5, Rb5 and Rb5Cs5 devices processed on top of SnO_X. The inset table shows the short-circuit current density of all devices as calculated from the integration of each devices' EQE and the solar irradiance spectrum at AM 1.5G.

We point out that the reduction of excess PbI_2 in the perovskite layer upon inorganic cation addition is not the origin of the observed PCE improvements. This is supported by comparing FAMA devices with 0%, 5% and 10% PbI_2 excess which show very similar photovoltaic performance (Figure 5.6). In order to elucidate the origin of the V_{oc} and FF improvement in perovskite solar cells upon Cs- and/or Rb-addition, we thoroughly investigated the change in charge carrier mobility, charge recombination rates and trap densities of the perovskite thin films.

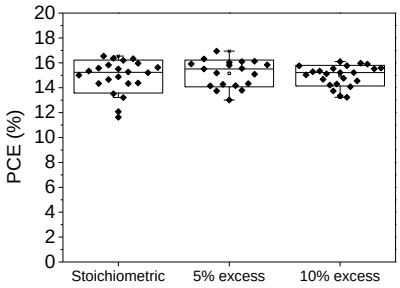

Figure 5.6 Distribution of PCE values for FAMA-based solar cells on compact TiO_2 with varying amount of PbI_2 in the perovskite precursor solution (0%, 5% and 10% excess). The backward *J*–*V* scan was evaluated for at least 19 cells each, showing that the amount of PbI_2 excess does not have a significant influence on the device performance.

5.3.2 Charge carrier transport

Macroscopic charge carrier transport (time-of-flight measurements)

To probe the impact of the Cs and Rb addition on charge carrier transport in the perovskite absorber, we performed time-of-flight (ToF) measurements on laterally contacted perovskite layers.[21] We generate charge carriers in the perovskite layer by illumination using pulsed laser excitation (λ = 510 nm) close to one of the gold electrodes. By simultaneously applying a constant external electric field of 5 kV cm^{-1} (for only a few hundreds of milliseconds to mitigate the effect of ionic migration), the photo-generated charge carriers (either electrons or holes) move across the film within the gap towards the opposite Au electrode. The resulting photocurrent transients show that the transit time t_{tr} that is required for charge carriers to travel laterally from the excitation spot to the opposite Au contact increases with increasing electrode distances (Figure 5.7).

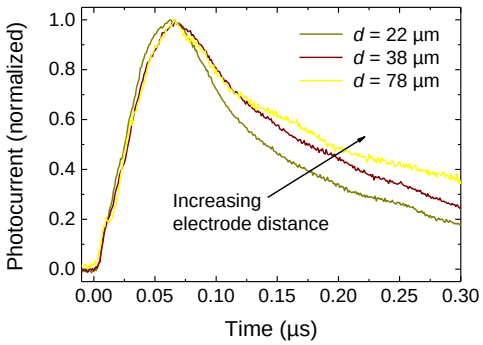

Figure 5.7 Representative photocurrent transients obtained for a FAMA sample after pulsed excitation and the simultaneously applied DC field for different inter-electrode distances in a ToF experiment. An increased electrode distance d results in longer ToF transit times t_{tr}.

A previously reported procedure[21] was employed to extract the transit time from the measured photocurrent transient. The average charge carrier mobility μ in the perovskite films can be approximated by the ToF equation:

$$\mu = \frac{d}{E \cdot t_{tr}} \tag{5.1}$$

with d as the inter-electrode distance, $E = U_{bias}/d$ the applied electric field and t_{tr} the ToF transit time. By plotting t_{tr} against d, the slope of the linear regression in Figure 5.8 is a direct measure for the mobility since the applied electric field was identical for all perovskite films. Depending on the

polarity of the applied electric field, holes or electrons can be probed as the mobile species since charges are locally generated near one electrode. Therefore, the mobility of holes (μ_h) or electrons (μ_e) can be differentiated using the ToF technique.

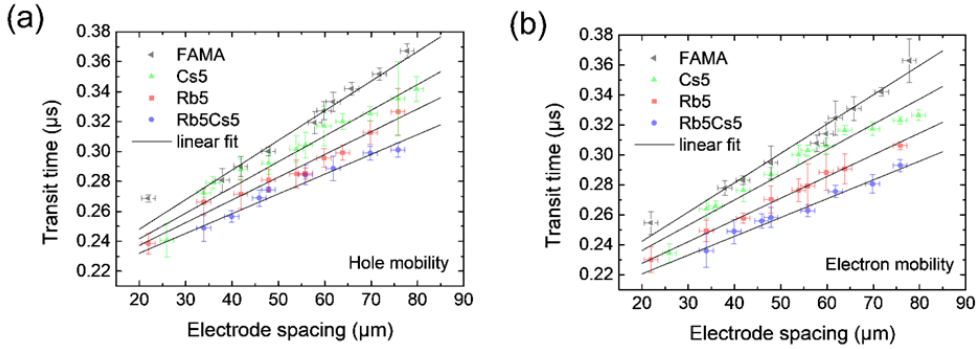

Figure 5.8 Determination of charge carrier mobilities in perovskite thin films using the ToF technique. Extracted transit times (t_{tr}) as a function of electrode distance d under (a) positive bias to extract hole mobility μ_h and (b) negative bias to extract electron mobility μ_e. The value for charge carrier mobility can be derived from the slope of the linear fits and are listed in Table 5.1.

Table 5.1 Charge carrier mobility of perovskite thin films determined by ToF measurements.

Sample	μ_h[cm^2 V^{-1}s^{-1}]	μ_e [cm^2 V^{-1}s^{-1}]	$\mu_{sum,ToF}$ [cm^2 V^{-1}s^{-1}]
FAMA	10	10	20
Cs5	11	12	23
Rb5	13	14	27
Rb5Cs5	15	16	31

Table 5.1 shows the charge carrier mobilities for the different perovskite films calculated from the regression slopes in Figure 5.8. In addition to the individual charge carrier mobility values, the sum of both electron and hole mobility $\mu_{sum,\ ToF}$ is also provided. Strikingly, all samples exhibit very similar mobility values for holes and electrons, indicating highly balanced charge transport over distances of at least 80 µm (maximum size of the in-plane electrode spacings). In comparison to the sum of mobility for FAMA ($\mu_{sum,ToF}$ = 20 cm^2 V^{-1}s^{-1}), Cs5 shows slightly increased mobilities ($\mu_{sum,ToF}$ = 23 cm^2 V^{-1}s^{-1}), while a stronger increase was found for Rb5 ($\mu_{sum,ToF}$ = 27 cm^2 V^{-1}s^{-1}). In particular, the combination of Rb and Cs as additives leads to a perovskite layer with mobility values reaching 31 cm^2 V^{-1}s^{-1}, which corresponds to a ~50% improvement compared to FAMA.

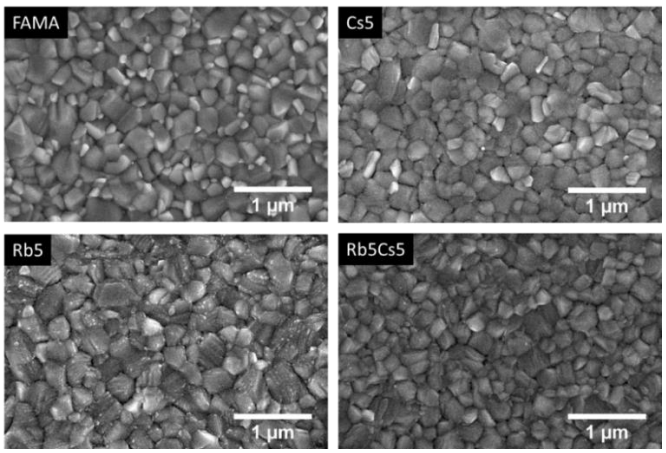

Figure 5.9 SEM top-view images of the different perovskite films fabricated on FTO/TiO_2 substrates.

In our ToF experiments, charge carriers need to travel laterally across various grain boundaries to the opposite electrode to generate a measureable photocurrent. Grain boundaries have been reported to include a high density of defect sites, leading to charge recombination and reduced photocurrent.[21, 22] SEM top-view images of the perovskite films show comparable crystal morphologies and grain sizes of 200–500 nm for FAMA, Cs5, Rb5 and Rb5Cs5 (Figure 5.9). Therefore, the observed increase in mobility through the addition of Rb and Cs to the perovskite precursor mixture cannot be soley ascribed to a lower density of grain boundaries within the probed distances. Nevertheless, it is possible that the inorganic cation additives (especially Rb) influence the barrier properties of the grain boundaries inside the perovskite layer, thereby improving inter-grain charge transport, which may result in higher mobility values. Regarding device efficiency, the lower mobility of Cs5 compared to Rb5 does not explain why Cs shows a larger PCE enhancement than Rb alone. Hence, it is necessary to investigate the change in trap density and recombination rates within the perovskite layer upon addition of the inorganic cations.

Microscopic charge carrier transport (time-resolved microwave conductivity measurements)

Further insight into the relationship between the addition of Cs and/or Rb to the FAMA perovskite and the associated mobilities and lifetimes of free charges can be gained through time-resolved microwave conductivity (TRMC) measurements. TRMC traces were measured at different light intensities and fitted according to a kinetic model to extract the trap densities and rate constants for second order recombination.[23, 24] In Figure 5.10, the intensity-normalized photoconductance

transients are plotted for the various bare perovskite samples on quartz substrates as a function of time after excitation at 650 nm. Typically, on pulsed excitation the photoconductance sharply rises as a result of the photo-generation of mobile charge carriers, which is followed by a decay due to charge recombination and/or immobilization of charge carriers in trap states. For all perovskite materials studied, we observe a gradual reduction in the charge carrier lifetime when increasing the laser intensity, which is characteristic for higher order recombination.[23]

Analogous to our previous work,[23, 25] we used a kinetic model to obtain quantitative information from the intensity-dependent TRMC traces. This kinetic model takes into account the generation of electrons and holes and their recombination via second order band–to–band recombination (k_2) or trap-assisted recombination, which will dominate when the charge carrier density is lower than the trap density N_T. Details on the fitting procedure can be found in Chapter 2.10. As shown in Figure 5.10 by the dotted black lines, excellent agreement is obtained between the modelled and the experimental TRMC traces. The rate constants for trap filling (k_T) and trap emptying (k_D) are modelled to be 1.0×10^{-9} cm^{-3} s^{-1} and 9.0×10^{-10} cm^{-3} s^{-1}, respectively, for all perovskite samples. The extracted values for trap densities, second order recombination rates and effective mobilities are summarized in Table 5.2.

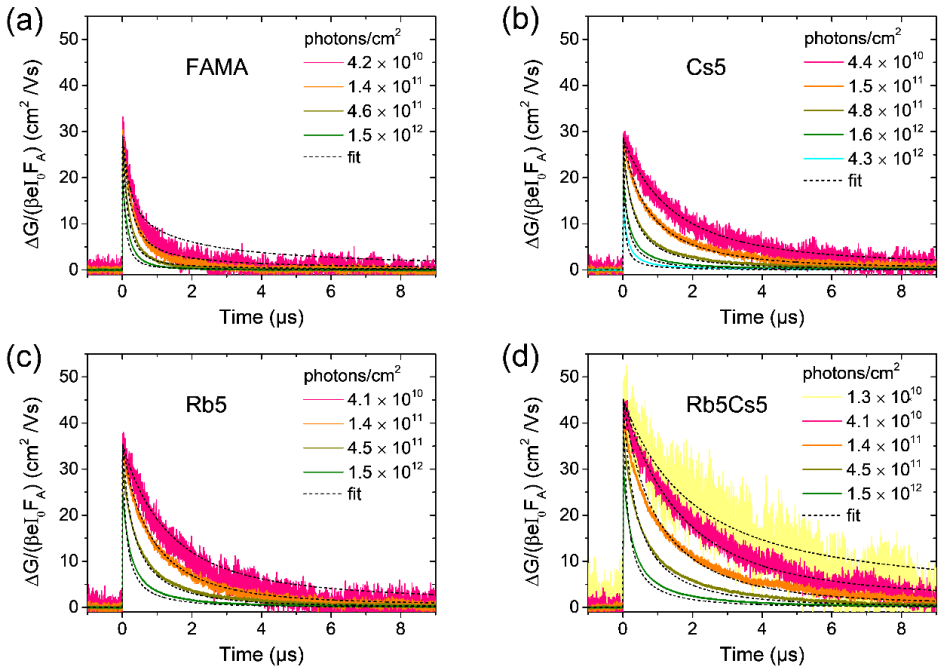

Figure 5.10 Time-resolved microwave conductivity (TRMC) traces recorded for different perovskites on quartz substrates at different excitation laser intensities. (a) FAMA, (b) Cs5, (c) Rb5 and (d) Rb5Cs5. The dotted black lines indicate the corresponding fits to the TRMC traces according to our kinetic model.

Table 5.2 Kinetic parameters for the recombination process, trapping and effective mobilities assessed by TRMC.

Sample	Second order recombination rate constant (k_2) [cm^3s^{-1}]	Trap density ($N_{T,TRMC}$) [cm^{-3}]	Effective mobility (μ_{TRMC}) [$cm^2\ V^{-1}s^{-1}$]
FAMA	6.0×10^{-10}	2.5×10^{15}	42
Cs5	4.2×10^{-10}	8.0×10^{14}	40
Rb5	3.5×10^{-10}	1.0×10^{15}	50
Rb5Cs5	3.0×10^{-10}	8.0×10^{14}	62

The FAMA and Cs5 perovskite films show relatively high local charge carrier mobilities (μ_{TRMC}) exceeding 40 $cm^2\ V^{-1}s^{-1}$. More importantly, a further improvement in charge carrier mobility can be found in Rb5 and, especially in Rb5Cs5 (μ_{TRMC} > 60 $cm^2\ V^{-1}s^{-1}$). Here we note that for TRMC measurements, the sum of both the electron and hole mobility is obtained from the signal.[23] Thus, the mobility values extracted from TRMC need to be compared with the sum of electron and hole mobility values $\mu_{sum,ToF}$ obtained from ToF (see Table 5.1). It is truly remarkable that the charge carrier mobilities as determined from TRMC and from ToF follow almost exactly the same trend. From this resemblance we can conclude that the Rb introduction leads to a definite increase of the charge carrier mobility.

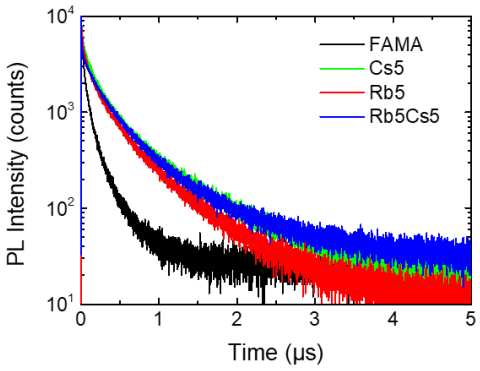

Figure 5.11 Time-resolved photoluminescence (PL) spectra of the different perovskite films. The excitation wavelength of the laser was fixed at 510 nm and the PL maximum around 780 nm was monitored using time-correlated single photon counting (TCSPC).

Furthermore, it is noteworthy that the second order recombination rate, k_2, is also reduced by the presence of the inorganic cation additives, Rb and Cs. Similarly to the improvement of charge carrier mobility, the reduction of the second order recombination rate constant is most pronounced in Rb5Cs5 and thus significantly extends the charge carrier lifetimes throughout the full range of excitation densities shown in Figure 5.10. An increase in charge carrier lifetime is also confirmed by time-resolved photoluminescence (PL) measurements, indicated by the prolonged PL lifetime in Cs5, Rb5 and Rb5Cs5 compared to FAMA (Figure 5.11). These observations show that the addition of Cs and Rb favorably slows down the effective second order band-to-band (electron-hole) recombination within the perovskite bulk material, which could explain the increased V_{oc} of the corresponding devices.

Both the change in k_2 and in μ_{TRMC} might be linked to alterations in the band structure of the perovskite compound, induced by the presence of the inorganic cations. Additionally, we note that the effective second order recombination rate in metal halide perovskite comprises both radiative and non-radiative processes.[26, 27] For instance, increasing radiative recombination could significantly enhance the charge carrier lifetime via reabsorption events.[28] Alternatively, since changing the cations (locally) affects the distances between the lead halide octahedra and their tilting angles, the retarded second order recombination in the presence of Rb and/or Cs could also be due to changes in the band structure.

The performance of perovskite solar cells is also related to the presence of trap states, which can act as recombination pathways for photo-generated charge carriers. Our TRMC results indicate a trap density of approximately $N_{T,TRMC} = 2.5 \times 10^{15}$ cm^{-3} in the FAMA perovskite sample. Interestingly, the introduction of Cs substantially reduces the trap density ($N_{T,TRMC} = 8.0 \times 10^{14}$ cm^{-3}), i.e. by a factor of three compared to the FAMA perovskite film, in line with the observed enhancement in the device performance for Cs5. When only Rb is added to the perovskite precursor solution, the resulting Rb5 film also reveals a lower trap density ($N_{T,TRMC} = 1.0 \times 10^{15}$ cm^{-3}) as compared to FAMA. However, the effect is smaller than for Cs-incorporation. When both Cs and Rb are introduced, as in Rb5Cs5, the trap density is comparable to the Cs5 sample, showing the same trend observed for the PCE values.

Our TRMC results thus suggest that the notable improvement of device performance in Cs5 and Rb5Cs5 cannot be simply assigned to an increase in mobility, but rather to a decrease of effective second order recombination rate as well as a lower trap density compared to FAMA. In order to obtain further insights into the amount and the energetic levels of these suggested trap states, we conducted thermally stimulated current (TSC) experiments on complete solar cells.

5.3.3 Defect spectroscopy

As an electrically sensitive technique, TSC allows for the investigation of whole devices, thus linking changes in the trap states to the respective device performance. The TSC measurements were conducted on complete solar cells differing only in the photoactive layer, which was one of the four perovskite types: FAMA, Cs5, Rb5 or Rb5Cs5. To obtain the TSC spectra, the devices were cooled to a temperature well below the activation energy of the investigated trap states (here: 30 K) in the dark. Subsequently, the trap states were optically filled via illumination with a cold LED array. In order to release the previously trapped charge carriers within the devices, the solar cells were gradually heated up to 300 K at a constant rate of 3 K min^{-1}. Further details regarding the TSC technique have been reported earlier by Baumann *et al*.[29] The respective TSC spectra for each solar cell are shown in Figure 5.12a.

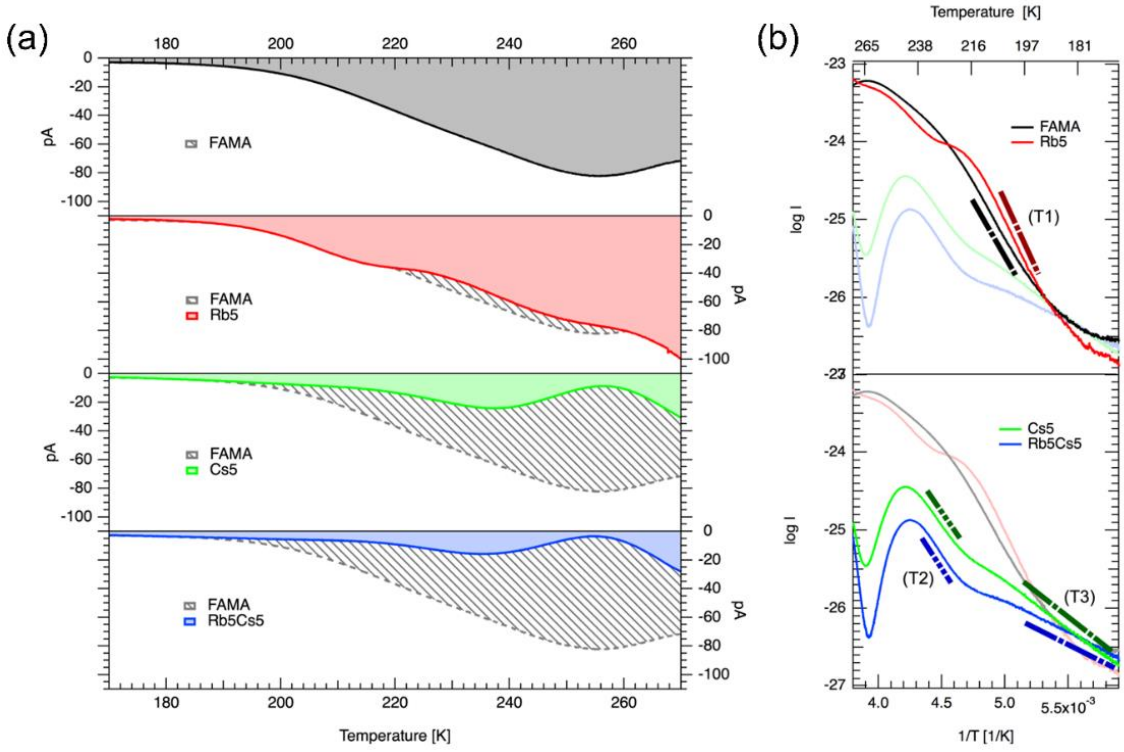

Figure 5.12 (a) TSC spectra of full solar cells employing FAMA, Cs5, Rb5 or Rb5Cs5 as the active perovskite layer. The hatched areas indicate the difference in the amount of traps in the respective perovskite solar cell compared to the FAMA-based device. (b) Arrhenius plots of the TSC spectra in the relevant temperature regions to estimate the activation energy of the trap states. The bars labeled T1, T2 and T3 mark the data range used for fitting according to the initial rise method.

For the pure FAMA based device, a very wide TSC signal can be identified, indicating a broad distribution of trap state energies within the device. Our results show that the exclusive addition of Rb to the FAMA precursor solution (Rb5) has only a negligible impact on the overall TSC signal intensity and shape. However, the introduction of Cs into the perovskite film (Cs5, Rb5Cs5) considerably reduces the TSC signal, indicating an overall reduction of the trap density. Instead of a broad TSC peak, a more distinct peak is visible at around 230–240 K for both Cs-containing systems. We can assess the depth of these trap states by estimating the activation energy of the trap states. Herein, the so-called initial rise method is used according to the equation:[30, 31]

$$I_{TSC} \propto exp\left(-\frac{E_A}{k_B T}\right) \tag{5.2}$$

where k_B is the Boltzmann constant and T the temperature, at which the TSC signal I_{TSC} starts to rise. The data range used to fit the initial rise is denoted in the corresponding Arrhenius plot of the TSC spectra in Figure 5.12b as T1, T2 and T3. Table 5.3 shows a summary of the activation energies of trap states for the devices with different perovskite absorber layers.

Table 5.3 Activation energies of trap states and trap densities in perovskite solar cells determined by TSC measurements.

Device	$E_{A,T1}$ [meV]	$E_{A,T2}$ [meV]	$E_{A,T3}$ [meV]	$N_{T,TSC}$ [cm^{-3}]
FAMA	248	-	-	7.3×10^{16}
Rb5	283	-	-	7.2×10^{16}
Cs5	-	195	105	2.2×10^{16}
Rb5Cs5	-	205	70	1.6×10^{16}

For the FAMA based device, trap states with an activation energy of $E_{A,T1,FAMA}$ = 248 meV are found (T1). With a slightly higher activation energy of $E_{A,T1,Rb5}$ = 283 meV, the trap states appear to shift even deeper into the band gap with the small amount of Rb added to the perovskite layer (Rb5). In contrast, the opposite behavior is found for the introduction of Cs, where the energetic depth of the deepest trap states in the system is reduced to $E_{A,T2,Cs5}$ = 195 meV as well as $E_{A,T2,Rb5Cs5}$ = 205 meV (T2). Furthermore, an additional but small contribution of energetically shallow trap states with a depth of $E_{A,T3,Cs5}$ = 105 meV and $E_{A,T3,Rb5Cs5}$ = 70 meV appears in both Cs-containing films (T3).

From the TSC measurements, it is not possible to deduce if the trap states found in Cs5 or Rb5Cs5 are also present in the broad background of deeper trap states in the FAMA or Rb5 samples. Neither can their polarity be determined. However, we note that Cs either leads to the removal of detrimental

deep traps or a shift of these traps closer to the conduction or valence band in the FAMA perovskite. Contrarily, Rb has almost no influence on either the density or the energetic distribution of those trap states. Our TRMC results support the possibility of a reduced number of traps within the perovksite layer upon Cs-addition. We judge the lower number of deeper traps to be beneficial for solar cell performance, as the recombination mediated by these states is reduced, which is in agreement with the improved V_{oc} of the Cs5 and Rb5Cs5 devices.

Finally, not only the energetic depth of the trap states is changed by the inorganic cation additive, but also the overall signal height, which is associated with the trap density. We note here that the trap density values deduced from TSC measurements constitute a lower limit, as charge carriers may also recombine after being released from the trap state during the measurement. Only those charge carriers released from the trap state and subsequently extracted at external contacts are detected by the TSC method. In order to estimate the lower limit of trap densities $N_{T,TSC}$ in the different perovskite solar cells, the TSC signal can be integrated over the elapsed time according to the equation:[32]

$$\int_{signal} I_{TSC} dt \leq e N_{T,TSC} Vol \qquad (5.3)$$

where *e* is the elementary charge and *Vol* is the volume of the perovskite layer. The estimated lower limits of trap densities are presented in Table 5.3, where the integral was calculated for the timespan of the temperature rise from 170–270 K.

Our results show that the addition of Cs removes a considerable amount of trap states from the system ($N_{T,TSC} = 2.2 \times 10^{16}$ cm^{-3}) as compared with FAMA devices (7.3×10^{16} cm^{-3}), which is not the case if only Rb is introduced (7.2×10^{16} cm^{-3}). With a trap density of $N_{T,TSC} = 1.6 \times 10^{16}$ cm^{-3}, the combination of both Rb and Cs shows the lowest value of all devices, corresponding to an almost 80% lower number of trap states in the Rb5Cs5 system compared to pure FAMA.

We point out that the TSC method does not directly indicate whether the detected traps are located in the bulk, at grain boundaries or at an interface with the transport layers. However, our TRMC measurements show the same trend as TSC in trap density reduction, while solely probing the local properties of the perovskite absorber layer. Combining these experimental results allows us to deduce that Cs significantly reduces the trap density in the bulk or in the grain boundaries of the perovskite material. We tentatively assign the discrepancy between the overall absolute values for the trap densities extracted from these two techniques to the presence of the charge transport layers and associated interfacial effects being additionally measured in TSC, which is under further investigation. However, since all solar cells probed by the TSC technique were fabricated with the same contact materials, it is reasonable to assume that the extracted trends from TSC can indeed be assigned to the different perovskite materials employed.

5.4 Discussion

The addition of Cs and/or Rb salts to the perovskite precursor solution has a strong impact on the film's crystallization behavior, confirming previous reports in literature.[2-4] One possible explanation for the change in the perovskite crystallization process is the lower solubility of rubidium and particularly cesium halides in DMF, compared to the perovskite precursors FAI and MABr.[11, 33-35] This may lead to the rapid formation of crystal nuclei already during the spin-coating procedure. In the presence of the inorganic cation additives, the formation of potentially defect-prone intermediate crystal phases such as mixed-dimensional hexagonal polytypes or DMSO-complexes is circumvented.[3, 36] In particular, Cs initiates the prompt formation of the quasi-cubic perovskite crystal phase, evident in the corresponding XRD peaks and the dark-brown color of non-annealed Cs5 and Rb5Cs5 films (Figure 5.13a–d). As a result, higher XRD peak intensities for the perovskite phase are found in Rb5, Cs5 and Rb5Cs5 films after annealing (Figure 5.13e) which indicates higher crystalline order than in pure FAMA. Besides improving the perovskite crystallization mechanism, the actual incorporation of the inorganic cations into the perovskite lattice probably plays a critical role in affecting the charge transport and trap landscape of the metal halide perovskite.

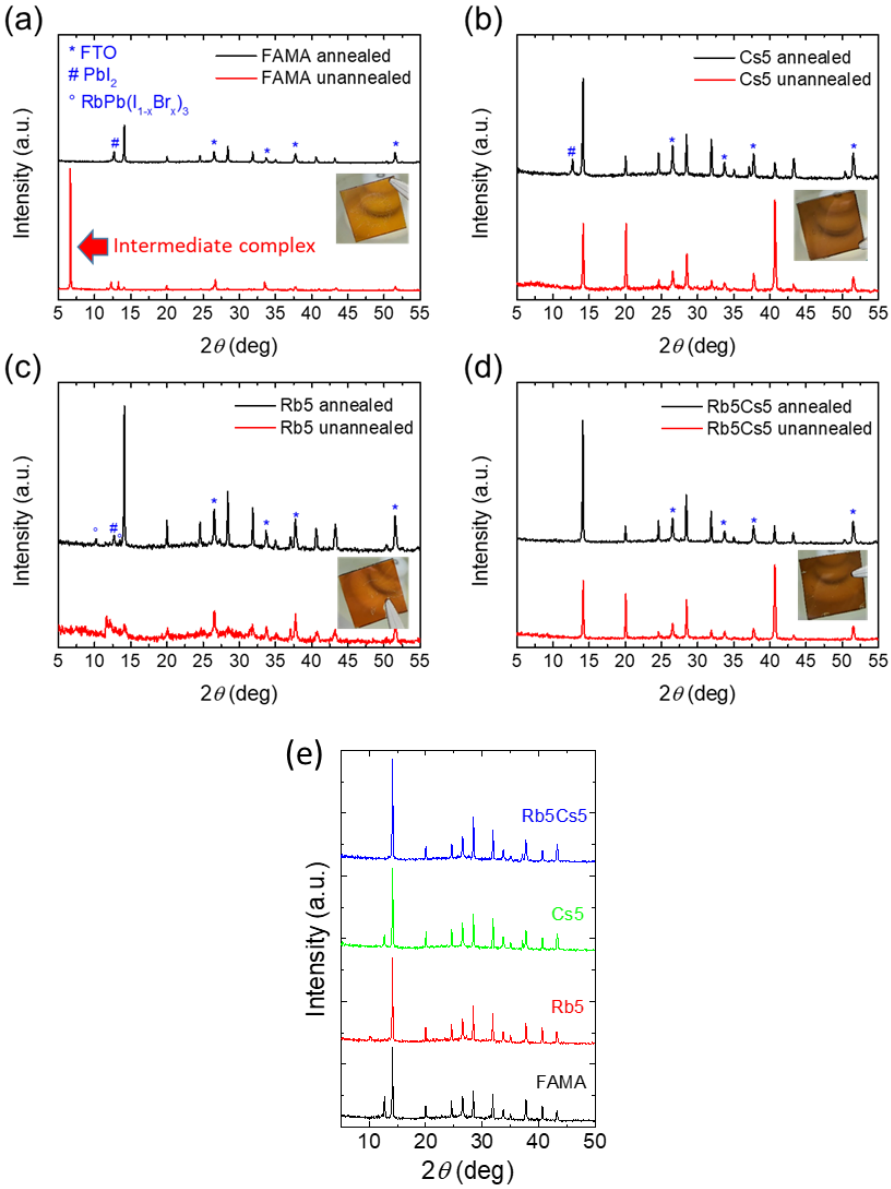

Figure 5.13 (a–d) XRD patterns of unannealed (red) and annealed (black) perovskite thin films on FTO/compact TiO_2 using different precursor solutions. (a) FAMA, (b) Cs5, (c) Rb5 and (d) Rb5Cs5. The insets show photographs of the respective unannealed film. (e) XRD patterns of multiple-cation perovskite films prepared on FTO/TiO_2 substrates after annealing.

Our complementary probing techniques reveal that the addition of Cs barely affects the charge carrier mobility, but considerably reduces the trap density and the effective second order recombination rate in the metal halide perovskite, which likely leads to the higher V_{oc} and therefore higher performance found in Cs containing devices. Interestingly, the local, contactless TRMC technique on bare perovskite films showed the same trends for the trap density as the TSC measurements obtained with

complete devices. Due to the excellent consistency between the TRMC and the TSC results, we assign the observed changes induced by Cs-addition rather to the bulk or boundaries of the perovskite crystals than solely to effects at the perovskite/transport layer interfaces.

By contrast, the Rb-addition leads to increased charge carrier mobilities in Rb5 compared to FAMA, which may be related to improved charge transport across the perovskite grain boundaries. However, with the high and balanced mobilities found in FAMA films, efficient charge collection and injection should be enabled, and mobility is unlikely to be the limiting factor for charge diffusion. Our results show that Rb has only a marginal effect on the trap landscape of the entire perovskite device. Since we only found a minor improvement in Rb5 device performance compared to FAMA, we suggest that in our samples it is the amount and nature of trap states inside the perovskite that mainly limits efficiency.

Despite the minimal impact of Rb on the PCE values obtained from *J–V* curves, we nonetheless observed improved power output stability and reduced *J–V* hysteresis in Rb containing devices (see Figure 5.1 and Figure 5.2). In the literature, the reduction of hysteresis in quadruple cation mixtures has been assigned to a lower defect density and thus a lower trap density within the perovskite crystals compared to triple cation mixtures without Rb.[13] Contrary to this, we see a reduced hysteresis in the case of Rb5Cs5 devices compared to Cs5 devices, where our TSC and TRMC results indicate rather similar trap densities. Therefore, it is unlikely that hysteresis is suppressed simply because of a reduction of traps in the bulk perovskite material. Alternatively, it has been suggested that the Rb-induced formation of larger perovskite crystals with fewer grain boundaries reduces ionic migration along grain boundaries, hence diminishing hysteresis.[13, 37] However, our SEM images reveal comparable grain sizes for the Cs5 and Rb5Cs5 samples examined here (Figure 5.9), ruling out the density of perovskite grain boundaries being the main reason for the reduced *J–V* hysteresis.

Instead, our study tallies with several recent publications and the combined results point to the following explanation: We recently found that 5–10% Cs cations can be incorporated into the FAMA perovskite structure, while the same amount of Rb cations does not form part of the perovskite lattice due to its unsuitably small ionic radius. As a result, the addition of 5–10% Rb mainly leads to the formation of non-perovskite side-phases such as $RbPb(I_{1-x}Br_x)_3$.[17] These findings are in excellent agreement with the most recent solid state NMR results on multiple-cation perovskites reported by Kubicki *et al.*[38] The fundamentally different effects of Cs and Rb cations on the FAMA perovskite crystal lattice (Figure 5.14) may explain their different impact on the perovskite's trap landscape, charge transport properties, device performance and hysteresis.

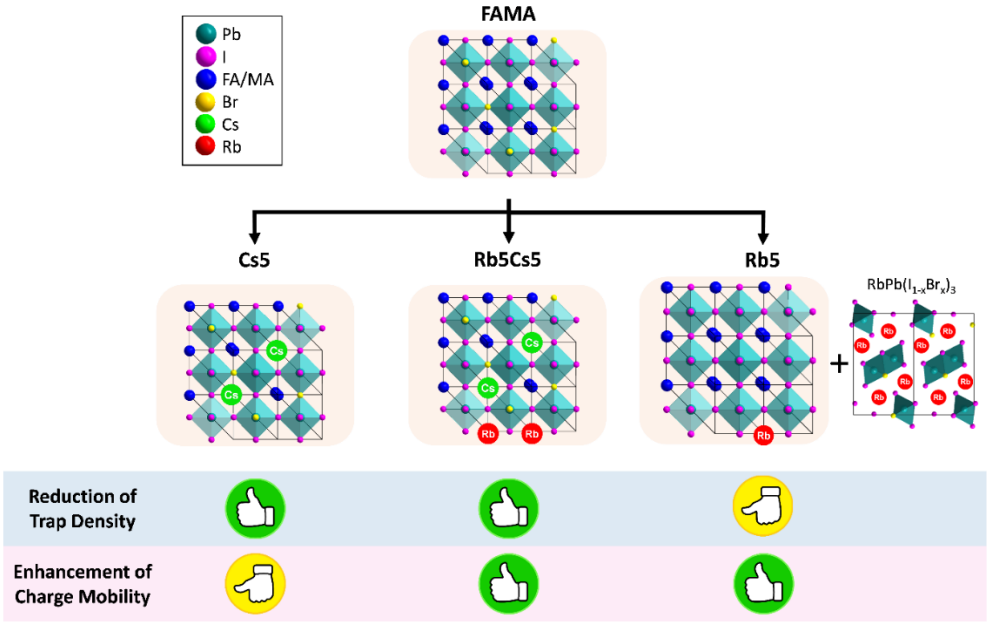

Figure 5.14 Schematic illustration of the hypothesized distribution of the inorganic cation additives within the perovskite crystal and the effect of Cs/Rb addition on the reduction of trap density and enhancement of charge carrier mobility within the perovskite layer.

Furthermore, charge accumulation and surface recombination at the interfaces between the perovskite and the selective charge transport layers have been shown to strongly affect *J*–*V* hysteresis.[39] We hypothesize that Rb could have an influence on these interfaces, as it is not fully incorporated into the perovskite crystal structure itself. To obtain information about the distribution of the cation additives within the perovskite layer, we performed time-of-flight secondary ion mass spectrometry (ToF-SIMS) measurements on the different perovskite films deposited on FTO/TiO_2 substrates (Figure 5.15). Indeed, the depth profile for the Rb5 sample shows a clear accumulation of Rb^+ species at the TiO_2 interface, while Cs^+ is very homogeneously distributed within the Cs5 film. In Rb5Cs5, the presence of Cs^+ leads to a more even distribution of Rb^+ which is in accordance with work by Philippe *et al.*, and only a slight Rb-enrichment still occurs between the perovskite layer and the substrate.[40]

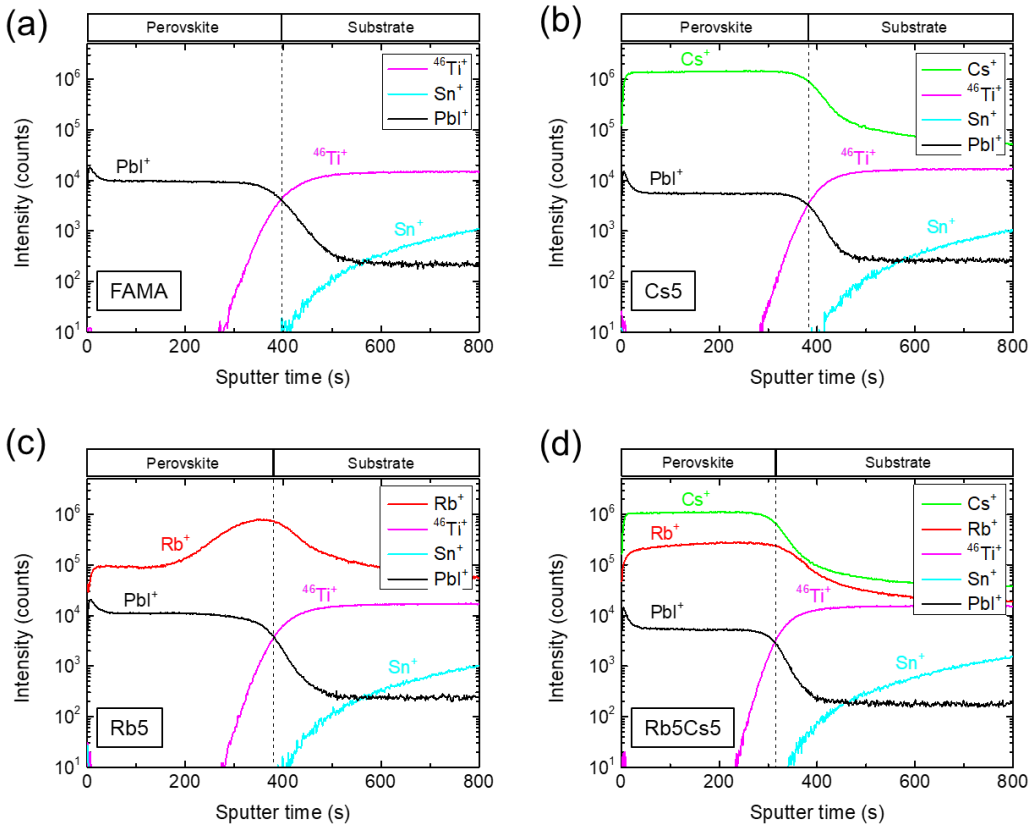

Figure 5.15 ToF-SIMS depth profiles for different perovskite films on FTO/TiO_2 substrates. (a) FAMA (b) Cs5 (c) Rb5 and (d) Rb5Cs5. The dotted line and the description on top of the graph ("Perovskite / Substrate") is a rough orientation for the respective interface.

Our ToF-SIMS results are in excellent agreement with recent work by Albadri *et al.*, who reported that surface passivation effects of Rb give rise to reduced recombination at the TiO_2/perovskite interface compared to triple cation systems without Rb.[41] We believe that the enrichment of Rb cations at the electron transport layer interface is possibly related to a reduction of surface recombination in the vicinity of the electron transporting layer, which in turn affects device hysteresis and power output stability. Furthermore, Guo *et al.* predicted by first-principle calculations that an accumulation of the Rb-additives at the surface of perovskite crystals is energetically favored over their incorporation into the inner atomic layers, possibly giving rise to altered properties of the grain boundaries between the crystals.[42] Consequently, this might not only explain the difference in charge carrier mobilities we identified in our ToF and TRMC experiments, but also offers an additional explanantion for the change in *J*–*V* hysteresis. We are currently carrying out investigations to further elucidate this matter.

5.5 Conclusions

By combining three complementary characterization techniques – ToF, TRMC and TSC measurements – we could establish the influence of Cs- and Rb-addition on the charge carrier mobilities, recombination rates and trap states of state-of-the-art multiple-cation perovskites. We found that Rb-addition leads to increased charge carrier mobilities in Rb5 compared to FAMA, but has only a marginal effect on the trap landscape of the perovskite layer. This results in a minor improvement in device performance of Rb5 compared to the FAMA control device. By contrast, Cs-incorporation significantly reduces the number and the depth of trap states in the perovskite crystals. However, Cs has barely any effect on the charge carrier mobility. The observed reduction in trap density is in excellent agreement with the boost in V_{oc} and FF for Cs-containing devices compared to FAMA. By combining Cs and Rb in quadruple cation (Rb–Cs–FA–MA) perovskite mixtures, we observe the highest mobility and the lowest trap density, resulting in solar cells with the highest stabilized power output. We conclude that in the examined multiple-cation perovskite solar cells, the bottleneck for device efficiency is mainly the amount and the nature of the traps rather than insufficient charge carrier mobility in the perovskite.

5.6 Methods

Perovskite precursor solutions

FAI and MABr were purchased from Dyesol. PbI_2 and $PbBr_2$ (99%) were purchased from TCI. CsI (99.9%) and all anhydrous solvents (DMSO, DMF, chlorobenzene) were purchased from Sigma-Aldrich and RbI from abcr GmbH. All chemicals were used without further purification. Perovskite precursor solutions for FAMA, Cs5, Rb5 and Rb5Cs5 were fabricated according to a previous report.[2, 17]

FAMA: Following the protocol reported by Saliba *et al*., a multiple cation mixed-halide perovskite solution was prepared by dissolving PbI_2 (508 mg, 1.1 mmol), $PbBr_2$ (80.7 mg, 0.22 mmol), FAI (171.97 mg, 1 mmol) and MABr (22.4 mg, 0.2 mmol) in 1 mL of a 4:1 (v/v) mixture of anhydrous DMF and DMSO. This non-stoichiometric precursor solution for $(FA_{0.83}MA_{0.17})Pb(I_{0.83}Br_{0.17})_3$ contains a 10 mol% excess of PbI_2 and $PbBr_2$, respectively, which was introduced to enhance device performance. The FAMA solution was filtrated through a 0.45 µm syringe filter before use. We note that volume changes upon dissolving the salts are expected.

Cs5: CsI (389.7 mg, 1.5 mmol) was dissolved in 1 mL DMSO and filtrated through a 0.45 µm syringe filter. To obtain the desired triple cation perovskite composition of ~5% Cs, 42 µL of the ~1.5 M CsI stock solution was added to 1 mL FAMA solution, yielding a nominal composition of $Cs_{0.05}[(FA_{0.83}MA_{0.17})]_{0.95}Pb(I_{0.83}Br_{0.17})_3$. The change in the I:Br ratio was neglected and we note that volume changes upon dissolving CsI in DMSO were not taken into consideration.

Rb5: RbI (318.5 mg, 1.5 mmol) was dissolved in 1 mL of a 4:1 (v/v) DMF:DMSO mixture and filtrated through a 0.45 µm syringe filter. To obtain the desired triple cation perovskite composition of ~5% Rb, 42 µL of the ~1.5 M RbI stock solution was added to 1 mL FAMA solution, yielding a nominal composition of $Rb_{0.05}[(FA_{0.83}MA_{0.17})]_{0.95}Pb(I_{0.83}Br_{0.17})_3$. However, it is likely that the Rb is effectively not (fully) incorporated into the perovskite structure. The change in the I:Br ratio was neglected and we note that volume changes upon dissolving RbI in the DMF:DMSO mixture were not taken into consideration.

Rb5Cs5: To obtain the quadruple cation perovskite composition of ~5% Rb and ~5% Cs, 42 µL of the RbI solution and 42 µL of the CsI solution were added to 1 mL FAMA solution, yielding a nominal composition of $Rb_{0.05}Cs_{0.05}[(FA_{0.83}MA_{0.17})]_{0.9}Pb(I_{0.83}Br_{0.17})_3$. The change in the I:Br ratio was neglected and we note that volume changes upon dissolving the Cs and Rb salts were not taken into consideration to calculate the additive concentration.

Perovskite film fabrication

75 µL of the perovskite precursor solution was spin-coated inside a nitrogen-filled glovebox at 1000 rpm and 4000 rpm for 10 s and 30 s, respectively. Approximately 20 s before the end of spinning, 500 µL of chlorobenzene was added to the film. The perovskite film formation was completed by annealing at 100 °C for 60 min on a hotplate.

Device fabrication

FTO coated glass substrates (7 Ω/sq) were patterned by etching with zinc powder and 3 M HCl solution and successively cleaned with deionized water, a 2% Hellmanex detergent solution, ethanol and finally treated with oxygen plasma for 5 min. A compact TiO_2 layer was deposited as a hole blocking layer on the substrate via a sol-gel approach. A mixture of 2 M HCl (35 µL) and anhydrous isopropanol (2.53 mL) was added dropwise to a solution of 370 µL titanium(IV) isopropoxide (Sigma-Aldrich) in isopropanol (2.53 mL) under vigorous stirring. The TiO_x solution was spin-coated dynamically onto the FTO substrates at 2000 rpm for 45 s, followed by annealing in air at

150 °C for 10 min and subsequently at 500 °C for 45 min. Alternatively, 10–15 nm compact SnO_x electron transport layers were prepared by atomic layer deposition (ALD) on FTO-coated glass substrates which were patterned and cleaned as in the TiO_2 preparation. Tetrakis(dimethylamino)tin(IV) (TDMSn, Strem, 99.99%) was used as a tin precursor. The deposition was conducted at 118 °C with a base pressure of 5 mbar in a Picosun R-200 Advanced ALD reactor. The tin precursor was held at 75 °C during depositions. Ozone gas was produced by an ozone generator (INUSA AC2025). Nitrogen (99.999%, Air Liquide) was used as the carrier and purge gas with a flow rate of 50 sccm per precursor line. The growth rate was determined via spectroscopic ellipsometry on Si(100) witness substrates. A Cauchy model was used for the tin oxide layer and the growth rate was 0.69 Å per cycle. After the deposition of the electron transporting layer and the perovskite layer, a spiro-OMeTAD hole transporter layer was applied. 1 mL of a solution of spiro-OMeTAD (Borun Chemicals, 99.8%) in anhydrous chlorobenzene (75 mg mL^{-1}) was doped with 10 µL tBP (Sigma-Aldrich, 96%) and 30 µL of a Li-TFSI (Sigma-Aldrich, 99.95%) solution in acetonitrile (170 mg mL^{-1}, Sigma-Aldrich, anhydrous) and deposited by spin-coating at 1500 rpm for 40 s and then 2000 rpm for 5 s. After storing the samples overnight in air at 25% relative humidity, 40 nm Au was deposited through a patterned shadow mask by thermal evaporation at 8×10^{-7} mbar to form the back electrode.

Thin film characterization

X-ray diffraction (XRD) measurements of thin films were performed with a Bruker D8 Discover X-ray diffractometer operating at 40 kV and 30 mA, employing Ni-filtered Cu $K_{\alpha 1}$ radiation (λ = 1.5406 Å) and a position-sensitive LynxEye detector. SEM images were recorded with a FEI Helios Nanolab G3 UC DualBeam scanning electron microscope. UV-VIS absorption spectra were recorded with a Perkin-Elmer Lambda 1050 spectrophotometer equipped with an integrated sphere. The thin films were placed under an angle of 10° inside the sphere to detect the total fraction of reflected and transmitted photons, from which the fraction of absorbed photons was determined as a function of wavelength. Time-resolved PL spectroscopy was performed with a Picoquant Fluotime 300 spectrofluorometer, using an excitation wavelength at 510 nm and by monitoring the PL emission maximum around 780 nm. The depth profiles of perovskite films on TiO_2/FTO-glass substrates were measured with a ToF-SIMS 5 setup from ION-TOF GmbH. Pulsed primary ions from a 30 keV Bi^+ liquid-metal ion gun were used as an analytical source, and a 10 keV O_2-cluster source was used as a sputtering ion source. The ToF-SIMS analysis was done on a 100 × 100 µm area inside the 300 × 300 µm sputtering crater.

Current-voltage characterization

J-V curves were recorded under ambient conditions using a Newport OrielSol 2A solar simulator with a Keithley 2400 source meter under simulated AM 1.5G sunlight, with an incident power of 100 mW cm^{-2}, calibrated with a Fraunhofer ISE certified silicon cell (KG5-filtered). The active area of the solar cells was defined with a square metal aperture mask of 0.0831 cm^2. After pre-biasing the device at 1.5 V for 5 s under illumination, *J-V* curves were recorded by scanning the input bias from 1.5 to 0 V (reverse scan) and then from 0 to 1.5 V (forward scan) at a scan rate of 0.1–0.2 V s^{-1}. For statistical evaluation, the photovoltaic parameters were extracted from the *J–V* curve showing the higher PCE value. The stabilized power output was measured by tracking the photocurrent at the maximum power point without pre-biasing the device.

Time-of-flight measurements

We deposited laterally spaced gold (Au) electrodes through a custom-made evaporation mask on top of clean glass substrates, resulting in inter-electrode distances ranging from 22 to 80 µm. Subsequently, the different perovskite layers were deposited on top of the glass/Au substrates via spin-coating and top-coated with a thin layer of Poly(methyl methacrylate) (PMMA) to prevent film degradation during the measurement. Generation of charge carriers within the perovskite absorber was induced by pulsed laser excitation at a wavelength of 510 nm. The laser system itself consists of an optical parametric oscillator (OPO), pumped by a Nd:YAG laser with a repetition rate of 20 Hz and a pulse length of 7 ns. Laterally contacted perovskite films were shortly illuminated from the semi-transparent glass/gold side and close to one contact by focusing the laser through an extra-long working distance microscope objective (spot size approximately 2 µm). An external DC field was applied through the gold electrodes only for the short measurement interval of a few hundred milliseconds to avoid effects due to ion migration. The constant electric field created a current flow which led to the respective ToF photocurrent transient. The generated *J–t* profiles were amplified and converted before being recorded with a fast oscilloscope.

Time-resolved microwave conductivity measurements

TRMC experiments were performed on perovskite films on quartz substrates according to a previously reported procedure.[25] The change in microwave power (probe frequency: 8.5 GHz) was monitored after pulsed excitation of the sample at 650 nm. The slow repetition rate of the laser of 10 Hz ensures full relaxation of all photo-induced charges to the ground state before the next laser

pulse hits the sample. Neutral density filters were used to vary the intensity of the incident light. The illuminated sample area was ~2.5 cm^2. The charge generation in the G_C is determined by the temporal profile (3.5 ns FWHM) and intensity of the laser pulse in combination with the optical absorption of the perovskite at the wavelength used. Before and during the photoconductance measurements, the samples were not exposed to moisture and air to prevent degradation.

Thermally stimulated current measurements

TSC measurements were conducted in a closed cycle He cryostat, with Helium as a contact gas for thermal coupling. To avoid any atmospheric exposure, solar cell samples were transferred via an integrated sample lock system from a glove box to the cryostat. Trap filling was achieved via illumination with an LED array for 10 min. After a dwell time of 10 min in the darkness, the sample was heated up to 300 K at a constant rate of 3 K min^{-1}. The TSC signal of the sample was detected by a Sub-Femtoamp Remote Source Meter (Keithley 6430) without the application of a bias voltage.

5.7 References

[1] Y. Hu, E. M. Hutter, P. Rieder, I. Grill, J. Hanisch, M. F. Aygüler, A. G. Hufnagel, M. Handloser, T. Bein, A. Hartschuh, K. Tvingstedt, V. Dyakonov, A. Baumann, T. J. Savenije, M. L. Petrus, P. Docampo, *Adv. Energy Mater.* **2018**, *8*, 1703057.

[2] M. Saliba, T. Matsui, K. Domanski, J.-Y. Seo, A. Ummadisingu, S. M. Zakeeruddin, J.-P. Correa-Baena, W. R. Tress, A. Abate, A. Hagfeldt, M. Grätzel, *Science* **2016**, *354*, 206.

[3] M. Saliba, T. Matsui, J.-Y. Seo, K. Domanski, J.-P. Correa-Baena, M. K. Nazeeruddin, S. M. Zakeeruddin, W. Tress, A. Abate, A. Hagfeldt, M. Gratzel, *Energy. Environ. Sci.* **2016**, *9*, 1989.

[4] J.-W. Lee, D.-H. Kim, H.-S. Kim, S.-W. Seo, S. M. Cho, N.-G. Park, *Adv. Energy Mater.* **2015**, *5*, 1501310.

[5] Z. Li, M. Yang, J.-S. Park, S.-H. Wei, J. J. Berry, K. Zhu, *Chem. Mater.* **2016**, *28*, 284.

[6] T. Duong, H. K. Mulmudi, H. Shen, Y. Wu, C. Barugkin, Y. O. Mayon, H. T. Nguyen, D. Macdonald, J. Peng, M. Lockrey, W. Li, Y.-B. Cheng, T. P. White, K. Weber, K. Catchpole, *Nano Energy* **2016**, *30*, 330.

[7] C. Yi, J. Luo, S. Meloni, A. Boziki, N. Ashari-Astani, C. Gratzel, S. M. Zakeeruddin, U. Rothlisberger, M. Gratzel, *Energy. Environ. Sci.* **2016**, *9*, 656.

[8] T. Liu, Y. Zong, Y. Zhou, M. Yang, Z. Li, O. S. Game, K. Zhu, R. Zhu, Q. Gong, N. P. Padture, *Chem. Mater.* **2017**, *29*, 3246.

[9] A. Binek, F. C. Hanusch, P. Docampo, T. Bein, *J. Phys. Chem. Lett.* **2015**, *6*, 1249.

[10] L.-Q. Xie, L. Chen, Z.-A. Nan, H.-X. Lin, T. Wang, D.-P. Zhan, J.-W. Yan, B.-W. Mao, Z.-Q. Tian, *J. Am. Chem. Soc.* **2017**, *139*, 3320.

[11] D. P. McMeekin, G. Sadoughi, W. Rehman, G. E. Eperon, M. Saliba, M. T. Hörantner, A. Haghighirad, N. Sakai, L. Korte, B. Rech, M. B. Johnston, L. M. Herz, H. J. Snaith, *Science* **2016**, *351*, 151.

[12] Y. Chang, L. Wang, J. Zhang, Z. Zhou, C. Li, B. Chen, L. Etgar, G. Cui, S. Pang, *J. Mater. Chem. A* **2017**, *5*, 4803.

[13] T. Duong, Y. Wu, H. Shen, J. Peng, X. Fu, D. Jacobs, E.-C. Wang, T. C. Kho, K. C. Fong, M. Stocks, E. Franklin, A. Blakers, N. Zin, K. McIntosh, W. Li, Y.-B. Cheng, T. P. White, K. Weber, K. Catchpole, *Adv. Energy Mater.* **2017**, *7*, 1700228.

[14] D. P. McMeekin, Z. Wang, W. Rehman, F. Pulvirenti, J. B. Patel, N. K. Noel, M. B. Johnston, S. R. Marder, L. M. Herz, H. J. Snaith, *Adv. Mater.* **2017**, 1607039.

[15] Y. H. Park, I. Jeong, S. Bae, H. J. Son, P. Lee, J. Lee, C.-H. Lee, M. J. Ko, *Adv. Funct. Mater.* **2017**, 1605988.

[16] M. Zhang, J. S. Yun, Q. Ma, J. Zheng, C. F. J. Lau, X. Deng, J. Kim, D. Kim, J. Seidel, M. A. Green, S. Huang, A. W. Y. Ho-Baillie, *ACS Energy Lett.* **2017**, 438.

[17] Y. Hu, M. F. Aygüler, M. L. Petrus, T. Bein, P. Docampo, *ACS Energy Lett.* **2017**, 2212.

[18] M. L. Petrus, Y. Hu, D. Moia, P. Calado, A. M. A. Leguy, P. R. F. Barnes, P. Docampo, *ChemSusChem* **2016**, *9*, 2699.

[19] Q. Chen, H. Zhou, T.-B. Song, S. Luo, Z. Hong, H.-S. Duan, L. Dou, Y. Liu, Y. Yang, *Nano Lett.* **2014**, *14*, 4158.

[20] C. Roldan-Carmona, P. Gratia, I. Zimmermann, G. Grancini, P. Gao, M. Graetzel, M. K. Nazeeruddin, *Energy. Environ. Sci.* **2015**, *8*, 3550.

[21] I. Grill, K. Handloser, F. C. Hanusch, N. Giesbrecht, T. Bein, P. Docampo, M. Handloser, A. Hartschuh, *Sol. Energy Mater. Sol. Cells* **2017**, *166*, 269.

[22] H. D. Kim, H. Ohkita, H. Benten, S. Ito, *Adv. Mater.* **2016**, *28*, 917.

[23] E. M. Hutter, G. E. Eperon, S. D. Stranks, T. J. Savenije, *J. Phys. Chem. Lett.* **2015**, *6*, 3082.

[24] S. D. Stranks, V. M. Burlakov, T. Leijtens, J. M. Ball, A. Goriely, H. J. Snaith, *Phys. Rev. Appl.* **2014**, *2*, 034007.

[25] E. M. Hutter, J.-J. Hofman, M. L. Petrus, M. Moes, R. D. Abellón, P. Docampo, T. J. Savenije, *Adv. Energy Mater.* **2017**, *7*, 1602349.

[26] J. M. Richter, M. Abdi-Jalebi, A. Sadhanala, M. Tabachnyk, J. P. H. Rivett, L. M. Pazos-Outón, K. C. Gödel, M. Price, F. Deschler, R. H. Friend, **2016**, *7*, 13941.

[27] E. M. Hutter, M. C. Gelvez-Rueda, A. Osherov, V. Bulovic, F. C. Grozema, S. D. Stranks, T. J. Savenije, *Nat Mater* **2017**, *16*, 115.

[28] L. M. Pazos-Outón, M. Szumilo, R. Lamboll, J. M. Richter, M. Crespo-Quesada, M. Abdi-Jalebi, H. J. Beeson, M. Vrućinić, M. Alsari, H. J. Snaith, B. Ehrler, R. H. Friend, F. Deschler, *Science* **2016**, *351*, 1430.

[29] A. Baumann, S. Väth, P. Rieder, M. C. Heiber, K. Tvingstedt, V. Dyakonov, *J. Phys. Chem. Lett.* **2015**, *6*, 2350.

[30] G. F. J. Garlick, A. F. Gibson, *Proceedings of the Physical Society* **1948**, *60*, 574.

[31] W. Graupner, G. Leditzky, G. Leising, U. Scherf, *Phys. Rev. B* **1996**, *54*, 7610.

[32] A. Kadashchuk, R. Schmechel, H. v. Seggern, U. Scherf, A. Vakhnin, *J. Appl. Phys.* **2005**, *98*, 024101.

[33] R. Alexander, E. C. F. Ko, Y. C. Mac, A. J. Parker, *J. Am. Chem. Soc.* **1967**, *89*, 3703.

[34] R. Hamaguchi, M. Yoshizawa-Fujita, T. Miyasaka, H. Kunugita, K. Ema, Y. Takeoka, M. Rikukawa, *Chem. Commun.* **2017**, *53*, 4366.

[35] R. E. Beal, D. J. Slotcavage, T. Leijtens, A. R. Bowring, R. A. Belisle, W. H. Nguyen, G. F. Burkhard, E. T. Hoke, M. D. McGehee, *J. Phys. Chem. Lett.* **2016**, *7*, 746.

[36] P. Gratia, I. Zimmermann, P. Schouwink, J.-H. Yum, J.-N. Audinot, K. Sivula, T. Wirtz, M. K. Nazeeruddin, *ACS Energy Lett.* **2017**, 2686.

[37] H.-S. Kim, N.-G. Park, *J. Phys. Chem. Lett.* **2014**, *5*, 2927.

[38] D. J. Kubicki, D. Prochowicz, A. Hofstetter, S. M. Zakeeruddin, M. Grätzel, L. Emsley, *J. Am. Chem. Soc.* **2017**, *139*, 14173.

[39] P. Calado, A. M. Telford, D. Bryant, X. Li, J. Nelson, B. C. O'Regan, P. R. F. Barnes, *Nat. Commun.* **2016**, *7*, 13831.

[40] B. Philippe, M. Saliba, J.-P. Correa-Baena, U. B. Cappel, S.-H. Turren-Cruz, M. Grätzel, A. Hagfeldt, H. Rensmo, *Chem. Mater.* **2017**, *29*, 3589.

[41] A. Albadri, P. Yadav, M. Alotaibi, N. Arora, A. Alyamani, H. Albrithen, M. I. Dar, S. M. Zakeeruddin, M. Grätzel, *J. Phys. Chem. C* **2017**, *121*, 24903.

[42] Y. Guo, C. Li, X. Li, Y. Niu, S. Hou, F. Wang, *J. Phys. Chem. C* **2017**, *121*, 12711.

6 Moisture stability of multiple-cation mixed-halide perovskites

This chapter is based on the following publication:

Y. Hu, M. F. Aygüler, M. L. Petrus, T. Bein, P. Docampo, Impact of Rubidium and Cesium Cations on the Moisture Stability of Multiple-Cation Mixed-Halide Perovskites. *ACS Energy Lett.* **2017**, *2*, 2212-2218. (DOI: 10.1021/acsenergylett.7b00731)

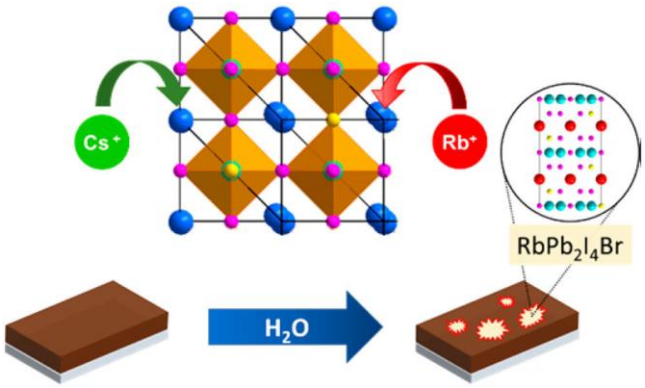

Adapted with permission.[1] Copyright 2017, American Chemical Society.

6.1 Abstract

Rubidium and cesium cations have been recently identified as enhancers for perovskite solar cell performance. However, the impact of these inorganic cations on the stability of the $(FA_{0.83}MA_{0.17})Pb(I_{0.83}Br_{0.17})_3$ perovskite crystal lattice has not been fully understood yet. Here, we show via *in situ* XRD and EDX measurements that the unsuitably small ionic radius of Rb^+ can lead to several non-photoactive side-products. During the perovskite film synthesis, $RbPb(I_{1-x}Br_x)_3$ is formed, while exposure to humid air leads to the rapid formation of another hitherto unreported side phase ($RbPb_2I_4Br$). The formation of the Rb-rich side phases does not only result in a loss of light absorption, but also extracts bromide ions from the photoactive perovskite phase, thereby reducing its band gap. In comparison, the moisture-assisted formation of a $CsPb_2I_4Br$ phase upon Cs-addition occurs on a significantly longer timescale than its Rb analog. While the incorporation of Cs^+ remains attractive for high-performance solar cells, the severe moisture-sensitivity of Rb-containing mixed-halide perovskites may create additional engineering challenges.

6.2 Introduction

Recently, inorganic cations such as rubidium and cesium have been reported as performance enhancers in the burgeoning field of perovskite solar cells, both in terms of power conversion efficiency (PCE) and device stability.[2-10] An impressive improvement in open-circuit voltage (V_{oc}) was achieved through the addition of RbI and CsI to the multiple-cation mixed-halide $(FA_{0.83}MA_{0.17})Pb(I_{0.83}Br_{0.17})_3$ perovskite, reaching stabilized efficiencies of up to 21.6%.[5, 7] Mixing organic cations such as formamidinium (FA) or methylammonium (MA) with small amounts of Rb^+ or Cs^+ cations can lead to a more favorable tolerance factor which facilitates the stabilization of the photoactive perovskite phase in a broad temperature range,[4] resulting in devices stable at 85 °C for 500 h under continuous illumination and maximum power tracking.[7] Yet, the complexity of the interplay between the different cations and halides increases significantly with every additional component that takes part in the perovskite formation. Therefore, the role of Rb^+ and Cs^+ cations within the perovskite's structure and their impact on the stability and optoelectronic properties are still under debate.

A simple, empirical measure for the stability of ABX_3 perovskite structures is Goldschmidt's tolerance factor:[11]

$$t = \frac{r_A + r_X}{\sqrt{2}\,(r_B + r_X)} \qquad (6.1)$$

with *r* being the ionic radius of each respective ion. Ionic compounds with a tolerance factor within the range between 0.8 and 1.0 are considered to be stable in a classical perovskite structure. For $CsPbI_3$ (t = 0.81), the tolerance factor suggests that Cs^+ can stabilize a classical perovskite structure consisting of corner-sharing lead-iodide octahedra.[4, 12, 13] Indeed, $CsPbI_3$ is known to undergo a phase transition from a room-temperature yellow phase into a black perovskite-type phase at 360 °C.[13-15] Upon Cs-insertion into $(FA_{0.83}MA_{0.17})Pb(I_{0.83}Br_{0.17})_3$, a contraction of the perovskite crystal lattice can be expected due to the significantly smaller ionic radius of Cs^+ (167 pm) compared to FA^+ (~253 pm) and MA^+ (~217 pm) cations.[16] In contrast, $RbPbI_3$ achieves a lower tolerance factor of t = 0.77 which indicates that Rb^+ (152 pm) is too small to stabilize this perovskite lattice, but instead leads to the formation of non-perovskite structures.[6, 7] Furthermore, unlike its Cs-based counterpart, $RbPbI_3$ does not undergo a phase transition to a black perovskite structure at elevated temperatures.[3, 17] Hence, the interaction of Cs^+ and Rb^+ with the iodide-dominated perovskite structure is potentially very different.

Understanding the effect of inorganic cations on the perovskite crystal lattice is not only crucial to boost solar cell performance, but also to eliminate potential degradation pathways. In this work, we elucidated the influence of Rb^+ and Cs^+ on the crystal structure of the state-of-the-art $(FA_{0.83}MA_{0.17})Pb(I_{0.83}Br_{0.17})_3$ hybrid perovskite compound. Furthermore, we investigated the impact of the inorganic cation additives on the perovskite's moisture stability and the resulting effects on solar cell performance. In particular, we show that the addition of Rb^+ to an iodide-bromide mixed-halide perovskite strongly affects the robustness of the perovskite phase toward humidity.

6.3 Results and discussion

We synthesized the perovskite composition employed in state-of-the-art photovoltaic devices $(FA_{0.83}MA_{0.17})Pb(I_{0.83}Br_{0.17})_3$ (FAMA), and added a defined amount of RbI or/and CsI according to a protocol reported by Saliba *et al*.[7] We denote the samples as Rbx, Csx and CsxRbx, with x being the percentage of Cs^+ or Rb^+ among the monovalent cations.

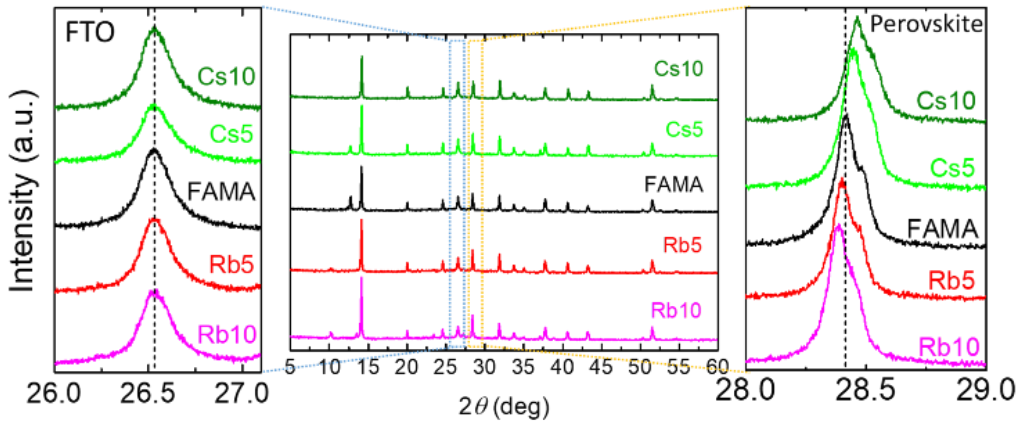

Figure 6.1 XRD patterns of multiple-cation mixed-halide perovskite films on glass/FTO/compact TiO_2 substrates upon addition of different amounts of RbI and CsI to the perovskite precursor solution. FAMA represents $(FA_{0.83}MA_{0.17})Pb(I_{0.83}Br_{0.17})_3$ and Csx (Rbx) refers to samples with the approximate molar percentage x of Cs^+ (Rb^+).

When it comes to the influence of the inorganic cations on the crystallization of the perovskite, one important question arises: Are Cs^+ and Rb^+ cations incorporated into the perovskite structure? Modifications of the perovskite lattice dimensions upon addition of inorganic cations can be deduced from a shift in the X-ray diffraction (XRD) peaks of the perovskite phase.[4, 7] To reveal this effect, we determined the exact XRD peak position of the (220) reflection for the FAMA perovskite film and compared it to samples with different amounts of added RbI and CsI (Figure 6.1). By using the (110) reflection of the FTO-glass substrate at $2\theta = 26.53°$ as a reference peak, we can exclude a misalignment of the experimental stage height as an origin for any XRD peak shift. Upon Cs-addition to FAMA, we observe that the reflection of the pristine FAMA perovskite phase at $2\theta = 28.41°$ shifts to larger diffraction angles for Cs5 (28.45°) and even further for Cs10 (28.47°). This finding is in agreement with previous reports[4, 5, 18] and can be interpreted as evidence for the inclusion of Cs^+ into the perovskite structure, therefore leading to a shrinkage of the perovskite lattice. As expected, the higher the Cs^+ concentration is in the perovskite precursor solution, the more pronounced is the shift to higher angles in the XRD pattern, and the larger is the contraction of the perovskite lattice. However, even more remarkable is the peak shift to lower angles observed for Rb5 ($2\theta = 28.40°$) and Rb10 ($2\theta = 28.38°$), which indicates an expansion of the perovskite lattice compared to FAMA. The same trend is also visible in a shift of the main perovskite peak around 14.1°, which is shown in Figure 6.2. Considering that Rb^+ has an even smaller ionic radius compared to Cs^+, we would expect an even stronger lattice contraction. Therefore, one can conclude that Rb^+ is not fully incorporated into the perovskite structure in contrast to Cs^+, although this does not explain the observed expansion of the crystal lattice.

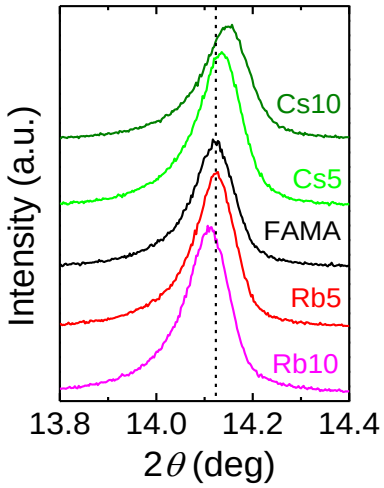

Figure 6.2 Magnified XRD patterns of perovskite films on FTO-glass substrates showing the peak shift for the main perovskite peak upon CsI and RbI addition. The dotted black line indicates the position of the peak maximum for FAMA. Cs-induced peak shift towards larger diffraction angles indicates lattice contraction, while Rb-induced peak shift towards smaller angles indicates lattice expansion.

In order to understand the shift to a lower angle of the perovskite lattice upon addition of Rb^+, we must look into the formation of the Rb-rich side phases. The XRD patterns of Rb5 and Rb10 exhibit an additional double peak at 2θ = 10.16° and 10.29°, which is more prominent for Rb10. This is typically assigned to the yellow orthorhombic, non-perovskite $RbPbI_3$ phase.[2, 3, 17, 19] However, we found that the characteristic (110) and (020) reflections of a freshly synthesized $RbPbI_3$ film are located at 10.03° and 10.20°, respectively (Figure 6.3). Hence, the XRD reflections originating from the side phases in the Rb5 and Rb10 samples belong to a smaller lattice than the pure iodide compound $RbPbI_3$. Since the casting solution contains a mixture of I^- and Br^-, it is reasonable to propose that the Rb-rich side phase is a mixed-halide structure of the form $RbPb(I_{1-x}Br_x)_3$. An estimated Br-content of $x \approx 0.16$ was found for the Rb-rich side phase in Rb10 and Rb5 by analyzing the XRD peak shift in spin-coated films from $RbPb(I_{1-x}Br_x)_3$ solutions with varying x (Figure 6.3). We note that this value corresponds to the approximate initial Br:I ratio in the perovskite precursor solution.

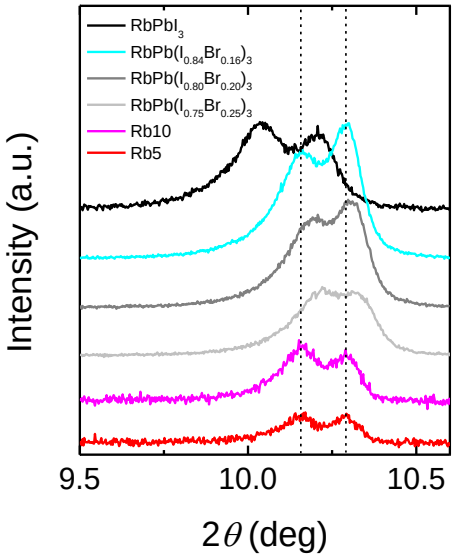

Figure 6.3 Magnified view on the XRD patterns of Rb5 and Rb10 compared to $RbPb(I_{1-x}Br_x)_3$ films on FTO-glass substrates. The dotted black lines indicate the positions of the peak maxima found in Rb5 and Rb10. The peak positions for the side phase formed in Rb5 and Rb10 upon perovskite formation are in well agreement with the $RbPb(I_{0.84}Br_{0.16})_3$ compound.

Compared to I^- ions (220 pm), the smaller Br^- ions (196 pm) have a higher compatibility of ionic radius in combination with Rb^+, resulting in a slightly higher tolerance factor (t = 0.78) and the existence of a high-temperature $RbPbBr_3$ perovskite phase.[20] This affinity between Rb^+ and Br^- can have an enormous impact on the composition and the stability of multiple-cation mixed-halide perovskite compounds. When the Rb-concentration is as high as 10% in Rb10, the formation of the $RbPb(I_{0.84}Br_{0.16})_3$ phase has leached a sufficiently large amount of bromide away from the perovskite lattice, such that an effective expansion of the (now I-rich) perovskite structure occurs, explaining the shift of its XRD main peak to a lower angle. Figure 6.4 represents a schematic illustration of the effect of CsI and RbI addition on the lattice dimensions of the FAMA perovskite phase. Our hypothesis is perfectly consistent with previous observations by Duong *et al.*[6] The latter authors also report a systematic red shift of both the photoluminescence peak and the absorption onset of the mixed-halide perovskite upon increased Rb-concentration, which can be related to a reduction of the Br-content within the perovskite through $RbPb(I_{0.84}Br_{0.16})_3$ formation. In contrast, due to the more suitable size of the Cs^+ ion to be incorporated into the perovskite lattice, neither Cs5 nor Cs10 exhibit a comparable side phase resulting from phase segregation.

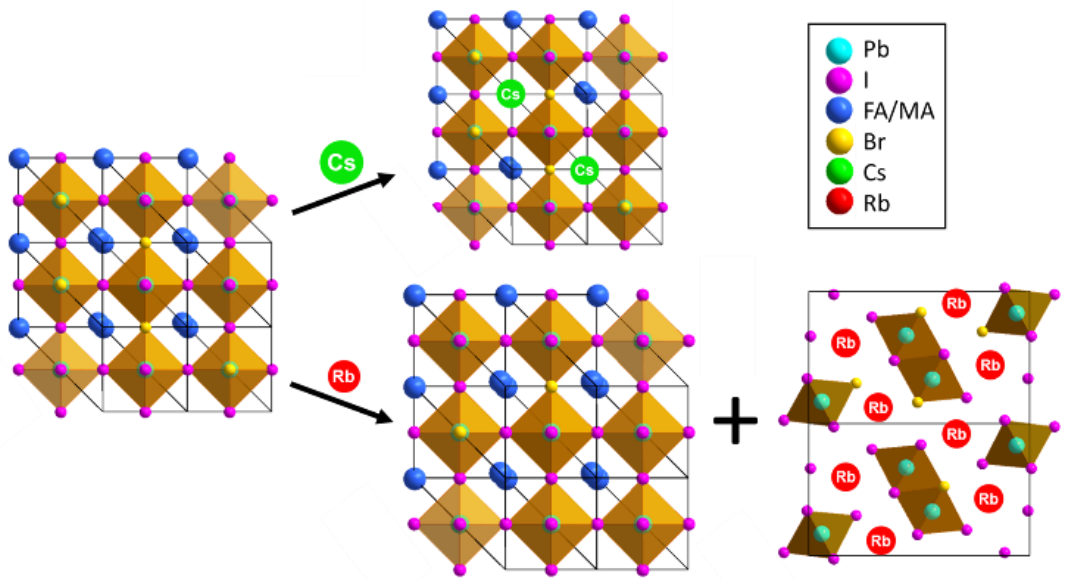

Figure 6.4 Schematic illustration of the effect of RbI and CsI addition on the multiple-cation mixed-halide perovskite structure. Lattice contraction by incorporation of Cs^+ cations into the perovskite structure versus lattice expansion due to Br-extraction from the perovskite structure and formation of an Rb- and Br-rich non-perovskite side phase $RbPb(I_{1-x}Br_x)_3$.

The instability of the perovskite lattice upon Rb-inclusion is further highlighted by exposing the perovskite films to humid air. Here, we performed *in situ* XRD measurements on FAMA, Cs5, Rb5 and Rb5Cs5 films upon exposure to air at 75% relative humidity (RH) to determine the degradation products. In order to exclude the influence of ambient light on the degradation process,[21] the humidity studies were conducted in the dark. Figure 6.5a–d depict the evolution of the XRD patterns for each sample prepared on glass substrates over a period of 60 min. Both FAMA and Cs5 show minor signs of degradation after 60 min, visible in a slightly increased PbI_2 peak at $2\theta = 12.7°$. In contrast, a strong reflection at 11.4° emerges for the Rb5 and the Rb5Cs5 film after only 15 min, and additional reflections at 22.9°, 34.7° and 46.8° appear upon longer exposure times.

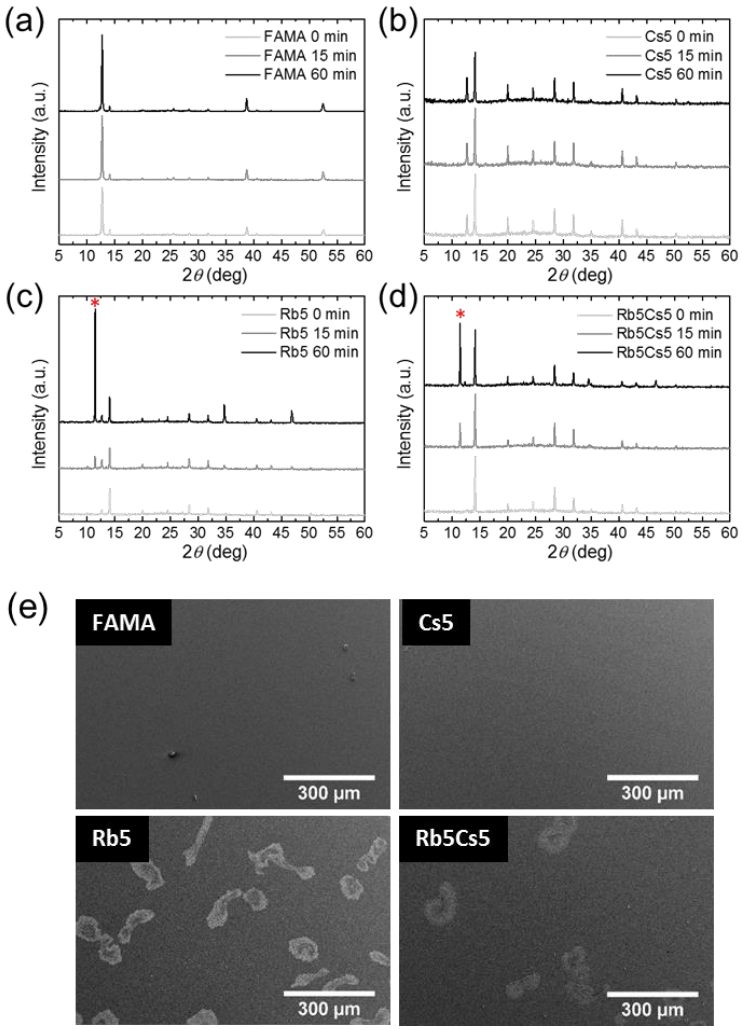

Figure 6.5 XRD patterns of (a) FAMA, (b) Cs5, (c) Rb5 and (d) Rb5Cs5 perovskite films on glass under *in situ* exposure to air at 75% RH over a course of 60 min. The most intense diffraction peak assigned to the moisture-induced degradation product for the Rb-containing samples is marked with a red asterisk. (e) SEM top-view images of perovskite films on glass/FTO/TiO_2 after exposure to humid air with 90% RH for 20 h.

These additional diffraction peaks can also be found at lower or higher humidity levels (Figure 6.6a) and are accompanied by the formation of transparent spots on the dark brown perovskite films that can be seen with the bare eye. Top-view SEM images of Rb5 and Rb5Cs5 films on FTO/TiO_2 substrates reveal the presence of irregularly shaped, bright areas (~100 µm in diameter) after exposing the samples to 90% RH for 20 h (Figure 6.5e). In comparison, FAMA and Cs5 do not show such inhomogeneity under the same conditions. Only after longer exposure times of 5 days, the Cs5 film exhibited some transparent imperfections and the corresponding XRD pattern showed a set of additional reflections at 2θ = 11.2°, 33.9° and 45.7° (Figure 6.6b), similar to the degradation product found on the Rb-containing samples.

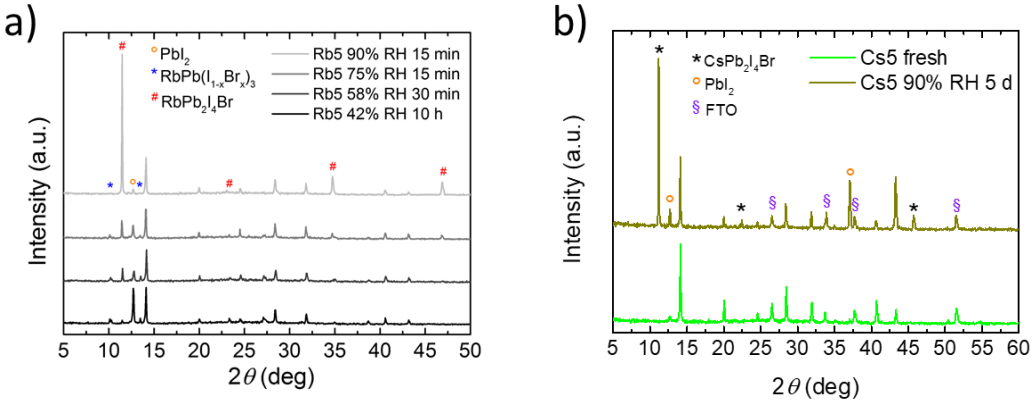

Figure 6.6 (a) XRD patterns of Rb5 films on glass upon exposure to different humidity levels in air. The diffraction peaks assigned to the $RbPb_2I_4Br$ side phase appear after different exposure times. (b) Cs5 perovskite film on FTO/TiO_2 before and after exposure to 90% RH for 5 days.

To understand the mechanism that induces the phase segregation within the perovskite films upon exposure to moisture, it is crucial to determine the chemical composition of the degradation products. Energy dispersive X-ray (EDX) spectroscopy is a powerful tool to assess the chemical composition of thin films with a µm-range spatial resolution. We determined the elemental composition of intact areas and, if present, phase separated ("degraded") areas for each perovskite sample by EDX measurements to identify the moisture-induced degradation products (Table 6.1). SEM images of the evaluated sample areas and EDX spectra are provided in Figure 6.7 and Figure 6.8.

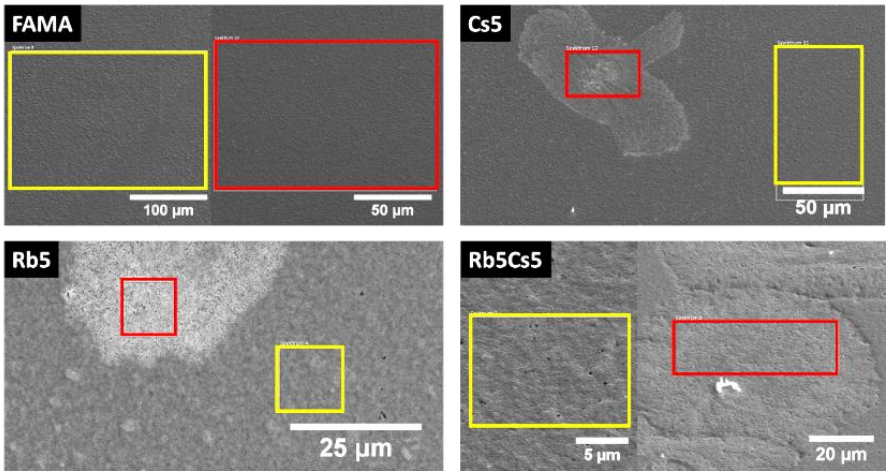

Figure 6.7 SEM top-view images of FAMA, Cs5, Rb5 and RbCs5 perovskite films and the evaluated areas for EDX elemental analysis of the intact (yellow) and degraded (red) areas.

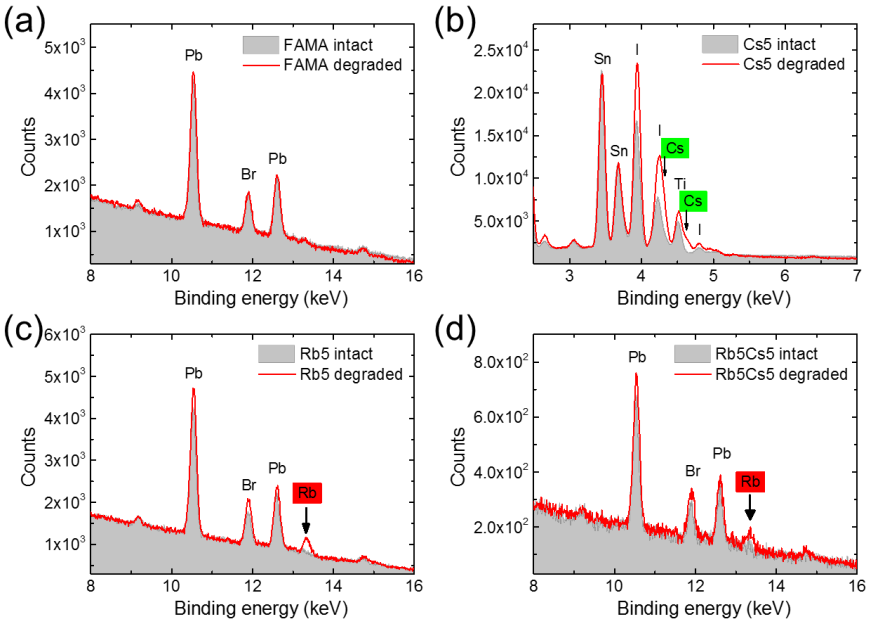

Figure 6.8 EDX spectra of the intact and degraded areas for (a) FAMA, (b) Cs5, (c) Rb5 and (d) Rb5Cs5 films after exposure to 90% RH.

Table 6.1 SEM-EDX elemental analysis of intact and phase separated areas of FAMA, Cs5, Rb5 and Rb5Cs5 perovskite films on FTO/TiO_2. The films were exposed to 90% RH in air at room temperature in the dark. The elemental composition is given in atomic percentage (at%).

Sample	Cs [at%]	Rb [at%]	Pb [at%]	I [at%]	Br [at%]
FAMA intact	-	-	26	61	13
FAMA degraded	-	-	26	61	13
Cs5 intact	2	-	25	60	13
Cs5 degraded	10	-	25	50	14
Rb5 intact	-	0	25	63	12
Rb5 degraded	-	14	24	50	12
Rb5Cs5 intact	2	0	24	61	13
Rb5Cs5 degraded	3	12	24	48	13

Table 6.1 shows that all samples exhibit a comparable Pb:I:Br ratio in their intact areas, corresponding to the precursor stoichiometry used in the perovskite solution. After exposure to 90% RH for 2 days, FAMA does not change its elemental stoichiometry and no apparent phase segregation is observed. However, we found significant differences between the elemental composition of the intact and the degraded areas of Rb5 and Rb5Cs5 after the moisture-induced phase segregation after

20 h. Compared to the intact areas, the degraded areas of Rb-containing samples show to be Rb- and Br-rich. More specifically, the Rb-content is increased from ~0% to 12–14% and the I-content is decreased from ~60% to ~50% in the degraded areas of Rb5 and Rb5Cs5, while the Br-content was constant (~13%). After a significantly longer exposure time of 5 days, the degraded areas in the Cs5 sample showed a Cs- and Br-rich phase segregation product with a comparable chemical composition as the one found in the Rb-containing perovskites. We note that, similar to $RbPb(I_{1-x}Br_x)_3$, the moisture-mediated formation of the Br-rich phase with either CsI or RbI replaces a significant amount of bromide the perovskite lattice with iodide, leading to a noticeable shift of the XRD peak to lower angles (Figure 6.9). Another indication for the loss of bromide within the perovskite structure after hydration of Rb5 and Rb5Cs5 is a decreased band gap of the perovskite phase, as revealed by the corresponding Tauc plots (Figure 6.10).

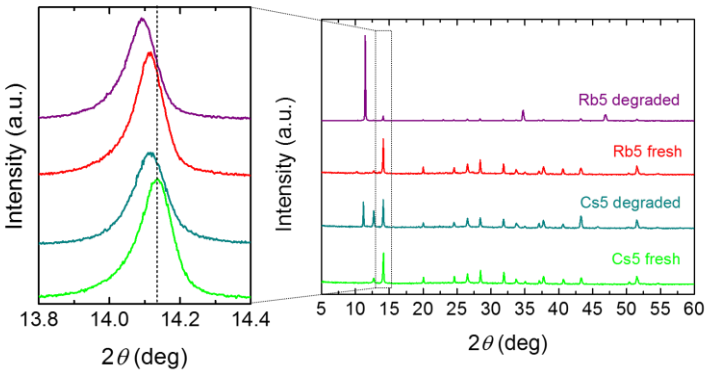

Figure 6.9 XRD patterns of fresh Cs5 and Rb5 samples compared to degraded samples after exposure to 90% RH. The magnified view (left) shows the peak shift towards smaller diffraction angles for the perovskite main peak in both samples upon moisture-induced phase segregation. The dotted black line indicates the position of the peak maximum for a fresh Cs5 sample.

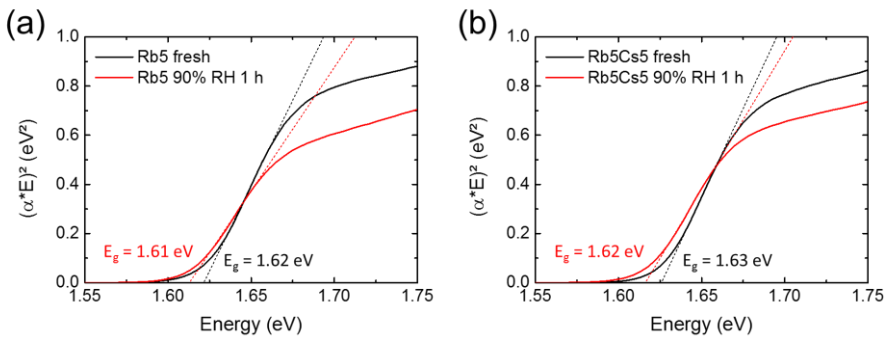

Figure 6.10 Tauc plots for (a) Rb5 and (b) Rb5Cs5 films on glass before and after exposure to 90% RH for 1 h.

Using the atomic composition determined for the degraded areas in Rb5, Rb5Cs5 and Cs5 from our EDX measurements (Table 6.1), we propose the chemical formula "$RbPb_2I_4Br$" and "$CsPb_2I_4Br$" for the phase segregation products. We suggest that these hitherto unreported crystal phases can be derived from the known compounds $RbPb_2Br_5$ and $CsPb_2Br_5$ by partially substituting bromide for iodide. The tetragonal crystal phase of $RbPb_2Br_5$ and $CsPb_2Br_5$ were first synthesized and characterized by Wells, obtained from the reaction of RbBr or CsBr with 2 equivalents of $PbBr_2$.[22-24] The reported transparency and water-stability of $RbPb_2Br_5$ and $CsPb_2Br_5$ crystals are in accordance with the properties we found for the moisture-induced phase segregation products in Rb5, Rb5Cs5 and Cs5.

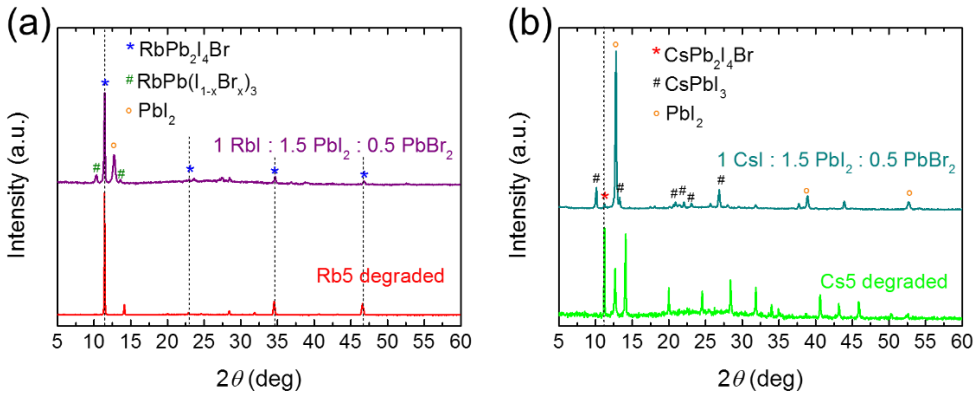

Figure 6.11 (a) XRD patterns of a degraded Rb5 film showing moisture-induced phase segregation compared to a film obtained from a precursor solution with $RbI:PbI_2:PbBr_2$ in a molar stoichiometry of 1:1.5:0.5. (b) XRD patterns of a degraded Cs5 film compared to a film obtained from a solution with $CsI:PbI_2:PbBr_2$ = 1:1.5:0.5. The dotted black lines indicates the peak positions of $RbPb_2I_4Br$ in (a) and $CsPb_2I_4Br$ in (b), respectively.

In order to verify the proposed formula $RbPb_2I_4Br$ (and $CsPb_2I_4Br$) derived from our EDX data, we spin-coated films derived from precursor solutions with the corresponding stoichiometry of RbI (CsI):PbI_2:$PbBr_2$ = 1:1.5:0.5. Strikingly, the XRD patterns of the resulting films exhibit exactly the same reflection at 2θ = 11.45° (11.20°) that is found for hydrated Rb5 (Cs5) samples, as shown in Figure 6.11. Thus, our proposed chemical formula for $RbPb_2I_4Br$ and $CsPb_2I_4Br$ are confirmed. As shown in previous moisture-stability studies, the presence of water molecules can significantly facilitate a reorganization and recrystallization of the perovskite grains.[25] Therefore, moisture can promote rapid phase segregation within the perovskite film under the formation of thermodynamically more favorable products. The spontaneous crystallization of $RbPb_2I_4Br$ simply

from a stoichiometric precursor solution even without the aid of water indicates a strong driving force towards the formation of this compound. A schematic illustration of our proposed degradation route for Rb-containing FAMA perovskite films is depicted in Figure 6.12.

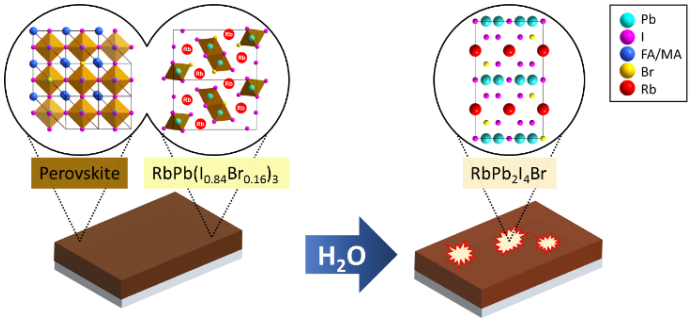

Figure 6.12 Schematic illustration of the moisture-induced degradation of Rb-containing multi-cation mixed-halide perovskite films.

It is important to note that the segregation of the $CsPb_2I_4Br$ phase takes place during a significantly longer timescale than $RbPb_2I_4Br$. Moreover, the $CsPb_2I_4Br$ phase was not observed in Rb5Cs5 samples after 20 h at 90% RH despite of the Rb:Cs ratio of 1:1, indicating that it is Rb^+ that induces rapid phase segregation first when water can act as a mediator. In the absence of bromide, degradation only took place with the emergence of $RbPbI_3$, PbI_2 and the yellow δ-phase of formamidinium lead iodide (Figure 6.13).[26] This observation provides further evidence for the strong affinity of Rb^+ to Br^- as discussed above regarding the $RbPb(I_{1-x}Br_x)_3$ formation.

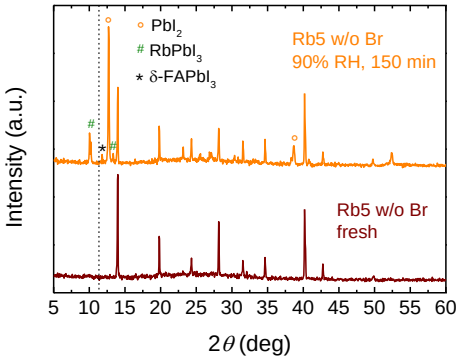

Figure 6.13 XRD patterns of iodide-only Rb5 perovskite films without bromide in the precursor solution before and after exposure to 90% RH. The dotted black line indicates the peak position of the $RbPb_2I_4Br$ phase. No $RbPb_2I_4Br$ is formed in the absence of bromide in the Rb5 precursor solution.

To investigate the effect of moisture-induced $RbPb_2I_4Br$ formation on the photovoltaic performance of perovskite solar cells, we fabricated devices with the architecture glass/FTO/TiO_2/perovskite/spiro-OMeTAD/Au. A full experimental description of the device fabrication and current-voltage (*J-V*) characterization are given in the Methods section. The as-prepared solar cells all show high performance with power conversion efficiency (PCE) values up to 17.75%. The corresponding *J-V* curves and the stabilized power output are displayed in Figure 6.14. We stored the unencapsulated devices (24 cells for each type of perovskite) in a humidity chamber with controlled 75% RH at room temperature and monitored the average PCE and short-circuit current density (J_{sc}) of the solar cells over 10 days.

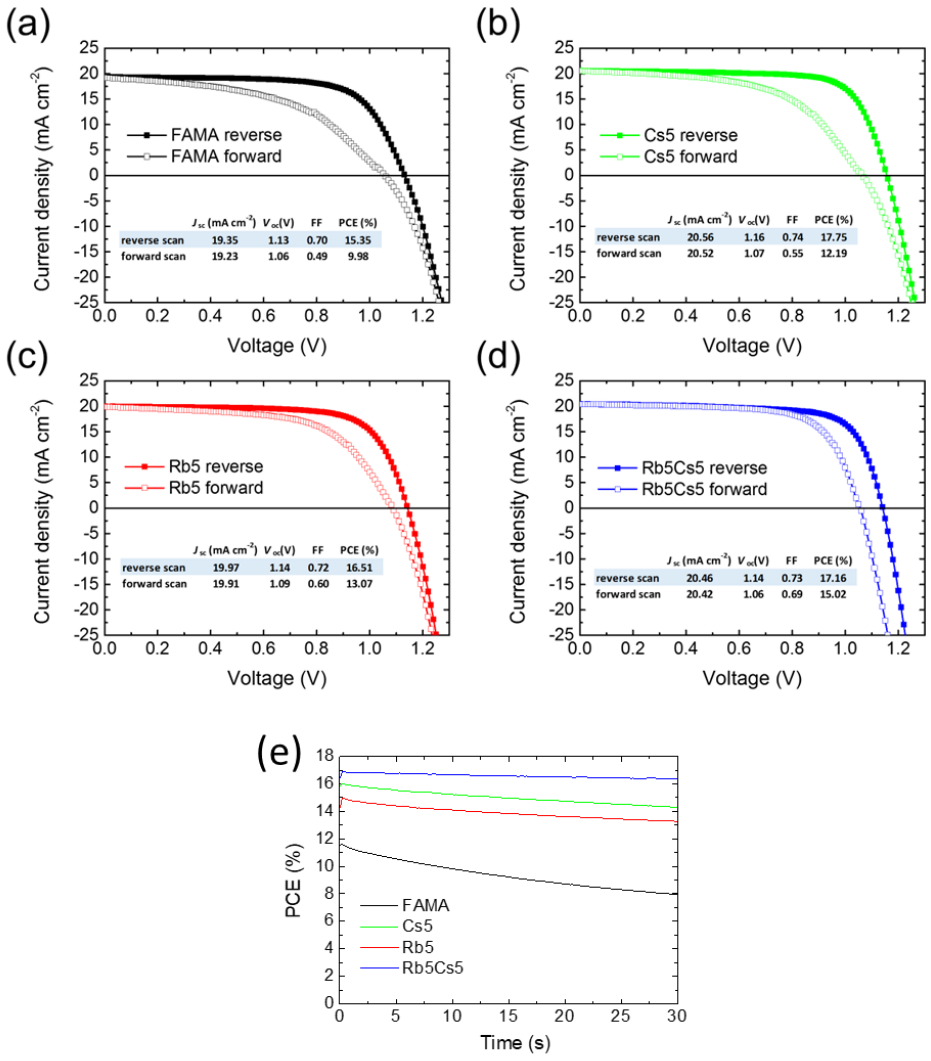

Figure 6.14 *J-V* curves for (a) FAMA, (b) Cs5, (c) Rb5 and (d) Rb5Cs5 champion devices under AM 1.5G illumination, recorded at a scan rate of 0.1 V s^{-1}. (e) Maximum power point tracking for the champion perovskite solar cells with the device architecture glass/FTO/compact TiO_2/perovskite/spiro-OMeTAD/Au under AM 1.5G illumination in air.

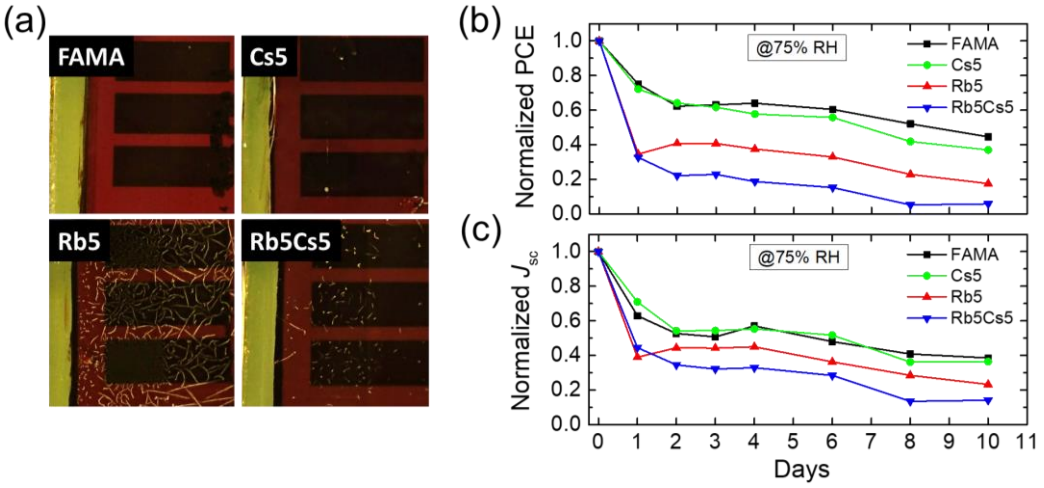

Figure 6.15 Moisture stability test on unencapsulated perovskite solar cells at 75% RH in air at room temperature in the dark. (a) Photographs of the devices after one day. (b) Evolution of the normalized power conversion efficiency and (c) short-circuit current density upon humidity exposure over a course of 10 days. 24 cell of each type of perovskite were tested and the efficiency values of each cell were obtained from *J-V* scans in the reverse direction with a scan rate of 0.2 V s^{-1}. The arithmetic means of the PCE and J_{sc} values were determined after a certain exposure time.

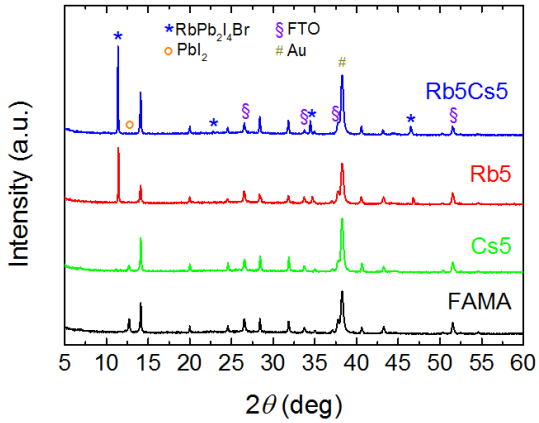

Figure 6.16 XRD patterns of unencapsulated perovskite solar cells after 1 day exposure to 75% RH at room temperature in the dark.

Figure 6.15a shows the appearance of transparent spots in the Rb5 and Rb5Cs5 samples after only one day, indicating advanced segregation of $RbPb_2I_4Br$ (as evidenced by XRD, see Figure 6.16). The partial transformation of the black perovskite phase into the $RbPb_2I_4Br$ phase leads to an irreversible loss of photoactive material. This is accompanied by a notable decrease in PCE already after one day

exposure to 75% RH for the Rb5 and Rb5Cs5 devices that can be linked to a loss of J_{sc} (Figure 6.15b–c). After 10 days, the Rb5 and Rb5Cs5 devices exhibit only ~18% and ~6% of their original average PCE values, respectively, compared to ~45% for FAMA and ~37% for Cs5. The further decreased performance of Rb5Cs5 compared to the Rb-only devices can be explained by the presence of Cs^+ in Rb5Cs5 films which enables additional degradation pathways through the formation of $CsPb_2I_4Br$. For the same reason, the Cs5 devices show a slightly larger decrease in photovoltaic performance than FAMA after more than 4 days at 75% RH. We observed the severe initial drop in PCE for Rb-containing solar cells also after one day at 58% RH (Figure 6.17a), indicating that device degradation through $RbPb_2I_4Br$ formation already takes place at a lower humidity level.

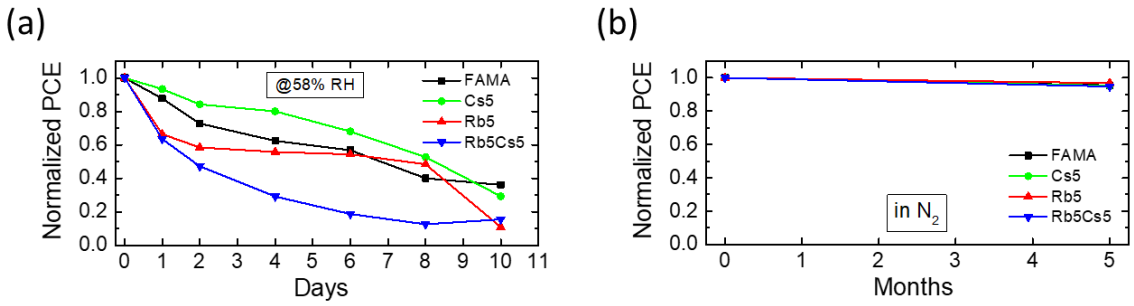

Figure 6.17 Monitoring the efficiency of unencapsulated perovskite solar cells (a) upon exposure to 58% RH at room temperature in the dark and (b) stored in a nitrogen-filled glovebox under exclusion of moisture at room temperature for 5 months. The reverse *J-V* scans of 20 cells under AM 1.5G illumination were evaluated for each type of perovskite and the arithmetic mean of the PCE values was determined over a course of 10 days. Scan rate: 0.2 V s^{-1}.

Our results demonstrate that moisture-induced phase segregation within the perovskite material can strongly affect the photovoltaic performance of perovskite solar cells, even before chemical decomposition of the perovskite (e.g. loss of the organic cations FA and MA) commences. We note that water plays a critical role as a mediator in the phase segregation process, since all devices stored under nitrogen at room temperature retain 95% of their initial performance even after 5 months (Figure 6.17b). Previous stability tests on Cs- and Rb-containing perovskite solar cells reported by Saliba *et al.* were conducted in the absence of water in a dry nitrogen atmosphere. Considering the different testing conditions, our results do not contradict the previously observed improvement in device stability through Cs- and Rb-addition.

6.4 Conclusion

In conclusion, the present study suggests that Cs^+ cations are incorporated into the multiple-cation mixed-halide $(FA_{0.83}MA_{0.17})Pb(I_{0.83}Br_{0.17})_3$ perovskite structure, leading to lattice contraction and stabilization of the photoactive perovskite phase. In contrast, RbI-addition induces the formation of non-photoactive, non-perovskite side phases such as $RbPb(I_{0.84}Br_{0.16})_3$ during film crystallization and $RbPb_2I_4Br$ upon moisture exposure. We assign the origin of the facile phase segregation could be the affinity between Rb and Br due to their more compatible ionic radii, which leads to thermodynamically more stable compounds than an iodide-based perovskite structure incorporating Rb. We demonstrate that the instability of Rb-containing mixed-halide perovskites opens up new degradation pathways through rapid phase segregation which can affect device performance before notable chemical decomposition of the perovskite takes place. Although device degradation upon exposure to humidity can be limited by encapsulation, low-cost deposition methods are generally performed under ambient conditions where the rapid phase segregation of the Rb-containing component, as described in this work, may already occur immediately after film deposition. Therefore, the severe moisture sensitivity of Rb-incorporating perovskites may create additional engineering challenges regarding the fabrication process for low-cost perovskite solar cells.

Furthermore, our results indicate that Rb^+ can cause a Br-deficiency in the mixed-halide perovskite structure via formation of the Br-rich side phases. Viewed from a more general perspective, our results have significant implications for photovoltaic applications using mixed-halide perovskite such as in tandem solar cells, where the desired band gap of the perovskite material is tailored by a defined halide ratio.[10] Therefore, we need to consider the choice of cations while taking into account the interplay between the different components for the perovskite formation. Directing the focus on both short-term and long-term device stability will be important for moving perovskite-based photovoltaics closer toward commercial applications.

6.5 Methods

Perovskite precursor solutions

The organic cation salts formamidinium iodide (FAI) and methylammonium bromide (MABr) were purchased from Dyesol, the lead halide compounds from TCI, CsI (99.9%) from Sigma-Aldrich and RbI from abcr GmbH. All chemicals were used without further purification.

FAMA: PbI_2 (508 mg, 1.1 mmol), $PbBr_2$ (80.7 mg, 0.22 mmol), FAI (171.97 mg, 1 mmol) and MABr (22.4 mg, 0.2 mmol) were dissolved in 800 µL of anhydrous DMF and 200 µL DMSO by heating the solution up to 100 °C. This non-stoichiometric $(FA_{0.83}MA_{0.17})Pb(I_{0.83}Br_{0.17})_3$ precursor solution contains a 10 mol% excess of PbI_2 and $PbBr_2$, respectively, which was introduced to enhance device performance. The FAMA solution was filtered through a 0.45 µm syringe filter before usage.

Cs5 and Cs10: CsI (389.7 mg, 1.5 mmol) was dissolved in 1 mL DMSO and filtrated through a 0.45 µm syringe filter, yielding an approximately 1.5 M CsI stock solution. To obtain the desired triple cation perovskite composition of approximately 5 mol% Cs, 42 µL of the CsI stock solution was added to 1 mL of the FAMA solution, yielding a nominal composition of $Cs_{0.05}[(FA_{0.83}MA_{0.17})]_{0.95}Pb(I_{0.83}Br_{0.17})_3$ for Cs5. The precursor solution for Cs10 was obtained by adding 84 µL of the CsI solution to 1 mL FAMA solution.

Rb5 and Rb10: RbI (318.5 mg, 1.5 mmol) was dissolved in 1 mL of a 4:1 (v/v) DMF:DMSO mixture and filtered through a 0.45 µm syringe filter. To obtain the nominal composition of $Rb_{0.05}[(FA_{0.83}MA_{0.17})]_{0.95}Pb(I_{0.83}Br_{0.17})_3$ with 5% Rb, 42 µL of the 1.5 M RbI stock solution was added to 1 mL of the FAMA solution. The precursor solution for Rb10 was obtained by adding 84 µL of the RbI solution to 1 mL of FAMA solution.

Rb5Cs5: To obtain the quadruple cation perovskite composition of 5% Rb and 5% Cs, 42 µL of the RbI stock solution and 42 µL of the CsI stock solution were added to 1 mL of FAMA solution, yielding a nominal composition of $Rb_{0.05}Cs_{0.05}[(FA_{0.83}MA_{0.17})]_{0.9}Pb(I_{0.83}Br_{0.17})_3$.

Film Synthesis

The deposition of the FAMA, Cs5, Rb5 and Rb5Cs5 perovskite layer was processed in a nitrogen-filled glovebox at 20–23 °C according to a similar protocol reported by Saliba *et al.*[7] The perovskite solution was deposited in a consecutive two-step spin-coating process at 1000 rpm and 4000 rpm for 10 s and 30 s, respectively. Approximately 20 s before the end of spinning, 500 µL of chlorobenzene (anhydrous, Sigma-Aldrich, 99.8%) was added to the film. The perovskite film formation was completed after annealing at 100 °C for 60 min on a hotplate.

To fabricate $RbPb(I_{1-x}Br_x)_3$ films, 1 M $RbPb(I_{1-x}Br_x)_3$ solutions with different Br-contents were prepared by dissolving RbI, $PbBr_2$ and PbI_2 in a 4:1 (v/v) DMF:DMSO mixture with the corresponding stoichiometry. For 1 mL solution, the amount of RbI (212.4 mg, 1 mmol) was held constant, while the $PbBr_2$:PbI_2 ratio was varied to obtain final Br-contents of approximately x = 0.16 (88.1 mg:350.4 mg), x = 0.20 (110.1 mg:322.7 mg) and x = 0.25 (137.6 mg:288.1 mg), respectively.

After dissolving the components at 100 °C, the same spin-coating procedure as for the perovskite films was conducted and the films were annealed at 100 °C for 60 min. Pale yellow films were obtained.

To reproduce the crystal phases $RbPb_2I_4Br$ found as products of moisture-induced phase separation in Rb5 and Rb5Cs5 samples, a stoichiometric solution of $RbI:PbI_2:PbBr_2$ = 1:1.5:0.5 was prepared. Therefore, RbI (106.18 mg, 0.5 mmol), PbI_2 (345.7 mg, 0.75 mmol) and $PbBr_2$ (91.75 mg, 0.25 mmol) were dissolved in 0.5 mL of a 4:1 (v/v) DMF:DMSO mixture. Then the same spin-coating procedure as for the perovskite films was conducted (without the chlorobenzene drip) and the samples were annealed at 100 °C for 10 min, yielding pale yellow films. For the reproduction of the $CsPb_2I_4Br$ phase, RbI was replaced by CsI (129.9 mg, 0.5 mmol).

Solar Cell Fabrication

FTO coated glass substrates (7 Ω/sq) were patterned by etching with zinc powder and 3 M HCl solution and successively cleaned with deionized water, a 2% Hellmanex detergent solution, ethanol and finally treated with oxygen plasma for 5 min. A compact TiO_2 layer was deposited as a hole blocking layer on the substrate via a sol-gel approach. Therefore, a mixture of 2 M HCl (35 µL) and anhydrous isopropanol (2.53 mL) was added dropwise to a solution of 370 µL titanium(IV) isopropoxide (Sigma-Aldrich) in isopropanol (2.53 mL) under vigorous stirring. The filtrated TiO_x solution was spin-coated dynamically onto the FTO substrates at 2000 rpm for 45 s, followed by annealing in air at 150 °C for 10 min and subsequently at 500 °C for 45 min. The deposition of the perovskite layer was conducted as described above for the thin film fabrication. For the hole transporter layer, 1 mL solution of spiro-OMeTAD (Borun Chemicals, 99.8%) in anhydrous chlorobenzene (75 mg/mL) was doped with 10 µL tBP (Sigma-Aldrich, 96%) and 30 µL of a 170 mg/mL Li-TFSI (Sigma-Aldrich, 99.95%) solution in acetonitrile (Sigma-Aldrich, anhydrous) and deposited by spin-coating at 1500 rpm for 40 s and then 2000 rpm for 5 s. After storing the samples overnight in air at 25% relative humidity, 40 nm Au was deposited through a patterned shadow mask by thermal evaporation at $8 \cdot 10^{-7}$ mbar to form the back electrode.

Characterization

X-ray diffraction: XRD measurements of thin films were performed with a Bruker D8 Discover X-ray diffractometer operating at 40 kV and 30 mA, employing Ni-filtered Cu $K_{\alpha 1}$ radiation (λ = 1.5406 Å) and a position-sensitive LynxEye detector. A step size of $\Delta 2\theta$ = 0.0026° was

employed to resolve the change in peak position of the perovskite's diffraction peak. For the *in situ* XRD measurements during the hydration process, a custom-made hydration chamber made of X-ray transparent polymers with a total volume around 250 mL was utilized. The air humidity within the hydration chamber was held constant employing vials filled with saturated salt solutions and measured using a hygrometer. The salts Na_2CO_3, NaCl, NaBr and K_2CO_3 were used for controlling the humidity level to 92%, 75%, 58% and 45% RH, respectively. All experiments were performed at room temperature (21 °C) without illumination.

Scanning electron microscopy: SEM images were recorded with an FEI Helios Nanolab G3 UC DualBeam scanning electron microscope, operated at an acceleration voltage of 5 kV. EDX spectra were recorded and evaluated with an Oxford Instruments AZTEC EDX-system. For EDX investigations, the samples were tilted to an angle of 52° with respect to the electron beam and an acceleration voltage of 20 kV was employed.

UV-Vis spectroscopy: UV-Vis absorption spectra were recorded using a Perkin Elmer Lambda 1050 spectrophotometer equipped with a 150 mm integrating sphere.

Current-voltage characteristics: J-V curves were recorded under ambient conditions using a Newport OrielSol 2A solar simulator with a Keithley 2400 source meter under simulated AM 1.5G sunlight, with an incident power of 100 mW cm^{-2}, calibrated with a Fraunhofer ISE certified silicon cell (KG5-filtered). The active area of the solar cells was defined with a square metal aperture mask of 0.0831 cm^2. After pre-biasing the device at 1.3 V for 5 s under illumination, *J-V* curves were recorded by scanning the input bias from 1.3 to 0 V (reverse scan) and then from 0 to 1.3 V (forward scan) at a scan rate of 0.1 V s^{-1}. All as-prepared devices show a comparable degree of hysteresis between the forward and reverse scan. The stabilized power output was measured by tracking the current at the maximum power point under AM 1.5G illumination without pre-biasing the device.

Moisture stability tests

Humidity studies on the perovskite solar cells were conducted in a glass container at a constant humidity level of 75% RH in air that was maintained by a saturated aqueous NaCl solution at the bottom of the jar. Humidity stability tests at 58% RH were performed in the same way using a NaBr solution. In order to exclude the influence of light exposure on the degradation process, the container was kept in the dark. The unencapsulated solar cells were placed onto a stage inside the sealed container being exposed to the moist air and without having direct contact with the solution. After a certain exposure time, the *J-V* curves of the devices were measured under ambient conditions and 1 sun illumination at a scan rate of 0.2 V s^{-1}. 24 cells were evaluated for each type of perovskite solar

cell for 75% RH and 20 cells for 58% RH. The arithmetic means of the PCE and J_{sc} values extracted from the reverse *J*-*V* scans were monitored over a course of 10 days. The stability of devices under the exclusion of water was determined by measuring the PCE of 20 cells for each type of perovskites after storage in a nitrogen-filled glovebox for 5 months.

6.6 References

[1] Y. Hu, M. F. Aygüler, M. L. Petrus, T. Bein, P. Docampo, *ACS Energy Lett.* **2017**, 2212.

[2] M. Zhang, J. S. Yun, Q. Ma, J. Zheng, C. F. J. Lau, X. Deng, J. Kim, D. Kim, J. Seidel, M. A. Green, S. Huang, A. W. Y. Ho-Baillie, *ACS Energy Lett.* **2017**, 438.

[3] Y. H. Park, I. Jeong, S. Bae, H. J. Son, P. Lee, J. Lee, C.-H. Lee, M. J. Ko, *Adv. Funct. Mater.* **2017**, 1605988.

[4] Z. Li, M. Yang, J.-S. Park, S.-H. Wei, J. J. Berry, K. Zhu, *Chem. Mater.* **2016**, *28*, 284.

[5] M. Saliba, T. Matsui, J.-Y. Seo, K. Domanski, J.-P. Correa-Baena, M. K. Nazeeruddin, S. M. Zakeeruddin, W. Tress, A. Abate, A. Hagfeldt, M. Gratzel, *Energy. Environ. Sci.* **2016**, *9*, 1989.

[6] T. Duong, H. K. Mulmudi, H. Shen, Y. Wu, C. Barugkin, Y. O. Mayon, H. T. Nguyen, D. Macdonald, J. Peng, M. Lockrey, W. Li, Y.-B. Cheng, T. P. White, K. Weber, K. Catchpole, *Nano Energy* **2016**, *30*, 330.

[7] M. Saliba, T. Matsui, K. Domanski, J.-Y. Seo, A. Ummadisingu, S. M. Zakeeruddin, J.-P. Correa-Baena, W. R. Tress, A. Abate, A. Hagfeldt, M. Grätzel, *Science* **2016**, *354*, 206.

[8] J.-W. Lee, D.-H. Kim, H.-S. Kim, S.-W. Seo, S. M. Cho, N.-G. Park, *Adv. Energy Mater.* **2015**, *5*, 1501310.

[9] C. Yi, J. Luo, S. Meloni, A. Boziki, N. Ashari-Astani, C. Gratzel, S. M. Zakeeruddin, U. Rothlisberger, M. Gratzel, *Energy. Environ. Sci.* **2016**, *9*, 656.

[10] D. P. McMeekin, G. Sadoughi, W. Rehman, G. E. Eperon, M. Saliba, M. T. Hörantner, A. Haghighirad, N. Sakai, L. Korte, B. Rech, M. B. Johnston, L. M. Herz, H. J. Snaith, *Science* **2016**, *351*, 151.

[11] V. M. Goldschmidt, *Naturwissenschaften* **1926**, *14*, 477.

[12] G. Kieslich, S. Sun, A. K. Cheetham, *Chem. Sci.* **2014**, *5*, 4712.

[13] D. M. Trots, S. V. Myagkota, *J. Phys. Chem. Solids* **2008**, *69*, 2520.

[14] G. E. Eperon, G. M. Paterno, R. J. Sutton, A. Zampetti, A. A. Haghighirad, F. Cacialli, H. J. Snaith, *J. Mater. Chem. A* **2015**, *3*, 19688.

[15] A. Swarnkar, A. R. Marshall, E. M. Sanehira, B. D. Chernomordik, D. T. Moore, J. A. Christians, T. Chakrabarti, J. M. Luther, *Science* **2016**, *354*, 92.

[16] G. Kieslich, S. Sun, A. K. Cheetham, *Chem. Sci.* **2015**, *6*, 3430.

[17] H. J. Haupt, F. Huber, H. Preut, *Z. Anorg. Allg. Chem.* **1974**, *408*, 209.

[18] Y. Chang, L. Wang, J. Zhang, Z. Zhou, C. Li, B. Chen, L. Etgar, G. Cui, S. Pang, *J. Mater. Chem. A* **2017**, *5*, 4803.

[19] J. Brgoch, A. J. Lehner, M. Chabinyc, R. Seshadri, *J. Phys. Chem. C* **2014**, *118*, 27721.

[20] M. Cola, V. Massarotti, R. Riccardi, C. Sinistri, *Z. Naturforsch. A* **1971**, *26*, 1328.

[21] S. Wang, Y. Jiang, Emilio J. Juarez-Perez, Luis K. Ono, Y. Qi, **2016**, *2*, 16195.

[22] H. L. Wells, *Am. J. Sci.* **1893**, *45*, 121.

[23] H. M. Powell, H. S. Tasker, *J. Chem. Soc.* **1937**, 119.

[24] H. L. Wells, *Am. J. Sci.* **1893**, *Series 3 Vol. 46*, 34.

[25] M. L. Petrus, Y. Hu, D. Moia, P. Calado, A. M. A. Leguy, P. R. F. Barnes, P. Docampo, *ChemSusChem* **2016**, *9*, 2699.

[26] A. Binek, F. C. Hanusch, P. Docampo, T. Bein, *J. Phys. Chem. Lett.* **2015**, *6*, 1249.

7 Phase purity and crystal orientation in 2D perovskite thin films

This chapter is based on the following manuscript:

Y. Hu, L. M. Spies, D. Alonso-Álvarez, P. Mocherla, H. Jones, J. Hanisch, T. Bein, P. R. F. Barnes, P. Docampo, Identifying and controlling phase purity in 2D hybrid perovskite thin films. *(submitted)*

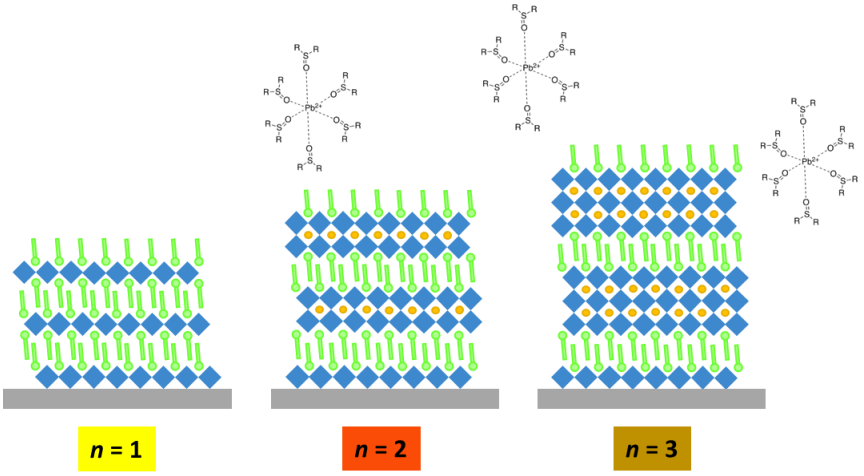

7.1 Abstract

Two-dimensional (2D) hybrid perovskites have attracted considerable attention due to their enormous structural and electronical variability, making this class of semiconductors interesting for photovoltaics, light-emitting diodes and lasers. 2D perovskites consist of sheets of bulky organic cations and a certain number of lead halide octahedra layers, arranged in an alternating way. Since the properties of these materials strongly depend on the octahedra layer thickness *n*, controlling the phase purity regarding *n* is important for any 2D perovskite thin film applications. Here, we show that using rationally chosen lead-complexing solvent additives offers a facile way to control the crystallization process in order to form 2D perovskite films with significantly reduced variation in *n* from the target value than films obtained by conventional fast-crystallization methods without solvent additives. The improved phase purity in the optimized $n = 2$ and $n = 3$ films is verified by X-ray diffraction, UV-Vis absorption and photoluminescence measurements. In addition, 2D perovskites films arising from additive-assisted growth exhibit an unusual crystal orientation with the perovskite interlayers predominantly aligned parallel to the substrate. We propose a simple film formation mechanism as an empirical explanation for the change in crystal disorder and orientation by using lead-complexing solvent additives. Improved control over the phase purity translates into a better control of the optoelectronic properties of 2D perovskite films and the horizontal crystal orientation makes this family of tunable organic-inorganic perovskites promising for applications where lateral charge transport is desired.

7.2 Introduction

Two-dimensional (2D) hybrid perovskites, also often referred to as Ruddlesden-Popper perovskites,[1, 2] have recently attracted considerable interest for various potential semiconductor applications, such as solar cells, light-emitting diodes (LEDs) or lasers.[3-9] This class of organic-inorganic lead halide perovskite materials consists of alternating sheets of vertex-sharing lead halide octahedra, which can accommodate small organic cations such as methylammonium (MA), and interlayers of bulky ammonium-terminated organic cations. The long-chained organic cations (LOCs) usually feature alkyl chains or phenyl-groups, which can form bilayers via van-der-Waals or π–π interactions, thus giving the 2D perovskite its periodic, layered crystal structure.[10-12] In the field of photovoltaics, the replacement of 3D hybrid perovskites by their 2D analogues as photo-absorbers has led to substantially enhanced moisture stability of the resulting perovskite solar cells, a feature that has been attributed to the hydrophobic side chains of the incorporated LOCs.[5, 13-18]

Although improving the moisture resistance of perovskite solar cells is important, the potential of 2D perovskites lies in their enormous structural tunability, which gives access to a large playground for tailoring their optoelectronic properties according to the application field.[3-6, 19] In particular, *n*, which is the number of octahedra sheets sandwiched between two organic interlayers, strongly determines the major features of the resulting 2D perovskite, such as band gap, exciton binding energy or photoluminescence.[13, 14, 19-23] A homologous series of Ruddlesden-Popper perovskite phases with the generic formula $(LOC)_2(MA)_{n-1}Pb_nI_{3n+1}$ where n = 1, 2, 3, 4 and 5 has been successfully synthesized by Kanatzidis and co-workers, using butylammonium cations as the organic spacer.[14, 24] The fabrication of 2D perovskite single crystals with defined octahedra layer thickness *n* was achieved by adjusting the ratio between the lead source, methylammonium iodide (MAI) and butylamine in the precursor solutions. The authors have shown that the band gap of the 2D perovskites can be tuned from 2.4 eV to 1.7 eV by increasing the octahedra layer thickness from n = 1 to n = 5 respectively.

To obtain thin films of 2D perovskites with the desired *n*-value, conventionally the corresponding perovskite single crystals or a stoichiometric mixture of the precursor components is dissolved in DMF, followed by a spin-coating and annealing process.[1, 2, 13, 14, 25] However, it has been largely overlooked that stoichiometry is not everything when it comes to the formation of 2D perovskite thin films on substrates. The crystallization dynamics for thin film growth are likely to be very different from single crystal growth and the nature of the substrate may influence the film formation as well. Therefore, we need to take into account that thin films resulting from spin-coating of a stoichiometric 2D perovskite precursor solution are not necessarily composed of the targeted *n*-phase if careful control of the crystallization process is neglected. Yet, controlling the phase purity regarding the octahedra layer thickness *n* is imperative to obtain the desired optoelectronic properties of the 2D perovskite thin film.

In this work, we establish a simple fabrication method to obtain $n \geq 2$ perovskite films with significantly less variation in *n* from the target value than in films prepared using conventional fast crystallization methods. By using appropriate lead-complexing additives in the solvent and careful control of the annealing procedure, a narrow distribution of *n* can be achieved in the resulting 2D perovskite film. By contrast, nominally n = 2 and n = 3 perovskite thin films spin-coated from DMF-solutions consist of a broad mixture of domains with different *n*-values when crystallized from conventional, fast-crystallization procedures. This disorder is verified by photoluminescence (PL) measurements. Time-of-flight secondary ion mass spectrometry (ToF-SIMS) measurements confirm a gradient in *n* within nominally n = 3 perovskite films, with decreasing *n*-value from top to bottom. In addition to minimized variation in *n*, our controlled crystallization procedure results in n = 2 and n = 3 films with perovskite and organic interlayers that are oriented exclusively parallel to the

substrate. This unusual crystal orientation makes the family of 2D perovskites interesting for device applications where lateral charge transport is required.

7.3 Results and discussion

We investigated the homologous $(PentA)_2(MA)_{n-1}Pb_nI_{3n+1}$ series as a model system for 2D perovskites using pentylammonium (PentA) as the bulky organic cation. Figure 7.1 shows a schematic illustration of the layered perovskite structure composed of the following building blocks: bulky PentA cations, small MA cations and corner-sharing $[PbI_6]^{4-}$ octahedra, where n is the number of octahedra layers sandwiched between two PentA layers. For the case of $n = \infty$ (which occurs in the absence of PentA), the resulting crystal structure corresponds to the 3D perovskite methylammonium lead iodide ($MAPbI_3$). First, to fabricate thin films of the 2D perovskites, pentylammonium iodide (PentAI), methylammonium iodide (MAI) and PbI_2 were mixed in the corresponding stoichiometry targeting a certain n-value and dissolved in DMF. Subsequently, the perovskite precursor solution was spin-coated on glass substrates in a one-step process following similar procedures as reported in literature.[13, 20, 24] The $MAPbI_3$ film was fabricated via an anti-solvent drip method according to a previously established protocol.[26]

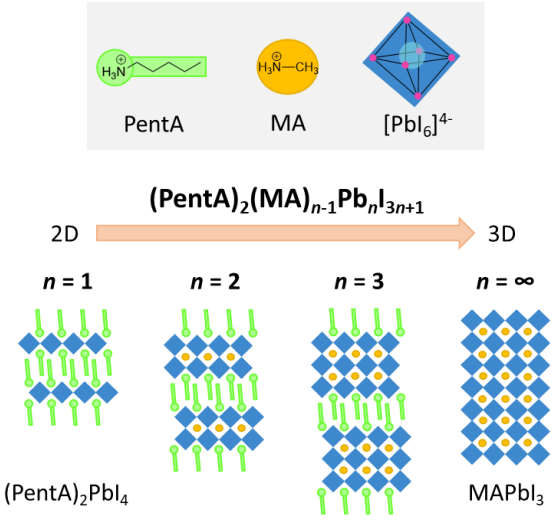

Figure 7.1 Schematic crystal structures of the homologous series of $(PentA)_2(MA)_{n-1}Pb_nI_{3n+1}$ perovskites with the n = 1 compound $(PentA)_2PbI_4$, intermediate MA–PentA mixed-cation 2D perovskites incorporating the PbI_6 octahedra layers with thickness n = 2 and n = 3, and $MAPbI_3$ as the $n = \infty$ case.

To characterize the crystal structure and the preferential orientation of the perovskite thin films, X-ray diffraction (XRD) measurements were performed. Figure 7.2a shows the XRD patterns of non-optimized n = 1, 2, 3 PentAMAPI films spin-coated from DMF-solutions and a $MAPbI_3$ film.

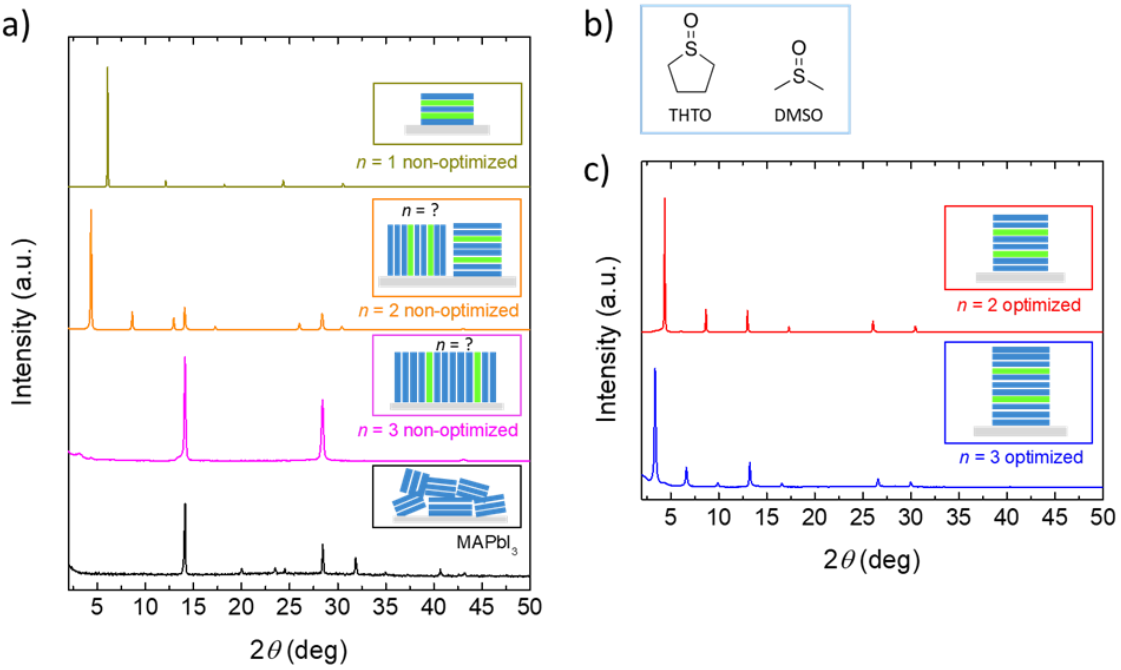

Figure 7.2 XRD patterns of $(PentA)_2(MA)_{n-1}Pb_nI_{3n+1}$ perovskites: (a) non-optimized n = 1, 2, 3 PentAMAPI films on glass substrates and a $MAPbI_3$ film for comparison. (b) Solvent additives used for controlled 2D perovskite film growth and (c) the resulting optimized n = 2 and n = 3 PentAMAPI films.

The presence or absence of certain diffraction peaks in XRD patterns of thin films recorded in the Bragg-Brentano scanning mode can give first indications for potentially preferred crystal orientation within the samples. Furthermore, the 2θ position of the diffraction peaks corresponding to the stacking direction of the perovskite interlayers reveals the dimensions of the unit cell and therefore the number of octahedra layers n. In our samples, the n = 1 film exhibits pronounced peaks at the diffraction angle 2θ = 6.1°, 12.1°, 18.2°, 24.3° and 30.5°, which can be indexed as the (002), (004), (006), (008) and (0010) reflections of the $(PentA)_2PbI_4$ phase. The high intensity of the diffraction peaks indicates very high crystallinity and the lack of other reflections can be assigned to a preferential orientation of the crystals along the (00l) direction. This trend of growing layers which are oriented exclusively parallel to the substrate surface has been shown for the vast majority of n = 1 Ruddlesden-Popper phase perovskites incorporating different ammonium-based cations.[25, 27-29] The XRD pattern of the n = 2 film shows a similar set of diffraction peaks at 4.3°, 8.6°, 12.9° and

17.3°, where the peak shift to smaller 2θ values corresponds to an increase in unit cell dimension from 14.5 Å to 20.5 Å. As expected, this incremental increase in interplanar distance is roughly the same as the layer thickness of a sheet of vertex-sharing PbI_6 octahedra. In addition, reflections at 14.1° and 28.4° can be ascribed to the (111) and (202) plane respectively. These two diffraction peaks occur when the alternating PentA and PbI_6 interlayers are oriented perpendicular to the substrate. The co-existence of the (111) and (202) diffraction peaks and the low angle (0*k*0) peaks indicates that both horizontally and vertically oriented regions are present in the $n = 2$ perovskite film, which agrees with previous reports.[2, 14]

In contrast, the non-optimized, nominally $n = 3$ film exclusively shows the (111) and the (202) reflection, which corresponds to the typical vertical orientation for high-*n* members of the 2D perovskite phase. This vertical orientation of the interlayers has been reported for different 2D perovskite systems with a precursor stoichiometry of $n > 2$.[1, 13, 17, 24, 30] The resulting XRD patterns resemble the one of the 3D analogue $MAPbI_3$, due to the same interplanar distance of ~6.3 Å which corresponds to the size of a PbI_6 octahedron. However, the strong preferential crystal orientation where the perovskite interlayers are aligned perpendicular to the substrate does not allow an unambiguous determination of the *n*-value from the XRD pattern recorded in the conventional Bragg-Brentano mode, since information about the periodicity in the lateral direction (in-plane) is not revealed.

To complement our XRD results, which only provide us with out-of-plane reflections of these highly textured perovskite films, we used grazing-incidence wide-angle X-ray scattering (GIWAXS) techniques to examine all possible crystal orientations within the thin films. The GIWAXS pattern of the non-optimized $n = 3$ film shows the (111) reflection at an azimuthal angle of $\chi = 0°$, verifying the exclusive vertical alignment of the perovskite interlayers with respect to the substrate (Figure 7.3a). Assuming that the $n = 3$ periodicity of the 2D perovskite is present in the lateral direction, the corresponding diffraction peaks around the azimuthal angle $\chi = \pm 90°$ at low q_{xy}-values are expected to be present. However, the absence of this feature suggests crystal disorder in the lateral direction of the non-optimized, nominally $n = 3$ film. Similar GIWAXS patterns have been shown for nominal $n = 3$, 4 or 5 films, which were identified as a mixture of multiple 2D perovskite phases with different *n*-values.[24, 31, 32]

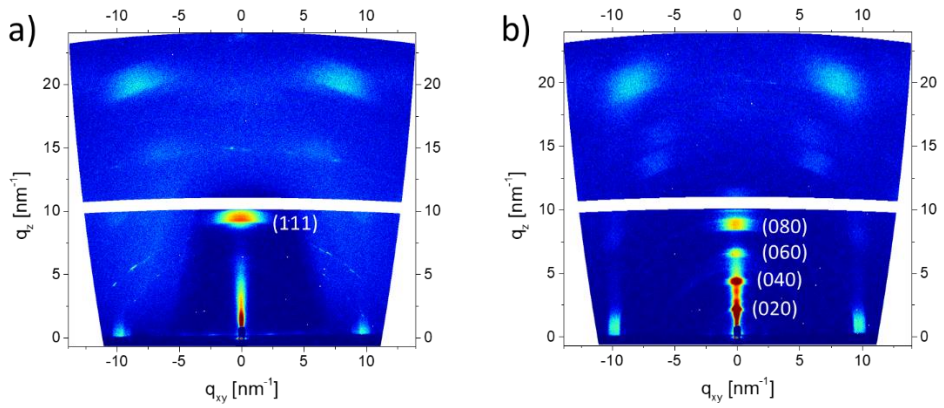

Figure 7.3 2D GIWAXS patterns of (a) non-optimized and (b) optimized *n* = 3 PentAMAPI films spin-coated on glass confirm the high degree of crystal orientation either perpendicular or parallel to the substrate.

Due to the close relationship between the *n*-value and the properties of the corresponding 2D perovskite, controlling its phase purity in thin film is vital for any optoelectronic applications using this class of material. We demonstrate that the phase purity regarding the *n*-value can be significantly improved for *n* = 2, 3 PentAMAPI films by carefully controlling the crystallization process of the 2D perovskite film. This can be achieved by suitable solvent additives such as DMSO or tetrahydrothiophene-1-oxide (THTO) in the precursor solution (see Figure 7.2b), combined with a slow annealing process during the perovskite film formation. Figure 7.2c shows the XRD patterns of the *n* = 2 and *n* = 3 PentAMAPI films prepared according to our optimized protocol using THTO and/or DMSO as solvent additives. Details about the optimized procedures are described in the Methods section (Table 7.1). We optimized the fabrication protocol regarding spin-coating speed, additive concentration and annealing temperature to obtain 2D perovskite films showing a narrow distribution of *n*-values which is close to the one targeted by the precursor stoichiometry. XRD was employed to monitor the optimization process for *n* = 2 (Figure 7.4) and *n* = 3 PentAMAPI (Figure 7.5) on glass substrates.

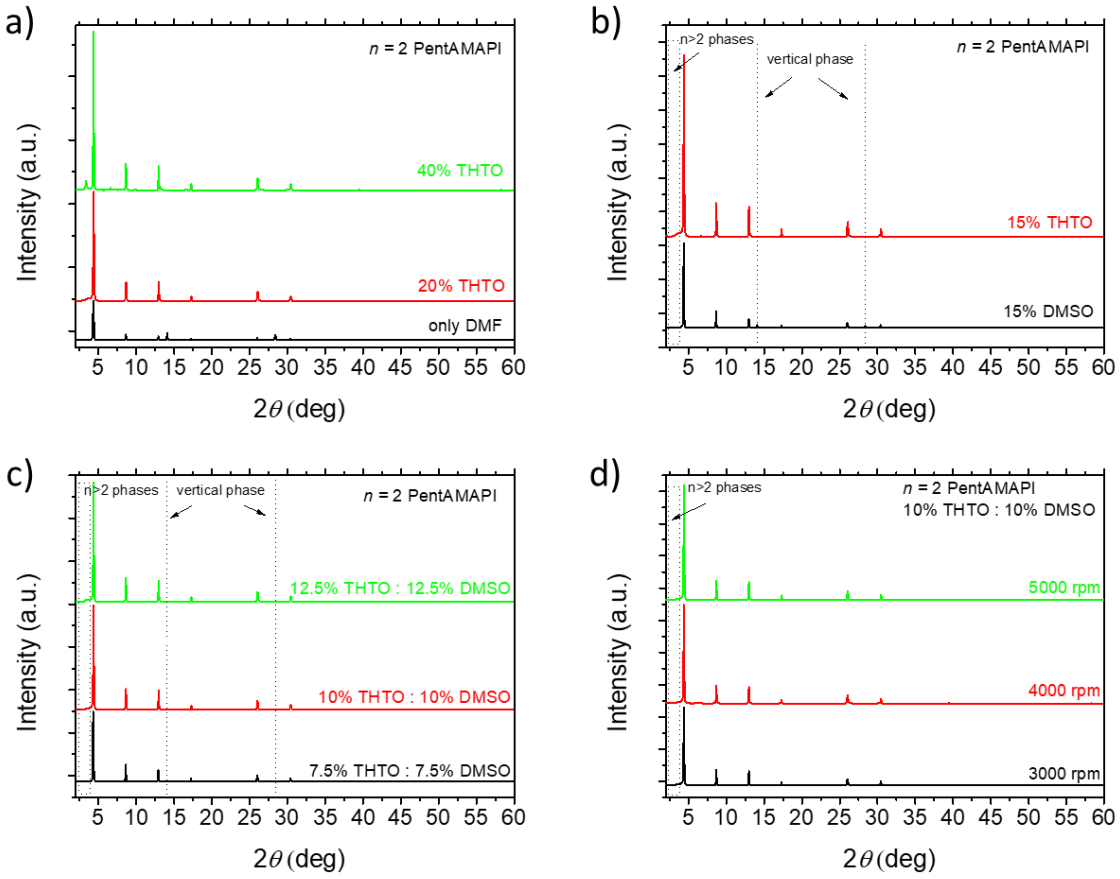

Figure 7.4 XRD patterns of films on glass substrates spin-coated from *n* = 2 PentAMAPI solutions with (a) different amounts of THTO as solvent additive, (b) 15% THTO or DMSO as additive, (c) different amounts of THTO and DMSO additives combined and (d) using different spinning speeds for the optimized precursor solution.

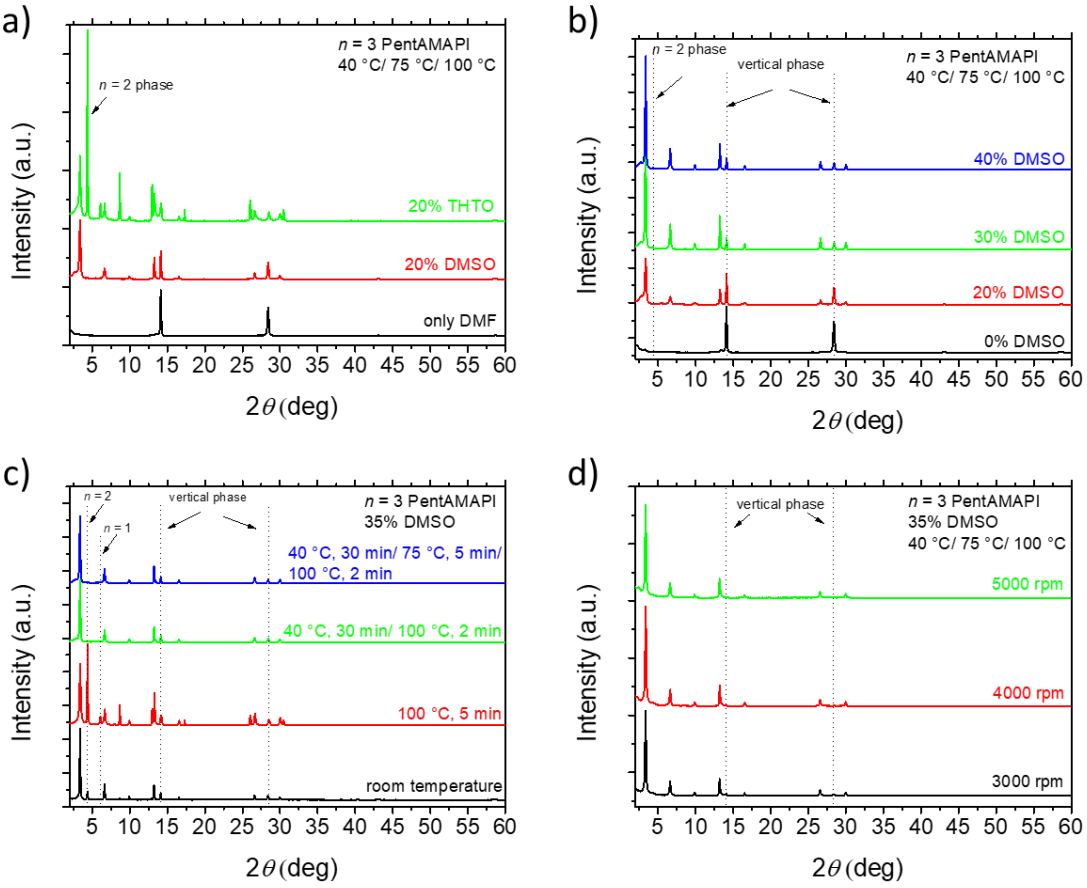

Figure 7.5 XRD patterns of films on glass substrates spin-coated from n = 3 PentAMAPI solutions with (a) 20% THTO or DMSO as solvent additive, (b) different amounts of DMSO additive, (c) varying annealing processes and (d) using different spinning speeds for the optimized precursor solution containing ~0.5 M PbI_2.

Compared to the non-optimized n = 2 and n = 3 films, the optimized 2D perovskite films exhibit strong (0k0) peaks for both samples. The presence of THTO in the n = 2 precursor solution leads to a significant increase in overall diffraction peak intensities (Figure 7.4a), verifying higher crystallinity of the n = 2 film grown with the additive-assisted approach. In particular, the diffraction peaks at 3.3°, 6.6°, 9.9° and 13.2° for the optimized n = 3 film show that, in addition to the high crystallinity, the perovskite interlayers exhibit an unusual orientation which is parallel to the substrate (Figure 7.2c). The "horizontal" orientation of the perovskite layers for n = 3 is verified by the corresponding GIWAXS pattern (Figure 7.3b), where the (0k0) signals do not form diffraction rings, but are exclusively found at an azimuthal angle χ = 0°. In contrast to the vertically oriented, non-optimized (nominally) n = 3 perovskite film, this allows us to unambiguously confirm the octahedra layer thickness to be n = 3 from the 2θ position of the (020) reflection in the conventional XRD pattern. The absence of the (111) and (202) reflections in the XRD pattern indicates that vertical

growth is largely suppressed in both optimized n = 2 and n = 3 films. To the best of our knowledge, this is the first demonstration of predominantly horizontally oriented 2D perovskite thin films with n > 1. The recipe for the n = 1 samples and our optimized protocols for n = 2 and n = 3 films were tested on different substrates, including FTO, FTO/ TiO_2, ITO and silicon. The XRD patterns shown in Figure 7.6 demonstrate that the 2D perovskite phase purity and crystal orientation is comparable for all tested substrates.

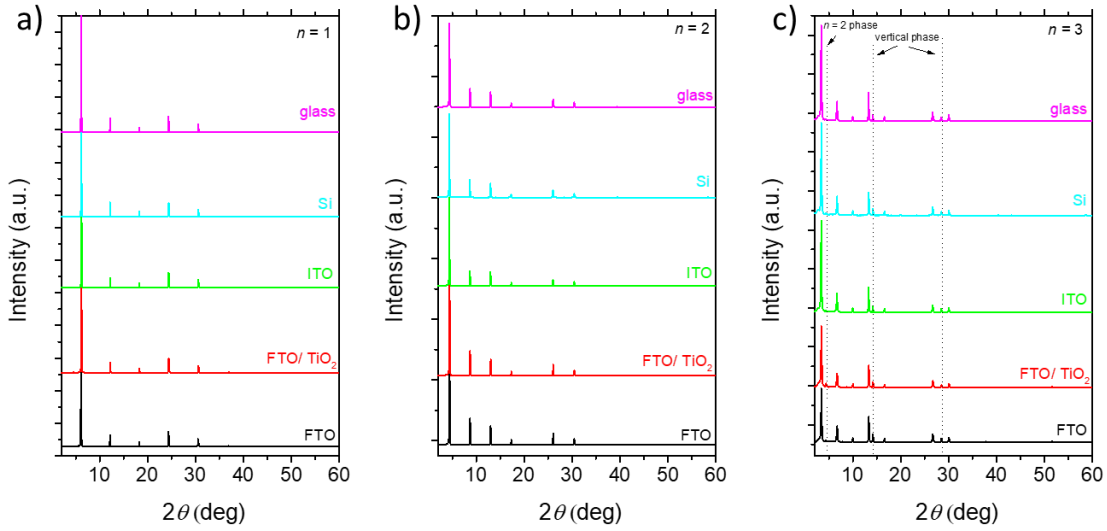

Figure 7.6 XRD patterns of 2D perovskite films spin-coated on different substrates using (a) n = 1, (b) optimized n = 2 and (c) optimized n = 3 precursor solutions with ~1 M PbI_2 concentration and optimized annealing conditions.

We note that a slow annealing procedure at a lower starting temperature is vital to obtain 2D perovskite films with satisfying phase purity. The best results were achieved by following a three-step drying sequence, with a stepwise increase of the annealing temperature from 40 °C to 75 °C to 100 °C (Table 7.1). When the n = 3 film, which included DMSO as an additive, was subjected directly to heating on a 100 ºC hotplate after spin-coating, the corresponding XRD pattern of the resulting film shows diffraction peaks of a mixture between horizontally oriented n = 1, 2 and 3 phases, indicating poor phase purity (Figure 7.5c).

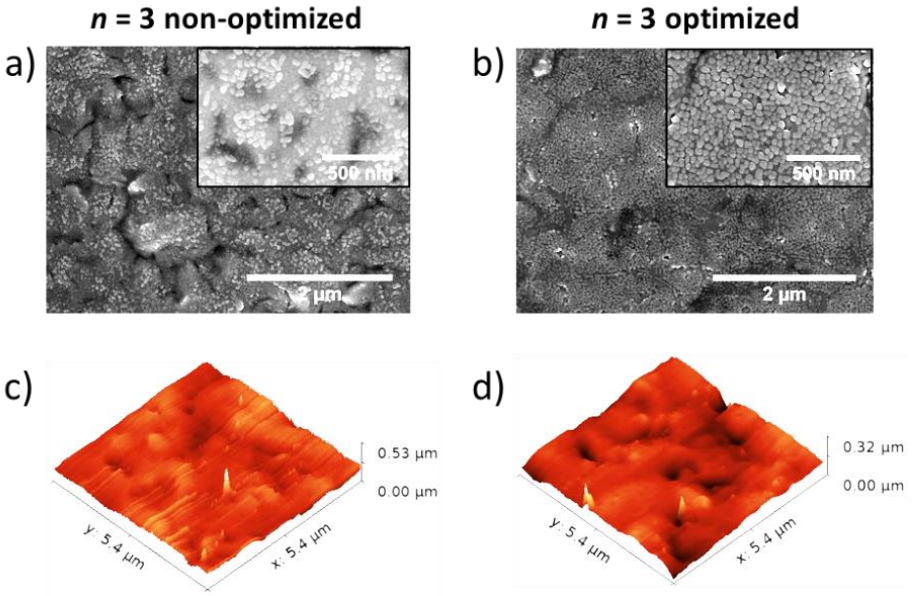

Figure 7.7 SEM top view images of the (a) non-optimized and (b) optimized n = 3 perovskite film with solvent additives prepared on FTO/TiO_2 substrates. The insets show SEM images at higher magnification. AFM images show the surface roughness of the (c) non-optimized and (d) optimized n = 3 perovskite film.

Scanning electron microscopy (SEM) top view images of the non-optimized and optimized n = 3 film reveal similar crystal morphologies with a grain size around 50 nm (Figure 7.7a–b). Encouragingly, the optimized n = 3 film exhibits significantly less cracks on the sample surface and the corresponding atomic force microscopy (AFM) images indicate significantly reduced root mean square film roughness (r_{rms} = 14 nm) compared to the non-optimized sample without solvent additives (r_{rms} = 25 nm), as shown in Figure 7.7c–d. The good film quality of the optimized 2D perovskite thin films is promising for various device applications, which require uniform layers to support sufficient charge transport. SEM images for the n = 1 and 2 samples are depicted in Figure 7.8.

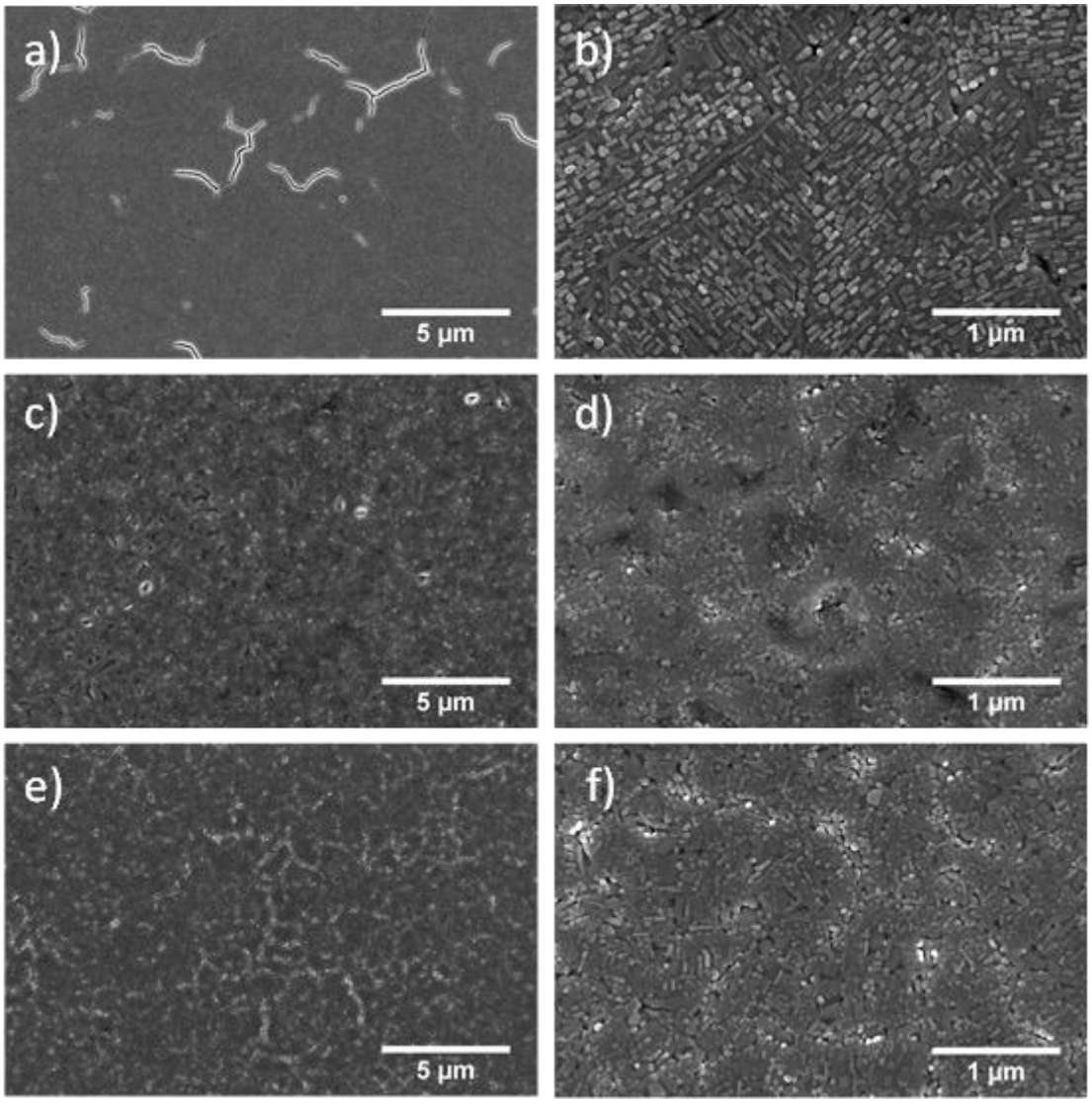

Figure 7.8 SEM top-view images of 2D perovskite films on FTO/TiO_2 substrates with (a–b) n = 1, (c–d) non-optimized n = 2, and (e–f) optimized n = 2.

Since the optoelectronic properties of 2D perovskites strongly depend on n, our structural analysis employing XRD techniques was complemented by optical characterization to obtain further insights into the phase purity of 2D perovskite thin films. Figure 7.9a shows the normalized UV-Vis absorption profiles of non-optimized n = 1, 2 and 3 perovskites films spin-coated from DMF solutions and a $MAPbI_3$ film for comparison. In agreement with previous reports, the absorption onsets of the 2D perovskites are substantially shifted to larger wavelength numbers with increasing n, which is visible in a change of the film's color (see inset Figure 7.9a).[2, 21] The n = 1 (yellow), n = 2 (red) and n = 3 (brown) films show distinct excitonic features at 488 nm, 563 nm and 605 nm, respectively.[14] The non-optimized n = 3 film also shows the signature of the n = 2 phase and vice

versa, hinting at a mixture of phases in both samples. In addition, the non-optimized nominally $n = 3$ sample exhibits an absorption tail up to 740 nm, which can be interpreted as an indication for the presence of $n > 3$ crystal regions with a narrower band gap than the nominal $n = 3$ phase, similar to the $MAPbI_3$ film ($n = \infty$) with a band gap of 1.6 eV and an absorption onset around 770 nm. By comparison, the optimized $n = 3$ film shows a less pronounced absorption tail (Figure 7.9c) and a reduced $n = 2$ absorption peak, giving evidence for a more narrow variation in n. The estimated band gaps for the optimized $n = 1$, 2 and 3 films are 2.3, 2.2 and 2.0 eV respectively, which is in agreement with the band gap values reported for the corresponding 2D perovskite single crystals.[2]

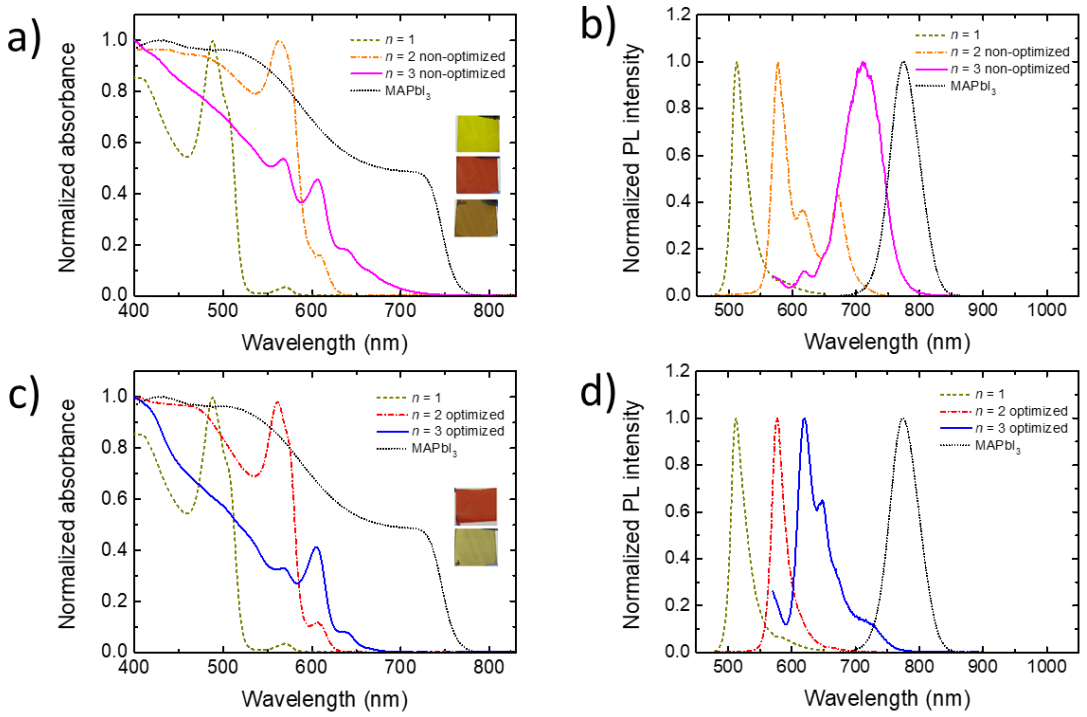

Figure 7.9 Normalized UV-Vis absorption spectra and PL spectra of (a–b) non-optimized and (c–d) optimized 2D perovskite films with $n = 2$ and $n = 3$ on glass compared to $n = 1$ and $MAPbI_3$ films. The insets in a) show photographs of the non-optimized $n = 1$ (yellow), $n = 2$ (red) and $n = 3$ (brown) films and the insets in c) show the optimized $n = 2$ and 3 PentAMAPI films, respectively.

Furthermore, we conducted photoluminescence (PL) measurements to evaluate the distribution of n within the 2D perovskite and potential charge transfer between these crystal domains. In Figure 7.9b, the room temperature steady-state PL spectra of a $MAPbI_3$ film and the non-optimized $n = 1$, 2 and 3 perovskites films are displayed. In agreement with literature values, the extreme cases $n = 1$ and $MAPbI_3$ ($n = \infty$) both show a single PL peak around 524 nm and 776 nm respectively, confirming

the phase purity of the perovskite films.[2, 33] The non-optimized n = 2 film shows the expected PL peak at 570 nm, accompanied by two additional peaks at 625 nm and 675 nm, which can be assigned to the n = 3 and n = 5 phase.[2, 24] Interestingly, the non-optimized n = 3 film exhibits only a minor peak at 625 nm, which coincides with the PL signature of n = 3 single crystals,[2] while the main PL feature consist of a broad peak with a maximum around 720 nm. This is consistent with all previous reports about $n \geq 3$ perovskite films, independent of the nature of the bulky organic cation or the film fabrication method.[1, 13, 14, 20, 24]

The discrepancy between the PL spectra of 2D perovskite singles crystals and the corresponding thin films fabricated from DMF solutions without solvent additives indicates a large variety of n within these perovskite films evolving from fast crystallization. Moreover, photoemission in these non-optimized 2D perovskite films seems to be dominated by recombination events from layers where $n >> 3$. To understand the origin of the observed emission from the large-n domains, we performed temperature-dependent PL measurements on non-optimized n = 3 perovskite films (Figure 7.10). Interestingly, after cooling down the sample to 30 K, several distinct PL peaks emerge, which can be ascribed to the presence of n = 2, 3, 4, 5 regions. As the temperature is gradually raised to 298 K, the distinct PL features of the low-n regions diminish, while the emission from the bulk-like large-n areas around 720 nm steadily increases. Assuming that structural changes such as phase transformation between the different regions do not occur, our results suggest that the observed PL peak of non-optimized n = 3 films can be rationalized by transport and relaxation of charge carriers from crystal regions of wide band gap ($n \leq 3$) to regions where the band gap approaches the bulk perovskite material ($n >> 3$). This is in accordance with recent reports by Liu *et al.*,[32] confirming rapid exciton transport from low-n regions to large-n regions on the picosecond scale at room temperature.

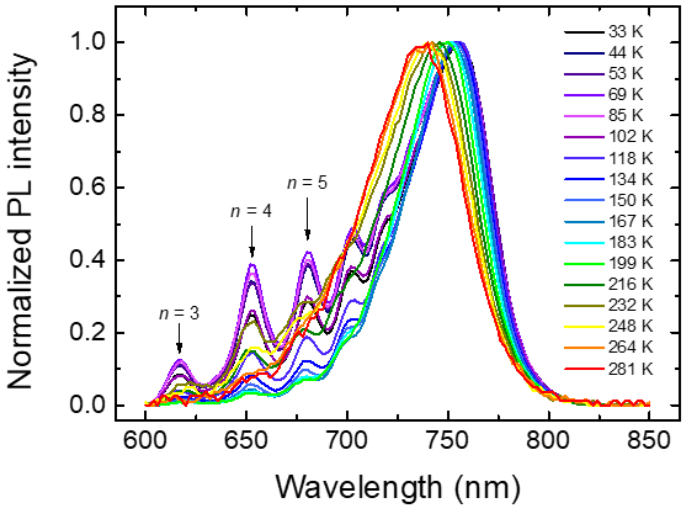

Figure 7.10 Normalized PL spectra of a non-optimized n = 3 PentAMAPI film on glass recorded at the temperature range from 33–281 K. The characteristic PL peaks of the n = 3, 4 and 5 perovskite phases are indicated.

In comparison, the PL spectra of the optimized n = 2 and n = 3 films using THTO and/or DMSO as solvent additives show predominantly one peak at 570 nm and 625 nm respectively (Figure 7.9d). These PL peaks match well with the PL profile of the corresponding n = 2 and n = 3 single crystals, as reported by Stompous *et al.*[2] In particular, the PL signal of the optimized n = 3 film exhibits only a small additional peak at 650 nm (n = 4) and a shoulder around 725 nm (n >> 3). Therefore, we conclude that the addition of DMSO or THTO and careful control of the annealing process result in 2D perovskite films with significantly less variation in n from the target value than films prepared without the solvent additives, which is in agreement with our XRD results.

Despite the improved phase purity of the additive-assisted formation of n = 3 PentAMAPI perovskite thin films regarding n, our PL analysis indicates that some large-n regions remain within the optimized films. In order to assess the spatial distribution of the different n-regions, time-of-flight secondary ion mass spectrometry (ToF-SIMS) measurements were performed. Since the n-value is determined by the ratio between MA and PentA cations, a comparison of the depth profiles of the MA^+ and $PentA^+$ species allows us to estimate the vertical distribution of the large-n regions.

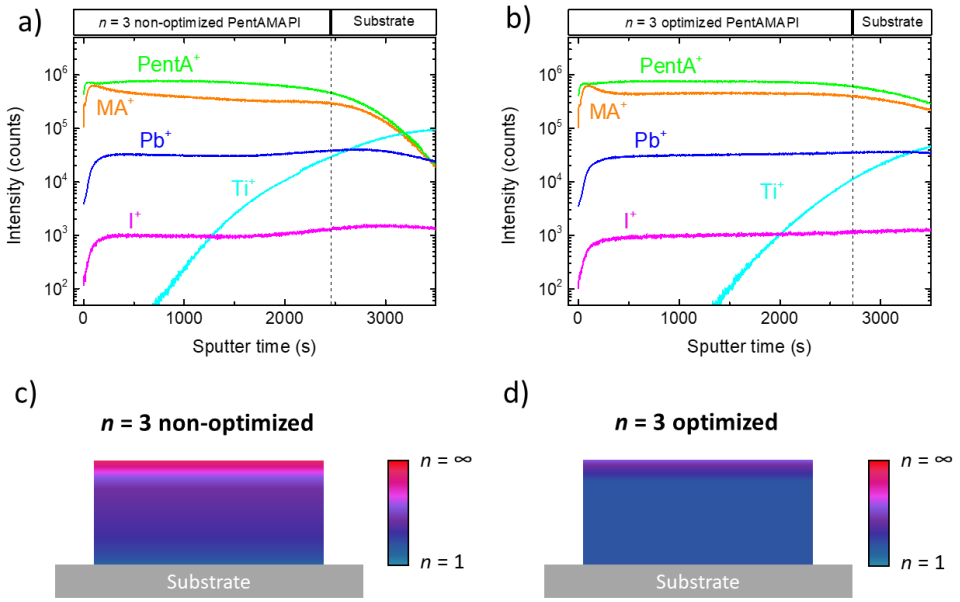

Figure 7.11 Positive ToF-SIMS depth profiles of (a) non-optimized and (b) optimized n = 3 perovskite film on FTO/TiO_2 substrates. The dotted line is a guide to the eye for the estimated interface between perovskite and TiO_2. Proposed vertical distribution of crystal regions with different n-values for (c) non-optimized and (d) optimized n = 3 films.

Figure 7.11a–b shows the positive ToF-SIMS depth profiles of the non-optimized and the optimized n = 3 films prepared on FTO/TiO_2 substrates. Similar trends are observed for both samples: the vertical distribution of $PentA^+$ cations is rather constant throughout the perovskite film, whereas a notable enrichment of MA^+ species is detected at the beginning of the sputtering process, i.e. at the film's surface. We interpret this observation as an indication for the formation of large-n regions on the very top of the perovskite film for both non-optimized and optimized n = 3 samples, with a gradient of decreasing n towards the bottom (Figure 7.11c–d). This finding is in excellent agreement with recent studies by Liu *et al.* and Shang *et al.*[31, 32] We note that the MA^+ depth profile for the optimized sample varies less after the initial rise than for the non-optimized sample. As evidenced by XRD and PL experiments, we observe a significantly improved phase purity for optimized n = 3 films. We therefore propose that the main phase is n = 3, as desired, with a small fraction of n > 3 phases at the sample surface.

Having identified several factors which affect the disparity in crystal disorder and orientation in 2D perovskite thin films, such as the precursor stoichiometry, the solvent and the annealing temperature, we need to understand how these factors relate to each other. Such knowledge may enable us to control the formation process of 2D perovskite films. Herein, we attempt to rationalize the large variation in n and the changes in crystal orientation, from horizontal to vertical, in 2D perovskite thin

films, caused by changes in precursor stoichiometry without adjusting the solvent. Moreover, we propose a simple film formation mechanism that offers a possible explanation for the role of the solvent additives and the annealing temperature in achieving an improved phase purity of 2D perovskite layers.

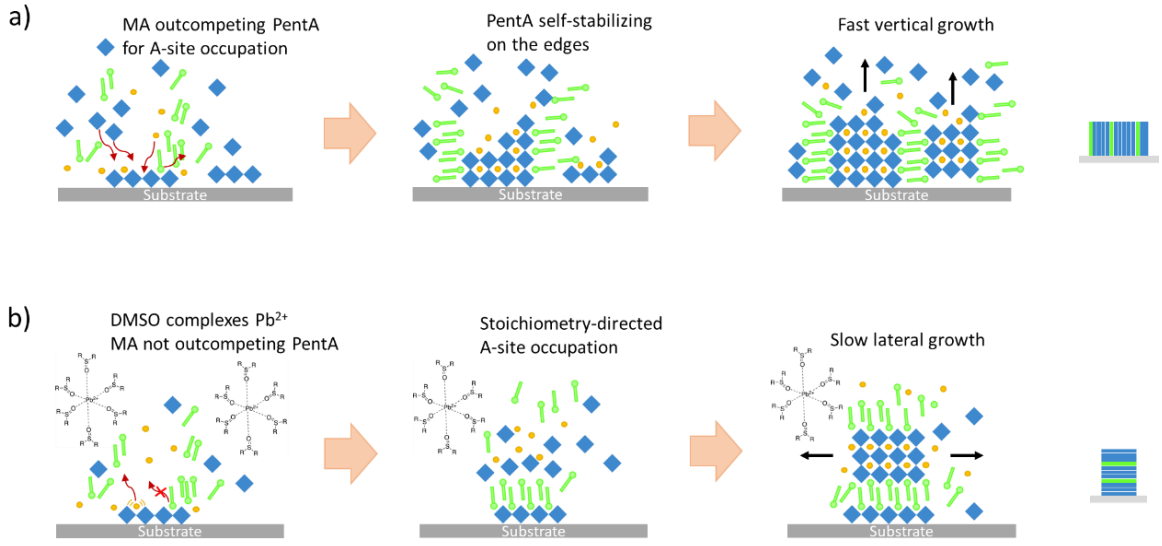

Figure 7.12 Schematic illustration of the hypothesized formation mechanism for (a) non-optimized n = 3 films via fast vertical growth and (b) optimized n = 3 films via solvent additive-assisted slow lateral growth.

Figure 7.12a shows a schematic illustration of the proposed crystallization mechanism for the non-optimized DMF-based n = 3 film. First, we assume that heterogeneous nucleation commences with the formation of PbI_6 octahedra clusters at the liquid–substrate interface. Since both MA and PentA cations possess a positively charged ammonium group to bind to the exposed A-site on top of the octahedra, a competition between these two species occurs. Despite the 1:1 ratio of MA and PentA, it is likely that MA outcompetes the PentA cations and successfully binds to the favorable A-site due to its smaller ionic radius and stronger dipole moment. The small MA cations can then be quickly "locked-in" by free PbI_x clusters, which are abundant in the DMF precursor solution. At the same time the facile evaporation of the DMF solvent induces fast vertical growth of perovskite layers, whereas the PentA cations are pushed to the edge of the growing perovskite "wall", stabilizing themselves via van-der-Waals forces between the alkyl chains and thus forming the organic bilayer. For $n > 2$, this rapid vertical growth seems to dominate, which could explain the broad distribution of octahedra layer thicknesses.

When DSMO or THTO is added to the precursor solution, the kinetics of the film growth change dramatically. It has been shown by Foley *et al.* that the sulfoxide group of DMSO and particularly THTO strongly interact with Pb^{2+} ions in the solution, forming stable complexes.[34, 35] The authors demonstrated that THTO slows down the crystallization process of $MAPbI_3$, which leads to an unusual (100) crystal orientation in the resulting 3D perovskite film. In the case of 2D perovskites, this interaction between solvent additive and Pb^{2+}, in combination with a slow annealing process at low temperatures, presumably has two major effects on the growth dynamics of the 2D perovskite film, as schematically illustrated in Figure 7.12b:

(i) Pb^{2+} is withheld in the liquid phase in the form of sulfoxide-complexes, thus reducing the amount of available PbI_x clusters, meaning that the MA cations cannot be immediately "locked-in" after occupying the A-sites. This might allow the large PentA cations to compete with the smaller MA cations for the preferred top A-site, thereby forming organic PentA bilayers parallel to the substrate.

(ii) The slow, controlled horizontal growth at low initial annealing temperatures enables the stoichiometry between MA and PentA to define the final layer thickness of the perovskite sheet. Our results show that this leads to 2D perovskite films which show substantially less variation in *n* from the target value than films grown from a fast crystallization process through immediate annealing at high temperatures.

Minimizing the variation in *n* within 2D perovskite films is not only important from a theoretical point of view, but it can also have a profound impact on device performance. The potential migration of mobile charge carriers in the mixed-phase 2D perovskite layer to low-*n* regions might result in a lower open-circuit voltage in perovskite solar cells than expected from a high band gap 2D perovskite material. In perovskite-based light emitting diodes (LEDs), this charge transfer in mixed-phase 2D perovskite layer might result in the requirement for a greater driving overpotential relative to the energy of emitted photons. Hence, approaches to control the disorder within 2D perovskites will have significant technological importance.

Another important aspect arising from the structural anisotropy of 2D perovskites is their crystal orientation when fabricated as thin films. To date, conventional preparation methods for thin films of 2D perovskite phases formed from $n > 2$ solutions result in layers oriented perpendicular to the substrate. For photovoltaic applications, this is considered to be an advantage since the standard solar cell architectures require transport of charge carriers perpendicular to the substrate. Charge transport is likely to be confined within the perovskite component of the layers, since the addition of organic interlayers oriented perpendicularly to the charge transport direction leads to a notable drop in current.[36] However, there are many potential applications of 2D perovskites where lateral charge transport would be beneficial, for example in a back-contact solar cell or a field effect transistor

architecture.[37-40] In this case, conducting perovskite layers which are oriented parallel to the substrate might also have a potential advantage of inhibiting the migration of ionic defects to or from the gate electrode, which might reduce screening of the gate voltage by ionic rather than electronic charge. By establishing a facile additive-assisted fabrication method to control the orientation of the perovskite layers, our work considerably enlarges the potential thin film-based application fields for 2D perovskites.

7.4 Conclusion

In conclusion, we established a simple one-step fabrication method for 2D perovskite films using lead-complexing solvent additives and a carefully controlled annealing process to substantially reduce the variation in the octahedra layer thickness n from the target value. Furthermore, we demonstrate that for the specific $n = 3$ case, our optimized films show similar PL features as reported for $n = 3$ perovskite single crystals, whereas the PL signal of films resulting from fast crystallization from DMF-solutions without solvent additives is largely dominated by photoemission from perovskite interlayers with $n >> 3$. In addition, our solvent engineering approach leads to predominantly horizontal crystal orientation in the $n = 2$ and $n = 3$ films, which opens the doorway for a wide range of potential applications of 2D perovskites which require lateral charge transport.

7.5 Methods

Synthesis of cation salts

PentAI crystals were synthesized by adding dropwise 15 mL HI (57 wt% in water, in-house supplier) to a mixture of 13.5 mL 1-pentylamine (99%, Sigma-Aldrich) and 100 mL ethanol (absolute, in-house supplier) under ice-cooling and vigorous stirring. The solution was stirred for 30 min at room temperature. After removal of the solvent by rotary evaporation at 50 °C, the white precipitate was redissolved several times in ethanol and recrystallized from dry isopropanol (in-house supplier). The obtained colorless crystals were filtered, washed with diethyl ether (anhydrous, Sigma-Aldrich) and dried in vacuum for 4 h.

Precursor Solutions

All steps of the preparation of the perovskite precursor solutions and the thin films were conducted in a glove box under dry nitrogen atmosphere. Using the generic chemical formula for the 2D hybrid lead halide perovskites $(PentA)_2(MA)_{n-1}Pb_nI_{3n+1}$, the stoichiometry of the precursors PentAI, MAI (Dyesol) and PbI_2 (99.99%, TCI) was determined for octahedra interlayer thicknesses of n = 1, 2 or 3. The PentAI:MAI:PbI_2 ratios were 2:0:1 mmol, 1:0.5:1 mmol, 0.4:0.4:0.6 mmol and 0.333:0.333:0.5 mmol for n = 1, 2, non-optimized n = 3 and optimized n = 3 respectively, in 1 mL of DMF (anhydrous, Sigma-Aldrich). An overview is given in Table 7.1. The precursors were dissolved at 100 °C, the bright yellow solution was cooled to room temperature and filtered through a 0.45 µm syringe filter. As solvent additives, 100 µL of THTO (97%, Sigma-Aldrich) and 100 µL DMSO (anhydrous, Sigma-Aldrich) were added to 1 mL of the DMF-based n = 2 precursor solution. Similarly, 350 µL DMSO was added to 1 mL of the n = 3 precursor solution for the optimized recipe. The stoichiometric $MAPbI_3$ solution contained 1.25 mmol of PbI_2 and MAI respectively, dissolved in a mixture of 800 µL DMF and 200 µL DMSO.

Thin Film Fabrication

For n = 1, 2 and non-optimized n = 3 films, 50 µL of the respective precursor solution was dynamically spin-coated on a plasma-cleaned glass substrate (2.5 × 2.5 cm) at 3000 rpm for 40 s. The optimized n = 3 films were spin-coated at 4000 rpm. Afterwards, the substrate was annealed on a hotplate to evaporate residual solvents and to further promote crystallization. The n = 1 and the non-optimized n = 2 and 3 films were annealed at 100 °C for 5 min. The optimized n = 2, 3 films were annealed first at 40 °C for 30 min, then at 75 °C for 5 min and finally at 100 °C for 2 min. $MAPbI_3$ was spin-coated in a two-step program at 1000 rpm and 5000 rpm for 10 s and 30 s respectively. 500 µL chlorobenzene (anhydrous, Sigma-Aldrich) were added as an anti-solvent to the spinning film at 15 s before the end. The $MAPbI_3$ sample was annealed at 40 °C for 40 min and finally at 100 °C for 10 min.

Table 7.1 Composition of precursor solutions and fabrication parameters for (non)-optimized n = 1, 2 and 3 PentA(MA)PI perovskite films.

		n = 1 non-optimized	n = 2 non-optimized	n = 3 non-optimized	n = 2 optimized	n = 3 optimized
precursor solution	PbI_2 [mg]	461.01	461.01	276.6	461.01	230.5
	MAI [mg]	0	79.48	63.6	79.48	53.0
	PentAI [mg]	430.34	215.17	86.1	215.17	71.7
	DMF [µL]	1000	1000	1000	1000	1000
	DMSO [µL]	0	0	0	100	350
	THTO [µL]	0	0	0	100	0
spin-coating	speed [rpm]	3000	3000	3000	3000	4000
annealing protocol		100 °C, 5 min	100 °C, 5 min	100 °C, 5 min	40 °C, 30 min; 75 °C, 5 min; 100 °C, 2 min	40 °C, 30 min; 75 °C, 5 min; 100 °C, 2 min

Characterization

XRD measurements were carried out with a Bruker D8 Discover X-ray diffractometer operating at 40 kV and 30 mA, employing Ni-filtered Cu $K_{\alpha1}$ radiation (λ = 1.5406 Å) and a position-sensitive LynxEye detector. A step size of $\Delta 2\theta$ = 0.05° and a scan speed of 0.1 s per step were employed.

2D grazing-incident wide angle X-ray scattering (GIWAXS) data were collected using an Anton-Paar Saxspace system equipped with a Cu $K_{\alpha1}$ microfocus source operated at 50 kV and 1 mA and an Eiger Dectris R 1M 2D detector. SEM images were recorded with an FEI Helios Nanolab G3 UC DualBeam scanning electron microscope, operated at an acceleration voltage of 4 kV.

AFM measurements were carried out with a NANOINK atomic force microscope in tapping mode with a scan rate of 0.3 Hz, a proportional gain of 30 and an integral gain of 15.

UV-Vis absorption spectra were recorded using a Perkin Elmer Lambda 1050 spectrophotometer equipped with a 150 mm integrating sphere.

Room temperature steady-state PL spectroscopy was performed with a Fluotime 300 spectrofluorometer (Picoquant). The samples were excited using a 405 nm (for n = 1 or 2) laser or a 510 nm laser (for n = 3 or $MAPbI_3$) operated at 20 MHz repetition rate and excited from the perovskite-coated side. To perform PL measurements as a function of temperature, the samples were placed in a closed cycle helium cryostat. The excitation source was a 485 nm pulsed laser (PicoQuant) with a repetition rate of 2 MHz and an average power of 0.6 µW. A mechanical chopper was used to measure the quasi-PL signal. The emitted PL was dispersed by a spectrometer (Acton SP2500i, Princeton Instruments) and measured by a GaAs photomultiplier tube (Photonic Solutions). The quasi-PL signal was recorded by a lock-in amplifier (SR830, Stanford Research).

Depth profiles of perovskite films on glass/FTO/TiO_2 substrates were measured with a ToF-SIMS 5 setup from IONTOF GmbH. Sputtering was performed using Ar^+-clusters with 2.5 keV ion energy on a 300 × 300 µm² raster size. Inside this sputter region an area of about 100 × 100 µm² was analyzed using Bi_3^+ ions with 30 keV ion energy.

7.6 References

[1] H. Tsai, W. Nie, J.-C. Blancon, C. C. Stoumpos, R. Asadpour, B. Harutyunyan, A. J. Neukirch, R. Verduzco, J. J. Crochet, S. Tretiak, L. Pedesseau, J. Even, M. A. Alam, G. Gupta, J. Lou, P. M. Ajayan, M. J. Bedzyk, M. G. Kanatzidis, A. D. Mohite, *Nature* **2016**, *536*, 312.

[2] C. C. Stoumpos, D. H. Cao, D. J. Clark, J. Young, J. M. Rondinelli, J. I. Jang, J. T. Hupp, M. G. Kanatzidis, *Chem. Mater.* **2016**, *28*, 2852.

[3] S. A. Veldhuis, P. P. Boix, N. Yantara, M. Li, T. C. Sum, N. Mathews, S. G. Mhaisalkar, *Adv. Mater.* **2016**, *28*, 6804.

[4] N. Wang, L. Cheng, R. Ge, S. Zhang, Y. Miao, W. Zou, C. Yi, Y. Sun, Y. Cao, R. Yang, Y. Wei, Q. Guo, Y. Ke, M. Yu, Y. Jin, Y. Liu, Q. Ding, D. Di, L. Yang, G. Xing, H. Tian, C. Jin, F. Gao, R. H. Friend, J. Wang, W. Huang, *Nat Photon* **2016**, *10*, 699.

[5] E. R. Dohner, A. Jaffe, L. R. Bradshaw, H. I. Karunadasa, *J. Am. Chem. Soc.* **2014**, *136*, 13154.

[6] M. E. Kamminga, H.-H. Fang, M. R. Filip, F. Giustino, J. Baas, G. R. Blake, M. A. Loi, T. T. M. Palstra, *Chem. Mater.* **2016**, *28*, 4554.

[7] X. Zhang, X. Ren, B. Liu, R. Munir, X. Zhu, D. Yang, J. Li, Y. Liu, D.-M. Smilgies, R. Li, Z. Yang, T. Niu, X. Wang, A. Amassian, K. Zhao, S. Liu, *Energy. Environ. Sci.* **2017**.

[8] R. Li, C. Yi, R. Ge, W. Zou, L. Cheng, N. Wang, J. Wang, W. Huang, *Appl. Phys. Lett.* **2016**, *109*, 151101.

[9] S. Kumar, J. Jagielski, N. Kallikounis, Y. H. Kim, C. Wolf, F. Jenny, T. Tian, C. Hofer, Y.-C. Chiu, W. J. Stark, T.-W. Lee, C.-J. Shih, *Nano Lett.* **2017**.

[10] J. Calabrese, N. L. Jones, R. L. Harlow, N. Herron, D. L. Thorn, Y. Wang, *J. Am. Chem. Soc.* **1991**, *113*, 2328.

[11] T. Ishihara, J. Takahashi, T. Goto, *Solid State Commun.* **1989**, *69*, 933.

[12] D. B. Mitzi, *J. Chem. Soc., Dalton Trans.* **2001**, 1.

[13] I. C. Smith, E. T. Hoke, D. Solis-Ibarra, M. D. McGehee, H. I. Karunadasa, *Angew. Chem. Int. Ed.* **2014**, *53*, 11232.

[14] D. H. Cao, C. C. Stoumpos, O. K. Farha, J. T. Hupp, M. G. Kanatzidis, *J. Am. Chem. Soc.* **2015**, *137*, 7843.

[15] Y. Hu, J. Schlipf, M. Wussler, M. L. Petrus, W. Jaegermann, T. Bein, P. Muller-Buschbaum, P. Docampo, *ACS Nano* **2016**, *10*, 5999.

[16] T. M. Koh, K. Thirumal, H. S. Soo, N. Mathews, *ChemSusChem* **2016**, *9*, 2541.

[17] C. Ma, C. Leng, Y. Ji, X. Wei, K. Sun, L. Tang, J. Yang, W. Luo, C. Li, Y. Deng, S. Feng, J. Shen, S. Lu, C. Du, H. Shi, *Nanoscale* **2016**, *8*, 18309.

[18] L. N. Quan, M. Yuan, R. Comin, O. Voznyy, E. M. Beauregard, S. Hoogland, A. Buin, A. R. Kirmani, K. Zhao, A. Amassian, D. H. Kim, E. H. Sargent, *J. Am. Chem. Soc.* **2016**, *138*, 2649.

[19] Z. Yuan, Y. Shu, Y. Xin, B. Ma, *Chem. Commun.* **2016**, *52*, 3887.

[20] R. L. Milot, R. J. Sutton, G. E. Eperon, A. A. Haghighirad, J. Martinez Hardigree, L. Miranda, H. J. Snaith, M. B. Johnston, L. M. Herz, *Nano Lett.* **2016**, *16*, 7001.

[21] W. Peng, J. Yin, K.-T. Ho, O. Ouellette, M. De Bastiani, B. Murali, O. El Tall, C. Shen, X. Miao, J. Pan, E. Alarousu, J.-H. He, B. S. Ooi, O. F. Mohammed, E. Sargent, O. M. Bakr, *Nano Lett.* **2017**, *17*, 4759.

[22] X. Wu, M. T. Trinh, D. Niesner, H. Zhu, Z. Norman, J. S. Owen, O. Yaffe, B. J. Kudisch, X. Y. Zhu, *J. Am. Chem. Soc.* **2015**, *137*, 2089.

[23] Z. Guo, X. Wu, T. Zhu, X. Zhu, L. Huang, *ACS Nano* **2016**, *10*, 9992.

[24] C. C. Stoumpos, C. M. M. Soe, H. Tsai, W. Nie, J.-C. Blancon, D. H. Cao, F. Liu, B. Traoré, C. Katan, J. Even, A. D. Mohite, M. G. Kanatzidis, *Chem* **2017**, *2*, 427.

[25] S. Zhang, P. Audebert, Y. Wei, A. Al Choueiry, G. Lanty, A. Bréhier, L. Galmiche, G. Clavier, C. Boissière, J.-S. Lauret, E. Deleporte, *Materials* **2010**, *3*, 3385.

[26] M. L. Petrus, Y. Hu, D. Moia, P. Calado, A. M. A. Leguy, P. R. F. Barnes, P. Docampo, *ChemSusChem* **2016**, *9*, 2699.

[27] D. B. Mitzi, D. R. Medeiros, P. R. L. Malenfant, *Inorg. Chem.* **2002**, *41*, 2134.

[28] S. Ahmad, P. K. Kanaujia, H. J. Beeson, A. Abate, F. Deschler, D. Credgington, U. Steiner, G. V. Prakash, J. J. Baumberg, *ACS Appl. Mater. Interfaces* **2015**, *7*, 25227.

[29] S. Gonzalez-Carrero, G. M. Espallargas, R. E. Galian, J. Perez-Prieto, *J. Mater. Chem. A* **2015**, *3*, 14039.

[30] Y. Lin, Y. Bai, Y. Fang, Q. Wang, Y. Deng, J. Huang, *ACS Energy Lett.* **2017**, 1571.

[31] Q. Shang, Y. Wang, Y. Zhong, Y. Mi, L. Qin, Y. Zhao, X. Qiu, X. Liu, Q. Zhang, *J. Phys. Chem. Lett.* **2017**, *8*, 4431.

[32] J. Liu, J. Leng, K. Wu, J. Zhang, S. Jin, *J. Am. Chem. Soc.* **2017**, *139*, 1432.

[33] J. A. Koza, J. C. Hill, A. C. Demster, J. A. Switzer, *Chem. Mater.* **2016**, *28*, 399.

[34] B. J. Foley, J. Girard, B. A. Sorenson, A. Z. Chen, J. Scott Niezgoda, M. R. Alpert, A. F. Harper, D.-M. Smilgies, P. Clancy, W. A. Saidi, J. J. Choi, *J. Mater. Chem. A* **2017**, *5*, 113.

[35] J. Stevenson, B. Sorenson, V. H. Subramaniam, J. Raiford, P. P. Khlyabich, Y.-L. Loo, P. Clancy, *Chem. Mater.* **2017**, *29*, 2435.

[36] Y. Hu, J. Schlipf, M. Wussler, M. L. Petrus, W. Jaegermann, T. Bein, P. Müller-Buschbaum, P. Docampo, *ACS Nano* **2016**, *10*, 5999.

[37] A. N. Jumabekov, E. Della Gaspera, Z. Q. Xu, A. S. R. Chesman, J. van Embden, S. A. Bonke, Q. Bao, D. Vak, U. Bach, *J. Mater. Chem. C* **2016**, *4*, 3125.

[38] X. Lin, A. N. Jumabekov, N. N. Lal, A. R. Pascoe, D. E. Gómez, N. W. Duffy, A. S. R. Chesman, K. Sears, M. Fournier, Y. Zhang, Q. Bao, Y.-B. Cheng, L. Spiccia, U. Bach, *Nat. Commun.* **2017**, *8*, 613.

[39] J. Liu, Y. Xue, Z. Wang, Z.-Q. Xu, C. Zheng, B. Weber, J. Song, Y. Wang, Y. Lu, Y. Zhang, Q. Bao, *ACS Nano* **2016**, *10*, 3536.

[40] S. P. Senanayak, B. Yang, T. H. Thomas, N. Giesbrecht, W. Huang, E. Gann, B. Nair, K. Goedel, S. Guha, X. Moya, C. R. McNeill, P. Docampo, A. Sadhanala, R. H. Friend, H. Sirringhaus, *Sci. Adv.* **2017**, *3*, e1601935.

8 Design of 2D/3D perovskite bilayers for stable solar cells

This chapter is based on the following publication:

Y. Hu, J. Schlipf, M. Wussler, M. L. Petrus, W. Jaegermann, T. Bein, P. Müller-Buschbaum, P. Docampo, Hybrid Perovskite/Perovskite Heterojunction Solar Cells. *ACS Nano* **2016**, *10* (6), 5999-6007. (DOI: 10.1021/acsnano.6b01535)

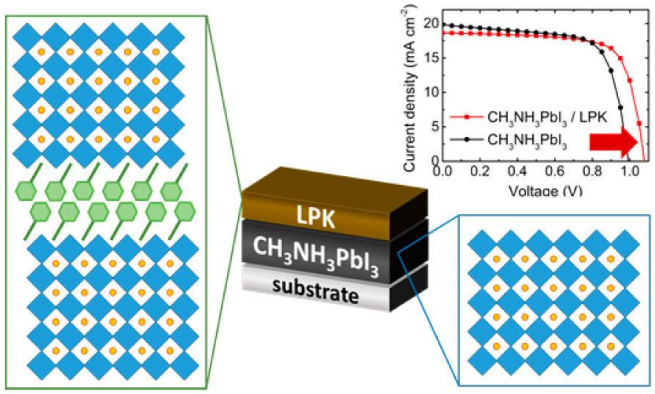

Adapted with permission.[1] Copyright 2017, American Chemical Society.

8.1 Abstract

Recently developed organic-inorganic hybrid perovskite solar cells combine low-cost fabrication and high power conversion efficiency. Advances in perovskite film optimization have led to an outstanding power conversion efficiency of more than 20%. Looking forward, shifting the focus toward new device architectures holds great potential to induce the next leap in device performance. Here, we report the demonstration of a perovskite/perovskite heterojunction solar cell. We developed a facile solution-based cation infiltration process to deposit layered perovskite (LPK) structures onto methylammonium lead iodide (MAPI) films. Grazing-incidence wide-angle X-ray scattering experiments were performed to gain insights into the crystallite orientation and the formation process of the perovskite bilayer. Our results show that the self-assembly of the LPK layer on top of an intact MAPI layer is accompanied by a reorganization of the perovskite interface. This leads to an enhancement of the open-circuit voltage and power conversion efficiency due to reduced recombination losses, as well as improved moisture stability in the resulting photovoltaic devices.

8.2 Introduction

Recently, a serious contender for the established photovoltaic technologies has emerged at an unprecedented pace: organic-inorganic hybrid perovskite solar cells (PSCs). Hybrid perovskites combine low material costs, solution processability and impressive device performance.[2-8] The state-of-the-art power conversion efficiency (PCE) has already exceeded 20% in less than five years of development.[9] This rapid progress has been fueled by a better understanding and control of the perovskite crystallization processes and thus improvements to the resulting film quality.[10-15] However, there is still room for improvement to reach the theoretical maximum of 31% efficiency.[16] Looking forward, shifting the focus toward new device architectures holds the potential to induce the next leap in device performance.

Interfacial engineering has been proven to be a versatile tool to boost the performance of mature photovoltaic technologies, such as crystalline Si.[17] Great efforts have been made to explore new interfacial materials for PSCs.[18-22] The common device architecture is based on an n-i-p heterojunction: the perovskite film is sandwiched between an electron transporter such as TiO_2[18] or PCBM[21, 22] and a hole transporting layer such as spiro-OMeTAD,[23] Poly(triarylamine) (PTAA),[24] or PEDOT:PSS[25]. Nevertheless, an all-perovskite junction with similar hybrid perovskites serving as charge extraction layers may overcome current limitations due to high conductivity and a reduction

of lattice mismatch between the crystal structures. The large variety of hybrid perovskites and the ability to tune their optical and electronic properties make a perovskite/perovskite heterojunction device a likely candidate to enhance device efficiency.

An example of a highly tunable perovskite system is the re-emerging family of layered perovskites (LPKs), which has attracted considerable attention due to unique crystal structures and optoelectronic properties.[26-31] By partially substituting small methylammonium cations for bulkier ones, the resulting compound resembles a multiquantum well structure with alternating layers of corner-sharing lead halide octahedra and sheets of long-chained hydrophobic cations. Tailoring the bulkier cation leads to a modulation of the density of states of the material, thereby giving access to a large variety of new optoelectronic materials. To date, however, LPKs generally show poor photovoltaic performance (PCE < 5%).[32, 33]

Here, we have developed a facile solution process to fabricate a MAPI/LPK heterojunction that unifies the benefits of both materials: a bottom MAPI layer ensures efficient light absorption and charge generation, whereas an LPK top layer serves as selective charge extraction layer and moisture barrier. The crystal structure of the self-organized LPK incorporating methylammonium (MA^+ = $CH_3NH_3^+$) and long-chained phenylethylammonium (PEA^+ = $C_6H_5C_2H_4NH_3^+$) or *n*-butylammonium (BA^+ = $C_4H_9NH_3^+$) cations was determined by X-ray diffraction (XRD). Grazing-incidence wide angle X-ray scattering (GIWAXS) experiments were performed to gain insights into the crystallite orientation and the formation process of the perovskite bilayer. This paper presents the demonstration of perovskite/perovskite heterojunction solar cells with device performances up to PCE = 16.84% due to enhanced open-circuit voltage and fill factor, complemented by enhanced moisture stability.

8.3 Results and discussion

8.3.1 Film fabrication and characterization

A schematic illustration of the perovskite/perovskite heterojunction is depicted in Figure 8.1a. To convert the top layer of the MAPI perovskite into an LPK, an isopropyl alcohol (IPA) solution containing methylammonium iodide (MAI) and phenylethylammonium iodide (PEAI) or *n*-butylammonium iodide (BAI) is spin-coated onto the MAPI film.

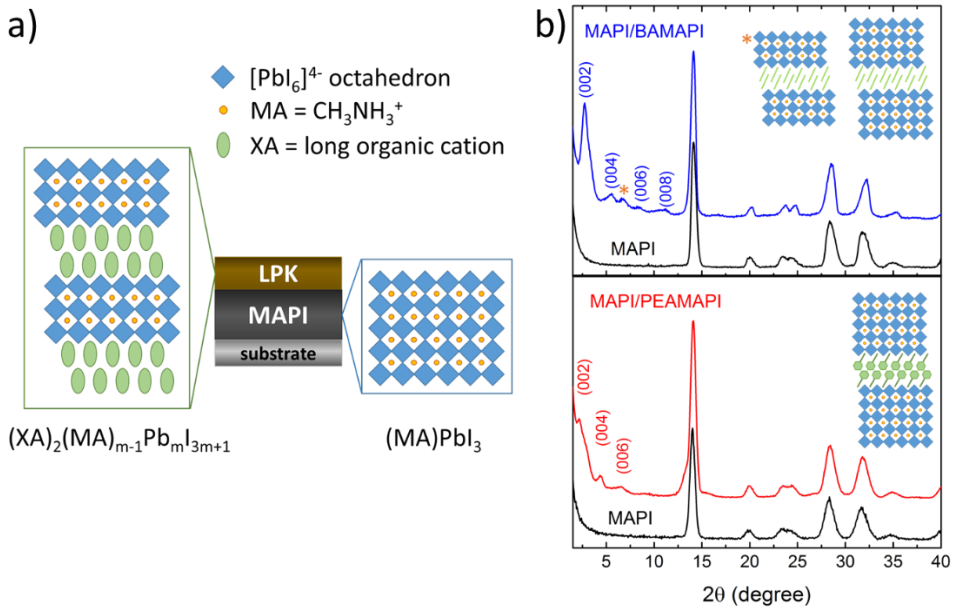

Figure 8.1 Structural analysis of the perovskite/perovskite heterojunction. (a) Schematic illustration of the crystal structures of methylammonium lead iodide (MAPI) and a layered perovskite (LPK), forming the junction. (b) XRD pattern of a MAPI film (black) compared to a MAPI/BAMAPI film (blue) and a MAPI/PEAMAPI film (red) recorded with grazing-incidence geometry. Both the MAPI bottom layer and the LPK top layer are probed with the X-rays at the incident angle of 0.5°. The insets show schematic representations of the corresponding LPK structure and the indexed peaks refer to expected (00*l*) reflections, respectively.

Figure 8.1b shows the X-ray diffraction (XRD) patterns of a MAPI film before and after treatment with a PEAI:MAI or BAI:MAI solution, respectively. Besides typical diffraction peaks of the tetragonal MAPI phase, the XRD pattern of the BAI:MAI modified perovskite film exhibits several additional reflections in the 2θ range at 2.73°, 5.56°, 8.43°, and 11.17°. The newly emerging peaks correspond to (00*l*) lattice planes (with $l = 2n$) of the previously reported layered perovskite $(BA)_2(MA)_3(Pb_4I_{13})$ (in the following referred to as BAMAPI).[32] In addition, a minor reflection appears at $2\theta = 6.81°$ (marked with an asterisk) which can be ascribed to the (004) planes of a related LPK: $(BA)_2(MA)_2(Pb_3I_{10})$. We note that the formation of BAMAPI is highly sensitive to the stoichiometry of the casting solution, meaning that an excess of one of the cations can lead to the crystallization of an LPK exhibiting a different thickness of the $[PbI_6]$ octahedra layers. In contrast, the XRD pattern of the PEAI:MAI treated MAPI film shows the signature of only one layered compound, with diffraction peaks at $2\theta = 2.16°$, 4.37°, and 6.53°, in addition to the MAPI reflections. Assuming a similar LPK structure, we can ascribe these features to the (00*l*) lattice planes of $(PEA)_2(MA)_4(Pb_5I_{16})$ (referred to as PEAMAPI) with an estimated interplanar spacing d_{002} = 40.8 Å

(Table 8.1). Details on the estimation of the peak positions for different potential LPK structures incorporating PEA^+ and MA^+ are given in the Methods section.

Table 8.1 Estimated 2θ positions of (00l) reflections for the series of layered perovskites $(PEA)_2(MA)_{m-1}(Pb_mI_{3m+1})$ with m as the thickness of $[PbI_6]$ octahedra layer, utilizing Cu $K_{\alpha 1}$ radiation, λ = 1.5406 Å.

Diffraction peaks		d_{002} [Å]	2θ [°] (002)	2θ [°] (004)	2θ [°] (006)
Experimental			2.16	4.37	6.53
Estimated	m = 4	34.7	2.54	5.09	7.63
	m = 5	40.8	2.16	4.32	6.48
	m = 6	46.9	1.88	3.77	5.65
	m = 7	53.0	1.67	3.33	5.00
	m = 8	59.1	1.49	2.99	4.48

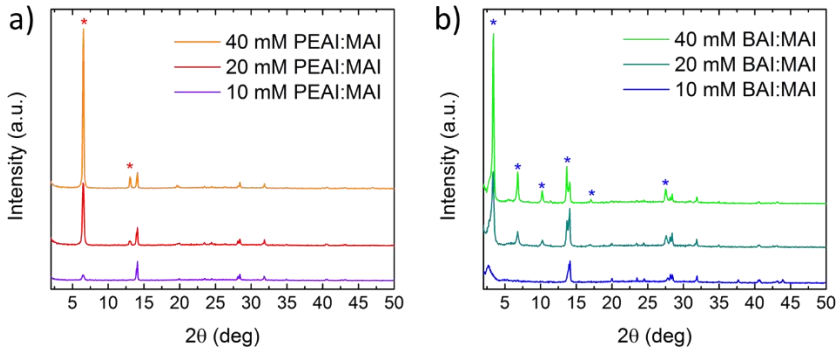

Figure 8.2 XRD patterns of (a) MAPI/PEAMAPI and (b) MAPI/BAMAPI bilayer films fabricated with different concentrations of the casting solution. The diffraction peaks of PEAMAPI and BAMAPI are marked with asterisks, respectively.

We fabricated MAPI/LPK bilayer films with different concentrations of the spin-coated cation mixture solution, and the corresponding XRD patterns are shown in Figure 8.2. An increase of the overall concentration leads to higher intensities of the PEAMAPI and BAMAPI reflections with narrower peak widths, indicating the formation of a thicker LPK top layer. We performed Scherrer analysis of the most intense (00l) reflection of the LPK phase to determine the crystallite size, which correlates with the thickness of the LPK top layer. The estimated crystallite sizes for the PEAMAPI and BAMAPI phases are summarized in Table 8.2. The increase in crystallite size with increasing

concentration confirms that the thickness of the self-assembled LPK layer can be tuned by the concentration of the casting solution. Besides, our results suggest that the addition of MAI to the spin-coated solution is necessary to form a pure LPK phase on top of an intact MAPI film. The absence of MAI in the solution leads to the crystallization of undesirable side phases such as PEAI (Figure 8.3).

Table 8.2 Estimated crystallite size of the layered perovskite $(BA)_2(MA)_{m-1}(Pb_mI_{3m+1})$ and $(PEA)_2(MA)_{m-1}(Pb_mI_{3m+1})$ fabricated with different concentrations of the respective casting solution.

Layered Perovskite	Casting solution	$[PbI_6]$ layer thickness	Reflection (*hkl*)	B_{total} [°]	2θ [°]	D [nm]
BAMAPI	10 mM BAI:MAI	$m = 4$	(002)	0.498	2.69	16
		$m = 3$	(002)	0.873	3.13	9
	20 mM BAI:MAI	$m = 4$	(002)	0.683	3.13	12
		$m = 3$	(002)	0.241	3.36	34
	40 mM BAI:MAI	$m = 4$	(002)	0.427	2.87	19
		$m = 3$	(002)	0.178	3.39	48
PEAMAPI	10 mM PEAI:MAI	$m = 5$	(006)	0.361	6.50	22
	20 mM PEAI:MAI	$m = 5$	(006)	0.277	6.50	29
	40 mM PEAI:MAI	$m = 5$	(006)	0.188	6.52	45

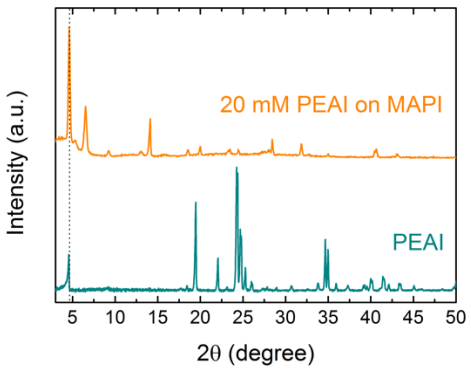

Figure 8.3 XRD pattern of a MAPI film treated with a 20 mM PEAI solution in isopropanol and powder XRD pattern of PEAI crystals. The absence of MAI in the casting solution leads to the crystallization of PEAI.

As the MAPI/PEAMAPI system offers better control over phase purity than MAPI/BAMAPI, we chose it as a model system to study the distribution of the LPK within the mixed-perovskite film. X-

ray photoelectron spectroscopy (XPS) is a powerful tool to probe the surface properties of thin films. The MAPI/PEAMAPI film and the MAPI film both exhibit a peak at 286.6 eV in the XPS spectrum (Figure 8.4), which can be ascribed to the C 1s signal of the carbon atom neighboring the NH_3^+-group in MA^+. The C 1s signal arising from MA^+ is also present in the MAPI/PEAMAPI film, since methylammonium is also incorporated in the layered PEAMAPI perovskite structure. However, the MAPI/PEAMAPI sample shows an additional peak at 285.4 eV, which is likely to originate from the C 1s signature of carbon atoms within the aromatic ring of the PEA^+ cations. As XPS is only surface-sensitive, this result confirms the formation of PEAMAPI on top of MAPI.

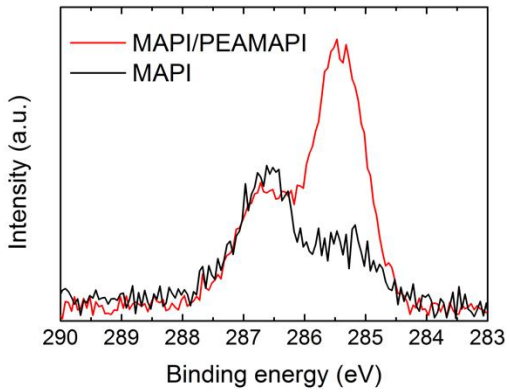

Figure 8.4 XPS spectra indicating the C 1s peaks of MAPI and MAPI/PEAMAPI films on glass, respectively.

Furthermore, grazing incidence wide-angle X-ray scattering (GIWAXS) has been proven to be a versatile technique to elucidate the crystallization mechanism of perovskite thin films as well as its effect on solar cell performance.[34-36] Here, we employed GIWAXS measurements to study the formation process of the MAPI/PEAMAPI heterojunction and to gain deeper insights into the crystallization process. Figure 8.5a–b depict the GIWAXS data obtained from a MAPI film and a MAPI/PEAMAPI perovskite bilayer film, with the in-plane component q_r and the vertical component q_z of the total momentum transfer q.

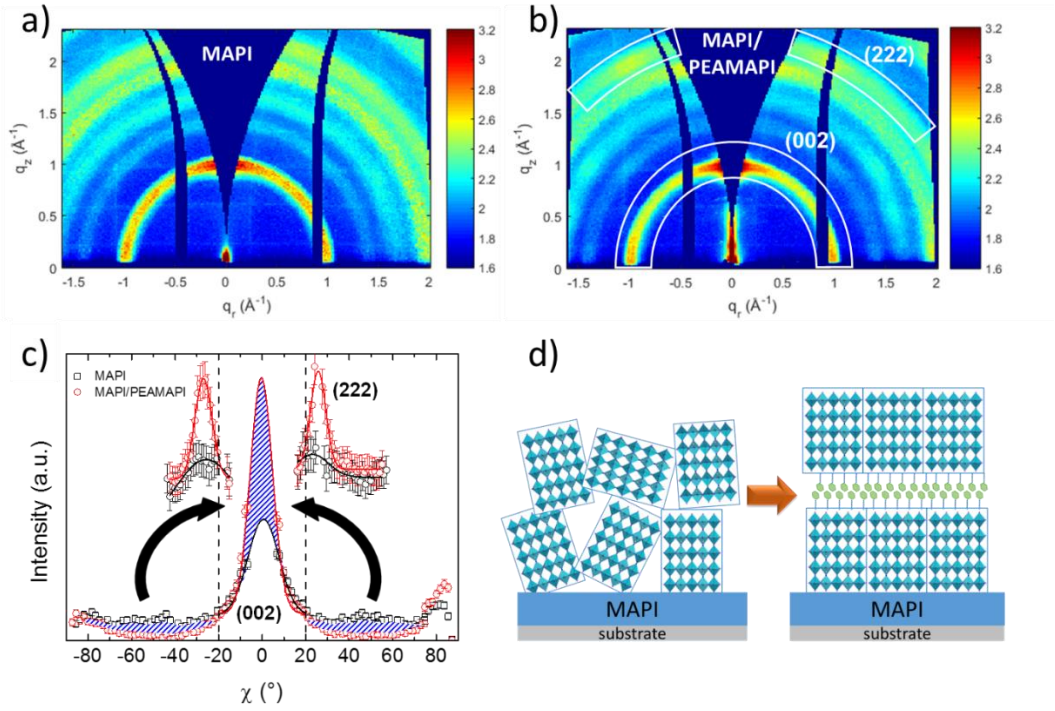

Figure 8.5 GIWAXS analysis for the perovskite/perovskite heterojunction. (a) 2D GIWAXS pattern of a MAPI film and (b) a MAPI/PEAMAPI bilayer film with highlighted (002) and (222) diffraction rings. (c). Azimuthal integration around $q = 1$ Å^{-1} (002) and $q = 2.2$ Å^{-1} (222) for quantitative evaluation of the conversion mechanism (dashed lines indicate the 2σ range). (d) Schematic interpretation of the surface reorganization of MAPI films upon PEAMAPI formation.

Both diffraction patterns exhibit the key features of the tetragonal MAPI perovskite structure, represented by the broad Debye-Scherrer rings at specific q values (e.g. $q = 1$ Å^{-1} corresponding to the (002) or (110) lattice planes). However, the GIWAXS pattern of the MAPI/PEAMAPI bilayer shows two features which differ from the MAPI film: the first one appears at low q values and does not form a complete ring pattern but is centered at $q_r = 0$ Å^{-1}. This indicates that the planes corresponding to this crystal structure are strongly oriented parallel to the substrate. We performed integration over all q values (Figure 8.6) and two distinct peaks at $q \approx 0.18$ Å^{-1} and 0.41 Å^{-1} are in agreement with the PEAMAPI peaks found in the XRD and thus corroborate the formation of a highly oriented PEAMAPI phase. The second feature is visible in the change of orientation distribution along the diffraction rings from the (002) and (004) planes of the tetragonal perovskite phase. The corresponding diffraction rings of the pure MAPI film (e.g. at $q = 1$ Å^{-1}) show a relatively homogeneous azimuthal intensity distribution, indicating an isotropic orientation distribution of the crystallites. In contrast, the MAPI/PEAMAPI film exhibits a higher diffraction intensity around $q_r = 0$ Å^{-1}, which suggests partial reorientation of crystallites upon formation of the PEAMAPI layer.

Considering the high orientation of the first feature at low q values we conclude that this increase in crystal orientation can be linked to the amount of PEAMAPI formed.

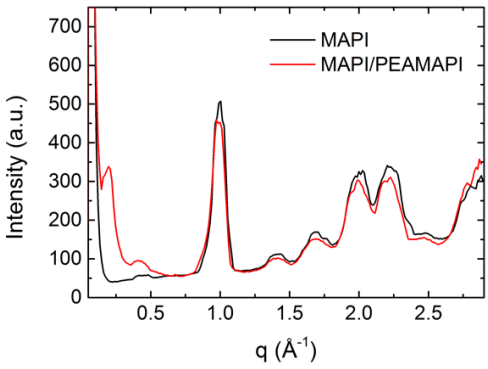

Figure 8.6 GIWAXS data for a MAPI film and a MAPI/PEAMAPI bilayer film, integrated over the complete q range. The two distinct peaks at $q \approx 0.18$ Å^{-1} and 0.41 Å^{-1} for the MAPI/PEAMAPI sample corroborate the formation of an oriented PEAMAPI perovskite layer.

Provided that the increased fraction of preferentially oriented crystallites arises only from the LPK, azimuthal integration around q = 1 Å^{-1} allows for quantitative evaluation of the conversion mechanism (Figure 8.5c): By fitting a Gaussian peak around the azimuthal angle χ = 0° and comparing differences of the areas within the 2σ range (95%) to the area outside this range, the amount of MAPI converted to PEAMAPI is determined as 7%. The use of a Gaussian peak shape to amend the data in the inaccessible range around χ = 0° is justified by comparison with an integration of the (222) peak. The beam footprint covers the entire sample at the incident angle of 0.4° and thus probes the same sample volume in both measurements. Consequently, the calculated difference directly translates to 7% of the film thickness or about 20 nm of PEAMAPI, equivalent to 4-5 layers of the LPK compound. This result is in very good agreement with the determined film thickness of PEAMAPI estimated from the Scherrer analysis of the (006) diffraction peak (see Table 8.2).

The above analysis assumes a more or less perfect orientation of the LPK layer parallel to the substrate. This assumption is justified by the following considerations: Spin-coating a PEAI:MAI solution from IPA presumably leads to a reorganization of the MAPI top layer, accompanied by fast deintercalation of MAI and intercalation of PEAI into the perovskite structure. PEA^+ cations form extended organic sheets due to steric effects, π-stacking of the phenyl-rings, and hydrogen-bonding interactions between the NH_3^+-group with the neighboring [PbI_6] octahedra layer, respectively.[27, 28, 37] It has been shown that long-chained organic cations can act as a template for the extremely

anisotropic growth of LPK crystals, resulting in films with a strong preferential crystal orientation.[32, 38, 39] In this case, the inorganic [PbI_6] octahedra layer sandwiched between two organic layers is thus confined parallel to the substrate (as illustrated in Figure 8.5d). This reorganization of the perovskite structure gives rise to the intensity increase around χ = 0° in the GIWAXS pattern of the MAPI/PEAMAPI film.

The integrity of the MAPI bottom layer is essential to justify our concept of a perovskite/perovskite heterojunction. Because of the size of PEA^+ and BA^+, these organic molecules are too large to be incorporated into the perovskite structure replacing MA^+, and can only form layered compounds. Moreover, any distortion in the MAPI lattice by percolated PEA^+ or BA^+ cations would be visible in the XRD patterns. As both standard wide-angle XRD and GIWAXS measurements indicate the existence of only two crystal phases – pristine MAPI and the layered perovskite – we do not expect compositional changes within the MAPI bottom layer.

8.3.2 Device performance

We fabricated planar heterojunction perovskite solar cells comprising a MAPI/PEAMAPI or MAPI/BAMAPI perovskite heterojunction. The final device configuration is glass/FTO/compact TiO_2/perovskite/spiro-OMeTAD/Au. A cross-sectional SEM image of a MAPI/PEAMAPI perovskite solar cell is depicted in Figure 8.7a.

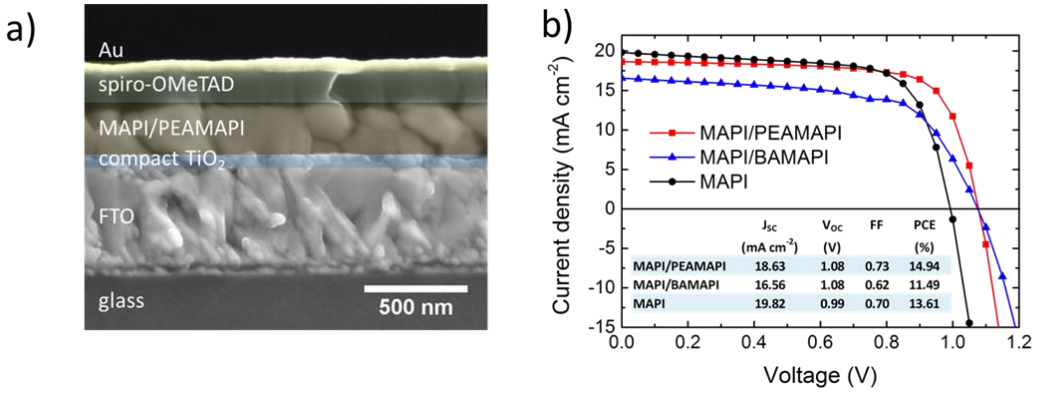

Figure 8.7 (a) SEM cross-section of a MAPI/PEAMAPI planar heterojunction solar cell. (b) *J-V* curves and characteristics of the best-performing devices comprising different perovskite layer configurations. Both MAPI/LPK heterojunction devices incorporate a 20–25 nm thick LPK top layer. Recorded under one sun AM 1.5G illumination at reverse bias sweep with a scan rate of 0.5 V s^{-1}. The inset table indicates the determined performance parameters for each type of device.

Figure 8.7b presents the current-voltage (*J-V*) curves of a MAPI/BAMAPI, MAPI/PEAMAPI, and a MAPI-based solar cells recorded under simulated AM 1.5G solar illumination by scanning the voltage from 2 V to 0 V. Both perovskite bilayer devices give significantly higher open-circuit voltages (V_{oc}) of 1.08 V than the device composed of pristine MAPI (V_{oc} = 0.99 V). The short-circuit current density (J_{sc}) of the MAPI/PEAMAPI-based device is slightly lower (J_{sc} = 18.63 mA/cm^2) compared to the reference cell (J_{sc} = 19.82 mA/cm^2), whereas the MAPI/BAMAPI cell suffers a more pronounced drop in photocurrent density (J_{sc} = 16.56 mA/cm^2). Ultimately, the resulting power conversion efficiency of the MAPI/PEAMAPI device (PCE = 14.94%) is improved compared to the nontreated MAPI cell (PCE = 13.61%), while the MAPI/BAMAPI device yields 11.49%. By utilizing a further optimized perovskite deposition protocol, a 16.84% MAPI/PEAMAPI cell with V_{oc} = 1.11 V was obtained. The corresponding *J-V* curves and the stabilized power output are given in Figure 8.8.

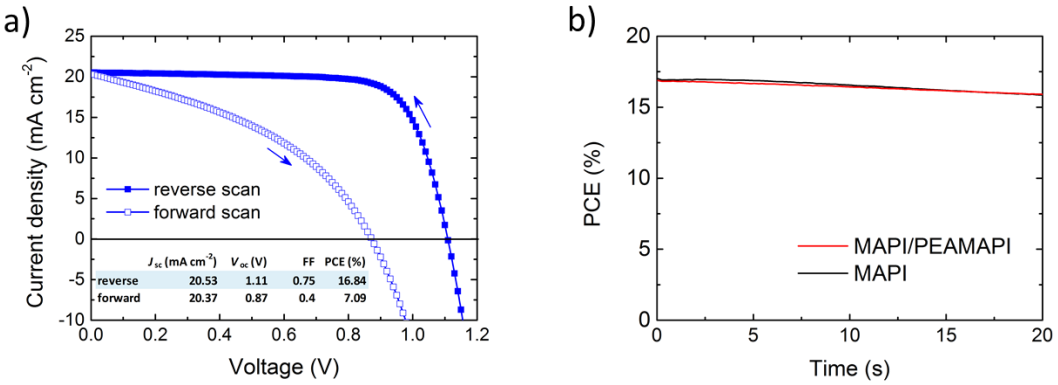

Figure 8.8 (a) *J-V* curves of a MAPI/PEAMAPI heterojunction champion cell fabricated via an optimized MAPI deposition method. Recorded under simulated AM 1.5G illumination with 100 mW cm^{-2} (scan rate: 0.1 V s^{-1}). (b) PCE as a function of time for a MAPI cell and a MAPI/PEAMAPI cell held to the maximum power voltage (~0.91 V reverse bias) under illumination.

The formation of an optimized LPK top layer affects the photovoltaic performance in two ways: a slight decrease in short-circuit current density and an increase in open-circuit voltage. The loss in J_{sc} can be attributed to two factors: first, charge transport is inhibited by the organic interlayers within the LPK film that in our samples are perpendicularly oriented to the direction of charge transport. With increasing thickness of the LPK layer, photogenerated charge carriers need to overcome a larger number of electronically insulating sheets formed by the bulky organic cations. This is evidenced by the dramatic loss in J_{sc} for devices prepared with higher concentrations of the PEAI:MAI casting solution (Figure 8.9a).

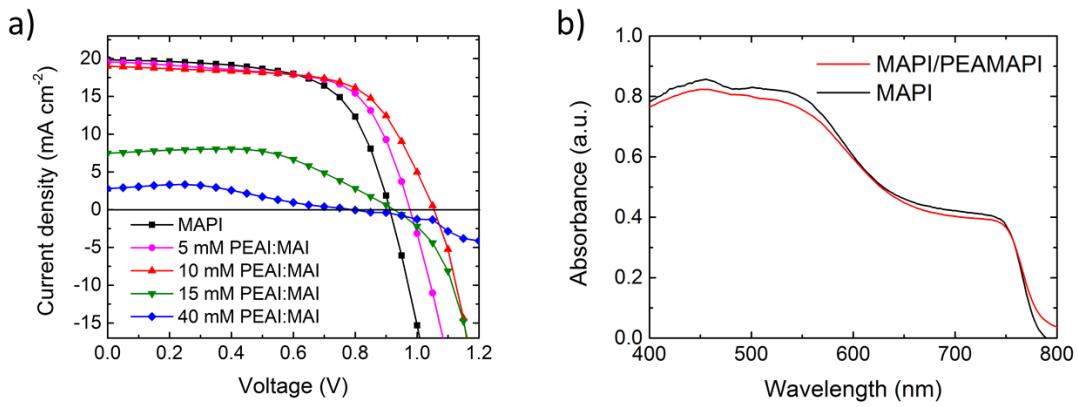

Figure 8.9 (a) *J-V* curves of a MAPI control cell and MAPI/PEAMAPI devices prepared with different concentrations of the PEAI:MAI casting solution. Recorded under simulated AM 1.5G sun light and reverse bias sweep (scan rate 0.5 V s^{-1}). (b) UV-Vis absorption spectra of a MAPI film and a MAPI/PEAMAPI film on glass, prepared with a 10 mM PEAI:MAI (1:1) solution.

Moreover, the MAPI/BAMAPI-based solar cell is composed of a larger number of organic interlayers than the MAPI/PEAMAPI device with a similar total LPK film thickness, thus leading to a larger drop in J_{sc} (Figure 8.7b). Second, the light absorption spectrum of a MAPI/PEAMAPI film reveals a slight decrease in absorbance compared to a pristine MAPI film (Figure 8.9b), as partial conversion into the LPK occurs. The loss in light absorption also contributes to the decrease in J_{sc}. Further studies were conducted on the MAPI/PEAMAPI system, which incorporates only a single phase LPK and demonstrates a higher photovoltaic performance than MAPI/BAMAPI-based devices.

The second effect of the PEAMAPI layer is an enhancement of V_{oc} and FF. It has been previously reported that an increase in V_{oc} and FF can be linked to a reduction of charge recombination rates through optimizing charge-selective contact materials.[40, 41] To investigate if this occurs in our perovskite/perovskite heterojunction, we examined the energy level alignment between MAPI and PEAMAPI with XPS measurements. The thickness of the optimized PEAMAPI top layer is around 20–22 nm, as estimated via GIWAXS experiments and Scherrer analysis. The recorded XPS results of a MAPI/PEAMAPI sample can therefore be attributed to the PEAMAPI material.

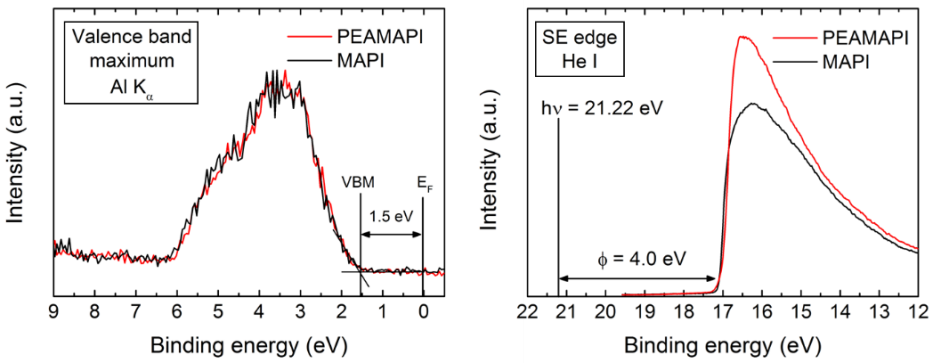

Figure 8.10 XPS spectra obtained for pure MAPI and a MAPI/PEAMAPI bilayer film. The left graph describes the energetic position of the valence band maximum (VBM) relative to the Fermi level E_F. The graph on the right shows the energy difference between the secondary electron edge and the He I radiation, which corresponds to the work function ϕ.

Figure 8.10 shows that the valence band onsets for MAPI and PEAMAPI are well aligned and both samples exhibit comparable work functions. Band gap estimations for the PEAMAPI compound are difficult, as the absorption profile of MAPI dominates the absorption spectrum of the MAPI/PEAMAPI sample (Figure 8.9b). However, Cao *et al.*[32] showed that the introduction of long-chained cations into the MAPI structure increases the band gap of the perovskite material. Accordingly, we expect PEAMAPI to exhibit a wider band gap than MAPI. Electronically speaking, this means that the valence bands of PEAMAPI and MAPI are well aligned and that the conduction band onset for PEAMAPI will be energetically higher. Electron transfer from MAPI to PEAMAPI would thus be uphill in energy and is inhibited (Figure 8.11). Charge recombination at the interface is further reduced with the LPK layer acting as a selective hole extraction layer between MAPI and spiro-OMeTAD, explaining our observed change in V_{oc} and FF.

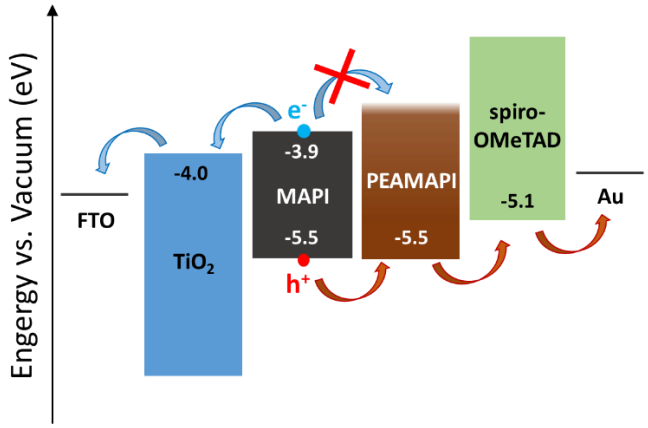

Figure 8.11 Schematic energy level diagram of a MAPI/PEAMAPI heterojunction solar cell.

Further evidence supporting this hypothesis is given by time-resolved photoluminescence (PL) spectroscopy. This technique provides insights into the recombination dynamics of photo-generated electron-hole pairs by monitoring the PL decay as a function of time. We evaluated the PL lifetime of MAPI and MAPI/PEAMAPI films with time-correlated single photon counting (TCSPC). The decrease in PL lifetime of the MAPI/PEAMAPI sample suggests PL quenching by the LPK layer, which supports the notion of hole transfer from MAPI into PEAMAPI (Figure 8.12). With this information in hand, we assign the increase in V_{oc} and FF observed for devices incorporating a MAPI/PEAMAPI heterojunction to a reduction in charge recombination rates. Moreover, the reorganization of the MAPI film surface upon PEA^+ insertion evidenced by the GIWAXS data is likely to reduce surface recombination, possibly also contributing to the observed increase in V_{oc} and FF.

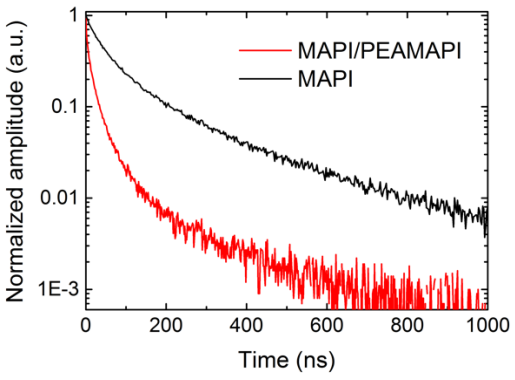

Figure 8.12 Time-resolved PL decay for a MAPI and a MAPI/PEAMAPI film on glass analyzed by TCSPC.

To verify the reproducibility of the *J-V* curve results, we evaluated the performance of 156 MAPI/PEAMAPI solar cells and 156 MAPI reference cells fabricated from different batches on different days. Figure 8.13 shows the statistical distribution of V_{oc}, J_{sc}, FF and PCE values for both types of devices. The findings are in good agreement with our observations from the champion cells.

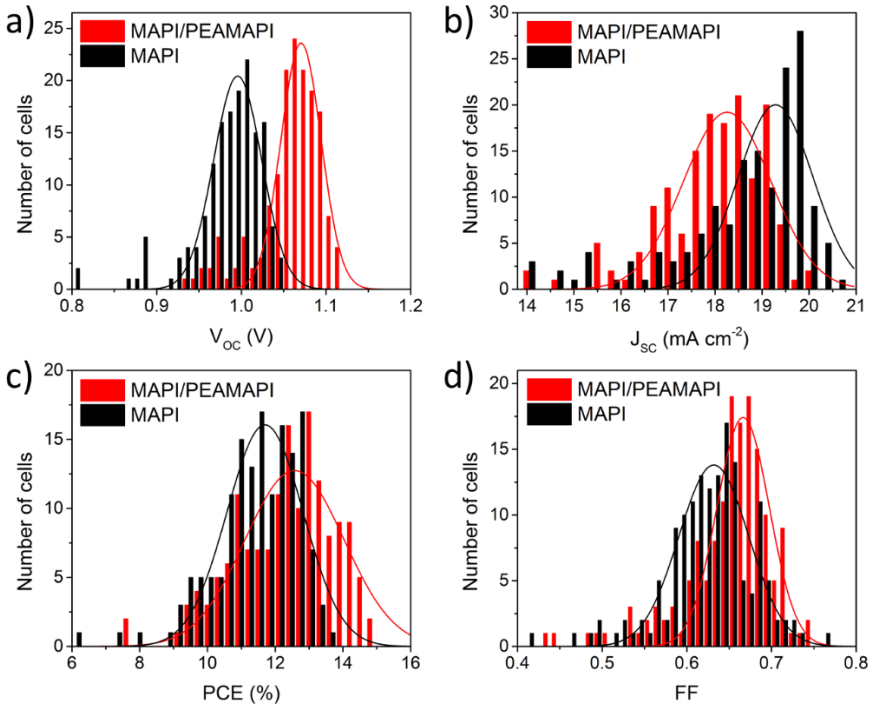

Figure 8.13 Statistical evaluation of the *J-V* data (reverse bias scans from 2 to 0 V) obtained for 156 MAPI/PEAMAPI devices and 156 MAPI devices. Comparison of (a) V_{sc}, (b) J_{sc}, (c) PCE and (d) FF.

Planar perovskite solar cells are notorious for their anomalous hysteresis in *J-V* measurements, that is, the *J-V* curve obtained from the forward bias scan (from 0 to 2 V) differs from the one obtained from the reverse bias scan (from 2 to 0 V). This phenomenon is usually assigned to ion migration within the perovskite layer.[42-45] We observed typical hysteretic behavior for MAPI and MAPI/LPK devices to approximately the same degree (Figure 8.14). By partially substituting MA^+ for the bulkier organic cations, fewer mobile ionic species are present in the perovskite lattice, which could induce less hysteresis in the perovskite/perovskite heterojunction devices. However, in our optimized devices, only 7% of the original MAPI film is converted into the layered perovskite, while a thick MAPI bottom layer (~250 nm) is maintained. Therefore, we do not observe a significant reduction of the usual hysteresis caused by ion migration.

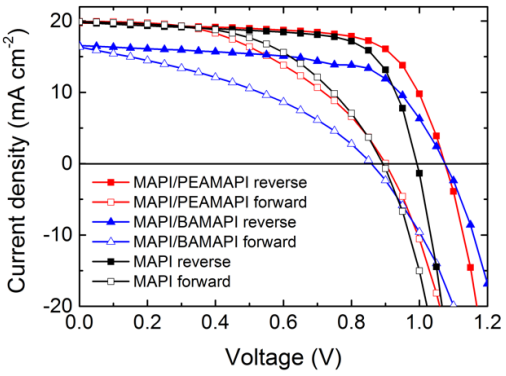

Figure 8.14 *J-V* hysteresis of photovoltaic devices comprising a MAPI/PEAMAPI, MAPI/BAMAPI or MAPI absorber layers. Recorded under simulated AM 1.5G sun light, reverse and forward bias scan (scan rate: 0.5 V s^{-1}).

In addition to the pursuit of better performing devices, ensuring the long-term stability of PSCs remains a major challenge. In particular, hybrid perovskites are known to be chemically unstable in the presence of moisture. Recently, it has been shown that LPKs incorporating hydrophobic long-chained organic cations are more resistant toward humidity-induced degradation.[33] Here, we studied the moisture stability of MAPI/PEAMAPI perovskite solar cells by exposing devices without any encapsulation to air at constant 75% relative humidity (RH) in a sealed container at room temperature.

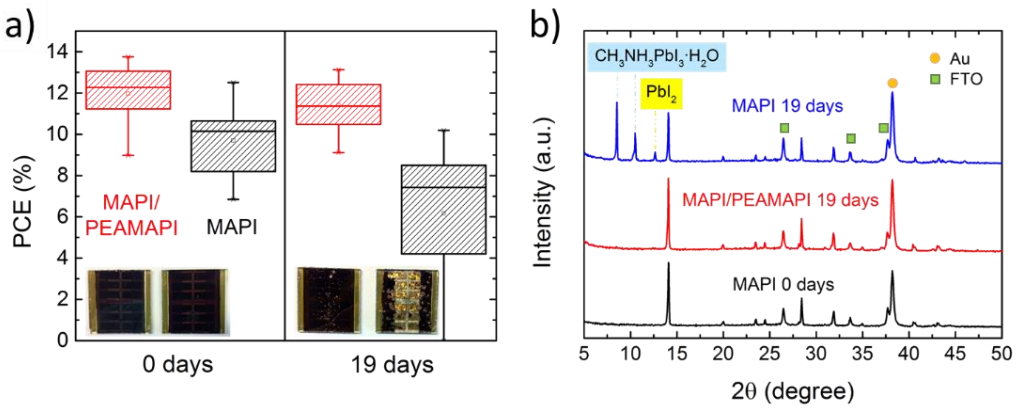

Figure 8.15 Device stability test at 75% RH in air at room temperature for 19 days. (a) Efficiency distribution for 20 MAPI/PEAMAPI and 20 MAPI devices before and after exposure to humidity. The insets show the corresponding photograph of a MAPI/PEAMAPI cell (left) compared to a MAPI control cell (right). (b) XRD patterns of an intact MAPI cell, a MAPI/PEAMAPI cell and a MAPI cell upon exposure to moisture.

Figure 8.15a presents the PCE of 20 MAPI cells and 20 MAPI/PEAMAPI cells before and after exposure to humid air at 75% RH. After 19 days, MAPI/PEAMAPI devices exhibit a significantly higher average efficiency (PCE = 11.4%) than the MAPI reference cells (6.1%). Strong decolorization of the MAPI solar cell indicates advanced degradation of the perovskite film, whereas the MAPI/PEAMAPI bilayer cell maintained the dark brown color of an intact perovskite absorber layer. Additional reflections in the XRD pattern of the degraded MAPI-based device originate from a MAPI hydrate ($CH_3NH_3PbI_3 \cdot H_2O$)[46, 47] and PbI_2 (Figure 8.15b), indicating the decomposition of the perovskite layer. In contrast, no degradation products can be identified in the XRD pattern of the MAPI/PEAMAPI device. In order to monitor the diffraction peaks of PEAMAPI before and after hydration, we prepared MAPI/PEAMAPI and pure MAPI samples on glass which were analyzed in grazing-incidence geometry at an incident angle of 0.5°. The corresponding XRD patterns (Figure 8.16) reveal that the MAPI sample shows degradation upon hydration at 75% RH for 2 h, whereas the MAPI/PEAMAPI sample does not show structural changes or degradation products. Our results verify the effect of the LPK top layer as a moisture barrier, which correlates with an improvement in device stability toward exposure to a high level of humidity.

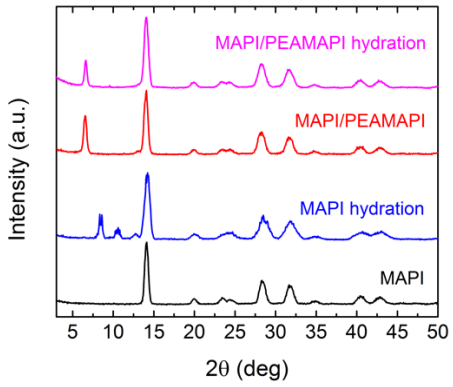

Figure 8.16 XRD patterns of a MAPI and a MAPI/PEAMAPI film before and after exposure to 75% RH for 2 h in air at room temperature.

8.4 Conclusion

To conclude, this paper shows that a perovskite/perovskite heterojunction architecture comprising MAPI and a layered perovskite compound can be fabricated via a solution-based cation infiltration process. The successful realization of two MAPI/LPK heterojunction systems incorporating

phenylethylammonium or *n*-butylammonium cations proves the versatility of the deposition method developed here. GIWAXS experiments reveal the preferential growth of the layered PEAMAPI perovskite, which is accompanied by a reorganization and reorientation of the MAPI top layer. We demonstrate that photovoltaic devices based on a MAPI/PEAMAPI heterojunction reach power conversion efficiencies of up to 16.84% due to an increase in open-circuit voltage and fill factor. Our results indicate that the LPK top layer may act as a selective charge extraction layer for MAPI perovskite, leading to reduced recombination losses within the device. With an optimized LPK layer thickness, the detrimental effects of the organic barriers on the charge transport and light absorption are compensated by the enhanced V_{oc} and FF. In addition, the enhancement in device stability towards exposure to moisture implies prolonged device lifetime, which is a crucial aspect for the implementation of perovskite-based photovoltaics in outdoor applications. The immense variety of organic cations that can be incorporated into the perovskite structure offers numerous possibilities to fine-tune and control the interface; from energy level alignment for graded band gap structures to the chemical stability of the system.[27, 33, 37, 48, 49]. We believe that designing perovskite/perovskite heterojunctions holds great potential to improve both device stability and photovoltaic performance of perovskite solar cells.

8.5 Methods

Synthesis of organic cation salts

PEAI crystals were synthesized by dropwise adding a solution of HI (Sigma-Aldrich, 57 wt% in water, 27 mL, 204 mmol) to a cold (0 °C) mixture of 2-phenylethylamine (Sigma-Aldrich, 25 mL, 198 mmol) and absolute ethanol (25 mL) under stirring. The colorless precipitate was collected by suction filtration and washed several times with diethyl ether. After recrystallization from isopropanol and drying under reduced pressure, colorless PEAI crystals were obtained. To synthesize BAI crystals, *n*-butylamine (Acros, 99.5%) was reacted with HI in the same way as described above for the PEAI synthesis. MAI crystals were obtained by adding an aqueous HI solution (10 mL, 76 mmol) dropwise to 24 mL (193 mmol) methylamine solution (Sigma-Aldrich, 33 wt% in absolute ethanol) diluted in 100 mL absolute ethanol at 0 °C under stirring. After further stirring for 2 h at room temperature, the solvent was removed at 45 °C by using a rotary evaporator and the colorless precipitate was recrystallized from absolute ethanol. Finally, the colorless MAI crystals were filtrated, washed with diethyl ether and dried overnight under vacuum.

Thin Film Preparation

Thin films of methylammonium lead iodide (MAPI) were prepared in a glovebox under dry nitrogen atmosphere, by following a protocol reported by Xiao *et al.*[50] First, clean glass substrates (2.5 × 2.5 cm^2) were treated in a plasma-cleaner with oxygen plasma for 5 min. MAI (0.4 g, 2.5 mmol) and PbI_2 (Sigma-Aldrich, 99%, 1.156 g, 2.5 mmol) were dissolved in 2 mL of DMF (Sigma-Aldrich, anhydrous) under stirring at 100 °C. The yellow solution was cooled and filtrated through a 0.45 µm syringe filter, affording a 1.25 M precursor solution of MAPI. Then 75 µL perovskite solution was dynamically spin-coated on a clean glass substrate at 5000 rpm for 30 s. With a delay time of 4-5 s, 200 µL of chlorobenzene (Sigma-Aldrich, anhydrous) was quickly introduced to the spinning film in order to promote MAPI crystallization. The sample was annealed on a hot plate at 100 °C for 10 min to remove residual solvents. Finally, homogeneous, dark-brown MAPI films were obtained. The conversion of the top layer of a MAPI thin film into the layered PEAMAPI perovskite structure was achieved by spin-coating an equimolar mixture of phenylethylammonium iodide (PEAI) and methylammonium iodide (MAI) in IPA (Sigma, anhydrous). PEAI and MAI were dissolved in IPA with different concentrations varying from 5 mM to 40 mM (the molarity refers to both PEAI and MAI). Subsequently, 75 µL PEAI:MAI solution was spin-coated on a MAPI film at 4000 rpm for 45 s and the films were annealed at 70 °C for 5 min to remove residual solvents. The preparation of MAPI/BAMAPI films followed the same protocol, using an equimolar solution of BAI and MAI dissolved in IPA.

Solar cell fabrication

For the device fabrication, FTO coated glass slides (Pilkington, 7 Ω/sq) were employed as substrates. The substrates were patterned by etching with zinc powder and 3 M HCl solution and successively cleaned with deionized water, 2% Hellmanex detergent solution, acetone, ethanol, and finally treated with oxygen plasma for 5 min. A TiO_2 compact layer was deposited as hole blocking layer on the substrate via a sol-gel approach. For this purpose, a mixture of 2 M HCl (35 µL) and anhydrous IPA (2.53 mL) was added dropwise to a solution of 370 µL of titanium(IV) isopropoxide (Sigma-Aldrich) in IPA (2.53 mL) under vigorous stirring. The clear TiO_x solution was spin-coated dynamically on the clean FTO substrates at 2000 rpm for 45 s, followed by annealing at 150 °C for 10 min on a hot plate. The TiO_2 compact layer was completed by sintering at 500 °C in air for 45 min, and the final substrates were cut into pieces of 3 × 3 cm^2. The deposition of the MAPI absorber layer and its partial conversion into PEAMAPI or BAMAPI was processed in a nitrogen-filled glovebox as described above for the thin film preparation.

For the fabrication of the best performing devices, a further optimized procedure for the MAPI film deposition was used. Here, a 1.2 M solution of PbI_2 (TCI, 98%) and MAI in a 4:1 (v/v) mixture of DMF and DMSO was deposited in a consecutive two-step spin-coating process at 1000 and 5000 rpm for 10 and 30 s, respectively. Approximately 15 s before the end of spinning, 500 µL of chlorobenzene was added to the film. After annealing the substrates at 100 °C for 10 min on a hotplate, MAPI films were formed. The generation of the PEAMAPI top layer by spin-coating a 10 mM PEAI:MAI (1:1) solution followed the same protocol as described above.

For the deposition of the hole transporter layer, a solution of spiro-OMeTAD in anhydrous chlorobenzene (75 mg/mL) was filtered through a 0.45 µm syringe filter. Then 10 µL of tBP (Sigma-Aldrich, 96%) and 30 µL of a 170 mg/mL Li-TFSI (Sigma-Aldrich, 99.95%) solution in acetonitrile (Sigma-Aldrich, anhydrous) were added to 1 mL of spiro-OMeTAD solution. The HTM was deposited on the device substrate by spin-coating at 2000 rpm for 45 s. The samples were stored overnight in a desiccator under air atmosphere with ~21% relative humidity. Finally, a 40 nm Au layer was deposited through a patterned shadow mask by thermal evaporation at $4 \cdot 10^{-6}$ mbar and a deposition rate of 0.1 nm/s in order to form the back electrode.

Film characterization

XRD measurements of thin films were performed with a Bruker D8 Discover X-ray diffractometer operating at 40 kV and 30 mA, employing Ni-filtered Cu $K_{\alpha 1}$ radiation (λ = 1.5406 Å) and a position-sensitive LynxEye detector. The Bragg-Brentano scanning geometry or an alternative grazing-incidence geometry with an incident angle of 0.5° was applied to record the data. Powder X-ray diffraction (PXRD) patterns were recorded on a STOE powder diffractometer equipped with a position-sensitive Mythen-1K detector in transmission geometry.

Estimation of 2θ positions of (00l) reflections for the series of layered hybrid perovskite $(PEA)_2(MA)_{m-1}(Pb_mI_{3m+1})$*:* the previously reported layered perovskite compounds $(PEA)_2(MA)_{m-1}(Pb_mI_{3m+1})$ with m = 1, 2, 3 exhibit (00l) reflections, where the position of the peaks shifts to lower angles with increasing m (m = number of $[PbI_6]$ octahedra sheets). The interplanar distance for the (002) crystallographic planes in the LPK structures is increased by approximately 6.1 Å for each additional octahedra layer, which coincides with the distance of two axial iodine atoms along the c-axis.[51] Following this trend and by employing the Bragg equation:

$$2d \sin\theta = n\lambda \qquad (8.1)$$

with d as the interplanar distance, θ as the diffraction angle, n as the order of diffraction and λ as the wavelength of the X-rays, we estimated the 2θ positions of (00l) peaks for the layered perovskite series with m = 4, 5, 6, 7, 8 in order to identify the low-angle reflections in the experimental XRD pattern of the treated MAPI film (see Table 8.1).

Estimation of the crystallite size of the layered perovskite phase: the crystallite size of the layered perovskite BAMAPI or PEAMAPI formed on top of a MAPI film can be estimated by analyzing the peak breadth of the corresponding X-ray diffraction peaks according the Scherrer equation:[52]

$$D = \frac{K\lambda}{B\cos\theta} \tag{8.2}$$

where D is the average crystallite size, K being the Scherrer shape factor, λ the wavelength of the used X-ray, B the full-width-half-maximum (FWHM) value of the peak in radians and θ the Bragg angle of the (hkl) reflection. We fit the most intense (00l) reflection of PEAMAPI with a Gaussian function to extract the FWHM of the peak. Since the (002) peak of BAMAPI is a superposition of two phases with the [PbI_6] octahedra layer thickness being m = 3 and m = 4, two Gaussians were fitted and a crystal size value for each phase was estimated. The instrument broadening of the peak was taken into account by fitting a Gaussian function to the (001) reflection of a highly crystalline methylammonium lead bromide sample. The measured peak broadening was considered as a convolution of two Gaussian functions correlating to the instrument contribution and the layered perovskite sample, respectively. The corrected FWHM B_{sample} can be calculated as following:[53]

$$B_{sample} = \sqrt{{B_{total}}^2 - {B_{instrument}}^2} \tag{8.3}$$

where $B_{instrument}$ was found to be 0.067°. A commonly used shape factor of K = 0.9 was employed and the determined crystallite sizes for different concentrations of the casting solution is summarized in Table 8.2.

GIWAXS measurements were conducted under vacuum using a Ganesha 300XL SAXS-WAXS system with a Cu K_α source. The samples were carefully aligned with a diode before each measurement and the scattering signal was recorded with a Pilatus 300k detector (Dectris). The incident angle was α_I = 0.4° and the sample–detector distance (SDD) was around 110 mm. The SDD was calibrated for each measurement individually using XRD data. The software GIXSGUI was used for data treatment and evaluation using the various corrections offered by the software.

Details on the calculation of the PEAMAPI layer thickness via GIWAXS analysis: the azimuthal integration was performed around q = 1 Å^{-1} and around q = 2.2 Å^{-1} which correspond to the Debye-Scherrer rings arising from the (002)/(110) and (213)/(114)/(310)/(222) lattice plane reflections of the MAPI crystals. For simplicity they are denoted as (002) and (222), respectively (cf. Figure 2c). In order to quantify the amount of oriented crystals for the (002) peak, the data were fit with a Gaussian function. The 2σ range of the Gaussian was defined as the oriented part as it accounts for 95% of the area underneath the peak. The 2σ range is marked in Figure 2c by dashed lines which divide the graph into three areas. The intensities of these individual areas were integrated and normalized by the total intensity, thus determining the ratio of randomly and preferentially oriented crystallites for the MAPI and the MAPI/PEAMAPI samples, respectively. We find that around 33% of the crystals in the MAPI sample have a (002) orientation (c-axis perpendicular to the substrate), whereas about 40% of the crystallites are oriented in the MAPI/PEAMAPI sample. Integration over the (222) peak showed the typical profile of a Gaussian function, thus justifying the use of this function for amending the inaccessible area around the azimuthal angle χ = 0°. The ratios of the integrated intensities agree very well for the (002) and (222) peaks with only slight deviations, which serve as an estimate for the uncertainty of the presented analysis. Assuming that the increase of oriented crystals is due to the formation of highly oriented PEAMAPI, (7.00 ± 0.47)% of the initial MAPI film is estimated to be converted into the LPK.

X-ray photoelectron spectroscopy (XPS) data were collected at a PHI Versaprobe II system at a pressure of 10^{-9} mbar. Monochromatic Al K_α radiation (1486.6 eV) and a hemispherical analyzer with a pass energy of 11.75 eV for C 1s and 23.5 eV for the valence region were used. The binding energies were calibrated at the Fermi-edge (0 eV) and Ag $3d_{5/2}$ (368.26 eV) on a sputtered silver reference. All spectra show photoemission in normal direction. The samples were exposed to ambient illumination during the measurement. The work function was determined by analyzing the secondary electron edge under He I (21.22 eV) illumination and an applied bias voltage of 3 V. A pass energy of 5.85 eV was used for the detector.

Scanning electron microscopy (SEM) images were recorded with a JEOL JSM-6500F scanning electron microscope, operated at an acceleration voltage of 5 keV.

UV-Vis absorption spectra were recorded using a Perkin Elmer Lambda 1050 spectrophotometer equipped with a 150 mm integrating sphere. Air (100% transmittance) and a Spectralon white standard (100% reflectance) were used for the instrument baseline.

Time-resolved photoluminescence (PL) spectroscopy was performed with a Fluotime 300 spectrofluorometer (Picoquant). The excitation wavelength was fixed at 510 nm and TCSPC data were collected by monitoring the PL emission maximum around 770 nm.

Device Characterization

Current-Voltage (*J-V*) characteristics of the perovskite solar cells were measured in air at ambient conditions using a Newport OrielSol 2A solar simulator with a Keithley 2401 source meter. The devices were illuminated through a shadow mask, yielding an active area of 0.083 cm^2. The *J-V* curves were recorded under standard AM 1.5G solar illumination from a 450 W xenon lamp, calibrated to a light intensity of 100 mW cm^{-2} with a Fraunhofer ISE certified silicon diode (KG5-filtered). A spectral mismatch factor of 1.002 was estimated following a previously established protocol.[54] Prior to each measurement, the cell was pre-biased at 2 V for 10 s under illumination. The input bias voltage was scanned from 2 to 0 V (referred to as reverse scan) in 0.05 V steps with a scan rate of 0.5 V s^{-1} and then from 0 to 2 V (forward scan) at the same scan rate. Devices fabricated according to the optimized protocol for the MAPI film deposition were pre-biased at 1.5 V for 10 s under illumination and the voltage was scanned in reverse (1.5 to 0 V) and forward direction (0 to 1.5 V) in 0.01 V steps with a scan rate of 0.1 V s^{-1}. For the maximum power aging measurements, the voltage was held constant at the maximum power voltage and the PCE was monitored over a period of 20 s.

Stability Test

Humidity studies on the perovskite solar cells were conducted in a shaded glass container at a constant relative humidity level of 75% that was maintained by a saturated aqueous sodium chloride solution at the bottom of the jar. The solar cell samples were placed onto a stage inside the sealed container being exposed to the moist air and without having direct contact with the solution. The humidity chamber was only opened when the samples were taken out for XRD and *J-V* analysis. As MAPI undergoes a reversible hydration process upon exposure to a highly humid environment,[46] the hydrated cells were stored under ambient conditions at ~25% RH for 4 h to let the perovskite material stabilize in air at lower humidity prior to the *J-V* measurements.

8.6 References

[1] Y. Hu, J. Schlipf, M. Wussler, M. L. Petrus, W. Jaegermann, T. Bein, P. Müller-Buschbaum, P. Docampo, *ACS Nano* **2016**, *10*, 5999.

[2] M. A. Green, A. Ho-Baillie, H. J. Snaith, *Nat. Photon.* **2014**, *8*, 506.

[3] N.-G. Park, *Mater. Today* **2015**, *18*, 65.

[4] C. S. Ponseca, T. J. Savenije, M. Abdellah, K. Zheng, A. Yartsev, T. Pascher, T. Harlang, P. Chabera, T. Pullerits, A. Stepanov, J.-P. Wolf, V. Sundström, *J. Am. Chem. Soc.* **2014**, *136*, 5189.

[5] C. Wehrenfennig, G. E. Eperon, M. B. Johnston, H. J. Snaith, L. M. Herz, *Adv. Mater.* **2014**, *26*, 1584.

[6] Q. Dong, Y. Fang, Y. Shao, P. Mulligan, J. Qiu, L. Cao, J. Huang, *Science* **2015**.

[7] D. Shi, V. Adinolfi, R. Comin, M. Yuan, E. Alarousu, A. Buin, Y. Chen, S. Hoogland, A. Rothenberger, K. Katsiev, Y. Losovyj, X. Zhang, P. A. Dowben, O. F. Mohammed, E. H. Sargent, O. M. Bakr, *Science* **2015**, *347*, 519.

[8] S. D. Stranks, G. E. Eperon, G. Grancini, C. Menelaou, M. J. P. Alcocer, T. Leijtens, L. M. Herz, A. Petrozza, H. J. Snaith, *Science* **2013**, *342*, 341.

[9] M. A. Green, K. Emery, Y. Hishikawa, W. Warta, E. D. Dunlop, *Prog. Photovolt. Res. Appl.* **2015**, *23*, 1.

[10] P. Docampo, F. C. Hanusch, S. D. Stranks, M. Döblinger, J. M. Feckl, M. Ehrensperger, N. K. Minar, M. B. Johnston, H. J. Snaith, T. Bein, *Adv. Energy Mater.* **2014**, *4*, 1400355.

[11] W. Nie, H. Tsai, R. Asadpour, J.-C. Blancon, A. J. Neukirch, G. Gupta, J. J. Crochet, M. Chhowalla, S. Tretiak, M. A. Alam, H.-L. Wang, A. D. Mohite, *Science* **2015**, *347*, 522.

[12] Y. Wu, A. Islam, X. Yang, C. Qin, J. Liu, K. Zhang, W. Peng, L. Han, *Energy. Environ. Sci.* **2014**, *7*, 2934.

[13] N. J. Jeon, J. H. Noh, Y. C. Kim, W. S. Yang, S. Ryu, S. I. Seok, *Nat. Mater.* **2014**, *13*, 897.

[14] W. S. Yang, J. H. Noh, N. J. Jeon, Y. C. Kim, S. Ryu, J. Seo, S. I. Seok, *Science* **2015**, *348*, 1234.

[15] N. Ahn, D.-Y. Son, I.-H. Jang, S. M. Kang, M. Choi, N.-G. Park, *J. Am. Chem. Soc.* **2015**, *137*, 8696.

[16] W. E. I. Sha, X. Ren, L. Chen, W. C. H. Choy, *Appl. Phys. Lett.* **2015**, *106*, 221104.

[17] J. Zhao, A. Wang, P. P. Altermatt, S. R. Wenham, M. A. Green, *Sol. Energy Mater. Sol. Cells* **1996**, *41*, 87.

[18] H. P. Zhou, Q. Chen, G. Li, S. Luo, T. B. Song, H. S. Duan, Z. R. Hong, J. B. You, Y. S. Liu, Y. Yang, *Science* **2014**, *345*, 542.

[19] Y. Li, Y. Zhao, Q. Chen, Y. Yang, Y. Liu, Z. Hong, Z. Liu, Y.-T. Hsieh, L. Meng, Y. Li, Y. Yang, *J. Am. Chem. Soc.* **2015**, *137*, 15540.

[20] J.-Y. Jeng, K.-C. Chen, T.-Y. Chiang, P.-Y. Lin, T.-D. Tsai, Y.-C. Chang, T.-F. Guo, P. Chen, T.-C. Wen, Y.-J. Hsu, *Adv. Mater.* **2014**, *26*, 4107.

[21] J. Seo, S. Park, Y. Chan Kim, N. J. Jeon, J. H. Noh, S. C. Yoon, S. I. Seok, *Energy. Environ. Sci.* **2014**, *7*, 2642.

[22] O. Malinkiewicz, A. Yella, Y. H. Lee, G. M. Espallargas, M. Graetzel, M. K. Nazeeruddin, H. J. Bolink, *Nat. Photon.* **2014**, *8*, 128.

[23] M. M. Lee, J. Teuscher, T. Miyasaka, T. N. Murakami, H. J. Snaith, *Science* **2012**, *338*, 643.

[24] J. H. Heo, S. H. Im, J. H. Noh, T. N. Mandal, C.-S. Lim, J. A. Chang, Y. H. Lee, H.-j. Kim, A. Sarkar, K. NazeeruddinMd, M. Gratzel, S. I. Seok, *Nat. Photon.* **2013**, *7*, 486.

[25] P. Docampo, J. M. Ball, M. Darwich, G. E. Eperon, H. J. Snaith, *Nat. Commun.* **2013**, *4*.

[26] D. B. Mitzi, S. Wang, C. A. Feild, C. A. Chess, A. M. Guloy, *Science* **1995**, *267*, 1473.

[27] D. B. Mitzi, *J. Chem. Soc., Dalton Trans.* **2001**, 1.

[28] Z. Cheng, J. Lin, *CrystEngComm* **2010**, *12*, 2646.

[29] A. Yangui, D. Garrot, J. S. Lauret, A. Lusson, G. Bouchez, E. Deleporte, S. Pillet, E. E. Bendeif, M. Castro, S. Triki, Y. Abid, K. Boukheddaden, *J. Phys. Chem. C* **2015**, *119*, 23638.

[30] X. Wu, M. T. Trinh, D. Niesner, H. Zhu, Z. Norman, J. S. Owen, O. Yaffe, B. J. Kudisch, X. Y. Zhu, *J. Am. Chem. Soc.* **2015**, *137*, 2089.

[31] J. Calabrese, N. L. Jones, R. L. Harlow, N. Herron, D. L. Thorn, Y. Wang, *J. Am. Chem. Soc.* **1991**, *113*, 2328.

[32] D. H. Cao, C. C. Stoumpos, O. K. Farha, J. T. Hupp, M. G. Kanatzidis, *J. Am. Chem. Soc.* **2015**, *137*, 7843.

[33] I. C. Smith, E. T. Hoke, D. Solis-Ibarra, M. D. McGehee, H. I. Karunadasa, *Angew. Chem. Int. Ed.* **2014**, *53*, 11232.

[34] M. Saliba, K. W. Tan, H. Sai, D. T. Moore, T. Scott, W. Zhang, L. A. Estroff, U. Wiesner, H. J. Snaith, *J. Phys. Chem. C* **2014**, *118*, 17171.

[35] Y.-C. Huang, C.-S. Tsao, Y.-J. Cho, K.-C. Chen, K.-M. Chiang, S.-Y. Hsiao, C.-W. Chen, C.-J. Su, U. S. Jeng, H.-W. Lin, *Sci. Rep.* **2015**, *5*, 13657.

[36] K. W. Tan, D. T. Moore, M. Saliba, H. Sai, L. A. Estroff, T. Hanrath, H. J. Snaith, U. Wiesner, *ACS Nano* **2014**, *8*, 4730.

[37] S. Zhang, G. Lanty, J.-S. Lauret, E. Deleporte, P. Audebert, L. Galmiche, *Acta Mater.* **2009**, *57*, 3301.

[38] K. Nobuaki, *Jpn. J. Appl. Phys.* **1997**, *36*, 6876.

[39] S. Ahmad, P. K. Kanaujia, H. J. Beeson, A. Abate, F. Deschler, D. Credgington, U. Steiner, G. V. Prakash, J. J. Baumberg, *ACS Appl. Mater. Interfaces* **2015**, *7*, 25227.

[40] Y. Zhang, M. Liu, G. E. Eperon, T. C. Leijtens, D. McMeekin, M. Saliba, W. Zhang, M. de Bastiani, A. Petrozza, L. M. Herz, M. B. Johnston, H. Lin, H. J. Snaith, *Mater. Horiz.* **2015**, *2*, 315.

[41] E. J. Juarez-Perez, M. Wuβler, F. Fabregat-Santiago, K. Lakus-Wollny, E. Mankel, T. Mayer, W. Jaegermann, I. Mora-Sero, *J. Phys. Chem. Lett.* **2014**, *5*, 680.

[42] C. Eames, J. M. Frost, P. R. F. Barnes, B. C. O/'Regan, A. Walsh, M. S. Islam, *Nat. Commun.* **2015**, *6*.

[43] E. L. Unger, E. T. Hoke, C. D. Bailie, W. H. Nguyen, A. R. Bowring, T. Heumuller, M. G. Christoforo, M. D. McGehee, *Energy. Environ. Sci.* **2014**, *7*, 3690.

[44] H. J. Snaith, A. Abate, J. M. Ball, G. E. Eperon, T. Leijtens, N. K. Noel, S. D. Stranks, J. T.-W. Wang, K. Wojciechowski, W. Zhang, *J. Phys. Chem. Lett.* **2014**, *5*, 1511.

[45] S. Meloni, T. Moehl, W. Tress, M. Franckevicius, M. Saliba, Y. H. Lee, P. Gao, M. K. Nazeeruddin, S. M. Zakeeruddin, U. Rothlisberger, M. Graetzel, *Nat. Commun.* **2016**, *7*.

[46] A. M. A. Leguy, Y. Hu, M. Campoy-Quiles, M. I. Alonso, O. J. Weber, P. Azarhoosh, M. van Schilfgaarde, M. T. Weller, T. Bein, J. Nelson, P. Docampo, P. R. F. Barnes, *Chem. Mater.* **2015**, *27*, 3397.

[47] F. Hao, C. C. Stoumpos, Z. Liu, R. P. H. Chang, M. G. Kanatzidis, *J. Am. Chem. Soc.* **2014**, *136*, 16411.

[48] G.-N. Liu, J.-R. Shi, X.-J. Han, X. Zhang, K. Li, J. Li, T. Zhang, Q.-S. Liu, Z.-W. Zhang, C. Li, *Dalton Trans.* **2015**, *44*, 12561.

[49] Y. Y. Li, C. K. Lin, G. L. Zheng, Z. Y. Cheng, H. You, W. D. Wang, J. Lin, *Chem. Mater.* **2006**, *18*, 3463.

[50] M. Xiao, F. Huang, W. Huang, Y. Dkhissi, Y. Zhu, J. Etheridge, A. Gray-Weale, U. Bach, Y.-B. Cheng, L. Spiccia, *Angew. Chem.* **2014**, *126*, 10056.

[51] C. C. Stoumpos, C. D. Malliakas, M. G. Kanatzidis, *Inorg. Chem.* **2013**, *52*, 9019.

[52] J. I. Langford, A. J. C. Wilson, *J. Appl. Crystallogr.* **1978**, *11*, 102.

[53] H. Savaloni, M. Gholipour-Shahraki, M. A. Player, *J. Phys. D: Appl. Phys.* **2006**, *39*, 2231.

[54] H. J. Snaith, *Energy. Environ. Sci.* **2012**, *5*, 6513.

9 Conclusion and outlook

9.1 Conclusion

In conclusion, this thesis has been dedicated to the elucidation of the moisture stability of hybrid perovskite solar cells: from understanding the factors which influence the degradation pathways, to developing novel 2D/3D perovskite structures which improve the device lifetime upon exposure to humidity.

We began our journey by exploring the moisture stability of the most common hybrid perovskite: methylammonium lead iodide. *In situ* measurements reveal that two structures of perovskite hydrates are formed as degradation products upon exposure to high humidity levels – first a monohydrate $CH_3NH_3PbI_3 \cdot H_2O$, followed by a dihydrate $(CH_3NH_3)_4PbI_6 \cdot 2\ H_2O$. Our results indicate that the initial decrease in photovoltaic performance upon exposure to humid air is related to the formation of the monohydrate around the perovskite grains, which inhibits charge transport across the photoabsorber layer. However, since we found that this reaction is reversible, the perovskite crystal structure and even the device performance can be recovered upon drying under low humidity conditions. This reversible hydration phenomenon needs to be considered when designing the testing conditions for moisture stability studies to ensure the collection of meaningful, representative data.

Furthermore, we revealed the influence of precursor stoichiometry on the degradation pathways that occur in methylammonium lead iodide under humid conditions. *In situ* XRD measurements confirm that a slight PbI_2 excess increases the moisture resistance of the perovskite film compared to stoichiometric precursor solutions, which we assigned to either a more favorable crystal termination or a protective PbI_2 layer around the perovskite grains. Surprisingly, an MAI excess first triggers a humidity-mediated recrystallization process within the perovskite film which improves the crystal quality and consequently the device efficiency, before deterioration commences. Our results highlight the importance of perovskite precursor stoichiometry not only regarding initial solar cell performance but also the moisture-induced degradation process.

We proceeded our studies with the state-of-the-art multiple-cation mixed-halide perovskites, which are expected to be more moisture stable than methylammonium lead iodide. First, we investigated the different roles of cesium and rubidium additives in the enhancement of device performance. By combining three complementary techniques – ToF, TRMC and TSC – we demonstrated that Cs improves overall PCE by reducing the density of deep trap states. Moreover, our results indicated

that Rb slightly increases charge carrier mobility and reduces *J-V* hysteresis, likely through surface passivation. Quadruple cation perovskites with the nominal composition $Rb_{0.05}Cs_{0.05}[(FA_{0.83}MA_{0.17})]_{0.9}Pb(I_{0.83}Br_{0.17})_3$ benefit from the effect of both cation additives and show the highest stabilized power output. Clarifying the different effects of Cs and Rb on the perovskite's crystal structure and electronic properties offers valuable guidance for the choice of perovskite composition in high-performance solar cells.

In addition, we discovered that the Rb-additive has a strong impact on the moisture stability of the multiple-cation mixed halide perovskite. Due to its small ionic radius, Rb^+ cations are not (fully) incorporated into the perovskite structure. Instead, the Rb-additive leads to the formation of side phases, such as $RbPb(I_{1-x}Br_x)_3$ during film crystallization under inert conditions. Upon exposure to humid air, Rb-containing perovskites show rapid phase segregation under the formation of transparent, bromide-rich $RbPb_2I_4Br$ crystallites, as verified by EDX analysis. A similar, but much slower process is observed for Cs-containing films, indicating that Cs is more suitable to stabilize the perovskite structure. Showing that the phase segregation in Rb-containing devices is accompanied by a decrease in device efficiency underlines the need for careful humidity control during the fabrication and operation of Rb-based perovskite solar cells.

To improve the resistance of hybrid perovskites against humidity, 2D perovskites incorporating bulky, hydrophobic organic cations have been explored. The optoelectronic properties of 2D perovskites strongly depend on the layer thickness of the lead halide interlayers, and the highly anisotropic crystal structure directs the charge transport within the material. Consequently, controlling both phase purity and crystallite orientation in 2D perovskite thin films is key for any potential device applications. We established a new protocol employing rationally chosen solvent additives and appropriate annealing protocols to obtain 2D perovskite films with improved phase purity and exclusively horizontal crystal orientation. This opens the doorway for the implementation of 2D perovskites into devices where lateral charge transport is desired.

However, in terms of photovoltaic performance, solar cells employing pure 2D perovskite thin films still lag behind their traditional 3D perovskite counterparts. In order to profit from the efficient charge separation and transport properties of the 3D perovskite, as well as from the enhanced moisture robustness of the 2D perovskite, we introduced the concept of a 2D/3D hybrid perovskite bilayer structure for the first time. A thin 2D perovskite top layer was sufficient to act as an effective moisture barrier and improved the interface between the perovskite and the hole transporting layer in solar cells, resulting in higher V_{oc}. The versatility of our 2D/3D hybrid perovskite concept is reflected in the numerous following reports using similar approaches to simultaneously guarantee high device performance and long-term stability.[1-7]

9.2 Outlook

Based on our successful establishment of a 2D/3D hybrid perovskite structure employing the traditional methylammonium lead iodide as the 3D perovskite material, it would be a logical next step to transfer this concept of dimensionality/interface engineering to multiple-cation mixed-halide perovskites to increase device efficiency. However, with regard to potential phase segregation in Rb-containing perovskites upon exposure to humidity, the choice of cation additives in the 3D perovskite layer needs to be revised carefully. Moreover, the degradation mechanisms in these multi-component 2D/3D structures require in-depth investigations and the large number of possible interactions between the different ions may create challenges for the data interpretation.

Since the moisture sensitivity of organic-inorganic perovskites mainly originates from the nature of the small organic cation methylammonium, fully inorganic perovskites such as $CsPbI_3$ have been explored as photoabsorbers.[8-10] Besides, inorganic compounds crystallizing in a so-called double perovskite structure such as $Cs_2AgBiBr_6$ have recently emerged as lead-free, environmentally stable alternatives to the traditional hybrid perovskite materials.[11-14] Although the device efficiency of these families of semiconductors is still far below the performance of their organic-inorganic analogues, a great potential of fully inorganic photoabsorbers has been predicted.[15-18] In particular, the interest for double perovskites is steadily growing, since two major factors impeding the ecological and commercial viability of perovskite-based photovoltaics are addressed: the toxicity of lead and the environmental stability of the perovskite layer.

In addition to improvement of the intrinsic stability of the perovskite material, the development of cost-effective encapsulation techniques for perovskite solar cells is vital to increase their long-term durability. The device lifetime needs to be significantly prolonged before perovskite-based photovoltaics can become industrially relevant and competitive to well-established technologies. Encouragingly, different sealing processes for both rigid and flexible substrates have already been reported in the past few years, extending the device lifetime up to several months.[19-23] Further progress of the encapsulation process in combination with achievements in the fundamental perovskite material design promise improvements in the long-term stability of perovskite solar cells under operational conditions. More extensive outdoor field testing, i.e. under simultaneous exposure to light, heat, air and moisture are imperative to assess the economic viability of this new photovoltaic technology.

9.3 References

[1] G. Grancini, C. Roldan-Carmona, I. Zimmermann, E. Mosconi, X. Lee, D. Martineau, S. Narbey, F. Oswald, F. De Angelis, M. Graetzel, M. K. Nazeeruddin, *Nat. Commun.* **2017**, *8*, 15684.

[2] K. T. Cho, G. Grancini, Y. Lee, E. Oveisi, J. Ryu, O. Almora, M. Tschumi, P. A. Schouwink, G. Seo, S. Heo, J. Park, J. Jang, S. Paek, G. Garcia-Belmonte, M. K. Nazeeruddin, *Energy. Environ. Sci.* **2018**.

[3] Z. Wang, Q. Lin, F. P. Chmiel, N. Sakai, L. M. Herz, H. J. Snaith, **2017**, *6*, 17135.

[4] T. M. Koh, V. Shanmugam, X. Guo, S. S. Lim, O. Filonik, E. M. Herzig, P. Muller-Buschbaum, V. Swamy, S. T. Chien, S. G. Mhaisalkar, N. Mathews, *J. Mater. Chem. A* **2018**, *6*, 2122.

[5] C. Ma, C. Leng, Y. Ji, X. Wei, K. Sun, L. Tang, J. Yang, W. Luo, C. Li, Y. Deng, S. Feng, J. Shen, S. Lu, C. Du, H. Shi, *Nanoscale* **2016**, *8*, 18309.

[6] Y. Lin, Y. Bai, Y. Fang, Z. Chen, S. Yang, X. Zheng, S. Tang, Y. Liu, J. Zhao, J. Huang, *J. Phys. Chem. Lett.* **2018**, *9*, 654.

[7] Y. Cho, A. M. Soufiani, J. S. Yun, J. Kim, D. S. Lee, J. Seidel, X. Deng, M. A. Green, S. Huang, A. W. Y. Ho‐Baillie, *Adv. Energy Mater.*, *0*, 1703392.

[8] R. E. Beal, D. J. Slotcavage, T. Leijtens, A. R. Bowring, R. A. Belisle, W. H. Nguyen, G. F. Burkhard, E. T. Hoke, M. D. McGehee, *J. Phys. Chem. Lett.* **2016**, *7*, 746.

[9] G. E. Eperon, G. M. Paterno, R. J. Sutton, A. Zampetti, A. A. Haghighirad, F. Cacialli, H. J. Snaith, *J. Mater. Chem. A* **2015**, *3*, 19688.

[10] R. J. Sutton, G. E. Eperon, L. Miranda, E. S. Parrott, B. A. Kamino, J. B. Patel, M. T. Hörantner, M. B. Johnston, A. A. Haghighirad, D. T. Moore, H. J. Snaith, *Adv. Energy Mater.* **2016**, *6*, 1502458.

[11] E. Greul, M. Petrus, A. Binek, P. Docampo, T. Bein, *J. Mater. Chem. A* **2017**, *5*, 19972.

[12] M. Pantaler, C. Fettkenhauer, H. L. Nguyen, I. Anusca, D. C. Lupascu, *MRS Advances* **2018**, 1.

[13] C. Wu, Q. Zhang, Y. Liu, W. Luo, X. Guo, Z. Huang, H. Ting, W. Sun, X. Zhong, S. Wei, S. Wang, Z. Chen, L. Xiao, *Advanced Science* **2018**, *5*, 1700759.

[14] W. Ning, F. Wang, B. Wu, J. Lu, Z. Yan, X. Liu, Y. Tao, J. M. Liu, W. Huang, M. Fahlman, L. Hultman, T. C. Sum, F. Gao, *Adv. Mater.*, *0*, 1706246.

[15] J. Yang, P. Zhang, S.-H. Wei, *J. Phys. Chem. Lett.* **2018**, *9*, 31.

[16] D. Bartesaghi, A. H. Slavney, M. C. Gélvez-Rueda, B. A. Connor, F. C. Grozema, H. I. Karunadasa, T. J. Savenije, *J. Phys. Chem. C* **2018**, *122*, 4809.

[17] A. H. Slavney, T. Hu, A. M. Lindenberg, H. I. Karunadasa, *J. Am. Chem. Soc.* **2016**, *138*, 2138.

[18] F. Giustino, H. J. Snaith, *ACS Energy Lett.* **2016**, *1*, 1233.

[19] H. C. Weerasinghe, Y. Dkhissi, A. D. Scully, R. A. Caruso, Y.-B. Cheng, *Nano Energy* **2015**, *18*, 118.

[20] F. Matteocci, L. Cinà, E. Lamanna, S. Cacovich, G. Divitini, P. A. Midgley, C. Ducati, A. Di Carlo, *Nano Energy* **2016**, *30*, 162.

[21] Y. I. Lee, N. J. Jeon, B. J. Kim, H. Shim, T. Y. Yang, S. I. Seok, J. Seo, S. G. Im, *Adv. Energy Mater.* **2018**, *8*, 1701928.

[22] R. Cheacharoen, N. Rolston, D. Harwood, K. A. Bush, R. H. Dauskardt, M. D. McGehee, *Energy. Environ. Sci.* **2018**, *11*, 144.

[23] F. Bella, G. Griffini, J.-P. Correa-Baena, G. Saracco, M. Grätzel, A. Hagfeldt, S. Turri, C. Gerbaldi, *Science* **2016**, *354*, 203.

Publications and Presentations

List of publications

1) Y. Hu,* E. M. Hutter,* P. Rieder,* I. Grill, J. Hanisch, M. F. Aygüler, A. G. Hufnagel, M. Handloser, T. Bein, A. Hartschuh, K. Tvingstedt, V. Dyakonov, A. Baumann, T. J. Savenije, M. L. Petrus, P. Docampo, "Understanding the Role of Cesium and Rubidium Additives in Perovskite Solar Cells: Trap States, Charge Transport, and Recombination" *Advanced Energy Materials*, **2018**, 1703057 (including front cover image).

2) M. L. Petrus, A. Music, A. C. Closs, J. C Bijleveld, M. Sirtl, Y. Hu, T. J. Dingemans, T. Bein, P. Docampo, "Design rules for the preparation of low-cost hole transporting materials for perovskite solar cells with moisture barrier properties" *Journal of Materials Chemistry A*, **2017**, *5*, 25200–25210.

3) Y. Hu, M.F. Aygüler, M.L. Petrus, T. Bein, P. Docampo, "Impact of Rubidium and Cesium Cations on the Moisture Stability of Multiple-Cation Mixed-Halide Perovskites" *ACS Energy Letters* **2017**, *2*, 2212-2218.

4) M. L. Petrus,* Y. Hu,* D. Moia, P. Calado, A. M. A. Leguy, P. R. F. Barnes, P. Docampo, "The Influence of Water Vapor on the Stability and Processing of Hybrid Perovskite Solar Cells Made from Non-Stoichiometric Precursor Mixtures" *ChemSusChem* **2016**, *9* (18), 2699-2707.

5) Y. Hu, J. Schlipf, M. Wussler, M. L. Petrus, W. Jaegermann, T. Bein, P. Müller-Buschbaum, P. Docampo, „Hybrid Perovskite/Perovskite Heterojunction Solar Cells" *ACS Nano* **2016**, *10* (6), 5999-6007.

6) A. Binek, M. L. Petrus, N. Huber, H. Bristow, Y. Hu, T. Bein, P. Docampo, "Recycling Perovskite Solar Cells To Avoid Lead Waste" *ACS Applied Materials & Interfaces* **2016**, *8* (20), 12881-12886.

7) L. Oesinghaus, J. Schlipf, N. Giesbrecht, L. Song, Y. Hu, T. Bein, P. Docampo, P. Müller-Buschbaum, „Toward Tailored Film Morphologies: The Origin of Crystal Orientation in Hybrid Perovskite Thin Films" *Advanced Materials Interfaces* **2016**, *3* (19) 1600403.

8) A. M. A. Leguy,* Y. Hu,* M. Campoy-Quiles, M. I. Alonso, O.J. Weber, P. Azarhoosh, M. van Schilfgaarde, M. T. Weller, T. Bein, J. Nelson, P. Docampo and P. R. F. Barnes, "Reversible Hydration of $CH_3NH_3PbI_3$ in Films, Single Crystals, and Solar Cells" *Chemistry of Materials* **2015**, *27* (9), 3397–3407.

9) D. D. Medina,* J. M. Rotter,* Y. Hu, M. Dogru, V. Werner, F. Auras, J. T. Markiewicz, P. Knochel and T. Bein, "Room temperature synthesis of covalent–organic framework films through vapor-assisted conversion" *Journal of the American Chemical Society* **2015**, *137*, 1016-1019.

10) A. Ranft, I. Pavlichenko, K. Szendrei, P. M. Zehetmaier, Y. Hu, A. von Mankowski, B.V. Lotsch, „1D photonic defect structures based on colloidal porous frameworks: reverse pore engineering and vapor sorption" *Microporous and Mesoporous Materials* **2015**, *216*, 216-224.

* These authors contributed equally to the work.

Oral presentations

1) Y. Hu, A. M. A. Leguy, M. Campoy-Quiles, M. I. Alonso, O. J. Weber, P. Azarhoosh, M. van Schilfgaarde, M. T. Weller, T. Bein, J. Nelson, P. R. F. Barnes, P. Docampo "Reversible hydration of $CH_3NH_3PbI_3$ in films, single crystals and solar cells" *E-MRS Fall Meeting*, **2015**, Warsaw, Poland

2) Y. Hu, A. M. A. Leguy, M. Campoy-Quiles, M. I. Alonso, O. J. Weber, P. Azarhoosh, M. van Schilfgaarde, M. T. Weller, T. Bein, J. Nelson, P. R. F. Barnes, P. Docampo "Humidity-induced hydration of methylammonium lead iodide perovskite: Understanding and prevention" *DPG Conference*, **2016**, Regensburg, Germany

3) Y. Hu, J. Schlipf, M. Wussler, W. Jaegermann, T. Bein, P. Müller-Buschbaum, P. Docampo "Hybrid perovskite/perovskite heterojunction solar cells" *HOPV Conference*, **2016**, Swansea, United Kingdom

4) Y. Hu "Solarzellen der Zukunft: Auf der Suche nach dem perfekten Material" *NIM NanoDay*, **2017**, Munich, Germany

5) Y. Hu, M. F. Aygüler, M. L. Petrus, T. Bein, P. Docampo "Rubidium-containing Mixed-Halide Perovskite Solar Cells Diagnosed with Aquaphobia" *PSCO Conference*, **2017**, Oxford, United Kingdom

6) Y. Hu, E. M. Hutter, P. Rieder, I. Grill, J. Hanisch, M. F. Aygüler, A. G. Hufnagel, M. Handloser, T. Bein, A. Hartschuh, K. Tvingstedt, V. Dyakonov, A. Baumann, T. J. Savenije, M. L. Petrus, P. Docampo, "Understanding the Role of Cesium and Rubidium Additives in Perovskite Solar Cells: Trap States and Charge Carrier Mobility" *HOPV Conference*, **2018**, Benidorm, Spain

Poster presentations

1) Y. Hu, A. M. A. Leguy, M. Campoy-Quiles, M. I. Alonso, O. J. Weber, P. Azarhoosh, M. van Schilfgaarde, M. T. Weller, T. Bein, J. Nelson, P. R. F. Barnes, P. Docampo "Reversible hydration of $CH_3NH_3PbI_3$ in films, single crystals and solar cells" *PSCO Conference,* **2015**, Lausanne, Switzerland

2) Y. Hu, A. M. A. Leguy, T. Bein, J. Nelson, P. R. F. Barnes, P. Docampo "Reversible hydration of methylammonium lead iodide in films, single crystals and solar cells" *SolTech Conference*, **2016**, Munich, Germany

3) Y. Hu, J. Schlipf, M. Wussler, W. Jaegermann, T. Bein, P. Müller-Buschbaum, P. Docampo "Hybrid perovskite/perovskite heterojunction solar cells" *CeNS Workshop*, **2016**, Venice, Italy

4) Y. Hu, J. Schlipf, M. Wussler, W. Jaegermann, T. Bein, P. Müller-Buschbaum, P. Docampo "Hybrid perovskite/perovskite heterojunction solar cells" *MRS Fall Meeting & Exhibit*, **2016**, Boston, USA

5) Y. Hu, A. M. A. Leguy, M. Campoy-Quiles, M. I. Alonso, O. J. Weber, P. Azarhoosh, M. van Schilfgaarde, M. T. Weller, T. Bein, J. Nelson, P. R. F. Barnes, P. Docampo "Reversible hydration of $CH_3NH_3PbI_3$ in films, single crystals and solar cells" *MRS Fall Meeting & Exhibit*, **2016**, Boston, USA

6) Y. Hu, J. Schlipf, M. Wussler, W. Jaegermann, T. Bein, P. Müller-Buschbaum, P. Docampo "Hybrid perovskite/perovskite heterojunction solar cells" *NIM Workshop Young Ideas in Nanoscience*, **2017**, Munich, Germany

7) Y. Hu, M. F. Aygüler, M. L. Petrus, T. Bein, P. Docampo "Impact of Rubidium and Cesium Cations on the Moisture Stability of Multiple-Cation Mixed-Halide Perovskites" *HOPV Conference*, **2018**, Benidorm, Spain